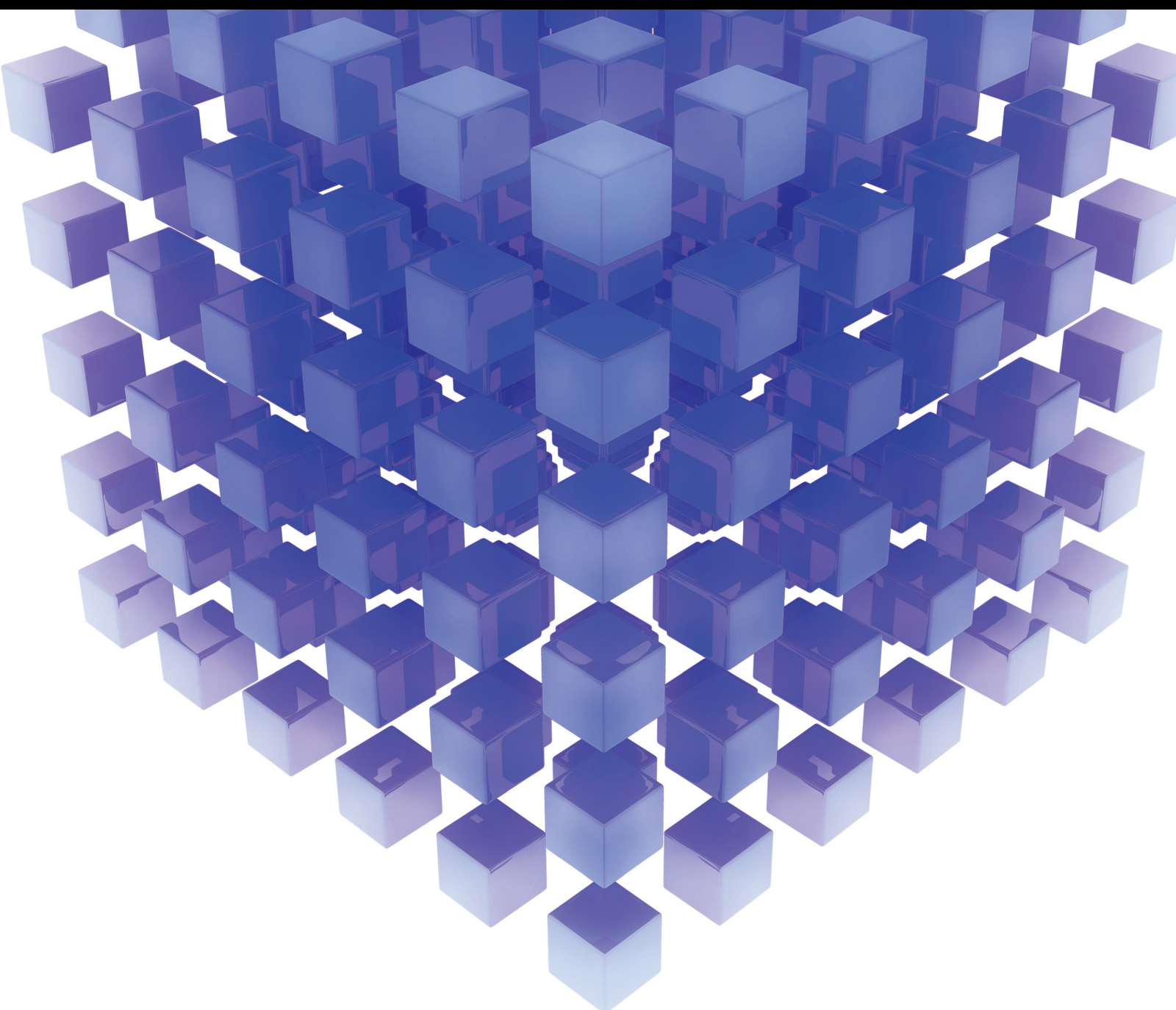


# AI-Based Condition Monitoring in Manufacturing Systems

Lead Guest Editor: Yuqing Zhou

Guest Editors: Anil Kumar and Weifang Sun





---

# **AI-Based Condition Monitoring in Manufacturing Systems**

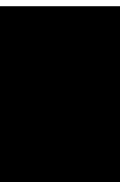
Mathematical Problems in Engineering

---

## **AI-Based Condition Monitoring in Manufacturing Systems**

Lead Guest Editor: Yuqing Zhou

Guest Editors: Anil Kumar and Weifang Sun




---

Copyright © 2021 Hindawi Limited. All rights reserved.

This is a special issue published in “Mathematical Problems in Engineering.” All articles are open access articles distributed under the Creative Commons Attribution License, which permits unrestricted use, distribution, and reproduction in any medium, provided the original work is properly cited.




# Chief Editor

Guangming Xie , China

## Academic Editors

Kumaravel A , India  
Waqas Abbasi, Pakistan  
Mohamed Abd El Aziz , Egypt  
Mahmoud Abdel-Aty , Egypt  
Mohammed S. Abdo, Yemen  
Mohammad Yaghoub Abdollahzadeh  
Jamalabadi , Republic of Korea  
Rahib Abiyev , Turkey  
Leonardo Acho , Spain  
Daniela Addessi , Italy  
Arooj Adeel , Pakistan  
Waleed Adel , Egypt  
Ramesh Agarwal , USA  
Francesco Aggogeri , Italy  
Ricardo Aguilar-Lopez , Mexico  
Afaq Ahmad , Pakistan  
Naveed Ahmed , Pakistan  
Elias Aifantis , USA  
Akif Akgul , Turkey  
Tareq Al-shami , Yemen  
Guido Ala, Italy  
Andrea Alaimo , Italy  
Reza Alam, USA  
Osamah Albahri , Malaysia  
Nicholas Alexander , United Kingdom  
Salvatore Alfonzetti, Italy  
Ghous Ali , Pakistan  
Nouman Ali , Pakistan  
Mohammad D. Aliyu , Canada  
Juan A. Almendral , Spain  
A.K. Alomari, Jordan  
José Domingo Álvarez , Spain  
Cláudio Alves , Portugal  
Juan P. Amezcua-Sanchez, Mexico  
Mukherjee Amitava, India  
Lionel Amodeo, France  
Sebastian Anita, Romania  
Costanza Arico , Italy  
Sabri Arik, Turkey  
Fausto Arpino , Italy  
Rashad Asharabi , Saudi Arabia  
Farhad Aslani , Australia  
Mohsen Asle Zaem , USA

Andrea Avanzini , Italy  
Richard I. Avery , USA  
Viktor Avrutin , Germany  
Mohammed A. Awadallah , Malaysia  
Francesco Aymerich , Italy  
Sajad Azizi , Belgium  
Michele Bacciocchi , Italy  
Seungik Baek , USA  
Khaled Bahlali, France  
M.V.A Raju Bahubalendruni, India  
Pedro Balaguer , Spain  
P. Balasubramaniam, India  
Stefan Balint , Romania  
Ines Tejado Balsera , Spain  
Alfonso Banos , Spain  
Jerzy Baranowski , Poland  
Tudor Barbu , Romania  
Andrzej Bartoszewicz , Poland  
Sergio Baselga , Spain  
S. Caglar Baslamisli , Turkey  
David Bassir , France  
Chiara Bedon , Italy  
Azeddine Beghdadi, France  
Andriette Bekker , South Africa  
Francisco Beltran-Carbajal , Mexico  
Abdellatif Ben Makhlof , Saudi Arabia  
Denis Benasciutti , Italy  
Ivano Benedetti , Italy  
Rosa M. Benito , Spain  
Elena Benvenuti , Italy  
Giovanni Berselli, Italy  
Michele Betti , Italy  
Pietro Bia , Italy  
Carlo Bianca , France  
Simone Bianco , Italy  
Vincenzo Bianco, Italy  
Vittorio Bianco, Italy  
David Bigaud , France  
Sardar Muhammad Bilal , Pakistan  
Antonio Bilotta , Italy  
Sylvio R. Bistafa, Brazil  
Chiara Boccaletti , Italy  
Rodolfo Bontempo , Italy  
Alberto Borboni , Italy  
Marco Bortolini, Italy

Paolo Boscariol, Italy  
Daniela Boso , Italy  
Guillermo Botella-Juan, Spain  
Abdesselem Boulkroune , Algeria  
Boulaïd Boulkroune, Belgium  
Fabio Bovenga , Italy  
Francesco Braghin , Italy  
Ricardo Branco, Portugal  
Julien Bruchon , France  
Matteo Bruggi , Italy  
Michele Brun , Italy  
Maria Elena Bruni, Italy  
Maria Angela Butturi , Italy  
Bartłomiej Błachowski , Poland  
Dhanamjayulu C , India  
Raquel Caballero-Águila , Spain  
Filippo Cacace , Italy  
Salvatore Caddemi , Italy  
Zuowei Cai , China  
Roberto Caldelli , Italy  
Francesco Cannizzaro , Italy  
Maosen Cao , China  
Ana Carpio, Spain  
Rodrigo Carvajal , Chile  
Caterina Casavola, Italy  
Sara Casciati, Italy  
Federica Caselli , Italy  
Carmen Castillo , Spain  
Inmaculada T. Castro , Spain  
Miguel Castro , Portugal  
Giuseppe Catalanotti , United Kingdom  
Alberto Cavallo , Italy  
Gabriele Cazzulani , Italy  
Fatih Vehbi Celebi, Turkey  
Miguel Cerrolaza , Venezuela  
Gregory Chagnon , France  
Ching-Ter Chang , Taiwan  
Kuei-Lun Chang , Taiwan  
Qing Chang , USA  
Xiaoheng Chang , China  
Prasenjit Chatterjee , Lithuania  
Kacem Chehdi, France  
Peter N. Cheimets, USA  
Chih-Chiang Chen , Taiwan  
He Chen , China



































Kebing Chen , China  
Mengxin Chen , China  
Shyi-Ming Chen , Taiwan  
Xizhong Chen , Ireland  
Xue-Bo Chen , China  
Zhiwen Chen , China  
Qiang Cheng, USA  
Zeyang Cheng, China  
Luca Chiapponi , Italy  
Francisco Chicano , Spain  
Tirivanhu Chinyoka , South Africa  
Adrian Chmielewski , Poland  
Seongim Choi , USA  
Gautam Choubey , India  
Hung-Yuan Chung , Taiwan  
Yusheng Ci, China  
Simone Cinquemani , Italy  
Roberto G. Citarella , Italy  
Joaquim Ciurana , Spain  
John D. Clayton , USA  
Piero Colajanni , Italy  
Giuseppina Colicchio, Italy  
Vassilios Constantoudis , Greece  
Enrico Conte, Italy  
Alessandro Contento , USA  
Mario Cools , Belgium  
Gino Cortellessa, Italy  
Carlo Cosentino , Italy  
Paolo Crippa , Italy  
Erik Cuevas , Mexico  
Guozeng Cui , China  
Mehmet Cunkas , Turkey  
Giuseppe D'Aniello , Italy  
Peter Dabnichki, Australia  
Weizhong Dai , USA  
Zhifeng Dai , China  
Purushothaman Damodaran , USA  
Sergey Dashkovskiy, Germany  
Adiel T. De Almeida-Filho , Brazil  
Fabio De Angelis , Italy  
Samuele De Bartolo , Italy  
Stefano De Miranda , Italy  
Filippo De Monte , Italy

José António Fonseca De Oliveira  
Correia , Portugal  
Jose Renato De Sousa , Brazil  
Michael Defoort, France  
Alessandro Della Corte, Italy  
Laurent Dewasme , Belgium  
Sanku Dey , India  
Gianpaolo Di Bona , Italy  
Roberta Di Pace , Italy  
Francesca Di Puccio , Italy  
Ramón I. Diego , Spain  
Yannis Dimakopoulos , Greece  
Hasan Dinçer , Turkey  
José M. Domínguez , Spain  
Georgios Dounias, Greece  
Bo Du , China  
Emil Dumic, Croatia  
Madalina Dumitriu , United Kingdom  
Premraj Durairaj , India  
Saeed Eftekhari Azam, USA  
Said El Kafhali , Morocco  
Antonio Elipse , Spain  
R. Emre Erkmen, Canada  
John Escobar , Colombia  
Leandro F. F. Miguel , Brazil  
FRANCESCO FOTI , Italy  
Andrea L. Facci , Italy  
Shahla Faisal , Pakistan  
Giovanni Falsone , Italy  
Hua Fan, China  
Jianguang Fang, Australia  
Nicholas Fantuzzi , Italy  
Muhammad Shahid Farid , Pakistan  
Hamed Faruqi, Iran  
Yann Favennec, France  
Fiorenzo A. Fazzolari , United Kingdom  
Giuseppe Fedele , Italy  
Roberto Fedele , Italy  
Baowei Feng , China  
Mohammad Ferdows , Bangladesh  
Arturo J. Fernández , Spain  
Jesus M. Fernandez Oro, Spain  
Francesco Ferrise, Italy  
Eric Feulvarch , France  
Thierry Floquet, France















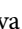
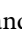
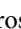







Eric Florentin , France  
Gerardo Flores, Mexico  
Antonio Forcina , Italy  
Alessandro Formisano, Italy  
Francesco Franco , Italy  
Elisa Francomano , Italy  
Juan Frausto-Solis, Mexico  
Shujun Fu , China  
Juan C. G. Prada , Spain  
HECTOR GOMEZ , Chile  
Matteo Gaeta , Italy  
Mauro Gaggero , Italy  
Zoran Gajic , USA  
Jaime Gallardo-Alvarado , Mexico  
Mosè Gallo , Italy  
Akemi Gálvez , Spain  
Maria L. Gandarias , Spain  
Hao Gao , Hong Kong  
Xingbao Gao , China  
Yan Gao , China  
Zhiwei Gao , United Kingdom  
Giovanni Garcea , Italy  
José García , Chile  
Harish Garg , India  
Alessandro Gasparetto , Italy  
Stylianos Georgantzinou, Greece  
Fotios Georgiades , India  
Parviz Ghadimi , Iran  
Ştefan Cristian Gherghina , Romania  
Georgios I. Giannopoulos , Greece  
Agathoklis Giaralis , United Kingdom  
Anna M. Gil-Lafuente , Spain  
Ivan Giorgio , Italy  
Gaetano Giunta , Luxembourg  
Jefferson L.M.A. Gomes , United Kingdom  
Emilio Gómez-Déniz , Spain  
Antonio M. Gonçalves de Lima , Brazil  
Qunxi Gong , China  
Chris Goodrich, USA  
Rama S. R. Gorla, USA  
Veena Goswami , India  
Xunjie Gou , Spain  
Jakub Grabski , Poland

Antoine Grall , France  
George A. Gravvanis , Greece  
Fabrizio Greco , Italy  
David Greiner , Spain  
Jason Gu , Canada  
Federico Guarracino , Italy  
Michele Guida , Italy  
Muhammet Gul , Turkey  
Dong-Sheng Guo , China  
Hu Guo , China  
Zhaoxia Guo, China  
Yusuf Gurefe, Turkey  
Salim HEDDAM , Algeria  
ABID HUSSANAN, China  
Quang Phuc Ha, Australia  
Li Haitao , China  
Petr Hájek , Czech Republic  
Mohamed Hamdy , Egypt  
Muhammad Hamid , United Kingdom  
Renke Han , United Kingdom  
Weimin Han , USA  
Xingsi Han, China  
Zhen-Lai Han , China  
Thomas Hanne , Switzerland  
Xinan Hao , China  
Mohammad A. Hariri-Ardebili , USA  
Khalid Hattaf , Morocco  
Defeng He , China  
Xiao-Qiao He, China  
Yanchao He, China  
Yu-Ling He , China  
Ramdane Hedjar , Saudi Arabia  
Jude Hemanth , India  
Reza Hemmati, Iran  
Nicolae Herisanu , Romania  
Alfredo G. Hernández-Díaz , Spain  
M.I. Herreros , Spain  
Eckhard Hitzer , Japan  
Paul Honeine , France  
Jaromir Horacek , Czech Republic  
Lei Hou , China  
Yingkun Hou , China  
Yu-Chen Hu , Taiwan  
Yunfeng Hu, China  
Can Huang , China  
Gordon Huang , Canada  
Linsheng Huo , China  
Sajid Hussain, Canada  
Asier Ibeas , Spain  
Orest V. Iftime , The Netherlands  
Przemyslaw Ignaciuk , Poland  
Giacomo Innocenti , Italy  
Emilio Insfran Pelozo , Spain  
Azeem Irshad, Pakistan  
Alessio Ishizaka, France  
Benjamin Ivorra , Spain  
Breno Jacob , Brazil  
Reema Jain , India  
Tushar Jain , India  
Amin Jajarmi , Iran  
Chiranjibe Jana , India  
Łukasz Jankowski , Poland  
Samuel N. Jator , USA  
Juan Carlos Jáuregui-Correa , Mexico  
Kandasamy Jayakrishna, India  
Reza Jazar, Australia  
Khalide Jbilou, France  
Isabel S. Jesus , Portugal  
Chao Ji , China  
Qing-Chao Jiang , China  
Peng-fei Jiao , China  
Ricardo Fabricio Escobar Jiménez , Mexico  
Emilio Jiménez Macías , Spain  
Maolin Jin, Republic of Korea  
Zhuo Jin, Australia  
Ramash Kumar K , India  
BHABEN KALITA , USA  
MOHAMMAD REZA KHEDMATI , Iran  
Viacheslav Kalashnikov , Mexico  
Mathiyalagan Kalidass , India  
Tamas Kalmar-Nagy , Hungary  
Rajesh Kaluri , India  
Jyotheeswara Reddy Kalvakurthi, India  
Zhao Kang , China  
Ramani Kannan , Malaysia  
Tomasz Kapitaniak , Poland  
Julius Kaplunov, United Kingdom  
Konstantinos Karamanos, Belgium  
Michal Kawulok, Poland

Irfan Kaymaz , Turkey  
Vahid Kayvanfar , Qatar  
Krzysztof Kecik , Poland  
Mohamed Khader , Egypt  
Chaudry M. Khalique , South Africa  
Mukhtaj Khan , Pakistan  
Shahid Khan , Pakistan  
Nam-Il Kim, Republic of Korea  
Philipp V. Kiryukhantsev-Korneev ,  
Russia  
P.V.V Kishore , India  
Jan Koci , Czech Republic  
Ioannis Kostavelis , Greece  
Sotiris B. Kotsiantis , Greece  
Frederic Kratz , France  
Vamsi Krishna , India  
Edyta Kucharska, Poland  
Krzysztof S. Kulpa , Poland  
Kamal Kumar, India  
Prof. Ashwani Kumar , India  
Michal Kunicki , Poland  
Cedrick A. K. Kwuimy , USA  
Kyandoghere Kyamakya, Austria  
Ivan Kyrchei , Ukraine  
Márcio J. Lacerda , Brazil  
Eduardo Lalla , The Netherlands  
Giovanni Lancioni , Italy  
Jaroslaw Latalski , Poland  
Hervé Laurent , France  
Agostino Lauria , Italy  
Aimé Lay-Ekuakille , Italy  
Nicolas J. Leconte , France  
Kun-Chou Lee , Taiwan  
Dimitri Lefebvre , France  
Eric Lefevre , France  
Marek Lefik, Poland  
Yaguo Lei , China  
Kauko Leiviskä , Finland  
Ervin Lenzi , Brazil  
ChenFeng Li , China  
Jian Li , USA  
Jun Li , China  
Yueyang Li , China  
Zhao Li , China

Zhen Li , China  
En-Qiang Lin, USA  
Jian Lin , China  
Qibin Lin, China  
Yao-Jin Lin, China  
Zhiyun Lin , China  
Bin Liu , China  
Bo Liu , China  
Heng Liu , China  
Jianxu Liu , Thailand  
Lei Liu , China  
Sixin Liu , China  
Wanquan Liu , China  
Yu Liu , China  
Yuanchang Liu , United Kingdom  
Bonifacio Llamazares , Spain  
Alessandro Lo Schiavo , Italy  
Jean Jacques Loiseau , France  
Francesco Lolli , Italy  
Paolo Lonetti , Italy  
António M. Lopes , Portugal  
Sebastian López, Spain  
Luis M. López-Ochoa , Spain  
Vassilios C. Loukopoulos, Greece  
Gabriele Maria Lozito , Italy  
Zhiguo Luo , China  
Gabriel Luque , Spain  
Valentin Lychagin, Norway  
YUE MEI, China  
Junwei Ma , China  
Xuanlong Ma , China  
Antonio Madeo , Italy  
Alessandro Magnani , Belgium  
Toqeer Mahmood , Pakistan  
Fazal M. Mahomed , South Africa  
Arunava Majumder , India  
Sarfranz Nawaz Malik, Pakistan  
Paolo Manfredi , Italy  
Adnan Maqsood , Pakistan  
Muazzam Maqsood, Pakistan  
Giuseppe Carlo Marano , Italy  
Damijan Markovic, France  
Filipe J. Marques , Portugal  
Luca Martinelli , Italy  
Denizar Cruz Martins, Brazil






























Francisco J. Martos , Spain  
Elio Masciari , Italy  
Paolo Massioni , France  
Alessandro Mauro , Italy  
Jonathan Mayo-Maldonado , Mexico  
Pier Luigi Mazzeo , Italy  
Laura Mazzola, Italy  
Driss Mehdi , France  
Zahid Mehmood , Pakistan  
Roderick Melnik , Canada  
Xiangyu Meng , USA  
Jose Merodio , Spain  
Alessio Merola , Italy  
Mahmoud Mesbah , Iran  
Luciano Mescia , Italy  
Laurent Mevel , France  
Constantine Michailides , Cyprus  
Mariusz Michta , Poland  
Prankul Middha, Norway  
Aki Mikkola , Finland  
Giovanni Minafò , Italy  
Edmondo Minisci , United Kingdom  
Hiroyuki Mino , Japan  
Dimitrios Mitsotakis , New Zealand  
Ardashir Mohammadzadeh , Iran  
Francisco J. Montáns , Spain  
Francesco Montefusco , Italy  
Gisele Mophou , France  
Rafael Morales , Spain  
Marco Morandini , Italy  
Javier Moreno-Valenzuela , Mexico  
Simone Morganti , Italy  
Caroline Mota , Brazil  
Aziz Moukrim , France  
Shen Mouquan , China  
Dimitris Mourtzis , Greece  
Emiliano Mucchi , Italy  
Taseer Muhammad, Saudi Arabia  
Ghulam Muhiuddin, Saudi Arabia  
Amitava Mukherjee , India  
Josefa Mula , Spain  
Jose J. Muñoz , Spain  
Giuseppe Muscolino, Italy  
Marco Mussetta , Italy

Hariharan Muthusamy, India  
Alessandro Naddeo , Italy  
Raj Nandkeolyar, India  
Keivan Navaie , United Kingdom  
Soumya Nayak, India  
Adrian Neagu , USA  
Erivelton Geraldo Nepomuceno , Brazil  
AMA Neves, Portugal  
Ha Quang Thinh Ngo , Vietnam  
Nhon Nguyen-Thanh, Singapore  
Papakostas Nikolaos , Ireland  
Jelena Nikolic , Serbia  
Tatsushi Nishi, Japan  
Shanzhou Niu , China  
Ben T. Nohara , Japan  
Mohammed Nouari , France  
Mustapha Nourelfath, Canada  
Kazem Nouri , Iran  
Ciro Núñez-Gutiérrez , Mexico  
Włodzimierz Ogryczak, Poland  
Roger Ohayon, France  
Krzysztof Okarma , Poland  
Mitsuhiro Okayasu, Japan  
Murat Olgun , Turkey  
Diego Oliva, Mexico  
Alberto Olivares , Spain  
Enrique Onieva , Spain  
Calogero Orlando , Italy  
Susana Ortega-Cisneros , Mexico  
Sergio Ortobelli, Italy  
Naohisa Otsuka , Japan  
Sid Ahmed Ould Ahmed Mahmoud , Saudi Arabia  
Taoreed Owolabi , Nigeria  
EUGENIA PETROPOULOU , Greece  
Arturo Pagano, Italy  
Madhumangal Pal, India  
Pasquale Palumbo , Italy  
Dragan Pamučar, Serbia  
Weifeng Pan , China  
Chandan Pandey, India  
Rui Pang, United Kingdom  
Jürgen Pannek , Germany  
Elena Panteley, France  
Achille Paolone, Italy

George A. Papakostas , Greece  
Xosé M. Pardo , Spain  
You-Jin Park, Taiwan  
Manuel Pastor, Spain  
Pubudu N. Pathirana , Australia  
Surajit Kumar Paul , India  
Luis Payá , Spain  
Igor Pažanin , Croatia  
Libor Pekař , Czech Republic  
Francesco Pellicano , Italy  
Marcello Pellicciari , Italy  
Jian Peng , China  
Mingshu Peng, China  
Xiang Peng , China  
Xindong Peng, China  
Yuexing Peng, China  
Marzio Pennisi , Italy  
Maria Patrizia Pera , Italy  
Matjaz Perc , Slovenia  
A. M. Bastos Pereira , Portugal  
Wesley Peres, Brazil  
F. Javier Pérez-Pinal , Mexico  
Michele Perrella, Italy  
Francesco Pesavento , Italy  
Francesco Petrini , Italy  
Hoang Vu Phan, Republic of Korea  
Lukasz Pieczonka , Poland  
Dario Piga , Switzerland  
Marco Pizzarelli , Italy  
Javier Plaza , Spain  
Goutam Pohit , India  
Dragan Poljak , Croatia  
Jorge Pomares , Spain  
Hiram Ponce , Mexico  
Sébastien Poncet , Canada  
Volodymyr Ponomaryov , Mexico  
Jean-Christophe Ponsart , France  
Mauro Pontani , Italy  
Sivakumar Poruran, India  
Francesc Pozo , Spain  
Aditya Rio Prabowo , Indonesia  
Anchasa Pramuanjaroenkij , Thailand  
Leonardo Primavera , Italy  
B Rajanarayan Prusty, India

Krzysztof Puszynski , Poland  
Chuan Qin , China  
Dongdong Qin, China  
Jianlong Qiu , China  
Giuseppe Quaranta , Italy  
DR. RITU RAJ , India  
Vitomir Racic , Italy  
Carlo Rainieri , Italy  
Kumbakonam Ramamani Rajagopal, USA  
Ali Ramazani , USA  
Angel Manuel Ramos , Spain  
Higinio Ramos , Spain  
Muhammad Afzal Rana , Pakistan  
Muhammad Rashid, Saudi Arabia  
Manoj Rastogi, India  
Alessandro Rasulo , Italy  
S.S. Ravindran , USA  
Abdolrahman Razani , Iran  
Alessandro Reali , Italy  
Jose A. Reinoso , Spain  
Oscar Reinoso , Spain  
Haijun Ren , China  
Carlo Renno , Italy  
Fabrizio Renno , Italy  
Shahram Rezapour , Iran  
Ricardo Rianza , Spain  
Francesco Riganti-Fulginei , Italy  
Gerasimos Rigatos , Greece  
Francesco Ripamonti , Italy  
Jorge Rivera , Mexico  
Eugenio Roanes-Lozano , Spain  
Ana Maria A. C. Rocha , Portugal  
Luigi Rodino , Italy  
Francisco Rodríguez , Spain  
Rosana Rodríguez López, Spain  
Francisco Rossomando , Argentina  
Jose de Jesus Rubio , Mexico  
Weiguo Rui , China  
Rubén Ruiz , Spain  
Ivan D. Rukhlenko , Australia  
Dr. Eswaramoorthi S. , India  
Weichao SHI , United Kingdom  
Chaman Lal Sabharwal , USA  
Andrés Sáez , Spain



Bekir Sahin, Turkey  
Laxminarayan Sahoo , India  
John S. Sakellariou , Greece  
Michael Sakellariou , Greece  
Salvatore Salamone, USA  
Jose Vicente Salcedo , Spain  
Alejandro Salcido , Mexico  
Alejandro Salcido, Mexico  
Nunzio Salerno , Italy  
Rohit Salgotra , India  
Miguel A. Salido , Spain  
Sinan Salih , Iraq  
Alessandro Salvini , Italy  
Abdus Samad , India  
Sovan Samanta, India  
Nikolaos Samaras , Greece  
Ramon Sancibrian , Spain  
Giuseppe Sanfilippo , Italy  
Omar-Jacobo Santos, Mexico  
J Santos-Reyes , Mexico  
José A. Sanz-Herrera , Spain  
Musavarah Sarwar, Pakistan  
Shahzad Sarwar, Saudi Arabia  
Marcelo A. Savi , Brazil  
Andrey V. Savkin, Australia  
Tadeusz Sawik , Poland  
Roberta Sburlati, Italy  
Gustavo Scaglia , Argentina  
Thomas Schuster , Germany  
Hamid M. Sedighi , Iran  
Mijanur Rahaman Seikh, India  
Tapan Senapati , China  
Lotfi Senhadji , France  
Junwon Seo, USA  
Michele Serpilli, Italy  
Silvestar Šesnić , Croatia  
Gerardo Severino, Italy  
Ruben Sevilla , United Kingdom  
Stefano Sfarra , Italy  
Dr. Ismail Shah , Pakistan  
Leonid Shaikhet , Israel  
Vimal Shanmuganathan , India  
Prayas Sharma, India  
Bo Shen , Germany  
Hang Shen, China

Xin Pu Shen, China  
Dimitri O. Shepelsky, Ukraine  
Jian Shi , China  
Amin Shokrollahi, Australia  
Suzanne M. Shontz , USA  
Babak Shotorban , USA  
Zhan Shu , Canada  
Angelo Sifaleras , Greece  
Nuno Simões , Portugal  
Mehakpreet Singh , Ireland  
Piyush Pratap Singh , India  
Rajiv Singh, India  
Seralathan Sivamani , India  
S. Sivasankaran , Malaysia  
Christos H. Skiadas, Greece  
Konstantina Skouri , Greece  
Neale R. Smith , Mexico  
Bogdan Smolka, Poland  
Delfim Soares Jr. , Brazil  
Alba Sofi , Italy  
Francesco Soldovieri , Italy  
Raffaele Solimene , Italy  
Yang Song , Norway  
Jussi Sopanen , Finland  
Marco Spadini , Italy  
Paolo Spagnolo , Italy  
Ruben Specogna , Italy  
Vasilios Spitas , Greece  
Ivanka Stamova , USA  
Rafał Stanisławski , Poland  
Miladin Stefanović , Serbia  
Salvatore Strano , Italy  
Yakov Strelniker, Israel  
Kangkang Sun , China  
Qiuqin Sun , China  
Shuaishuai Sun, Australia  
Yanchao Sun , China  
Zong-Yao Sun , China  
Kumarasamy Suresh , India  
Sergey A. Suslov , Australia  
D.L. Suthar, Ethiopia  
D.L. Suthar , Ethiopia  
Andrzej Swierniak, Poland  
Andras Szekrenyes , Hungary  
Kumar K. Tamma, USA




Yong (Aaron) Tan, United Kingdom  
Marco Antonio Taneco-Hernández , Mexico  
Lu Tang , China  
Tianyou Tao, China  
Hafez Tari , USA  
Alessandro Tasora , Italy  
Sergio Teggi , Italy  
Adriana del Carmen Téllez-Anguiano , Mexico  
Ana C. Teodoro , Portugal  
Efstathios E. Theotokoglou , Greece  
Jing-Feng Tian, China  
Alexander Timokha , Norway  
Stefania Tomasiello , Italy  
Gisella Tomasini , Italy  
Isabella Torcicollo , Italy  
Francesco Tornabene , Italy  
Mariano Torrisi , Italy  
Thang nguyen Trung, Vietnam  
George Tsiatas , Greece  
Le Anh Tuan , Vietnam  
Nerio Tullini , Italy  
Emilio Turco , Italy  
Ilhan Tuzcu , USA  
Efstratios Tzirtzilakis , Greece  
FRANCISCO UREÑA , Spain  
Filippo Ubertini , Italy  
Mohammad Uddin , Australia  
Mohammad Safi Ullah , Bangladesh  
Serdar Ulubeyli , Turkey  
Mati Ur Rahman , Pakistan  
Panayiotis Vafeas , Greece  
Giuseppe Vairo , Italy  
Jesus Valdez-Resendiz , Mexico  
Eusebio Valero, Spain  
Stefano Valvano , Italy  
Carlos-Renato Vázquez , Mexico  
Martin Velasco Villa , Mexico  
Franck J. Vernerey, USA  
Georgios Veronis , USA  
Vincenzo Vespri , Italy  
Renato Vidoni , Italy  
Venkatesh Vijayaraghavan, Australia

Anna Vila, Spain  
Francisco R. Villatoro , Spain  
Francesca Vipiana , Italy  
Stanislav Vitek , Czech Republic  
Jan Vorel , Czech Republic  
Michael Vynnycky , Sweden  
Mohammad W. Alomari, Jordan  
Roman Wan-Wendner , Austria  
Bingchang Wang, China  
C. H. Wang , Taiwan  
Dagang Wang, China  
Guoqiang Wang , China  
Huaiyu Wang, China  
Hui Wang , China  
J.G. Wang, China  
Ji Wang , China  
Kang-Jia Wang , China  
Lei Wang , China  
Qiang Wang, China  
Qingling Wang , China  
Weiwei Wang , China  
Xinyu Wang , China  
Yong Wang , China  
Yung-Chung Wang , Taiwan  
Zhenbo Wang , USA  
Zhibo Wang, China  
Waldemar T. Wójcik, Poland  
Chi Wu , Australia  
Qihong Wu, China  
Yuqiang Wu, China  
Zhibin Wu , China  
Zhizheng Wu , China  
Michalis Xenos , Greece  
Hao Xiao , China  
Xiao Ping Xie , China  
Qingzheng Xu , China  
Binghan Xue , China  
Yi Xue , China  
Joseph J. Yame , France  
Chuanliang Yan , China  
Xinggang Yan , United Kingdom  
Hongtai Yang , China  
Jixiang Yang , China  
Mijia Yang, USA  
Ray-Yeng Yang, Taiwan


Zaoli Yang , China  
Jun Ye , China  
Min Ye , China  
Luis J. Yebra , Spain  
Peng-Yeng Yin , Taiwan  
Muhammad Haroon Yousaf , Pakistan  
Yuan Yuan, United Kingdom  
Qin Yuming, China  
Elena Zaitseva , Slovakia  
Arkadiusz Zak , Poland  
Mohammad Zakwan , India  
Ernesto Zambrano-Serrano , Mexico  
Francesco Zammori , Italy  
Jessica Zangari , Italy  
Rafal Zdunek , Poland  
Ibrahim Zeid, USA  
Nianyin Zeng , China  
Junyong Zhai , China  
Hao Zhang , China  
Haopeng Zhang , USA  
Jian Zhang , China  
Kai Zhang, China  
Lingfan Zhang , China  
Mingjie Zhang , Norway  
Qian Zhang , China  
Tianwei Zhang , China  
Tongqian Zhang , China  
Wenyu Zhang , China  
Xianming Zhang , Australia  
Xuping Zhang , Denmark  
Yinyan Zhang, China  
Yifan Zhao , United Kingdom  
Debao Zhou, USA  
Heng Zhou , China  
Jian G. Zhou , United Kingdom  
Junyong Zhou , China  
Xueqian Zhou , United Kingdom  
Zhe Zhou , China  
Wu-Le Zhu, China  
Gaetano Zizzo , Italy  
Mingcheng Zuo, China

# Contents

## **Study on Dispersion Stability and Friction Characteristics of C60 Nanomicrosphere Lubricating Additives for Improving Cutting Conditions in Manufacturing Process**

Jing-Shan Huang , Hao Sun, Xi Wang, Bin-Qiang Chen, and Bin Yao   
Research Article (11 pages), Article ID 2724743, Volume 2021 (2021)

## **A Potential Failure Mode and Effect Analysis Method of Electromagnet Based on Intuitionistic Fuzzy Number in Manufacturing Systems**

Jihong Pang, Jinkun Dai, and Faqun Qi   
Research Article (12 pages), Article ID 9998526, Volume 2021 (2021)




## **Camshaft Loosening Diagnosis on the Basis of Generalised Force Recognition at the Centre of Gravity of an Engine**

Chuanyan Xu , Lixue Meng, Ruyan Gong, Xun Gong, and Aijuan Li  
Review Article (8 pages), Article ID 1908329, Volume 2021 (2021)


## **Identification of Engine Inertia Parameters and System Dynamic Stiffness via In Situ Method**

Chuanyan Xu , Xun Gong, Lixue Meng, and Aijuan Li  
Research Article (16 pages), Article ID 6439762, Volume 2021 (2021)







## **New Tool Wear Estimation Method of the Milling Process Based on Multisensor Blind Source Separation**

Chen Gao , Sun Bintao , Heng Wu, Mengjuan Peng, and Yuqing Zhou   
Research Article (11 pages), Article ID 9985870, Volume 2021 (2021)


## **An Improved Tool Wear Monitoring Method Using Local Image and Fractal Dimension of Workpiece**

Haicheng Yu, Kun Wang , Ruhai Zhang, Xiaojun Wu, Yulin Tong, Ruiyuan Wang, and Dedao He  
Research Article (11 pages), Article ID 9913581, Volume 2021 (2021)

## **Predictive Maintenance and Sensitivity Analysis for Equipment with Multiple Quality States**

Xiao Wang , Deyi Xu , Na Qu , Tianqi Liu , Fang Qu , and Guowei Zhang   
Research Article (10 pages), Article ID 4914372, Volume 2021 (2021)

## **Kernel Regression Residual Decomposition Method to Detect Rolling Element Bearing Faults**

Xiaoqian Wang, Dali Sheng, Jinlian Deng , Wei Zhang, Jie Cai, Weisheng Zhao, and Jiawei Xiang   
Research Article (10 pages), Article ID 5523098, Volume 2021 (2021)

## Research Article

# Study on Dispersion Stability and Friction Characteristics of C60 Nanomicrosphere Lubricating Additives for Improving Cutting Conditions in Manufacturing Process

Jing-Shan Huang <sup>1,2</sup>, Hao Sun,<sup>3</sup> Xi Wang,<sup>1,2</sup> Bin-Qiang Chen,<sup>1,2</sup> and Bin Yao <sup>1,2</sup>

<sup>1</sup>School of Aerospace Engineering, Xiamen University, Xiamen 361005, China

<sup>2</sup>Shenzhen Research Institute of Xiamen University, Shenzhen 518000, China

<sup>3</sup>AECC Harbin Dongan Engine Co., Ltd., Harbin 150060, China

Correspondence should be addressed to Bin Yao; [aeroiiet@126.com](mailto:aeroiiet@126.com)

Received 13 April 2021; Accepted 5 October 2021; Published 19 October 2021

Academic Editor: Yuqing Zhou

Copyright © 2021 Jing-Shan Huang et al. This is an open access article distributed under the Creative Commons Attribution License, which permits unrestricted use, distribution, and reproduction in any medium, provided the original work is properly cited.

Antifriction lubrication is an important research hotspot in the manufacturing field. A high-performance lubricating additive is of great significance for condition monitoring in the metal cutting process system. To improve cutting conditions in manufacturing process, we study the dispersion stability and tribological properties of fullerene nanoparticles in HM32 antiwear lubricating fluid. Fullerene nanoparticles are fully integrated into HM32 antiwear lubricating fluid by electromagnetic stirring and ultrasonic oscillation. The dispersion stability of fullerene nanoparticles in HM32 antiwear lubricating fluid was comprehensively studied by microscope scanning experiment, static sedimentation experiment, and absorption experiment. The four-ball friction experiment was operated to investigate the extreme pressure property and tribological property of lubricating fluids with fullerene concentration ranging from 100 ppm to 1000 ppm. The results show that fullerene nanoparticle can significantly improve the extreme pressure property and wear resistance of HM32 basic lubricating fluid. Meanwhile, we found that an excessively high concentration of fullerene nanoparticles will increase the friction and wear of the four-ball friction pair. The best concentration of fullerene nanoparticles is 200 ppm. When the fullerene concentration reaches 200 ppm, the maximum nonsintering load is significantly increased, and the friction coefficient and the steel ball wear scar diameter are significantly reduced.

## 1. Introduction

With the development of modern industry, the requirements for precision, efficiency, and reliability of mechanical equipment have become increasingly strict. The lubrication technology is of significant importance in the mechanical equipment field. The energy waste caused by friction and wear has seriously hindered the rapid development of the industry. The economic losses caused by the failure of mechanical parts due to friction and wear account for a large proportion of the GDP [1]. Meanwhile, high-performance lubricating additives can promote the stable operation of the cutting process system. It is of great significance to the condition monitoring in the metal cutting process [2]. Therefore, reducing the friction and

wear in mechanical equipment is a subject of great social significance.

In recent years, domestic and foreign scholars have conducted extensive researches on the friction reduction and operational stability of the manufacturing process. Based on learning machine methods [3–6], signal processing algorithms [7–9], and simulation modelling technologies [10, 11], scholars have explored tool wear condition detection [12–16], bearing condition monitoring [17–21], ball screw detection [22, 23], mechanical signature analysis [24, 25], nanoparticle cutting fluid [26, 27], and so on in the cutting process system. In particular, improving lubrication technology is the most effective way to reduce the friction and wear in the manufacturing process. Countries all over the world attach great importance to the research of antiwear

and antifriction technologies. For most mechanical equipment, adding lubricant between friction surfaces is the main method to reduce friction and wear. Lubricants can not only reduce the friction coefficient and slow down wear, but also continuously absorb heat from the friction surface to prevent damage to parts and tools. In addition, lubricants can wash away metal chips and dust generated by friction and wear. However, the effectiveness of traditional lubricants is limited. It is necessary to add various additives in the lubricant to enhance the lubricity [28]. In the metal cutting process, nanomicrosphere lubricating additives can be applied in the cutting fluid to enhance the lubrication and antiwear properties of the cutting fluid [29]. By fully mixing the nanomicrosphere lubricating additives and the cutting fluid, the cutting fluid containing the nanoparticles is added to the cutting fluid circulation system. Nanoparticles infiltrate into the contact surface between the cutting tool and the workpiece or chips with the cutting fluid, turning the sliding friction between the tool and the workpiece into rolling/sliding mixed friction. Meanwhile, it can reduce the direct contact between the tool-chip peak points, decrease the tool-chip bonding friction and chip fibrosis, and reduce the cutting force and cutting heat in the manufacturing process. Therefore, the application of nanomicrosphere lubricating additives can reduce cutting tool wear, delay tool life, and improve production efficiency in the mechanical manufacturing process. Nowadays, using nanoparticles as lubricant additives has become a research hotspot in the lubrication field.

Nanomaterial lies in the transition zone between macroscopic matter and microscopic atoms and molecules, which make it exhibit many distinctive properties [30]. Nanoparticle has the characteristics of surface effect, small size effect, quantum size effect, and macroscopic quantum tunneling effect. Nanoparticles are mainly used as friction reducers, antiwear agents, and extreme pressure agents in lubrication [31–35]. They have the potential to replace traditional lubricant additives.

Some lubrication mechanisms have been proposed in the literature. When nanoparticles are used as lubricant additives, it led to the following effects:

- (1) Rolling effect: nanoparticles are easy to roll when doing relative movement between friction pairs. It turns the sliding friction into rolling friction between the surfaces of the friction pair. The generated heat is reduced by reducing the contact area. Meanwhile, the nanoparticles play a supporting role and improve the carrying capacity [36].
- (2) Protective film: the nanoparticles are adsorbed to the surface of the friction pair in the friction and wear process due to the high ratio of surface area-to-volume. The exchange of material molecules occurs between the friction pair and the lubricating material under the tribochemical reaction [37]. Therefore, a reaction film with low shear strength and high hardness is formed. The reaction film prevents direct contact between the friction pairs and improves the wear resistance.
- (3) Mending effect: there are some scratches and holes on the surface of the friction pair. Nanoparticles enter these holes due to their small size. Consequently, it provides a flat surface that reduces friction and cutting temperature [38]. The mending effect is beneficial to the release of stress and the improvement of tribological properties.
- (4) Polishing effect: some hard nanoparticles are polishing materials. They can process ultrasurface with root mean square roughness (RMS) ranging from 0.1 to 1.0 nm [39]. Nanoparticles will also produce mechanical polishing on the surface of the friction pair during the friction process. The friction coefficient and the contact pressure of the contact surfaces are reduced after nanoparticle polishing [40].
- (5) Chemical reaction: nanoparticles may also chemically react with the friction pair surface to form a lubricating film. For example, a lubricant containing Cu nanoadditives reacts with the steel surface to form a lubricating film composed of Cu, FeS, and FeSO<sub>4</sub> [41].

Nanolubricants show many advantages compared to traditional lubricants [42–44]. The oil film strength of nanoparticle additives is higher than that of traditional additives [45]. The suspension density and uniformity of nanoparticle additives are also much higher than those of traditional additives [46]. In addition, nanoparticle additives are more environmentally friendly than traditional additives [47].

Nowadays, using nanoparticles as lubricant additives has become a research hotspot in the lubrication field. The research and application of nanoparticle lubricating additives in lubricating systems provide new ideas for advanced lubricating materials. In recent years, many scholars and experts have conducted a lot of research work on the dispersion stability and lubrication mechanism of nanolubricants. Imene et al. [48] used a transmission nanoindenter to observe that spherical MoS<sub>2</sub> nanoparticles exhibit a rolling effect when the positive pressure is less than 100 MPa. It significantly improves the lubricant carrying capacity and reduces the friction coefficient and wear. Peng et al. [49] prepared SiO<sub>2</sub> nanoparticles and diamond nanoparticles with good dispersion in lubricants and discussed their tribological properties. It is found that SiO<sub>2</sub> nanoparticles and diamond nanoparticles are filled in the more severely worn microregions to repair the friction surface. Xia et al. [50] found that inorganic nanoparticles can form a boundary lubricant film on the friction surface under high temperature and high pressure. In addition, the nanoparticles deposited between the friction surfaces can fill the surface pits and damaged parts to reduce friction and wear. Xu et al. [51] prepared a water-soluble nano-Cu additive with an average particle size of 3.5 nm using in situ surface modification. Using nano-Cu particles as a water-based lubricant additive can reduce the friction coefficient and wear rate of pure water by about 50%. It shows that the nanocopper particles have excellent antifriction and

antiwear properties. Zhao et al. [52] modified graphene with Span-80 as a dispersant to make it uniformly and stably dispersed in the base oil. It is found that graphene can improve the friction and wear performance of CGr15/bronze friction pair. Graphene has the most obvious antiwear effect at 60°C and 100°C, and the friction coefficient and wear rate are reduced by 78% and 95%, respectively. GUPTA [53] used three nanofluids of aluminum oxide (Al<sub>2</sub>O<sub>3</sub>), molybdenum disulfide (MoS<sub>2</sub>), and nanographite to optimize the cutting force, tool wear, cutting temperature, and surface finish during MQL turning of titanium alloys. PADMINI [54] studied the effect of vegetable oil-based nMoS<sub>2</sub> nanofluid in the steel turning process. It was found that nMoS<sub>2</sub> nanofluid can effectively reduce cutting force, temperature, tool wear, and surface roughness. Sharma et al. [55] studied the effect of Al<sub>2</sub>O<sub>3</sub>/graphene hybrid nanoparticle additives in the AISI 304 steel turning process to improve the tribological properties of lubricants. The developed hybrid nanolubricant significantly reduces tool side wear and cutting temperature. Cetin and Kilincarslan [56] used the suspension of borax-ethylene glycol and colloidal suspension of borax-ethylene glycol-nanosilver particles as cutting fluid for milling of AA7075-T6 material. It is found that borax and nanosilver additives can improve the lubrication function and heat transfer properties.

The research on the tribological properties of fullerene C<sub>60</sub>, which has a unique spherical shape and high hardness, is attracting increasing attention. Fullerene C<sub>60</sub> is a molecule with a hollow cage structure composed of 60 C atoms connected by C-C bonds. It consists of twelve five-member rings and twenty six-member rings. Its appearance resembles a football. Its molecular diameter is about 0.71 nm and the inner cavity diameter is about 0.3 nm [57]. The unique spherical structure of fullerene (C<sub>60</sub>) gives it strong pressure resistance. Its pressure resistance is higher than that of diamond, and its microstrength is as high as 18 GPa. The hardness of C<sub>60</sub> crystal increases with the increase of pressure, and its structure transforms to diamond structure. Under low pressure, fullerene molecules can roll on the graphite surface. Its strong intramolecular force, weak intermolecular force, and low surface energy make it promising as a high-grade lubricant for molecular rolling balls. Therefore, whether under low pressure or high pressure, fullerene C<sub>60</sub> may become an excellent lubricant [58–60]. Hirata et al. [61] used diamond to prepare fullerene under high temperature conditions and tested the friction properties on the surface of the friction pair composed of steel balls and silicon wafers. The results show that the addition of fullerene on the surface of the friction pair exhibits good antifriction performance and antiwear performance, which is significantly better than oil-free lubrication and graphite. Yao et al. [62] used a four-ball machine to investigate the tribological properties of onion-like fullerenes. The results show that fullerenes have good antifriction properties. Its antifriction performance is better than that of carbon nanotubes, and the wear scar on the surface is lighter and more regular. Yan et al. [63] prepared the C<sub>60</sub>/C<sub>70</sub> mixture by arc method and dispersed C<sub>60</sub>/C<sub>70</sub> in paraffin oil by solvent evaporation method. The research results on the SRV

testing machine show that C<sub>60</sub>/C<sub>70</sub> nanoparticles can increase the extreme pressure load of paraffin oil by 3 times and reduce its friction coefficient by 1/3, which can significantly reduce the wear of the friction pair. Hong et al. [64] synthesized a fullerene-styrene-maleic anhydride terpolymer and dissolved it in ethanolamine aqueous solution. The results of the four-ball friction tester show that the terpolymer lubricant additive significantly improves the load-bearing capacity and antifriction ability of the base fluid. According to the test results, it is speculated that the fullerene copolymer nanospheres not only effectively isolate the surfaces of the two friction pairs to improve the bearing capacity and reduce wear, but also generate microelastic rolling lubrication to reduce the friction coefficient. Li et al. [65] used a four-ball machine to investigate the extreme pressure and antiwear properties of C<sub>60</sub> additives in liquid paraffin. The results show that C<sub>60</sub> additive has good extreme pressure and antiwear performance under higher load and higher speed, and it has high chemical stability.

It can be seen from the above literature that fullerene shows good tribological properties between the friction pairs due to the super molecular structure and good chemical inertness. In addition, fullerene has a certain aromaticity and can be well dissolved in organic solvents. The diameter of the C<sub>60</sub> nanospherical particles dissolved in the cutting fluid is very small. Its molecule is a hollow spherical structure. The density of C<sub>60</sub> nanoparticles is 1.65 g/cm<sup>3</sup>, which is closer to the density of water (density: 1.00 g/cm<sup>3</sup>) and that of raw cutting oil (density: 0.869 g/cm<sup>3</sup>). So it is easy to be suspended in the HM32 antiwear lubricating fluid by the dispersion method, and the cutting oil penetrates into the contact surface between the tool and the workpiece or the chip. Meanwhile, the C<sub>60</sub> nanoparticles have high compressive strength, and the C<sub>60</sub> nanospherical particles have high thermal stability. The melting point is above 3000°C. Therefore, it has innate advantages as a lubricant additive. However, the research on its lubrication performance, mechanism, and application is not comprehensive enough.

In this paper, fullerene nanoparticles are used as the additive of HM32 antiwear lubricating fluid to study the dispersion stability and tribological properties. Firstly, the fullerene particles and the Group III base oil are electromagnetically stirred under normal temperature condition to prepare fullerene additives. Then, the fullerene additive and HM32 antiwear lubricating fluid are electromagnetically stirred at room temperature. Finally, the fullerene nanomicrosphere lubricating fluid is ultrasonically oscillated for long time to make the fullerene nanoparticles uniformly dispersed. The dispersion stability of fullerene nanoparticles in HM32 antiwear lubricating fluid was characterized by microscope scanning, precipitation tests, and ultraviolet spectroscopy. Then a four-ball friction tester was used to carry out the friction and wear test. The friction characteristics and extreme pressure performance of 7 kinds of lubricating fluids with fullerene concentration ranging from 100 ppm to 1000 ppm were measured. The experimental results show that fullerene nanoparticle can significantly improve the extreme pressure property and wear resistance of HM32 basic lubricating fluid. The best concentration of fullerene nanoparticles

is 200 ppm. When the fullerene concentration reaches 200 ppm, the maximum nonsintering load increases by 36.01%, the sintering load increases by 100.81%, the friction coefficient decreases by 41.28%, and the wear mark diameter of the steel ball decreases by 10.40%. Meanwhile, we found that an excessively high concentration of fullerene nanoparticles will increase the friction and wear of the four-ball friction pair. It may be that too many fullerene nanoparticles are more likely to agglomerate to produce macromolecular fullerenes. It increases the internal friction of lubricating oil molecules and deteriorates the tribological properties of lubricating fluid.

## 2. Materials and Methods

*2.1. Fullerene Characterization and Lubricant Additives' Preparation.* The fullerene nanoparticles used in this paper are from Xiamen Funa New Material Technology Co., Ltd. The purity of the fullerene solid particles is analyzed and calculated by liquid chromatography. The purity of C60 is calculated to be 99.950%. The equipment used is Shimadzu liquid chromatography SPD-16 by integrating the peak area of HPLC (High-Performance Liquid Chromatography). The chromatogram data of the C60 product and the purity calculation table is shown in Table 1.

The microscopic morphology of fullerene C60 nanoparticles is shown in Figure 1. The photographing equipment used is the ZEISS Gemini SEM 500 field emission scanning electron microscope. It can be seen from the micrograph image that the fullerene solid particles are composed of several spherical fullerene molecular clusters.

We choose Total HM32 construction machinery antiwear hydraulic oil as the base fluid. The HM32 antiwear hydraulic oil has excellent antiwear properties and hydraulic stability. It is widely used in mechanical hydraulic systems and metal cutting systems. Firstly, the fullerene particles and Group III base oil are electromagnetically stirred under normal temperature conditions to prepare fullerene additives. The electromagnetic stirring lasts up to 4 hours to fully disperse the fullerene particles. Then, the fullerene additive and the HM32 antiwear lubricating fluid were continuously electromagnetically stirred at room temperature for 4 hours. Finally, the fullerene nanomicrosphere lubricating fluid was ultrasonically oscillated for 2 hours to make the fullerene nanoparticles uniformly dispersed in the base fluid. We have prepared a total of 6 suspensions with fullerene mass fractions: 100 ppm, 200 ppm, 300 ppm, 400 ppm, 500 ppm, and 1000 ppm.

*2.2. Dispersibility and Stability Test of Fullerene Nanoparticles.* We characterized the dispersion stability of fullerene nanoparticles in the HM32 antiwear lubricating fluid through microscope scanning experiment, static sedimentation experiment, and absorption experiment.

*2.2.1. Microscope Scanning Experiment.* We scan and photograph the nanofullerene particle suspension after electromagnetic stirring and ultrasonic oscillation. The nanofullerene particle suspension is dropped on a clean

silicon wafer. The silicon wafers used are ultrasonically shaken and cleaned in an ethanol/acetone mixed solution for one hour, and they are dried in a drying box. We put the silicon wafer dripped with the fullerene suspension on the heating table for a constant temperature heating treatment at 300 degrees Celsius for 2 hours to ensure that the liquid in the suspension evaporates away and the fullerene nanoparticles remain on the silicon wafer. Finally, the dried silicon wafer with fullerene nanoparticles was microscopically photographed. The photographing equipment used is a ZEISS Gemini SEM 500 field emission scanning electron microscope. The actual instrument is shown in Figure 2. By observing the distribution of fullerene nanoparticles, we can analyze the distribution of fullerene nanoparticles in the suspension.

*2.2.2. The Static Sedimentation Experiment.* The static sedimentation experiment refers to letting the fullerene nanoparticle suspension solution stand still and settle under gravity. The static precipitation method mainly evaluates the stability of the fullerene additive in the lubricating fluid by visually observing the change process of the supernatant liquid height and the precipitation volume. The lower the supernatant height the smaller the volume of the sedimentation. It indicates that the stability of the fullerene additive in the lubricating fluid is better. Conversely, the higher the supernatant height the larger the precipitation volume. It indicates that the stability of the fullerene additive in the lubricating fluid is worse.

The prepared fullerene nanoparticle suspension is placed in a ventilated and dry place. We take pictures of the fullerene nanoparticle suspensions at regular intervals. Afterwards, we observe the precipitation of the suspension with different storage time to analyze the dispersion stability of the fullerene nanoparticles in the suspension.

*2.2.3. The Absorption Experiment.* The absorption experiment is to measure the absorbance of the fullerene nanoparticle suspension supernatant with an ultraviolet spectrophotometer. The absorbance value is proportional to the number of fullerene nanoparticles in the suspension. Absorbance is defined as

$$\text{absorbance} = \lg\left(\frac{I_0}{I}\right), \quad (1)$$

where  $I_0$  stands for the incident light intensity and  $I$  stands for the transmitted light intensity.

The higher the absorbance value is, the more the fullerene nanoparticles are contained in the upper solution per unit volume. It means that the dispersion of particles in the suspension is better. Therefore, we use the absorption spectrophotometric method to evaluate the dispersibility of the fullerene additives in the lubricating fluid. The prepared fullerene nanoparticle suspension is placed in an ultraviolet-visible spectrometer for spectrum measurement. The instrument used is Shimadzu UV-Vis spectrophotometer-2600. The actual instrument is shown in Figure 3.



TABLE 1: The chromatogram data of the C60 product and the purity calculation.

Peak no.	Time	Area	Peak start time	Peak end time	Area (%)	Remark
1	5.110	1046	4.908	5.383	0.008	
2	8.178	13453835	7.700	10.408	99.950	C60
3	9.272	892	9.117	9.400	0.007	C60 oxides
4	16.708	4757	16.092	17.325	0.035	
Total		13460529			100.000	

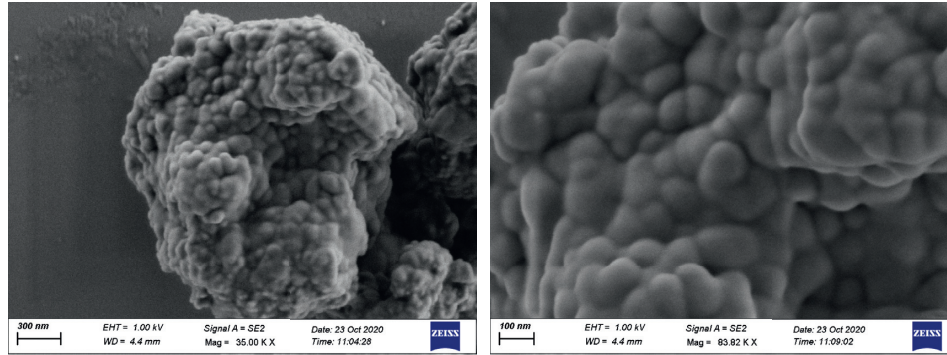


FIGURE 1: Microscopic morphology of fullerene C60 nanoparticles.



FIGURE 2: ZEISS Gemini SEM 500 field emission scanning electron microscope.

We put the fullerene nanoparticle suspension into a clean spectroscopic dish. The spectrometer was cleaned by ultrasonic shaking in a mixed solution of ethanol/acetone for one hour. Then the spectroscopic dish containing the fullerene nanoparticle suspension was placed into the UV-2600 to obtain the spectrum corresponding to the fullerene nanoparticle suspension. We measure the spectrum of each fullerene nanoparticle suspension in an ultraviolet-visible spectrometer at regular intervals. We observe the change process of the suspension spectrum for different storage time to analyze the dispersion stability of the fullerene nanoparticles in the suspension.

2.3. Friction and Wear Test of Fullerene Nanoparticles.

We use the Xiamen Tianji MS-10J four-ball friction testing machine to carry out the friction and wear test of the C60 nanoparticle suspension. The four-ball friction machine is a point contact tester, which can accurately measure the wear value in a short time and requires only a small sample amount. The four-ball machine can measure the friction properties of lubricating oils, as well as extreme pressure and wear properties, including lubrication properties that protect the friction pair from scratches, seizures, sintering, or other wear phenomena under heavy loads. Therefore, the four-ball friction tester is widely used in the determination of the antiwear performance and load-bearing capacity of lubricants.

The physical map of the equipment is shown in Figure 4. The testing machine adopts the load control mode of automatic loading and realizes stepless speed regulation through the servo motor. The friction pair used in this article is a four-ball friction pair, and the main structure diagram is shown in Figure 5.

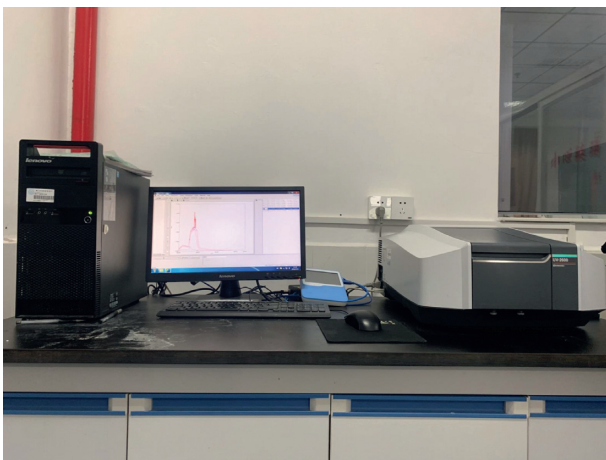


FIGURE 3: Shimadzu UV-Vis spectrophotometer-2600.





FIGURE 4: Four-ball friction testing machine MS-10J (produced by Xiamen Tianji Automation Co., Ltd.).

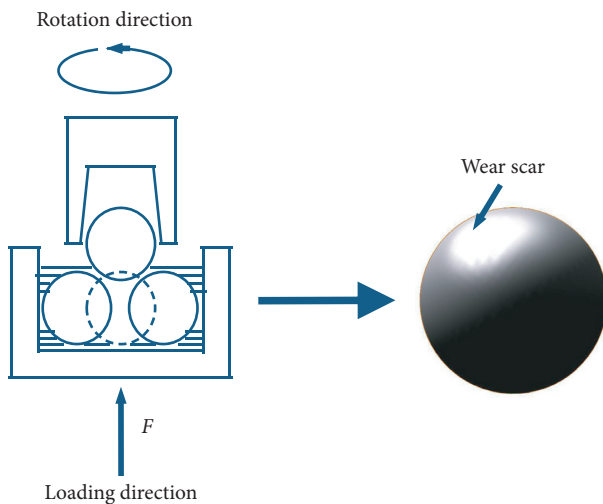


FIGURE 5: Schematic diagram of four-ball friction and wear tester device.

The three steel balls in the lower oil box are in contact with each other, and the steel balls in the upper clamp are in point contact with the three steel balls. The friction pair is made of GCr15, the diameter is 12.70 mm, and the hardness is HRC60. Before starting the experiment, the fullerene nanoparticle suspension was poured into the oil box below. Therefore, the steel balls can be completely immersed in the test solution. We operated the numerical control system to control the loading load of the lower fixture and the loading speed of the upper fixture when all four steel balls are in contact. In this way, friction can be generated between the friction pairs and wear spots can be obtained on the three steel balls. The steel ball wear and sintering tests were carried out by the four-ball friction tester to evaluate the largest nonseizure load PB, sintering load PD, and wear scar

diameter of the steel ball friction pair under the fullerene suspension lubrication.

### 3. Results and Discussion

**3.1. Study on Dispersion Stability of Fullerene Nanomicrosphere Lubricating Additives.** The microscopic morphology of 300 ppm fullerene nanoparticle suspension is shown in Figure 6. From the microscopic morphology of the fullerene nanoparticle suspension, it can be seen that the fullerene nanoparticles are relatively uniformly distributed on the silicon wafer. The fullerene nanoparticles present agglomerated spherical shape. The oil molecules show ring shape structure. What is more, the molecular film formed by the fullerene nanomolecules and oil molecules is uniformly mixed together. It preliminarily shows that the fullerene nanoparticles are uniformly dispersed in the HM32 base fluid.

We place the prepared fullerene nanoparticle suspension in a ventilated and dry environment for static sedimentation. The lubricating fluids with seven fullerene concentrations after standing for 10 days and 20 days are shown in Figure 7. It can be seen from Figure 7 that there is still no clear liquid in the upper region of the fullerene nanoparticle suspension and no precipitation in the lower region after standing for 20 days. Each bottle of fullerene nanoparticle suspension maintains a uniform color. It preliminarily shows that the prepared fullerene nanoparticle suspension can maintain a uniform distribution of fullerene nanoparticles over time and has excellent dispersion stability.

Figure 8 shows the UV spectrum of 7 kinds of lubricating fluids with fullerene concentration ranging from 100 ppm to 1000 ppm. It can be seen from Figure 8 that the UV spectrum of the fullerene nanoparticle suspension after standing for 20 days is very similar to the original UV spectrum. It shows that the concentration of fullerene nanoparticles in the upper region of the fullerene nanoparticle suspension does not change significantly. It indicates that the prepared fullerene nanoparticle suspension can maintain a uniform distribution of fullerene nanoparticles for a long time and has excellent dispersion stability.

### 3.2. Study on Friction Characteristics of C60 Nanomicrosphere Lubricating Additives

**3.2.1. Extreme Pressure Performance of Fullerene Nanoparticles in HM32 Base Fluid.** In order to comprehensively investigate the extreme pressure performance of fullerene nanoparticles in the HM32 base fluid, we measured the maximum seizure-free load and sintering load of seven kinds of lubricating fluids with different fullerene concentrations ranging from 100 ppm to 1000 ppm. The results are shown in Table 2. It can be seen from Table 2 that fullerene nanoparticles have a significant impact on the extreme pressure performance of the HM32 base fluid. When the fullerene concentration reached 200 ppm, the maximum nonseize load increased by 36.01% and the sintering load increased by 100.81%. But when the concentration is increased to more than 200 ppm, the maximum nonjamming load is basically maintained at the

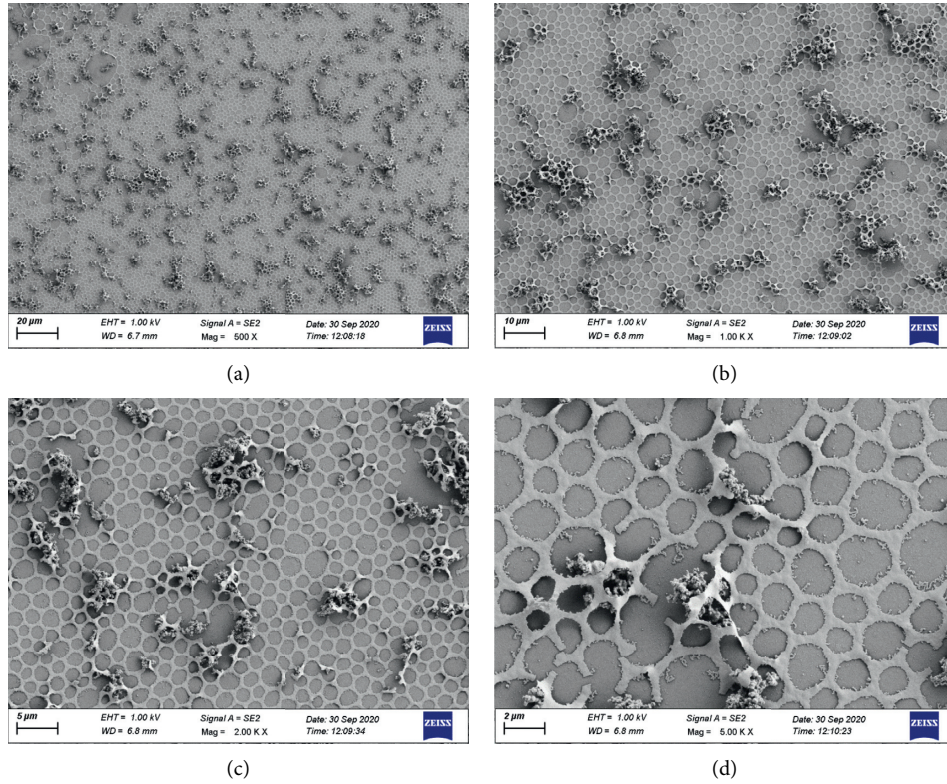


FIGURE 6: Microscopic morphology of 300 ppm fullerene nanoparticle suspension.

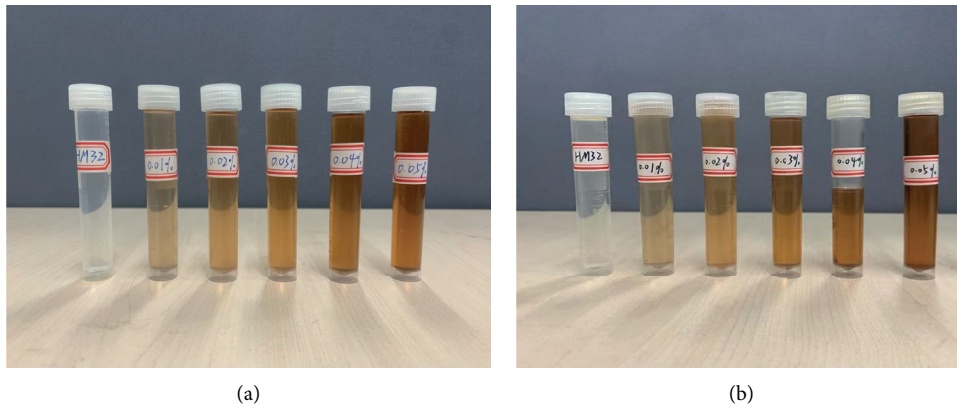


FIGURE 7: Fullerene nanoparticle suspension: (a) left for 10 days and (b) left for 20 days.

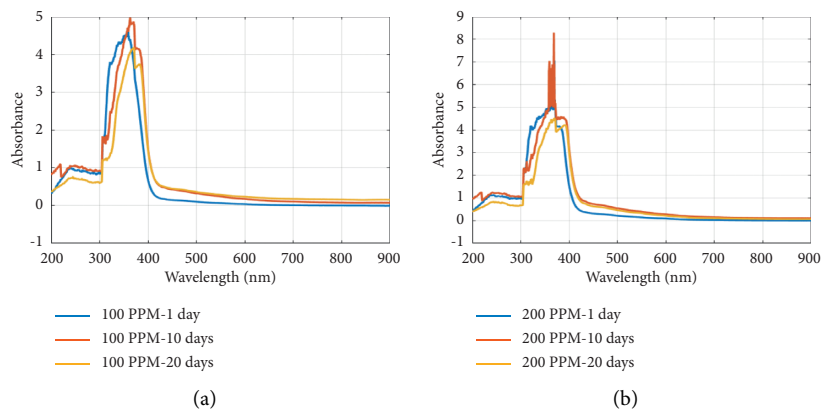


FIGURE 8: Continued.

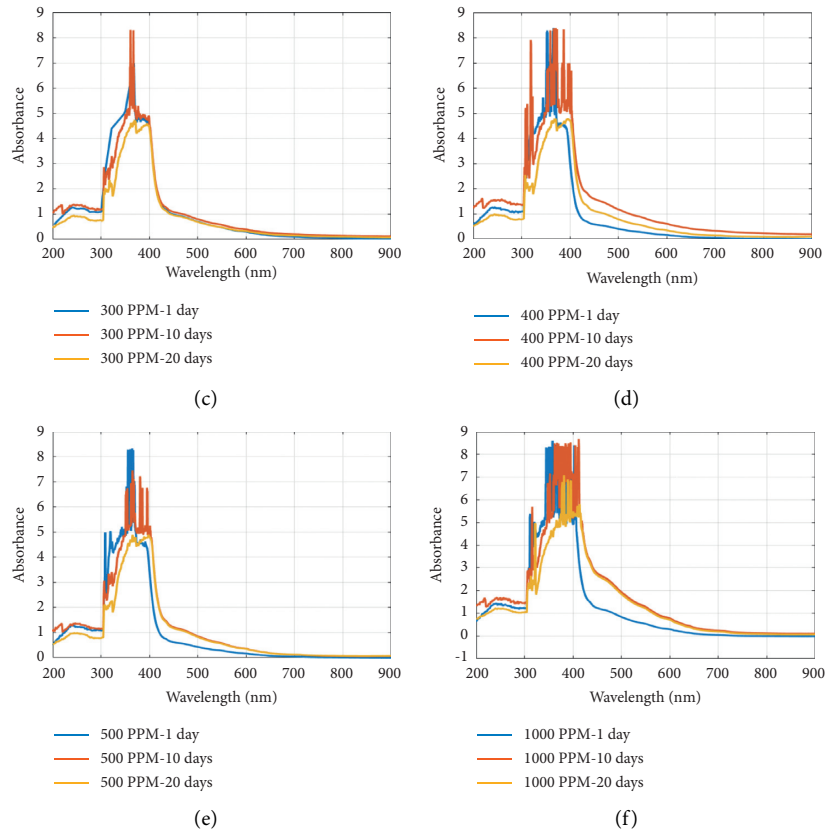


FIGURE 8: The UV spectrum of fullerene nanoparticles lubricating fluids.

TABLE 2: Extreme pressure properties of fullerene nanoparticles in the HM32 base oil.

Lubricating fluid	The largest nonseizure load (PB) (N)	The sintering load (PD) (N)
HM32	647	1235
HM32 + 100 ppm C60 nanoparticle	765	1782
HM32 + 200 ppm C60 nanoparticle	880	2480
HM32 + 300 ppm C60 nanoparticle	892	2504
HM32 + 400 ppm C60 nanoparticle	901	2513
HM32 + 500 ppm C60 nanoparticle	900	2528
HM32 + 1000 ppm C60 nanoparticle	912	2550

same level, and the increase rate of the sintering load is significantly reduced. As the concentration increases, the extreme pressure performance has not been further improved. It indicates fullerene nanoparticles can significantly improve the extreme pressure performance of lubricants. However, it is difficult to further improve the extreme pressure performance of lubricating base fluid when the fullerene nanoparticles concentration exceeds a certain amount.

**3.2.2. Friction Properties of Fullerene Nanoparticles in HM32 Base Fluid.** In order to comprehensively investigate the extreme pressure performance of fullerenes in the HM32 base fluid, the friction coefficient and steel ball wear scar diameter (WSD) of seven fullerene lubricating fluids after a four-ball long grinding test under a 200 N normal load were measured. The results are shown in Table 3. It can be seen

from Table 3 that fullerenes show significant antiwear and antiwear properties. Especially when the concentration is 200 ppm, the friction coefficient and the diameter of the wear scar of the steel ball are significantly improved. When the fullerene concentration reached 200 ppm, the friction coefficient decreased by 41.28% and the wear scar diameter of the steel ball decreased by 10.40%. However, when the concentration increased to more than 200 ppm, the friction coefficient and steel ball wear scar diameter did not continue to significantly decrease or even fluctuate, and the antiwear and antiwear performance were not further improved. It indicates that a proper concentration of fullerene nanoparticles can significantly improve the antiwear and antiwear properties of the HM32 base fluid, but an excessively high concentration of fullerene nanoparticles will increase friction and wear. It may be that too many fullerene nanoparticles are more likely to agglomerate to produce

TABLE 3: Friction properties of fullerene nanoparticles in the HM32 base oil (normal load 200 N).

Lubricating fluid	Friction coefficient	The wear scar diameter (mm)
HM32	0.109	0.519
HM32 + 100 ppm C60 nanoparticle	0.086	0.498
HM32 + 200 ppm C60 nanoparticle	0.064	0.465
HM32 + 300 ppm C60 nanoparticle	0.069	0.447
HM32 + 400 ppm C60 nanoparticle	0.078	0.487
HM32 + 500 ppm C60 nanoparticle	0.067	0.509
HM32 + 1000 ppm C60 nanoparticle	0.071	0.513

macromolecular fullerenes, which cannot form an adsorption film on the friction surface. It will also increase the internal friction of the lubricating oil molecules, making the tribological properties of the lubricating oil worse.

#### 4. Conclusions

In order to explore the application prospects of fullerene lubricating additives, this paper thoroughly studies the dispersion stability and tribological property of fullerene nanoparticles in lubricating fluids. In this paper, a fullerene nanoparticle suspension was prepared by a combination of electrolytic stirring and ultrasonic dispersion. The dispersion stability of fullerene nanoparticles in HM32 antiwear lubricating fluid was comprehensively studied by microscope scanning experiment, static sedimentation experiment, and absorption experiment. Finally, the reliability of the preparation method for fullerene nanoparticle suspension was verified. The four-ball friction experiment method was used to investigate the extreme pressure and tribological properties of 7 kinds of lubricating fluids with fullerene concentration ranging from 100 ppm to 1000 ppm. The results show that fullerene nanoparticle can significantly improve the extreme pressure performance and wear resistance of HM32 basic lubricating fluid.

Through the research of this paper, the following conclusions can be drawn:

- (1) The combination of electromagnetic stirring and ultrasonic dispersion is a very effective process to maintain the dispersion stability of fullerene nanoparticles in the lubricating base liquid. It can keep the fullerene nanoparticle suspension in a stable state for a long time without precipitation.
- (2) Fullerene nanoparticles have a significant improvement effect on the extreme pressure performance of HM32 base fluid. The maximum nonsintering load increases by 36.01% and the sintering load increases by 100.81% when the fullerene concentration reaches 200 ppm. However, it is difficult to further improve the extreme pressure performance of the HM32 lubricating base fluid when the fullerene nanoparticles concentration exceeds 200 ppm.
- (3) Fullerene has significant antiwear property. The friction coefficient decreases by 41.28% and the steel ball wear scar diameter decreases by 10.40% when the fullerene concentration reaches 200 ppm. However, an excessively high concentration of

fullerene nanoparticles will increase friction and wear. It may be that too many fullerene nanoparticles are more likely to agglomerate to produce macromolecular fullerenes. It increases the internal friction of lubricating oil molecules and deteriorates the tribological properties of lubricating oil.

#### Data Availability

The data used to support the findings of this study are available from the corresponding author upon request.

#### Conflicts of Interest

The authors declare that the research was conducted in the absence of any commercial or financial relationships that could be construed as a potential conflict of interest.

#### Authors' Contributions

Jingshan Huang and Bin Yao conceived the lubricating additives; Jingshan Huang and Hao Sun performed the experiment; Jingshan Huang preprocessed and analyzed the data; Jingshan Huang wrote the paper; Xi Wang and Bin-qiang Chen reviewed and edited the manuscript; all authors read and approved the manuscript.

#### References

- [1] J. Luo and J. Li, "The progress and future of tribology," *Lubrication & Sealing*, vol. 12, pp. 1–12, 2010.
- [2] I. El-Thalji and E. Jantunen, "A summary of fault modelling and predictive health monitoring of rolling element bearings," *Mechanical Systems and Signal Processing*, vol. 60–61, pp. 252–272, 2015.
- [3] L. Jing, M. Zhao, P. Li, and X. Xu, "A convolutional neural network based feature learning and fault diagnosis method for the condition monitoring of gearbox," *Measurement*, vol. 111, pp. 1–10, 2017.
- [4] J. Ou, H. Li, G. Huang, and G. Yang, "Intelligent analysis of tool wear state using stacked denoising autoencoder with online sequential-extreme learning machine," *Measurement*, vol. 167, Article ID 108153, 2020.
- [5] Q. Nazir and C. Shao, "Online tool condition monitoring for ultrasonic metal welding via sensor fusion and machine learning," *Journal of Manufacturing Processes*, vol. 62, no. 5, pp. 806–816, 2021.
- [6] P. D. Deshpande, B. P. Gautham, A. Cecen, S. Kalidindi, A. Agrawal, and A. Choudhary, "Application of statistical and machine learning techniques for correlating properties to composition and manufacturing processes of steels," in



- Proceedings of the 2nd World Congress on Integrated Computational Materials Engineering (ICME)*, 2013.
- [7] B.-q. Chen, B.-x. Zheng, C.-q. Wang, and W.-f. Sun, "Adaptive sparse detector for suppressing powerline component in EEG measurements," *Frontiers in Public Health*, vol. 9, Article ID 669190, 2021.
  - [8] B. Chen, B. Zheng, and W. Sun, "Ultra-resolution spectral correction based on adaptive linear neuron for biomedical signal processing," *Frontiers in Public Health*, vol. 9, Article ID 682377, 2021.
  - [9] B. Chen, Y. Li, W. Sun, and W. He, "Removal of power line interference from ECG signals using adaptive notch filters of sharp resolution," *IEEE Access*, vol. 7, pp. 150667–150676, 2019.
  - [10] A. M. Khorasani and A. Kootsookos, "Modeling and optimization of the cutting fluid flow and parameters for increasing tool life in slot milling on st52," *International Journal of Modeling Simulation & Scientific Computing*, vol. 4, no. 2, pp. 270–326, 2013.
  - [11] F. Wei, K. Zhang, S. Cai, C. Sun, W. Sun, and B. Liu, "A force model for face grinding using digital graphic scanning (DGS) method," *International Journal of Advanced Manufacturing Technology*, vol. 113, pp. 3261–3270, 2021.
  - [12] F. J. Alonso and D. R. Salgado, "Analysis of the structure of vibration signals for tool wear detection," *Mechanical Systems and Signal Processing*, vol. 22, no. 3, pp. 735–748, 2008.
  - [13] W. Song, S. Deng, J. Yang, and Q. Cheng, "Tool wear detection based on duffing-holmes oscillator," *Mathematical Problems in Engineering*, vol. 2008, Article ID 510406, 15 pages, 2008.
  - [14] S. Dutta, A. Datta, N. D. Chakladar, S. K. Pal, S. Mukhopadhyay, and R. Sen, "Detection of tool condition from the turned surface images using an accurate grey level co-occurrence technique," *Precision Engineering*, vol. 36, no. 3, pp. 458–466, 2012.
  - [15] A. Siddhpura and R. Paurobally, "A review of flank wear prediction methods for tool condition monitoring in a turning process," *International Journal of Advanced Manufacturing Technology*, vol. 65, no. 1–4, pp. 371–393, 2013.
  - [16] W. Sun, H. Gao, S. Tan, Z. Wang, and L. Duan, "Wear detection of WC-Cu based impregnated diamond bit matrix based on SEM image and deep learning," *International Journal of Refractory Metals and Hard Materials*, vol. 98, Article ID 105530, 2021.
  - [17] P. Junior, D'Addona, M. Doriana, and P. R. Aguiar, "Dressing tool condition monitoring through impedance-based sensors: Part 1—PZT diaphragm transducer response and EMI sensing technique," *Sensors*, vol. 18, no. 12, 2018.
  - [18] M. D. Prieto, G. Cirrincione, A. G. Espinosa, J. A. Ortega, and H. Henao, "Bearing fault detection by a novel condition-monitoring scheme based on statistical-time features and neural networks," *IEEE Transactions on Industrial Electronics*, vol. 60, no. 8, pp. 3398–3407, 2013.
  - [19] A. Fatemeh, T. Antoine, and T. Marc, "Tool condition monitoring using spectral subtraction and convolutional neural networks in milling process," *International Journal of Advanced Manufacturing Technology*, vol. 98, pp. 3217–3227, 2018.
  - [20] D. Azad and K. Ramji, "Identification of bearing assembly defects using finite element analysis and condition monitoring techniques," *International Journal of Engineering Research & Technology*, vol. 1, pp. 1–5, 2012.
  - [21] H. O. A. Ahmed, M. L. D. Wong, and A. K. Nandi, "Intelligent condition monitoring method for bearing faults from highly compressed measurements using sparse over-complete features," *Mechanical Systems and Signal Processing*, vol. 99, pp. 459–477, 2018.
  - [22] Y. Huang and Y. Shin, "Method of intelligent fault diagnosis of preload loss for single nut ball screws through the sensed vibration signals," *International Journal of Mechanical and Mechatronics Engineering*, vol. 6, no. 5, 2012.
  - [23] P. C. Tsai, C. C. Cheng, and Y. C. Hwang, "Ball screw preload loss detection using ball pass frequency," *Mechanical Systems and Signal Processing*, vol. 48, no. 1–2, pp. 77–91, 2014.
  - [24] T. R. Lin, E. Kim, and A. C. C. Tan, "A practical signal processing approach for condition monitoring of low speed machinery using peak-hold-down-sample algorithm," *Mechanical Systems and Signal Processing*, vol. 36, no. 2, pp. 256–270, 2013.
  - [25] J. Huang, B. Chen, L. Yang, and W. Sun, "Fractal geometry of wavelet decomposition in mechanical signature analysis," *Measurement*, vol. 173, no. 5, Article ID 108571, 2020.
  - [26] A. K. Sharma, R. K. Singh, A. R. Dixit, and A. K. Tiwari, "Novel uses of alumina-MoS<sub>2</sub> hybrid nanoparticle enriched cutting fluid in hard turning of AISI 304 steel," *Journal of Manufacturing Processes*, vol. 30, pp. 467–482, 2017.
  - [27] S. E. Mustafa, M. Ali, A. Iqbal, M. B. N. Shaikh, and R. Hassan, "Formulation and analysis of cost-effective environment-friendly metal cutting nanofluids using zinc oxide on turning of AISI 52100 steel using MQL," *Engineering Research Express*, vol. 3, 2020.
  - [28] X. Sun, *The Influence of Graphene and Carbon Nanotubes on the Friction Properties of Lubricants*, Harbin Institute of Technology, Harbin, China, 2017.
  - [29] V. Vasu and K. Kumar, "Analysis of nanofluids as cutting fluid in grinding EN-31 steel," *Nano-Micro Letters*, vol. 3, no. 4, pp. 209–214, 2011.
  - [30] S. Wen, *Nanotribology*, Tsinghua University Press, Beijing, China, 1998.
  - [31] G. Duursma, K. Sefiane, and A. Kennedy, "Experimental studies of nanofluid droplets in spray cooling," *Heat Transfer Engineering*, vol. 30, no. 13, pp. 1108–1120, 2009.
  - [32] E. G. Zadoshenko, V. E. Burlakova, and A. A. Novikova, "Effect of nickel nanopowder on lubrication behaviour of low-temperature grease in steel-steel tribosystem," *Tribology: Materials, Surfaces & Interfaces*, vol. 14, no. 1, pp. 1–8, 2019.
  - [33] G.-Z. Zhu, Y.-Z. Gao, S.-Y. Liu, and H.-C. Zhang, "Antiwear and self-repairing mechanisms of magnesium hydroxysilicate composite powder as a lubricating oil additive for steel-steel pair," *Journal of Tribology*, vol. 32, no. 2, pp. 183–188, 2012.
  - [34] Q. Wan, Yi Jin, P. Sun, and Y. Ding, "Rheological and tribological behaviour of lubricating oils containing platelet MoS<sub>2</sub> nanoparticles," *Journal of Nanoparticle Research*, vol. 16, no. 5, pp. 1–9, 2014.
  - [35] S. Kwon, J.-H. Ko, K.-J. Jeon, Y.-H. Kim, and J. Y. Park, "Enhanced nanoscale friction on fluorinated graphene," *Nano Letters*, vol. 12, no. 12, pp. 6043–6048, 2012.
  - [36] X. Yan, *Study on Dispersion Stability and Tribological Properties of Nano-Serpentine/GO in Base Lubricating Oil*, Yanshan University, Qinhuangdao, China, 2019.
  - [37] H. Liu, S.-M. Zhang, P.-Y. Zhang, and Y.-J. Zhang, "Preparation of bismuth nanoparticles via a thermal decomposition process and evaluation of their tribological properties in synthetic ester oils," in *Proceedings of the 14th IFToMM World Congress*, pp. 547–555, Taipei, Taiwan, 2015.
  - [38] S. H. Musavi, B. Davoodi, and S. A. Niknam, "Effects of reinforced nanofluid with nanoparticles on cutting tool wear morphology," *Journal of Central South University*, vol. 26, no. 5, pp. 1050–1064, 2019.

- [39] H. Xie, *Study on the Tribological Properties and Lubricant Mechanisms of Nanolubricants for Magnesium Alloys Rolling*, Chongqing University, Chongqing, China, 2016.
- [40] F. Jian and Y. Zhao, "Wear self-compensating tribological effects of lubricating additives," *Materials Protection*, vol. 39, pp. 34–36, 2006.
- [41] C. Zhang, S. Zhang, S. Song et al., "Preparation and tribological properties of surface-capped copper nanoparticle as a water-based lubricant additive," *Tribology Letters*, vol. 54, no. 1, pp. 25–33, 2014.
- [42] S. Ingle, A. Charanpahari, K. Amol, S. S. Umareb, D. V. Bhat, and J. Menghani, "Tribological behavior of nano TiO<sub>2</sub> as an additive in base oil," *Wear*, vol. 301, no. 1-2, pp. 776–785, 2013.
- [43] T. Luo, X. Wei, L. Huang, and F. Yang, "Tribological properties of Al<sub>2</sub>O<sub>3</sub> nanoparticles as lubricating oil additives," *Ceramics International*, vol. 40, no. 5, pp. 7143–7149, 2014.
- [44] M. Gulzar, H. Masjuki, M. Varman et al., "Improving the AW/EP ability of chemically modified palm oil by adding CuO and MoS<sub>2</sub> nanoparticles," *Tribology International*, vol. 88, pp. 271–279, 2015.
- [45] R. Chou, A. H. Battez, J. J. Cabello, J. L. Viesca, A. Osorio, and A. Sagastume, "Tribological behavior of polyalphaolefin with the addition of nickel nanoparticles," *Tribology International*, vol. 43, no. 12, pp. 2327–2332, 2010.
- [46] S. Yang, X.-J. Wang, X.-F. Li, and X. Li, "Influence of pH and SDBS on the stability and thermal conductivity of nanofluids," *Energy & Fuels*, vol. 23, no. 5, pp. 270–278, 2009.
- [47] Z. Jia, P. Wang, Y. Xia, H.-b. Zhang, X. Pang, and B. Li, "Tribological behaviors of diamond-like carbon coatings on plasma nitrided steel using three BN-containing lubricants," *Applied Surface Science*, vol. 255, no. 13-14, pp. 6666–6674, 2009.
- [48] L. Imene, D. Fabrice, V. Beatrice, and M. Jean-Michel, "Real time TEM imaging of compression and shear of single fullerene-like MoS<sub>2</sub> nanoparticle," *Tribology Letters*, vol. 45, pp. 131–141, 2011.
- [49] D. X. Peng, Y. Kang, R. M. Hwang, S. S. Shyr, and Y. P. Chang, "Tribological properties of diamond and SiO<sub>2</sub> nanoparticles added in paraffin," *Tribology International*, vol. 42, no. 6, pp. 911–917, 2009.
- [50] Y. Xia, W. Yang, X. Ma et al., "Research on the improvement of anti-wear properties of lubricating oil by nanometer copper powder," *Lubrication and Sealing*, vol. 5, pp. 43–44, 1998.
- [51] Y.-H. Xu, G.-B. Yang, S.-M. Zhang, and P.-Y. Zhang, "Preparation of water-soluble nano-copper and its tribological properties," *Acta Tribology*, vol. 32, no. 2, pp. 165–170, 2012.
- [52] L. Zhao, Z. Cai, Z. Zhang, and X. Zhang, "Tribological properties of graphene as effective lubricant additive in oil on textured bronze surface," *Chinese Journal of Materials Research*, vol. 30, no. 1, pp. 57–62, 2016.
- [53] M. K. Gupta, P. K. Sood, and V. S. Sharma, "Optimization of machining parameters and cutting fluids during nano-fluid based minimum quantity lubrication turning of titanium alloy by using evolutionary techniques," *Journal of Cleaner Production*, vol. 135, pp. 1276–1288, 2016.
- [54] R. Padmini, P. V. Krishna, and G. K. M. Rao, "Effectiveness of vegetable oil based nanofluids as potential cutting fluids in turning AISI 1040 steel," *Tribology International*, vol. 94, pp. 490–501, 2016.
- [55] A. K. Sharma, A. K. Tiwari, A. R. Dixit, R. K. Singh, and M. Singh, "Novel uses of alumina/graphene hybrid nanoparticle additives for improved tribological properties of lubricant in turning operation," *Tribology International*, vol. 119, pp. 99–111, 2018.
- [56] M. H. Cetin and S. K. Kilincarslan, "Effects of cutting fluids with nano-silver and borax additives on milling performance of aluminium alloys," *Journal of Manufacturing Processes*, vol. 50, pp. 170–182, 2020.
- [57] L. Hong, *Study on the Synthesis and Tribological Properties of Water-Soluble Fullerene Copolymer Nano-Microsphere Lubricating additives*, Huazhong University of Science and Technology, Wuhan, China, 2001.
- [58] L. Hong, J. Luo, and X. Hu, "Tribological research progress of fullerene (C60)," *Lubrication and Sealing*, vol. 27, no. 1, pp. 31–33, 2002.
- [59] D. G. Tochil'nikov, "Effect of fullerene black additives on boundary sliding friction of steel counterbodies lubricated with mineral oil," *Journal of Friction and Wear*, vol. 33, no. 2, pp. 94–100, 2012.
- [60] J. Lee, "Enhancement of lubrication properties of nano-oil by controlling the amount of fullerene nanoparticle additives," *Tribology Letters*, vol. 28, pp. 203–208, 2007.
- [61] A. Hirata, M. Igarashi, and T. Kaito, "Study on solid lubricant properties of carbon onions produced by heat treatment of diamond clusters or particles," *Tribology International*, vol. 37, no. 11-12, pp. 899–905, 2004.
- [62] Y. Yao, X. Wang, and J. Guo, "Tribological property of onion-like fullerenes as lubricant additive," *Materials Letters*, vol. 62, pp. 2524–2527, 2008.
- [63] F. Yan, Z. Jin, and X. Zhang, "Study on the tribological properties of C60/C70 as lubricant additives," *Tribology Journal*, vol. 13, no. 1, pp. 59–62, 1993.
- [64] L. Hong, W. Guan, and D. Liao, "Tribological behavior of fullerene-styrene-maleic anhydride terpolymer," *Applied Chemistry*, vol. 17, no. 2, pp. 180–182, 2000.
- [65] J. Li, Li Han, and W. Sun, "Research on the tribological properties of C60," *Chinese Journal of Tribology*, vol. 20, no. 4, pp. 307–309, 2000.

## Research Article

# A Potential Failure Mode and Effect Analysis Method of Electromagnet Based on Intuitionistic Fuzzy Number in Manufacturing Systems

Jihong Pang,<sup>1,2</sup> Jinkun Dai,<sup>2</sup> and Faqun Qi <sup>2</sup>

<sup>1</sup>College of Business, Shaoxing University, Shaoxing 312000, China

<sup>2</sup>College of Mechanical and Electrical Engineering, Wenzhou University, Wenzhou 325035, China

Correspondence should be addressed to Faqun Qi; [qifaqunqq@163.com](mailto:qifaqunqq@163.com)

Received 15 May 2021; Accepted 5 August 2021; Published 23 August 2021

Academic Editor: Francesco Tornabene

Copyright © 2021 Jihong Pang et al. This is an open access article distributed under the Creative Commons Attribution License, which permits unrestricted use, distribution, and reproduction in any medium, provided the original work is properly cited.

Failure mode and effect analysis (FMEA) is a systematic activity in the stage of product design and process design. However, the traditional FMEA has some shortcomings in practical application, such as too many evaluation languages, uncertain weights of influencing factors, and uncertain weights of evaluation members. This paper presents an FMEA evaluation method in manufacturing system based on similarity measure, nonlinear programming model, and intuitionistic fuzzy number (IFN). Firstly, the IFN is used to evaluate failure mode, which overcomes the defect of traditional FMEA evaluation value. Secondly, the weight of failure evaluation team members is solved according to the concept of similarity measure to make up for the blank of evaluation members' weight aiming at the shortage of unknown weight. Then, the definition of consensus measure is introduced to make the evaluators reach a consensus, and the weights of influencing factors of failure modes (FMs) are calculated. Finally, the weights of evaluators and influencing factors are calculated by IFN algorithm and score function, and the score value of each FM is obtained to rank instead of risk priority number (RPN). The objectivity and practicability of the new method are verified by the example of failure mode for an attractive electromagnet manufacturing system.

## 1. Introduction

FMEA is a systematic activity in product design stage and process design stage. The subsystems and parts of FMEA are analyzed one by one to identify all potential FMs and their possible consequences, so as to take necessary measures in advance to improve the quality and reliability of products. FMEA was originally carried out in the product design phase of the aerospace industry in the 1960s to help improve safety and reliability [1]. In addition, FMEA enables an organization to proactively prevent failure, not just respond to it [2]. FMEA is also a simple method to solve the complex failure mode evaluation process [3]. Because of its simple and easy operation, FMEA is widely used in transportation, energy, medical, and supply chain transportation [4, 5].

On the other hand, the traditional FMEA process is used to evaluate the FMs of products or systems by team

members. The severity, occurrence, and detection (S, O, D) of FMs according to their own professional knowledge are calculated by the scores of each failure mode [6]. Although FMEA is widely used, it has some inherent defects. To ensure the objectivity of FMEA, we must ensure that the evaluation language of failure mode should conform to the actual situation, so as to make a more comprehensive and specific description of failure mode. However, the traditional FMEA uses natural language to carry out evaluation, which does not conform to the psychological changes of the evaluation members in reality [7]. Secondly, the weight of factors is also the key to affect the final evaluation results [8]. For example, the weights of influencing factors are evenly distributed by traditional FMEA, which will lead to great difference between the calculation results and the actual situation [9]. In the actual production, the evaluation members in different working positions have different understanding of the

definition and importance of failure; it is necessary to accurately calculate the weight of each evaluation member in the evaluation team to determine the failure mode sequencing [10, 11].

In order to improve the shortcomings of the traditional FMEA, many scholars and researchers have carried out more rigorous research on this method and made it more objective and true to reflect the impact of failure. So, further research in this area would be needed. A comprehensive risk ranking method to improve the performance of FMEA was developed by using interval-valued intuitionistic fuzzy sets (IVIFs) and multiattribute boundary approximation area comparison (MABAC). In addition, a linear programming model to obtain the optimal weight of risk factors was established under the condition of incomplete prior knowledge of weight information [12]. A new integrated fuzzy intelligent FMEA framework was proposed. The framework adopts the combination of fuzzy set theory, analytic hierarchy process (AHP), and data envelopment analysis (DEA) to deal with uncertainty and improve the reliability of risk assessment. All of these are achieved by employing a heterogeneous expert group. RPN, time, and cost are used as indicators to determine the efficiency of FMEA mode and determine the appropriate priority and corrective measures [13]. An interactive method to deal with the possible uncertainties in the evaluation process was proposed by using the fuzzy set theory. In order to deal with the weight of subjective and objective uncertainties, the AHP and entropy weight method were adopted [14]. A new method combining evidence theory, intuitive fuzzy set (IFS), and belief entropy has been proposed to determine the weight of team members to analyze FMs [15]. A hybrid FMEA framework has been developed which integrates the Portuguese abbreviation for interactive and multicriteria decision method with the Choquet integration method. Under this framework, the uncertainty in risk assessment is described by generalized trap type fuzzy numbers [16]. A consensus-based FMEA group decision-making framework was proposed. The purpose of this framework is to classify FMs into several ordinal risk classes. Assuming that FMEA participants provide their preferences in a linguistic manner using the possibility hesitant fuzzy linguistic information, a consensus driven method is proposed to generate the weight of risk factors in the FMEA framework. On this basis, the consensus rules based on optimization guided by the minimum adjustment distance strategy are calculated, and an interaction model for consensus is developed to generate consensus failure mode risk classes [17]. A triangular distribution-based basic probability assignment (TDBPA) method based on triangular distribution was presented within the framework of Dempster–Shafer evidence theory, the conflict risk levels assessed by different experts. The modified RPN model based on fusion assessment could calculate the ranking of FMs [18]. A new comprehensive multicriteria decision-making (MCDM) method and fuzzy multiattribute ideal real comparative analysis (FMAIRCA) were proposed. It combines the first method to calculate the fuzzy relative importance between risk factors by using quantitative method [19]. In order to improve the

performance of classical FMEA, the weights of influencing factors are determined by using the fuzzy optimization method, and a fuzzy VIKOR approach was used to evaluate the security policies and analyze the content of five press agencies in expert decision making [20].

In this paper, the concept of similarity measurement is used to solve the weights of evaluation members and makes up for the blank of obtaining weights of evaluation members on the basis of existing research further to improve the FMEA. In the same time, the definition of consensus measurement is introduced to reach consensus on the evaluation of the evaluators, and the weights of influencing factors are solved by using the approved method. The remainder of this paper is arranged as follows: in Section 2, a decision process of electromagnet FMEA is presented. Section 3 describes the IFN evaluation of failure mode with a form of influencing factors. In Section 4, the weight of evaluation members and influencing factors is determined by comprehensive calculation, and the IFN of FMs is obtained. The scores of each failure mode are obtained and sorted according to the score function. An illustrative example of FMEA of electromagnet is shown in Section 5. The last chapter summarizes the work done in this paper.

## 2. Flow Chart of FMEA of Electromagnet

FMEA methodically breaks down the analysis of complex manufacturing processes of electromagnet into manageable steps. FMEA can be used to identify potential failure modes for electromagnet and determine their impacts during production and fabrication. The flow chart of FMEA of electromagnet is shown in Figure 1.

To achieve the desired effect of this paper, the following key steps are taken. Step 1: determine the target and risk level of the electromagnet product risk analysis, collect the potential failure mode and failure impact, and the evaluation team evaluates the failure mode by using the IFN. Step 2: according to the incomplete weight information in FMEA, the similarity measure is used to determine the weight of evaluation team members. Step 3: for the influencing factors of failure, the evaluation members use IFNs for comparative evaluation and form a comparison matrix. In order to find the optimal solution of the influencing factors, the exact weight of the influencing factors is derived from the preference relation of the comparison matrix. Step 4: after the weight information in FMEA is all determined, simple intuitionistic fuzzy weighted geometry (SIFWG) is used to aggregate the evaluation information and weight information, and the score of each failure mode is calculated according to the definition of intuitionistic fuzzy score function, and the order is made.

## 3. Evaluation of IFNs on FMs and Influencing Factors

In 1965, Zadeh defined the mathematical meaning of IFs for the first time [21] and opened a new chapter of fuzzy mathematics. In 1986, Atanassov popularized fuzzy sets, and



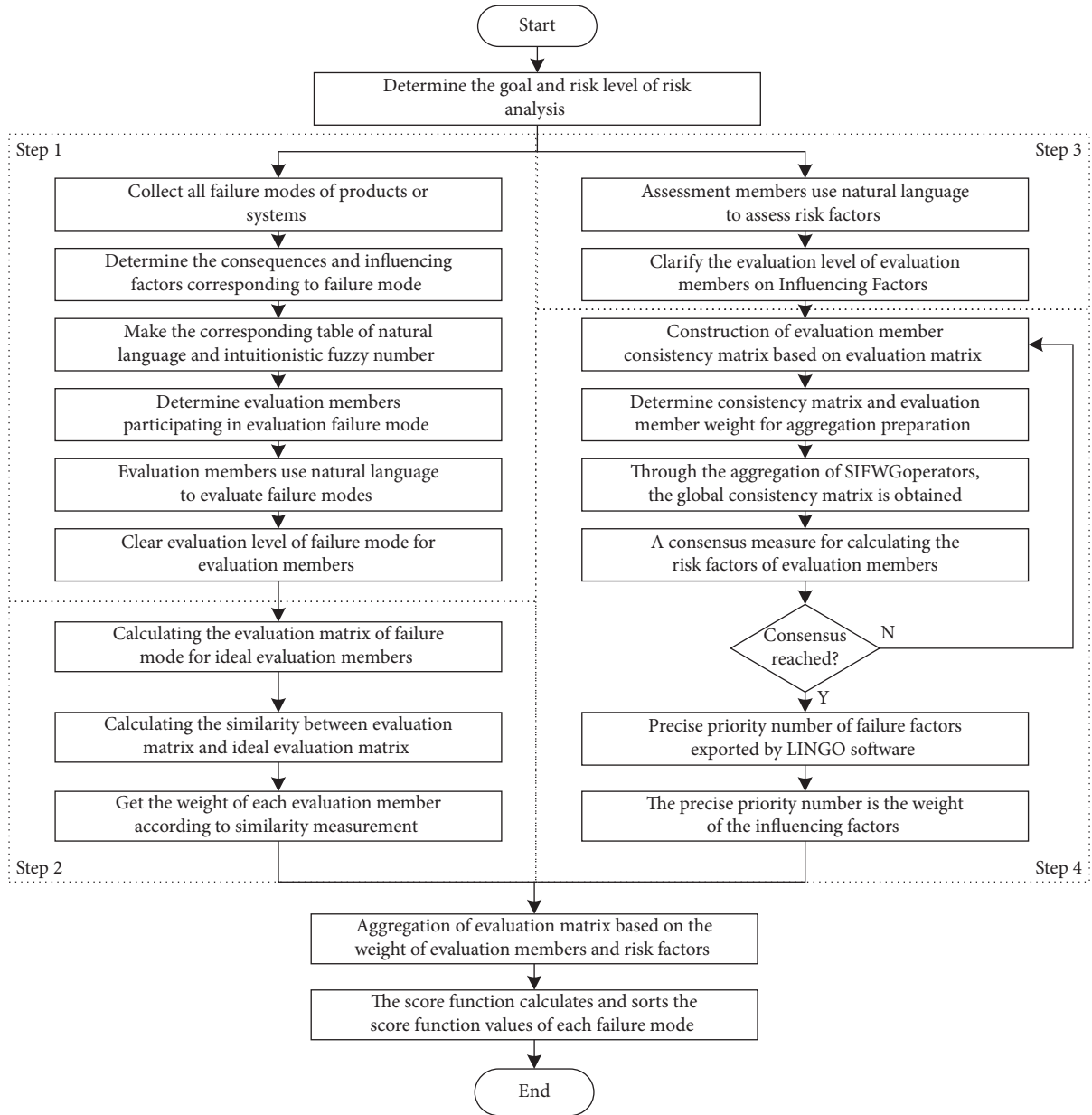


FIGURE 1: Flow chart of FMEA of electromagnet.

it was also the first time to express the relationship between an element and a specific set with the three indexes of membership degree, nonmembership degree, and hesitation, and he put forward the concept of IFSs [22]. Let the set  $X$  be a universe of discourse, the fuzzy set  $F$  on  $X$  is represented by membership degree  $\mu_F, \mu_F: X \rightarrow [0, 1]$ , and then the membership degree of  $x$  in the set  $F$  is denoted by  $\mu_F(x)$ . IFS is an object that has the following form:

$$A = \{x, \mu_A(x), \nu_A(x) | x \in X\}, \quad (1)$$

where  $\mu_A(x)$ ,  $\nu_A(x)$  means the membership degree and nonmembership degree of the element  $x \in X$  to  $A$ , respectively, with the condition that for all  $x \in X$ , then

$$\begin{aligned} 0 \leq \mu_A(x) &\leq 1, \\ 0 \leq \nu_A(x) &\leq 1, \\ 0 \leq \nu_A(x) + \mu_A(x) &\leq 1. \end{aligned} \quad (2)$$

3.1. Basic Operation Law of IFN. Let  $a = (\mu_a, \nu_a)$  be IFN, then the basic operation law of IFN is displayed as follows [23]:

$$\lambda a = (1 - (1 - \mu_a)^\lambda, \nu_a^\lambda), \quad (3)$$

$$a^\lambda = (\mu_a^\lambda, 1 - (1 - \nu_a)^\lambda), \quad (4)$$

$$\bigoplus_{j=1}^n a_j = \left( 1 - \prod_{j=1}^n (1 - \mu_a), \prod_{j=1}^n \nu_{a_j} \right), \quad (5)$$

$$\bigoplus_{j=1}^n a_j = \left( \prod_{j=1}^n \mu_{a_j}, 1 - \prod_{j=1}^n (1 - \nu_a) \right). \quad (6)$$

3.2. *Ranking Rules of IFNs.* Let  $a = (\mu_a, \nu_a)$  be IFN; its score function  $S(a)$  and accuracy function  $H(a)$  are expressed, respectively, by the following formulas:

$$S(a) = |\mu_a - \nu_a|, \quad (7)$$

$$H(a) = \mu_a + \nu_a. \quad (8)$$

Let  $a_i = (\mu_{a_i}, \nu_{a_i})$  and  $a_j = (\mu_{a_j}, \nu_{a_j})$  be two IFNs, then the procedure of comparing the magnitude of two IFNs is introduced as follows:

$$\text{if } S(a_i) < S(a_j), \text{ then } a_i < a_j. \quad (9)$$

If  $S(a_i) = S(a_j)$ , then we can get the following conclusions:

$$\text{If } H(a_i) < H(a_j), \text{ then } a_i < a_j. \quad (10)$$

$$\text{If } H(a_i) = H(a_j), \text{ then } a_i = a_j. \quad (11)$$

Because the similarity function is improved on the basis of score function, all similarity functions  $L(a)$  conform to the rules of score function.

## 4. Failure Mode and Effect Analysis

FMEA is a comprehensive calculation of decision information of failure mode by comprehensive decision personnel. The total proportion of influencing factors by each evaluation member can directly affect the ranking of final failure mode. Therefore, the weights of objective evaluation members and influencing factors are determined before the final comprehensive calculation.

4.1. *Determination of the Weight of Evaluation Members.* Considering all possible options, we select the risk assessment

matrices  $X^k = [x_{ij}^k]_{m \times n} = [\mu_{ij}^k, \nu_{ij}^k]_{m \times n}$ , where  $k = 1, \dots, l$ , and adopt many ways to estimate the evaluation model. Next, the ideal assessment of the failure mode can be the average of a single risk assessment matrix, and the expression of ideal matrix is shown as follows [24]:

$$X^* = [x_{ij}^*]_{m \times n} = [\mu_{ij}^*, \nu_{ij}^*]_{m \times n}, \quad (12)$$

where  $x^* = 1/lx_{ij}^k, k = 1, \dots, l$ , and  $\mu_{ij}^* = 1 - \prod_{k=1}^l (1 - \mu_{ij}^k)^{1/l}$ ,  $\nu_{ij}^* = \prod_{k=1}^l (\nu_{ij}^k)^{1/l}$ ,  $i = 1, \dots, m$ ,  $j = 1, \dots, n$ .

Let  $a_1 = (\mu_{a_1}, \nu_{a_1})$  and  $a_2 = (\mu_{a_2}, \nu_{a_2})$  be two IFNs, then the interval-valued intuitionistic fuzzy Euclidean distance is calculated as

$$d(a_1, a_2) = \sqrt{\frac{1}{2} \left( (\mu_1 - \mu_2)^2 + (\nu_1 - \nu_2)^2 \right)}. \quad (13)$$

Let  $X^1 = (x_{ij}^1)_{m \times n} = (\mu_{ij}^1, \nu_{ij}^1)$ ,  $X^2 = (x_{ij}^2)_{m \times n} = (\mu_{ij}^2, \nu_{ij}^2)$  be two interval-valued intuitionistic fuzzy matrixes, then the similarity measure of the two matrixes is defined as

$$\text{sim}(X^1, X^2) = \frac{\sum_{i=1}^m \sum_{j=1}^n d(x_{ij}^1, x_{ij}^{2c})}{\sum_{i=1}^m \sum_{j=1}^n (d(x_{ij}^1, x_{ij}^{2c}) + d(x_{ij}^1, x_{ij}^2))}, \quad (14)$$

where  $d$  is the Euclidean distance,  $x_{ij}^{2c} = (\nu_{ij}^2, \mu_{ij}^2)$ ,  $0 \leq \text{sim}(X^1, X^2) \leq 1$ , when  $X^1 = X^2$ ,  $\text{sim}(X^1, X^2) = 1$ .

Next, the similarity between the evaluation results of each evaluator and the ideal evaluation results is obtained

$$\text{sim}(X_k, X^*) = \frac{\sum_{i=1}^m \sum_{j=1}^n d(x_{ij}^k, x_{ij}^{*c})}{\sum_{i=1}^m \sum_{j=1}^n (d(x_{ij}^k, x_{ij}^{*c}) + d(x_{ij}^k, x_{ij}^*))}, \quad (15)$$

where  $X^{*c} = [x_{ij}^{*c}]_{m \times n} = [\nu_{ij}^*, \mu_{ij}^*]_{m \times n}$ .

At last, the weights of the FMEA team members are determined as follows:

$$\lambda_k = \frac{\text{sim}(X_k, X^*)}{\sum_{k=1}^l \text{sim}(X_k, X^*)}. \quad (16)$$

## 4.2. Determination of the Weight of Influencing Factors

4.2.1. *Construction of Perfect Product Consistency Matrix.* In the traditional AHP, the consistency ratio (CR) is used to measure the consistency of the product relation. In this paper, the intuitionistic fuzzy matrix of  $R = (r_{ik})_{m \times m} = (\mu_{ik}, \nu_{ik})$  is constructed into a perfect product consistent intuitionistic fuzzy matrix  $R^p = (r_{ik}^p)_{m \times m}$  by using the following algorithm:

(1) If  $k > i + 1$ ,  $r_{ik}^p = (\mu_{ik}^p, \nu_{ik}^p)$ , where

$$\mu_{ik}^p = \frac{\sqrt[k-i-1]{\prod_{k-1}^{t=i+1} \mu_{it} \mu_{tk}}}{\sqrt[k-i-1]{\prod_{k-1}^{t=i+1} \mu_{it} \mu_{tk}} + \sqrt[k-i-1]{\prod_{k-1}^{t=i+1} (1 - \mu_{it})(1 - \mu_{tk})}}, \quad (17)$$

$$\nu_{ik}^p = \frac{\sqrt[k-i-1]{\prod_{k-1}^{t=i+1} \nu_{it} \nu_{tk}}}{\sqrt[k-i-1]{\prod_{k-1}^{t=i+1} \nu_{it} \nu_{tk}} + \sqrt[k-i-1]{\prod_{k-1}^{t=i+1} (1 - \nu_{it})(1 - \nu_{tk})}}. \quad (18)$$

(2) If

$$k = i + 1, \quad r_{ik}^p = r_{ik}. \quad (19)$$

(3) If

$$k < i + 1, \quad r_{ik}^p = (\nu_{ik}^p, \mu_{ik}^p). \quad (20)$$

4.2.2. *Determination and Iterative Modification of Consistency Measure.* Generally, the level of evaluation members is basically the same, and the evaluation results obtained should coincide. However, the inconsistency of evaluation results cannot be avoided in real life. The process of group consensus is to find the final solution accepted by the evaluated personnel. The following gives an algorithm to reach consensus.

Step 1: calculating the consensus degree of evaluation members,

$$C_l = 1 - \frac{\sum_{1 \leq i \leq j \leq m} (|\mu_{ij}^p - \mu_{ij}^*| + |\nu_{ij}^p - \nu_{ij}^*| + |\pi_{ij}^p - \pi_{ij}^*|)}{(m-1)(m-2)}. \quad (21)$$

If the consensus degree reaches the critical value  $\gamma$  of group consensus, the result of SIFWG will be output; otherwise, turn to step 2.

Step 2: revising according to the formula,

$$\mu_{ij}^{lp} = (\mu_{ij}^{lp})^\xi \times (\mu_{ij}^*)^{1-\xi}, \nu_{ij}^{lp} = (\nu_{ij}^{lp})^\xi \times (\nu_{ij}^*)^{1-\xi}, \quad (22)$$

where  $R^{lp} = (r_{ik}^{lp})_{m \times n} = (\mu_{ij}^{lp}, \nu_{ij}^{lp})_{m \times n}$  is the perfect product consistent intuitionistic fuzzy matrix of evaluator  $l$ .

Step 3: calculating the consensus degree.

In this paper, we use the new modified perfect product consistent intuitionistic fuzzy matrix to calculate the consensus degree. If it meets the critical value, the new modified perfect product consistent intuitionistic fuzzy matrix is aggregated with SIFWG operator to form a new aggregation matrix. If it does not meet the critical value, turn to Step 2 until it meets the critical value.

4.2.3. *Aggregation of Evaluation Information and Derivation of Influencing Factors' Weight.* According to above-mentioned algorithm, the perfect product consistency intuitionistic fuzzy matrix  $R^p = (r_{ik}^p)_{m \times n}$  is obtained. For information aggregation, there are many operators that can be used. This paper uses SIFWG operator, because the matrix before aggregation has consistency, and because the after aggregation through SIFWG operator has the same consistency. Then, the matrix  $R^* = (r_{ij}^*)_{m \times n} = (\mu_{ij}^*, \nu_{ij}^*)$  of SIFWG aggregation is obtained, which is shown in the following:

$$\mu_{ij}^* = \prod_{k=1}^l (\mu_{ij}^p)^{\lambda_k}, \nu_{ij}^* = \prod_{k=1}^l (\nu_{ij}^p)^{\lambda_k}, \quad i = 1, \dots, m, j = 1, \dots, n. \quad (23)$$

According to the accurate priority derivation method of IFNs, the nonlinear programming model is solved by LINGO software, and the weight of influencing factors is obtained directly [25]. Based on the standard operation of LINGO software, we take the matrix as an example to show the nonlinear programming model:

$$\begin{aligned} \min f &= \sum_{i=1}^{m-1} \sum_{k=i+1}^m (\rho_{ik} + \delta_{ik}), \\ \text{s.t.} &\begin{cases} \frac{\omega_i}{\omega_i + \omega_k} + \rho_{ik} - \mu_{ik} \geq 0, \\ \frac{\omega_i}{\omega_i + \omega_k} - \delta_{ik} + \nu_{ik} \geq 0, \\ \sum_{i=1}^m \omega_i = 1, \omega_i \in [0, 1], \\ \rho_{ik} \geq 0, \delta_{ik} \geq 0, \rho_{ik} * \delta_{ik} = 0. \end{cases} \end{aligned} \quad (24)$$

Export  $\omega = (\omega_s, \omega_o, \omega_d)$ , where  $i = 1, \dots, m-1; k = i+1, \dots, m$ ,  $\rho_{ik}, \delta_{ik}$  is the relaxation variable,  $\mu_{ik} - \rho_{ik} \leq \omega_i / \omega_i + \omega_k \leq 1 - \nu_{ik} + \delta_{ik}$ .

4.3. *Potential Failure Mode Score and Ranking.* In this paper, we present the integrate evaluator and influence factor weights with evaluation information, which is shown as

$$FM_i = \sum_{k=1}^l \lambda_k (\mu_{ij}^k, \mu_{ij}^k) \omega_s + \sum_{k=1}^l \lambda_k (\mu_{ij}^k, \mu_{ij}^k) \omega_o + \sum_{k=1}^l \lambda_k (\mu_{ij}^k, \mu_{ij}^k) \omega_d, \quad (25)$$

where the evaluation information of  $k$  assessor is  $(\mu_{ij}^k, \mu_{ij}^k) i = 1, \dots, m, j = 1, \dots, n$ .

Finally, the IFN  $(\mu_{FM}, \nu_{FM})$  of failure mode is obtained. According to the score function formula of IFN, the score of each failure mode is sorted.

## 5. An Example

This chapter is divided into two sections. Section 5.1 shows the calculation process and precautions of each part of the new method through an evaluation example of the attractive electromagnet. Section 5.2 illustrates the objectivity and practicability of this method by comparing with the other three methods.

5.1. *An Example in Manufacturing Systems.* The attractive electromagnet itself has a plunger. When the coil is energized, it will attract the plunger to a certain distance and transmit the movement to other loads requiring mechanical action. The structure is shown in Figure 2. They are widely used in electromagnetic relays, solenoid valves, and other products. When the suction electromagnet works, it not only needs to complete the specified movement but also needs to be in the position. The iron reaches the load area, so the consequence of its failure mode is very serious. This paper takes the FMEA of suction electromagnet in the early stage of production as an example to verify the practicability and objectivity of this paper. Since the evaluation information of evaluation members in this paper is in natural language, it is necessary to convert natural language into IFN for

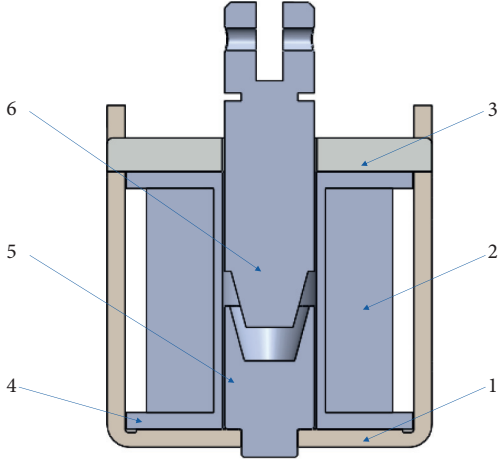


FIGURE 2: Schematic diagram of suction electromagnet structure.

calculation. The corresponding table of natural language and IFN is shown as Table 1, and the main FMs are shown in Table 2.

The company organized three evaluators to evaluate the  $S$ ,  $O$ , and  $D$  of the fault in natural language mode according to the evaluation criteria of influencing factors in Tables 3–5.

Also, the results of the computations are shown in Table 6.

Then, according to the corresponding table of natural language and IFN in Table 1, the evaluation table in natural language is transformed into the form of IFN; calculated results are given in Table 7.

According to formulas (14)–(20), the weight of evaluation members is determined,  $\lambda_1 = 0.316$ ,  $\lambda_2 = 0.34$ , and  $\lambda_3 = 0.344$ .

The comparison matrix is obtained by comparing the influence factors of the evaluation members, as shown in Table 8.

The natural language in Table 8 is transformed into IFN according to the corresponding table of natural language and IFN, and then according to algorithm 1, the perfect product consistent intuitionistic fuzzy matrix is constructed, as shown in Table 9.

According to the SIFWG aggregation operator of formula (23), the weight of all evaluators,  $\lambda$ , has been obtained,  $\lambda_1 = 0.316$ ,  $\lambda_2 = 0.34$ , and  $\lambda_3 = 0.344$ , for example, the aggregation result of membership degree of influencing factor  $S$  compared with that of influencing factor  $O = 0.7^{0.316} * 0.8^{0.34} * 0.8^{0.344} = 0.7669$ . The aggregation result of nonmembership degree  $= 0.2^{0.316} * 0.1^{0.34} * 0.1^{0.344} = 0.1245$ . Similarly, other polymerization results are shown in Table 10.

According to formula (21), the consensus degree of each evaluator is  $C_1 = 0.5722$ ,  $C_2 = 0.7422$ ,  $C_3 = 0.8537$ . If the critical value of consensus degree  $C$  is set to 0.5, then all three evaluators meet the critical value, and it is generally considered that consensus can be reached only when the critical value  $C = 0.85$ . Then, it is modified according to formula (22), where the iterative operation is taken as  $\xi = 0.5$ . After three iterations, the consensus reached is

TABLE 1: Table of natural language and IFNs for failure mode assessment.

Natural language	IFN
Extremely low (EL)	(0.10, 0.90)
Very low (VL)	(0.10, 0.75)
Low (L)	(0.25, 0.60)
Medium low (ML)	(0.40, 0.50)
Medium (M)	(0.50, 0.50)
Medium high (MH)	(0.60, 0.30)
High (H)	(0.70, 0.20)
Very high (VH)	(0.80, 0.10)
Extremely high (EH)	(0.90, 0.10)
Definitely high (DH)	(1.00, 0.00)

$C'_1 = 0.8682$ ,  $C'_2 = 0.8528$ ,  $C'_3 = 0.9544$ . When consensus is reached, the matrix aggregated by SIFWG operators is shown in Table 11.

According to algorithm 3, the nonlinear programming model is constructed as follows:

$$\min f = \rho_{12} + \delta_{12} + \rho_{13} + \delta_{13} + \rho_{23} + \delta_{23}, \quad (26)$$

$$\text{s.t.} \begin{cases} \frac{\omega_1}{\omega_1 + \omega_2} + \rho_{12} - 0.79 \geq 0, \\ \frac{\omega_1}{\omega_1 + \omega_3} + \rho_{13} - 0.667 \geq 0, \\ \frac{\omega_2}{\omega_2 + \omega_3} + \rho_{23} - 0.575 \geq 0, \\ \frac{\omega_1}{\omega_1 + \omega_2} - \delta_{12} + 0.107 \geq 0, \\ \frac{\omega_1}{\omega_1 + \omega_3} - \delta_{13} + 0.25 \geq 0, \\ \frac{\omega_2}{\omega_2 + \omega_3} - \delta_{23} + 0.323 \geq 0, \\ \omega_1 + \omega_2 + \omega_3 = 1, \\ 0 \leq \omega_1 \leq 1, 0 \leq \omega_2 \leq 1, 0 \leq \omega_3 \leq 1, \\ \rho_{12} \geq 0, \rho_{13} \geq 0, \rho_{23} \geq 0, \\ \delta_{12} \geq 0, \delta_{13} \geq 0, \delta_{23} \geq 0, \\ \rho_{12} * \delta_{12} = 0, \rho_{13} * \delta_{13} = 0, \rho_{23} * \delta_{23} = 0. \end{cases} \quad (27)$$

In this paper, we use LINGO software to solve formulas (26) and (27) and then derive the weight of each influencing factor in Figure 3.

From Figure 3, we can see  $\omega_1 = 0.684$ ,  $\omega_2 = 0.182$ , and  $\omega_3 = 0.134$ ; in turn, the corresponding is  $\omega_S = 0.684$ ,  $\omega_O = 0.182$ , and  $\omega_D = 0.134$ .

According to formula (25) and the operation rules of IFNs, such as the final score calculation in  $FM_1$ , the score after the weight of comprehensive influencing factors is calculated first, and the calculation formula is as follows:

TABLE 2: Failure mode analysis table.

No.	Failure mode	Failure effect	Failure reason
F1	Poor insulation	Product leakage	Insufficient insulation level of material
F2	The strength of the spool is not enough, and the product splits after winding	Magnetic flux leakage products	(i)Low strength of plastic materials (ii)Improper design of spool (iii)Excessive tension design
F3	Short circuit/open circuit of product after power on and heating	Cannot drive the action of customer organization, customer cannot use it	Insufficient temperature resistance of materials
F4	Insufficient strength of end foot	Affect customer installation	Improper soldering and assembly design
F5	Poor surface roughness	Affect product life	Improper design of dimensional tolerance
F6	Poor concentricity	Customer unable to install or not suitable for installation	Improper design of dimensional tolerance
F7	The magnetic force of the product is insufficient after being electrified	Unable to drive customer organization action	(i)The magnetic permeability of the material is insufficient, and the attraction is insufficient after being electrified (ii)Improper design
F8	Residual magnetic field after power on	Unable to drive customer organization action	(i)The magnetic permeability of the material is insufficient, and the attraction is insufficient after being electrified (ii)The thickness of the lower wall is thin
F9	Appearance corrosion and rust	Poor appearance, customer dissatisfied	The antirust layer is too thin and the process is improper

TABLE 3: S assessment criteria.

Influence	Assessment criteria: severity of consequences (customer impact)	Grade
Failure of laws and regulations affecting safety or government	Work safety is affected or government regulations are not met without any warning	DH
	In case of warning, it will affect work safety or not comply with government regulations	EH
Loss or reduction of expected function	Loss of basic function (electromagnet does not work and does not affect safety)	VH
	Expected function reduction (electromagnet can work, performance level is reduced)	H
Loss or reduction of secondary function	Loss of secondary function (failure of comfort and convenience function)	MH
	Lower secondary function (lower comfort and convenience function level)	M
Customer feedback	Electromagnets work, and most customers (>75%) perceive noise and appearance	ML
	Electromagnets work, and some customers (50%) perceive noise and appearance	L
	The electromagnet works, and a small number of customers (<25%) are aware of noise and appearance	VL
No impact	No detectable impact	EL

TABLE 4: O assessment criteria.

Possibility of failure	Evaluation criteria: the possibility of causes	Grade
Very high	New technology and new design without corresponding history	DH
High	Inevitable failure due to new design, new application, or change of operating conditions	EH
	New design, new application, or change of operating conditions may lead to failure	VH
	Uncertain failures due to new design, new application, or change of operating conditions	H
Medium	Failure of similar design and design test	MH
	Occasional failures in design and testing	M
	Isolated failures in similar designs and design tests	ML
Low	Almost identical designs and isolated failures in design testing	L
	Almost the same design and undetected failure in design testing	VL
Very low	By preventing controllable failures	EL

TABLE 5: *D* assessment criteria.

Opportunity discovery	Evaluation criteria: possibility of discovery through design control	Grade
Very very low	There is no current design control that cannot be found or analyzed	EL
Very low	Design analysis has weak discovery ability	VL
Low	Verification of a product that has passed testing (subsystem or system testing, e.g., noise and shipping) prior to release	L
Medium low	Verification of products using fault testing before product release (testing of subsystem or system failure)	ML
Medium	Verification of products using failure testing before product release (durability testing subsystem or system, such as function check)	M
Medium high	Product validation by testing before design freezing	MH
High	Product confirmation by fault test before design freezing	H
Very high	Use old test to confirm products before design freezing	VH
Very very high	Design data analysis has strong ability of discovery	EH
Extremely high	FMs cannot occur because of a fully preventive design	DH

TABLE 6: Evaluation table of evaluators in natural language.

Failure mode	Evaluators								
	E1			E2			E3		
	S	O	D	S	O	D	S	O	D
F1	VH	EL	VL	VH	L	VL	VH	VL	EL
F2	VH	L	EL	H	L	VL	H	EL	VL
F3	MH	VL	ML	VH	EL	VL	VH	VL	VL
F4	MH	L	EL	VH	VL	M	VH	L	EL
F5	M	VL	ML	MH	L	EL	MH	L	L
F6	EH	EL	VL	EH	L	M	EH	EL	EL
F7	VH	L	VL	MH	M	L	MH	L	L
F8	MH	M	L	VH	EL	EL	H	VL	VL
F9	M	VL	VL	M	VL	VL	M	VVL	VL

TABLE 7: Evaluation table under IFN.

Failure mode	Evaluators																	
	E1						E2						E3					
	S		O		D		S		O		D		S		O		D	
F1	0.8	0.1	0.1	0.75	0.1	0.75	0.8	0.1	0.25	0.6	0.1	0.75	0.8	0.1	0.1	0.75	0.1	0.9
F2	0.8	0.1	0.25	0.6	0.1	0.9	0.7	0.2	0.25	0.6	0.1	0.75	0.7	0.2	0.1	0.75	0.1	0.75
F3	0.6	0.3	0.1	0.75	0.5	0.5	0.8	0.1	0.1	0.9	0.1	0.75	0.8	0.1	0.1	0.75	0.1	0.75
F4	0.6	0.3	0.25	0.6	0.1	0.9	0.8	0.1	0.1	0.75	0.5	0.5	0.8	0.1	0.25	0.6	0.1	0.9
F5	0.5	0.5	0.1	0.75	0.4	0.5	0.6	0.3	0.25	0.6	0.1	0.9	0.6	0.3	0.25	0.6	0.25	0.6
F6	0.9	0.1	0.1	0.9	0.1	0.75	0.9	0.1	0.5	0.5	0.5	0.9	0.1	0.1	0.9	0.1	0.9	
F7	0.8	0.1	0.25	0.6	0.1	0.75	0.6	0.3	0.25	0.6	0.25	0.6	0.6	0.3	0.25	0.6	0.25	0.6
F8	0.6	0.3	0.5	0.5	0.1	0.9	0.8	0.1	0.1	0.9	0.1	0.9	0.7	0.2	0.1	0.75	0.1	0.75
F9	0.5	0.5	0.1	0.75	0.1	0.75	0.5	0.5	0.1	0.75	0.1	0.75	0.5	0.5	0.1	0.9	0.1	0.75

TABLE 8: Comparison of influencing factors.

Evaluator E1				Evaluator E2				Evaluator E3			
O	S	O	D	O	S	O	D	O	S	O	D
S	M	H	MH	S	M	VH	M	S	M	VH	H
O	H'	M	ML	O	VH'	M	M	O	VH'	M	H
D	MH'	ML'	M	D	M'	M'	M	D	H'	H'	M

Here,  $H'$  is the complement of  $H$  natural language. For example, the IFN corresponding to  $H$  natural language is  $(0.70, 0.20)$ , and then the IFN corresponding to  $H'$  natural language is  $(0.20, 0.70)$ .

TABLE 9: Perfect product consistency intuitionistic fuzzy matrix for every evaluator.

Evaluator E1								
	S		O		D			
S	0.5	0.5	0.7	0.2	0.667	0.25		
O	0.2	0.7	0.5	0.5	0.4	0.5		
D	0.25	0.667	0.5	0.4	0.5	0.5		

Evaluator E2								
	S		O		D			
S	0.5	0.5	0.8	0.1	0.667	0.25		
O	0.1	0.8	0.5	0.5	0.5	0.5		
D	0.25	0.667	0.5	0.5	0.5	0.5		

Evaluator E3								
	S		O		D			
S	0.5	0.5	0.8	0.1	0.667	0.25		
O	0.1	0.8	0.5	0.5	0.7	0.2		
D	0.25	0.667	0.2	0.7	0.5	0.5		

TABLE 10: Evaluation information of influencing factors after aggregation.

	S		O		D	
S	0.5000	0.5000	0.7669	0.1245	0.6670	0.2500
O	0.1245	0.7669	0.5000	0.5000	0.5231	0.3648
D	0.2500	0.6670	0.3648	0.5231	0.5000	0.5000

TABLE 11: Aggregation matrix after iterative operation.

	S		O		D	
S	0.500	0.500	0.790	0.107	0.667	0.250
O	0.107	0.790	0.500	0.500	0.575	0.323
D	0.250	0.667	0.323	0.575	0.500	0.500

Local optimal solution found.

Objective value: 0.8578657E-01

Infeasibilities: 0.000000

Total solver iterations: 7

Elapsed runtime seconds: 1.93

Model Class: NLP

Total variables: 9

Nonlinear variables: 3

Integer variables: 0

Total constraints: 11

Nonlinear constraints: 6

Total nonzeros: 30

Nonlinear nonzeros: 12

Variable	Value	Reduced Cost
A12	0.000000	0.1727102
B12	0.000000	1.000000
A13	0.000000	1.000000
B13	0.8578657E-01	0.000000
A23	0.000000	0.4383739
B23	0.000000	1.000000
W1	0.6838540	0.000000
W2	0.1817840	0.000000
W3	0.1343621	0.000000

FIGURE 3: Influencing factor weight derivation chart.

TABLE 12: Summary of final results.

Failure mode	Score	Sort
F1	6.658	9
F2	6.812	8
F3	7.018	6
F4	7.299	5
F5	7.664	2
F6	6.943	7
F7	7.482	4
F8	7.497	3
F9	8.011	1

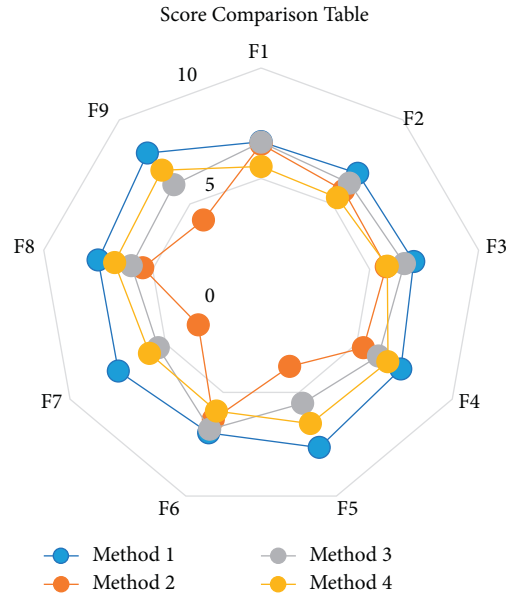


FIGURE 4: Comparison score table.

$$0.684 * (0.9, 0.1) + 0.684 * (0.8, 0.1) + 0.684 * (0.8, 0.1) + 0.182 * (0.1, 0.8) + 0.182 * (0.1, 0.9) + 0.182 * (0.1, 0.8) + 0.134 * (0.1, 0.9) + 0.134 * (0.1, 0.8) + 0.134 * (0.1, 0.9) = 6.658. \tag{28}$$

Similarly, the final scores for other FMs are calculated and ranked according to the final scores, as shown in Table 12.

5.2. *Discussions.* This approved method is compared with the other three methods in terms of final scores. The three methods for comparison are traditional FMEA, only calculating the weight of influencing factors, and only calculating the weight of evaluating personnel. Except for the weight, the other steps are the same as the new method. The score table is shown in Figure 4.

It is obvious from the two tables that there is a big difference between the traditional FMEA ranking and the score of this new method. This is because the traditional FMEA does not specify the weight of influencing factors and the weight of evaluation members; so, when the score function is used to calculate the score, the value of evaluation content is all involved in the calculation. However, from the above calculation, the result is  $\omega_s = 0.684$ ,  $\omega_o = 0.182$ ,

$\omega_d = 0.134$ ,  $\omega_{E1} = 0.316$ ,  $\omega_{E2} = 0.34$ ,  $\omega_{E3} = 0.344$ . According to the operation rules of IFNs, the rule calculation is carried out twice, and the proportion of each calculation is the weight. On the other hand, the calculated results are quite different from the default weight, especially the weight of influencing factors, so there will be a lot of differences in scores. If we evaluate according to the 10-point system, the final score difference may be more crucial.

## 6. Conclusions

To avoid the disadvantages of traditional FMEA, this paper presents IFN to reflect the final ranking of evaluation team for electromagnet in manufacturing systems. The failure evaluation mode is a general and comprehensive decision of the consequences and effects of failure. Based on the distinguishing features of subordination degree and non-subordination degree of IFN, the error of final calculation failure mode score can be reduced to a more manageable



level. In addition, this paper supplements the incomplete determination of weight information with traditional FMEA and calculates the best evaluation information by using the concept of similarity measure.

On the other hand, in view of the unknown weight of influencing factors, this paper compares and evaluates influencing factors by many evaluators forming a contrast matrix. A nonlinear programming model based on the contrast matrix of influencing factors was built to simulate the evaluation results of the weight of influencing factors. Then, the absolute distance between each evaluator's decision information and the best decision information are calculated in two different ways. The contributions of this paper lie in that we put forward a potential FMEA method of electromagnet based on IFN in empirical study. This paper also discusses the further improving measures of IFN and presents future research directions for other mechanical and electrical products.

### Data Availability

The data of this paper come from the practice and experimental design of enterprises.

### Conflicts of Interest

The authors declare that they have no conflicts of interest.

### Acknowledgments

This work was supported by the National Natural Science Foundation of China (nos. 72071149 and 71671130) and Provincial Natural Science Foundation, Zhejiang, China (no. LY20G010014).

### References

- [1] M. Giannakis and T. Papadopoulos, "Supply chain sustainability: a risk management approach," *International Journal of Production Economics*, vol. 171, pp. 455–470, 2016.
- [2] Y. Geum, Y. Cho, and Y. Park, "A systematic approach for diagnosing service failure: service-specific FMEA and grey relational analysis approach," *Mathematical and Computer Modelling*, vol. 54, no. 11-12, pp. 3126–3142, 2011.
- [3] M. S. Kirkire, S. B. Rane, and J. R. Jadhav, "Risk management in medical product development process using traditional FMEA and fuzzy linguistic approach: a case study," *Journal of Industrial Engineering International*, vol. 11, no. 4, pp. 595–611, 2015.
- [4] S. Dorosti, M. Fathi, S. J. Ghouschi et al., "Patient waiting time management through fuzzy based failure mode and effect analysis," *Journal of Intelligent and Fuzzy Systems*, vol. 38, no. 6, pp. 1–12, 2020.
- [5] W. Huang, Y. Li, X. Kou et al., "Using a FMEA-TIFIAD approach to identify the risk of railway dangerous goods transportation system," *Group Decision and Negotiation*, vol. 10, no. 10, pp. 1–33, 2020.
- [6] H.-C. Liu, L. Liu, and N. Liu, "Risk evaluation approaches in failure mode and effects analysis: a literature review," *Expert Systems with Applications*, vol. 40, no. 2, pp. 828–838, 2013.
- [7] S.-S. He, Y.-T. Wang, J.-J. Peng, and J.-Q. Wang, "Risk ranking of wind turbine systems through an improved FMEA based on probabilistic linguistic information and the TODIM method," *Journal of the Operational Research Society*, vol. 4, pp. 1–14, 2021.
- [8] M. D. Ramere and O. T. Laseinde, "Optimization of condition-based maintenance strategy prediction for aging automotive industrial equipment using FMEA," *Procedia Computer Science*, vol. 180, no. 16, pp. 229–238, 2021.
- [9] H.-W. Lo, J. J. H. Liou, C.-N. Huang, and Y.-C. Chuang, "A novel failure mode and effect analysis model for machine tool risk analysis," *Reliability Engineering & System Safety*, vol. 183, pp. 173–183, 2019.
- [10] Y.-X. Xue, J.-X. You, X.-D. Lai, and H.-C. Liu, "An interval-valued intuitionistic fuzzy MABAC approach for material selection with incomplete weight information," *Applied Soft Computing*, vol. 38, pp. 703–713, 2016.
- [11] J. Qin, Y. Xi, and W. Pedrycz, "Failure mode and effects analysis (FMEA) for risk assessment based on interval type-2 fuzzy evidential reasoning method," *Applied Soft Computing*, vol. 89, pp. 106–134, 2020.
- [12] H.-C. Liu, J.-X. You, and C.-Y. Duan, "An integrated approach for failure mode and effect analysis under interval-valued intuitionistic fuzzy environment," *International Journal of Production Economics*, vol. 207, pp. 163–172, 2019.
- [13] S. Daneshvar, M. Yazdi, and K. A. Adesina, "Fuzzy smart failure modes and effects analysis to improve safety performance of system: case study of an aircraft landing system," *Quality and Reliability Engineering International*, vol. 36, no. 3, pp. 890–909, 2020.
- [14] Y. Mohammad, "Improving failure mode and effect analysis (FMEA) with consideration of uncertainty handling as an interactive approach," *International Journal on Interactive Design and Manufacturing*, vol. 13, pp. 441–458, 2018.
- [15] Z. Liu and F. Xiao, "An intuitionistic evidential method for weight determination in FMEA based on belief entropy," *Entropy*, vol. 21, no. 3, pp. 211–227, 2019.
- [16] W. Wang, X. Liu, X. Chen, and Y. Qin, "Risk assessment based on hybrid FMEA framework by considering decision maker's psychological behavior character," *Computers & Industrial Engineering*, vol. 136, pp. 516–527, 2019.
- [17] H. Zhang, Y. Dong, I. Palomares-Carrascosa et al., "Failure mode and effect analysis in a linguistic context: a consensus-based multiattribute group decision-making approach," *IEEE Transactions on Reliability*, vol. 99, pp. 1–17, 2018.
- [18] H. Zheng and Y. Tang, "A novel failure mode and effects analysis model using triangular distribution-based basic probability assignment in the evidence theory," *IEEE Access*, vol. 8, pp. 66813–66827, 2020.
- [19] S. Boral, S. K. Chaturvedi, V. N. A. Naikan et al., "An integrated approach for fuzzy failure modes and effects analysis using fuzzy AHP and fuzzy MAIRCA," *Engineering Failure Analysis*, vol. 108, pp. 104195–104211, 2019.
- [20] Z.-p. Tian, J.-q. Wang, and H.-y. Zhang, "An integrated approach for failure mode and effects analysis based on fuzzy best-worst, relative entropy, and VIKOR methods," *Applied Soft Computing*, vol. 72, pp. 636–646, 2018.
- [21] A. M. Talib, "Fuzzy VIKOR Approach to evaluate the information security policies and analyze the content of press agencies in gulf countries," *Journal of Information Security*, vol. 11, no. 4, pp. 189–200, 2020.
- [22] L. Li and W. Yue, "Dynamic uncertain causality graph based on Intuitionistic fuzzy sets and its application to root cause analysis," *Applied Intelligence*, vol. 50, no. 1, pp. 241–255, 2020.
- [23] X. Zhang and Z. Xu, "Soft computing based on maximizing consensus and fuzzy TOPSIS approach to interval-valued

- intuitionistic fuzzy group decision making,” *Applied Soft Computing*, vol. 26, pp. 42–56, 2015.
- [24] Z. Yue, “Application of the projection method to determine weights of decision makers for group decision making,” *Scientia Iranica*, vol. 19, no. 3, pp. 872–878, 2012.
- [25] F. L. Gaol and T. Matsuo, “The simulation of implications of sensor technology on the new product development to solve lot-sizing problems with fuzzy approach,” *Journal of Sensors*, vol. 2020, Article ID 3503895, 15 pages, 2020.

## Review Article

# Camshaft Loosening Diagnosis on the Basis of Generalised Force Recognition at the Centre of Gravity of an Engine

Chuanyan Xu <sup>1</sup>, Lixue Meng,<sup>1</sup> Ruyan Gong,<sup>2</sup> Xun Gong,<sup>1</sup> and Aijuan Li<sup>1</sup>

<sup>1</sup>School of Automotive Engineering, Shandong Jiaotong University, Jinan 250023, China

<sup>2</sup>Weihai Institute of Metrology and Inspection for Product Quality Standards, Weihai 264200, China

Correspondence should be addressed to Chuanyan Xu; 254883652@qq.com

Received 22 June 2021; Accepted 12 August 2021; Published 20 August 2021

Academic Editor: Anil Kumar

Copyright © 2021 Chuanyan Xu et al. This is an open access article distributed under the Creative Commons Attribution License, which permits unrestricted use, distribution, and reproduction in any medium, provided the original work is properly cited.

A valve mechanism supports the working process of an engine cylinder, and a camshaft is a key component required to open and close a valve. When a camshaft loosens, the balance of the engine disrupts. In the meanwhile, the generalised force at its centre of gravity (CG) alters. This study proposed a novel technique to detect camshaft loosening based on recognising the generalised force at the CG of the engine. We conducted Hanning windowed interpolation of discrete spectra to extract the precise phase and amplitude by utilising the acceleration signals at the engine cylinder and mounts and cylinder head. We then accurately computed the generalised force at the CG. Finally, we accurately extracted the camshaft loosening features by analysing the main harmonic orders for the generalised force. As indicated by simulations, our method can be used to effectively detect combustion engine faults involving camshaft loosening.

## 1. Introduction

A camshaft is a key component required to open and close the valve in an engine valve distribution mechanism. Camshaft projections are in contact with a tappet. Excessive stress due to contact between the camshaft projection and the tappet roller may cause wear failure [1]. Additionally, under long service time, a camshaft is subject to alternating load torque, bending moment, and impact load. It possibly operates with an angular vibration along with a bending vibration. Bearing and bush wear and camshaft loosening can lead to overall wear and unpleasant noise. The efficiency and reliability of camshafts decrease because of inaccurate movement, eventually resulting in force variations at the centre of gravity (CG). An injection pump camshaft of a truck diesel engine failed after a mere 13,000 km run because fatigue cracks were initiated at the keyway root through circumferential tangential stress because the stationary frictional force between the camshaft cone and timer working on keyway edges was inadequate [2]. A diesel engine camshaft underwent instantaneous circumferential cracking that propagated brittly due to tensile stress generated at the site of camshaft straightening [3].

Du and Yu [4] developed an engine power assembly and accompanying valve train. They compared the vibration acceleration signals of the engine cylinder head in normal and fault states to determine the loosening fault features of camshaft bearings. Diagnosis using mechanical systems is a key subject in modern industry. In recent years, intelligent methods have been widely used in structural diagnosis to detect faults in 3D printers. Li et al. introduced an extreme-learning-machine-based intelligent solution for fault diagnosis that used a low-cost and precise attitude sensor and helped diagnostic measure studies for determining faults in delta 3D printers [5, 6]. Kumar et al. developed a diagnostic technique based on deep learning to recognise defects in two-wheeler vehicle engines [7]. Ting et al. [8] determined the cluster centre in a radial basis function neural network by using the  $K$ -means clustering algorithm to study faults in camshaft grinders. Fault samples are critical to initiate an artificial intelligence (AI) mode. However, achieving convenient and thorough sampling in actual applications is difficult because mostly mechanical systems are healthy and normal. Thus, it becomes difficult to attain AI model training even with sufficient fault samples [9].

The diagnosis of camshaft faults must be effectual and accurate to ensure that the engine operates as usual [10]. Vibration signals, containing a large amount of fault information, are extensively utilised to diagnose faults [11–14]. The vibration pattern of an engine can offer diverse information about its state. In most cases, engine faults are manifested directly as the fluctuation of generalised force at the engine CG, achieved by utilising the acceleration signals at the engine mounts. Xu et al. computed generalised force at the engine CG and extracted features to detect single and continuous/intermittent double cylinder misfires [15]. The primary vertical force for a four-cylinder four-stroke motor refers to the second-order force, and the half- and first-order forces are nearly zero [16]. However, the force at the CG varies with camshaft faults.

Our study proposes a novel technique to detect camshaft loosening based on recognising the generalised force at the engine CG. We extracted the precise phase, frequency, and amplitude through Hanning windowed interpolation. Two prime advantages of our detection method are its high fault sensitivity and less subjectivity to external factors and experimental conditions.

The following presents the organization of the rest of the paper. Section 2 introduces the identification principles for generalised force at the CG. Section 3 describes the diagnostic procedure for camshaft loosening based on the computed generalised force and illustrates the simulation results. The conclusions are made in Section 4.

## 2. Theoretical Fundamentals

**2.1. Generalised Force Estimation Method.** As shown in Figure 1, a powertrain mounting system is simplified into a six-degree-of-freedom vibration model to calculate the engine excitation force.

Assuming a slight movement of the engine mount system, the kinematic equation for the power assembly mounting system is

$$M\ddot{Q}(t) + C\dot{Q}(t) + KQ(t) = F(t), \quad (1)$$

where  $M$  denotes the  $6 \times 6$  rigid mass matrix of the engine,  $C$  denotes the  $6 \times 6$  damping matrix,  $K$  denotes the  $6 \times 6$  stiffness matrix, and  $Q$  and  $F$  are the generalised displacements at the engine CG and  $6 \times 1$  generalised force vector, respectively.

$$M_{6 \times 6} = \begin{bmatrix} m & 0 & 0 & 0 & mz_c & -my_c \\ 0 & m & 0 & -mz_c & 0 & mx_c \\ 0 & 0 & m & my_c & -mx_c & 0 \\ 0 & -mz_c & my_c & J_{xxo} & -J_{xyo} & -J_{xzo} \\ mz_c & 0 & -mx_c & -J_{xyo} & J_{yyo} & -J_{yzo} \\ -my_c & mx_c & 0 & -J_{xzo} & -J_{yzo} & J_{zzo} \end{bmatrix}, \quad (2)$$

where  $m$  is the engine mass;  $x_c$ ,  $y_c$ , and  $z_c$  are the CG coordinates in the  $OXYZ$  reference system;  $J_{xxo}$ ,  $J_{yyo}$ , and  $J_{zzo}$  are the inertial moments for  $X$ ,  $Y$ ,  $Z$  coordinates, separately; and  $J_{xyo}$ ,  $J_{yzo}$ , and  $J_{xzo}$  are the cross inertial moments.

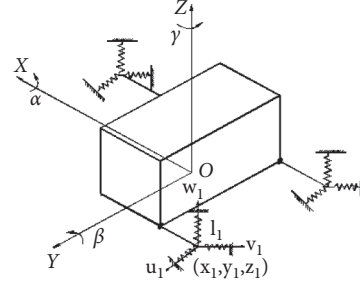


FIGURE 1: Simplified model of a powertrain.

$$K_{6 \times 6} = \begin{bmatrix} k_{xx} & k_{xy} & k_{xz} & k_{x\alpha} & k_{x\beta} & k_{x\gamma} \\ k_{yx} & k_{yy} & k_{yz} & k_{y\alpha} & k_{y\beta} & k_{y\gamma} \\ k_{zx} & k_{zy} & k_{zz} & k_{z\alpha} & k_{z\beta} & k_{z\gamma} \\ k_{\alpha x} & k_{\alpha y} & k_{\alpha z} & k_{\alpha\alpha} & k_{\alpha\beta} & k_{\alpha\gamma} \\ k_{\beta x} & k_{\beta y} & k_{\beta z} & k_{\beta\alpha} & k_{\beta\beta} & k_{\beta\gamma} \\ k_{\gamma x} & k_{\gamma y} & k_{\gamma z} & k_{\gamma\alpha} & k_{\gamma\beta} & k_{\gamma\gamma} \end{bmatrix}, \quad (3)$$

where  $k_{xx}$ ,  $k_{yy}$ , and  $k_{zz}$  are the total reciprocating stiffnesses of elastic support;  $k_{xy}$ ,  $k_{xz}$ , and  $k_{zy}$  are the coupling stiffnesses of elastic support; and  $k_{\alpha\alpha}$ ,  $k_{\beta\beta}$ , and  $k_{\gamma\gamma}$  are the rotary stiffnesses about the coordinate axis.

$$F_{6 \times 1} = \begin{Bmatrix} F_x \\ F_y \\ F_z \\ M_x \\ M_y \\ M_z \end{Bmatrix}, \quad (4)$$

$$Q_{6 \times 1} = \begin{Bmatrix} X_o \\ Y_o \\ Z_o \\ \alpha \\ \beta \\ \gamma \end{Bmatrix},$$

where  $F_x$ ,  $F_y$ , and  $F_z$  represent transitional applied forces;  $M_x$ ,  $M_y$ , and  $M_z$  represent the applied moments about point  $O$ ;  $X_o$ ,  $Y_o$ , and  $Z_o$  are point  $O$ 's transitional displacements; and  $\alpha$ ,  $\beta$ , and  $\gamma$  are point  $O$ 's rotational displacements.

Using Fourier transformation on the two sides of equation (1), we derive

$$\left[ M - \frac{K}{(2\pi f)^2} - \frac{jC}{2\pi f} \right] \ddot{Q}(f) = F(f). \quad (5)$$

Considering  $s$  points at which acceleration can be determined, where the coordinates of the  $i$ th point ( $i = 1, \dots, s$ ) for the CG are  $[x_i \ y_i \ z_i]$ , the following equation can be derived under a "slight" motion hypothesis:

$$A = E\ddot{Q}. \quad (6)$$

Accordingly,  $\ddot{Q}$  can be computed using the least-squares method:

$$\ddot{Q} = (E^T E)^{-1} E^T A, \quad (7)$$

where  $E$  is the transpose matrix and  $A$  denotes the acceleration vectors in three orthogonal directions for all the points.

$$E = \begin{bmatrix} 1 & 0 & 0 & 0 & z_1 & -y_1 \\ 0 & 1 & 0 & -z_1 & 0 & x_1 \\ 0 & 0 & 1 & y_1 & -x_1 & 0 \\ & & & \cdots & & \\ 1 & 0 & 0 & 0 & z_s & -y_s \\ 0 & 1 & 0 & -z_s & 0 & x_s \\ 0 & 0 & 1 & y_s & -x_s & 0 \end{bmatrix},$$

$$A = [A_{x1}(f) \ A_{y1}(f) \ A_{z1}(f) \ \cdots \ A_{xs}(f) \ A_{ys}(f) \ A_{zs}(f)]. \quad (8)$$

We can precisely extract the acceleration signal phases and amplitudes by exploiting the engine acceleration signals at the mounts and block by using discrete spectrum interpolation. The generalised force at the CG [17] is given by

$$F(f) = \left[ M - \frac{1}{\omega^2} K^* \right] (E^T E)^{-1} E^T A. \quad (9)$$

At local coordinates, the mount complex stiffnesses in the three directions are given as

$$\begin{aligned} K^* &= K + j\omega C \\ &= K + jK', \end{aligned} \quad (10)$$

where  $j = \sqrt{-1}$  and  $K' = \omega C = 2\pi f C$  are the loss stiffnesses.

The phase difference of the gas-pressure torque for each cylinder of an  $i$ -cylinder engine is  $4\pi/i$ , which varies with the engine ignition order. The highest amplitude of the first harmonic order  $k=i/2$  appears in the resultant torque spectrum. The primary harmonic orders of a 4-cylinder 4-stroke 4-cylinder engine include  $k=i/2, i, 3i/2$ . Figure 2 shows the phase angle graphs for a typical 4-cylinder 4-stroke 4-cylinder 4-cylinder engine, the firing order of which is 1-3-4-2.

Considering the same contribution by each cylinder to the engine torque, primary orders in the torque's structure are merely present due to gas forces, which are multiples of half the cylinder quantity for the 4-cylinder 4-stroke engine (Figure 2). Besides, the primary harmonic orders for the torque are the 2nd, 4th, and 6th orders, when the engine runs as usual. Primary harmonic orders change in the event of a fault.

**2.2. Interpolation Method for Discrete Spectrum.** Equation (9) requires accurate extraction of the amplitudes, frequencies, and phases of the engine mounts and block. However, actual test signals contain noise. In discrete spectral analyses, no-

integer period sampling leads to erroneous amplitude, frequency, and phase [18–21]. Conventional FFT extracts a highly errored generalised force, especially for the phase. Before the correction, the first harmonic of the acceleration shows similar errors to those for absolute phases. Thus, attaining accurate relative phases between acceleration responses leads to a decrease in the error estimates of the generalised force. However, in the 2nd harmonic, phase errors vary, provided the failure of maximum spectral lines is within different frequencies, and alterations are present in the relative phases [17]. The interpolation method is used to estimate frequency bias based on the amplitude ratio of the first two maximum spectral lines. Consider  $x(t)$  as a single sequence of the harmonic signal and its amplitude, frequency, and phase as  $f_0$ ,  $A$ , and  $\theta_0$ , respectively. Then,

$$x(t) = A \cos(2\pi f_0 t + \theta_0). \quad (11)$$

Through equispaced sampling using  $N$  sampling points at sampling frequency  $f_0$ , we get a new sampling sequence:

$$x(n) = A \cos\left(2\pi f_0 \frac{n}{N} + \theta_0\right). \quad (12)$$

Applying Fourier transformation to equation (12), it becomes

$$X_w(k) = \frac{1}{N} \sum_{k=0}^{N-1} w(n)x(n)e^{-j2\pi nk/N}, \quad (13)$$

where  $w(n)$  is the window function.

After correction, the amplitude and phase are given by

$$\hat{A} = \frac{X_w(k)}{W(\nabla f^1)}, \quad (14)$$

$$\hat{\theta}_0 = \arctan\left(\frac{I_k}{R_k}\right) + \pi \nabla f^1,$$

where  $X_w(k)$  is the amplitude of the maximum spectral line of the discrete spectrum of harmonic signals, that is, the greatest amplitude in the major lobe, and  $W(\nabla f^1)$  is the spectral mode function.

The rectangle window is expressed as

$$W(\nabla f^1) = \frac{\sin(\pi \nabla f^1)}{\pi \nabla f^1}. \quad (15)$$

The Hanning window is expressed as

$$W(\nabla f^1) = \frac{\sin c(\nabla f^1)}{1 - \nabla f^1}. \quad (16)$$

Highly accurate amplitudes can be attained even at a considerably low sound-to-noise ratio (SNR) of  $-2.33$  dB. The maximum error rates for the rectangle and Hanning windows are 4.5% and 6%, respectively. The phase precision for the Hanning window is  $<10^\circ$ ; however, due to an improper interpolation direction in the interpolation technique that is multiplied with the rectangular window when  $\text{SNR} = 2.33$  dB and  $\nabla f_1 \leq 0.25$ , the resulting error is

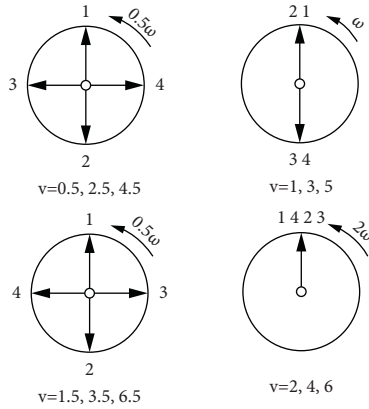


FIGURE 2: Phase angle graphs of gas-pressure torques for the 4-cylinder 4-stroke engine.

relatively large. The Hanning window is twice in width as the rectangle window, leading to a significant reduction in the possibility of interpolation direction error, and there is no arch exception [18]. Hence, we applied Hanning windowed interpolation discrete spectrum in order to extract the phase, amplitude, and frequency of the engine acceleration signals.

### 3. Camshaft Loosening Diagnosis Based on Generalised Force Recognition

**3.1. Simulation Models.** The engine valve mechanism comprises a cam, a lifter, valves, valve springs, and a camshaft. Each component has a certain mass and elasticity to produce an elastic deformation during motion. The valve train produces high acceleration when running at a high speed and is subject to a specific dynamic load. In the dynamic analysis, the components of the valve mechanism are simplified into an equivalent lumped mass and an equivalent spring, respectively. Thus, the lumped mass-spring vibration model can be applied to perform the dynamic analysis of the valve mechanism. The dynamic model of the valve train has been designed based on AVL Excite Timing Drive and includes double overhead camshafts for a 4-cylinder 4-stroke engine. The component unit of the valve train contains parts such as a valve stem, valve seat, camshaft bearing, cam, lifter, and spring and phase units, in sync with the composition of the valve mechanism. Figure 3 presents the logic schematic diagram of the component connections of the valve train.

We performed a high-quality FEA using AVL Excite and multibody dynamics modelling for an in-line 4-cylinder 4-stroke engine installed with mounts (Figure 4). First, an engine crankshaft and powertrain finite element model is established. The finite element has an enormous degree of freedom; thus, its matrix is simplified using MSC Nastran to improve the computational efficiency. Next, the coupled multibody dynamics model is set up based on the AVL Excite. The excitation force includes the force of a gas explosion and the inertial forces of reciprocation and rotation. All excitation forces are included in our model to ensure that the vibration is similar to that of an actual engine. The explosion pressure for each cylinder is set based on the

cylinder pressure plot. The cylinder pressure curve of an engine running at a speed of 2000 rpm at full load condition is shown in Figure 5. The piston load of each cylinder at regular intervals, the pressure load of each cylinder wall, and the load torque at the flywheel output are generated automatically by the software as per the firing order. The same is applied to the corresponding nodes. The valve mechanism force can be considered an extended load of the powertrain, which contains valve seat force, valve spring force, and camshaft support force. The other force is the piston striking force produced due to the gap between the piston and the cylinder liner.

For determining the valve train excitation force, we used the valve train model based on the Excite Timing Drive and loaded the calculated force into the Power Unit model. The data connection interface is preferred for both models. The piston striking force is calculated using excited Piston and Rings, and the dynamic striking force of five nodes is distributed in the height direction of the main and vice thrust side of the cylinder liner. The calculated piston striking force is also considered an extended force loaded into the corresponding nodes of the powertrain model.

Table 1 presents the CG of the power assembly and the mount locations. Table 2 presents the power assembly's inertia parameters excluding those of the piston, connecting rod, and crankshaft. The three mounts have a stiffness of  $3 \times 10^5$  N/m and damping of 200 N s/m.

**3.2. Camshaft Bearing Loosening Fault Setting.** The simulation of loosening bearing faults is created by removing the SRBS unit from the model, provided that fixation of intake and exhaust camshafts at the cylinder head is achieved using five sliding bearings. No effect is exerted by the loosening bearing on the pressing camshaft. In the present simulation, the bearing of the intake camshaft of cylinder-3 (SRBS int4) is removed so that bearing-4 has a zero acting force throughout the work cycle, and the dynamic driving force of cylinder-3's intake and exhaust valves is transmitted to the cylinder through the adjacent bearings 3 and 5 only. Figures 6 and 7 display the bearing forces of bearing 3 and 5, respectively, at 2,000 rpm under normal and faulty scenarios. When the bearing of cylinder-3 loosens, the supporting force of the adjacent bearing changes to a large extent.

The excitation force of the valve mechanism is taken as the input force for the engine powertrain. The acting force of the camshaft on the cylinder head is mainly transmitted through the bearing. The valve train excitation force is calculated based on the valve train model, followed by introducing force into the Power Unit model through the loading points as shown in Figure 8.

**3.3. Camshaft Loose Diagnosis.** The loosening of the camshaft bearing changes the generalised force at the CG. Thus, the fault features of camshaft bearing loosening can be determined by calculating the generalised force based on the vibration signals of the engine system. The Hanning windowed interpolation, as mentioned in Section 2.2, is used for the precise phase, frequency, and amplitude extraction of the

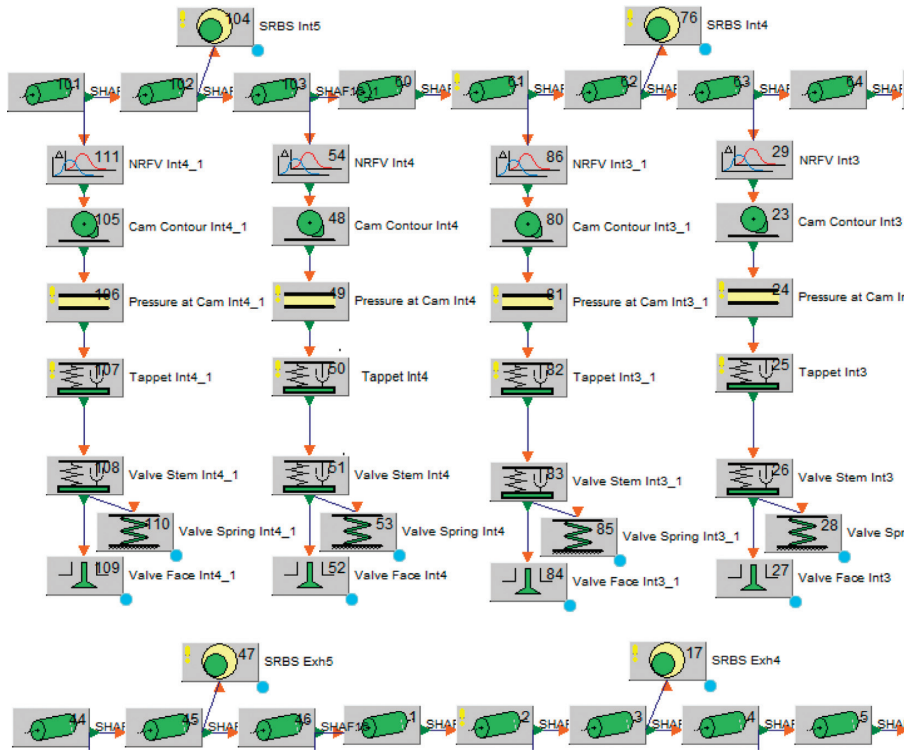


FIGURE 3: Valve train logic of component connections.

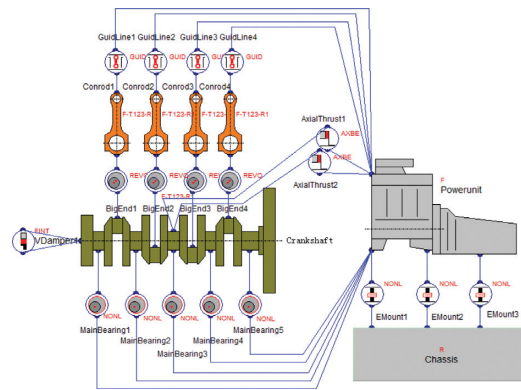


FIGURE 4: Engine logic of component connections.

three engine acceleration signals at the cylinder block, head, and mounts, respectively. The generalised force computation at the CG is determined using equation (9).

The engine has a firing order of 1-3-4-2. The frequency of the excitation signal of the 4-cylinder 4-stroke engine is twice that of the engine RPM. The vibration signals produced by the engine are the superposition of the fundamental frequency signal and its higher frequency signal, based on the harmonic signal characteristics. Under normal conditions, the primary harmonic orders of engine vibration signal are the 2nd, 4th, and 6th orders, respectively, whereas the 0.5th order is nearly zero. The highest amplitude of the 2nd harmonic appears on the resultant torque spectrum. Additionally, the signal of the engine block vibration conforms to the same law.

The vertically generalised force, identified under normal conditions, is shown in Figure 9. The amplitude of the 2nd harmonic is the highest, whereas the amplitude of the 0.5th harmonic is closer to zero, which is consistent with the theoretical analysis. Camshaft loosening was induced in cylinder-3 by removing the intake camshaft bearing SRBS Int4 (Figure 1). In this case, a large impact is observed after each alternate revolution by the engine, and its frequency is half of the engine RPM. The loosening of the camshaft leads to the formation of another excitation force cycle, and the crankshaft rotates twice per cycle. It also leads to an increase in the amplitude of the 0.5th harmonic and its multiples increases considerably (Figure 10).



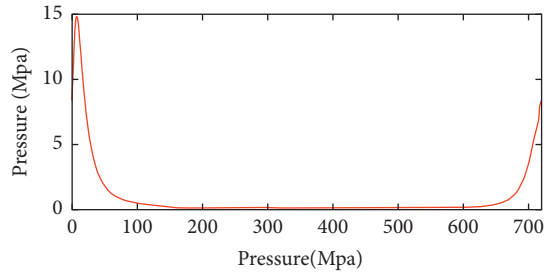


FIGURE 5: Pressure curve of the cylinder at 2000 rpm.

TABLE 1: Engine CG and mount positions.

	X	Y	Z
Engine c.g.	139.3 mm	9.8 mm	91.9 mm
Mount 1	0	285.2 mm	122 mm
Mount 2	73 mm	-254 mm	-45.5 mm
Mount 3	554.5 mm	-80.4 mm	-148.1 mm

TABLE 2: Engine inertia variables.

Mass	Moment of inertia			Product of inertia		
$m$	$J_{xx}$	$J_{yy}$	$J_{zz}$	$J_{xy}$	$J_{yz}$	$J_{xz}$
111 kg	4.13 kg m <sup>2</sup>	9.67 kg m <sup>2</sup>	8.13 kg m <sup>2</sup>	0.16 kg m <sup>2</sup>	-0.16 kg m <sup>2</sup>	1.12 kg m <sup>2</sup>

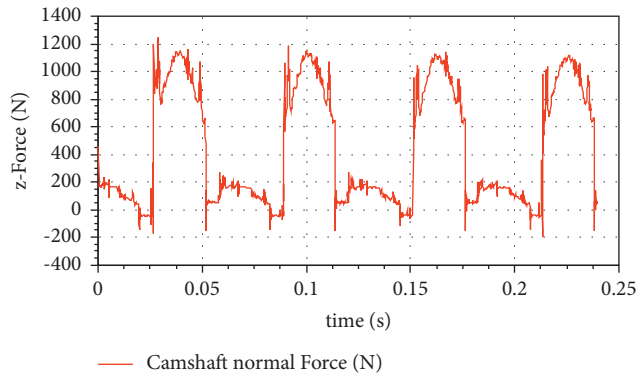


FIGURE 6: Camshaft force under normal condition.

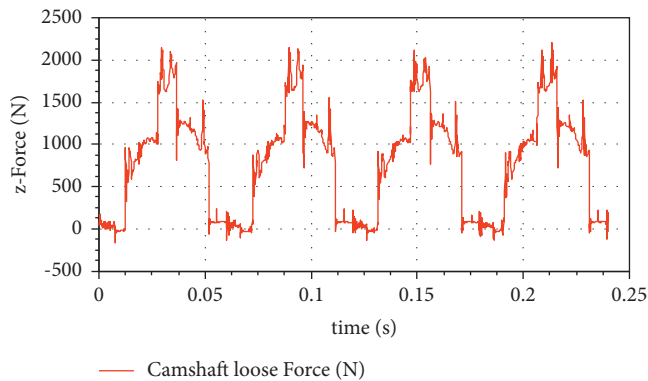


FIGURE 7: Camshaft force in faulty state.



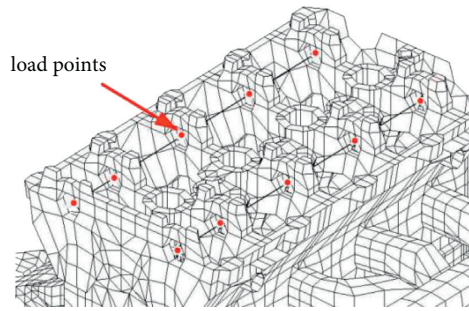


FIGURE 8: Bearing force load point.

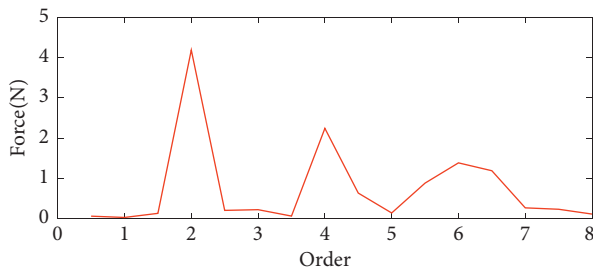


FIGURE 9: Generalised vertical force identified at the engine CG.

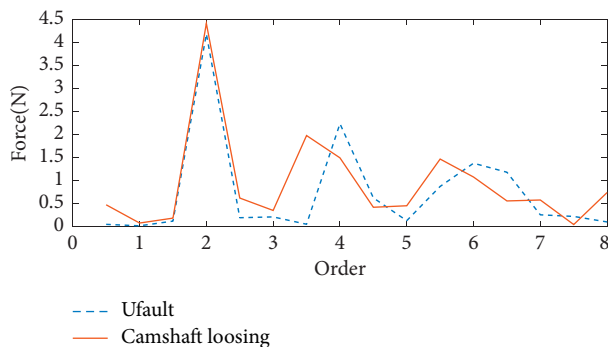


FIGURE 10: Vertical generalised force of camshaft loosing.

## 4. Conclusions

This study proposed a novel technique for detecting camshaft loosening, which was used for analysing the order of the harmonics of the generalised force at the CG. Precise phase, frequency, and amplitude extraction were conducted using the Hanning windowed interpolation, thereby achieving the generalised force accurately at the CG.

The proposed method is effective in diagnosing the fault induced due to camshaft loosening as demonstrated by the simulation results based on the AVL software. The loosening of the camshaft changes the generalised force at the CG. The amplitude of the 0.5th harmonic and its multiples increase sharply because the crankshaft rotates twice per cycle. The 0.5th harmonic and its multiples increase when the rate of change reaches half of the engine speed.

## Data Availability

No data were used to support this study.

## Conflicts of Interest

The authors declare that there are no conflicts of interest regarding the publication.

## Acknowledgments

This work was supported under Grant nos. 51405272 and 51505258 from the National Natural Science Foundation of China and partially supported by the Natural Science Foundation of Shandong Province (ZR2020ME126), the Youth Science and Technology Project of Shandong Provincial Colleges and Universities (Grant no. 2019KJB019), Shandong Provincial Major Scientific and Technological Innovation Project (2019JZZY020617), Shandong Provincial Key Research and Development Program (2019GNC106071), and State Key Laboratory of Mechanical Behavior and System Safety of Traffic Engineering Structures, China (Grant no. 1903).

## References

- [1] H. L. Bi, "Wear analysis of a camshaft and roller tappet of an engine," Master's thesis, Shandong University, Jinan, China, 2017.
- [2] W. Y. Zhi and X. L. Xu, "Failure analysis on fractured diesel engine camshafts," *Journal of Failure Analysis and Prevention*, vol. 9, no. 1, pp. 39–42, 2009.
- [3] X. Duan, J. Long, C. Li, and D. Cabrera, "Intelligent fault diagnosis of 3D printers based on reservoir computing," *International Journal of Performability Engineering*, vol. 15, no. 12, pp. 3171–3178, 2019.
- [4] C. Y. Du and F. F. Yu, "Analysis of engine camshaft bearing loosening fault based on model simulation and vibration signal," *Advanced Materials Research*, vol. 694–697, pp. 896–900, 2013.
- [5] X. Y. Li, J. W. Guo, X. J. Jia, S. H. Zhang, and Z. Y. Liu, "Intelligent fault diagnosis of delta 3D printers using attitude sensors based on extreme learning machines," *International Journal of Performability Engineering*, vol. 15, no. 12, pp. 3196–3208, 2019.
- [6] S. Zhang, M. Wang, C. Du, and E. Estupinan, "Local and global SR for bearing sensor-based vibration signal classification," *International Journal of Performability Engineering*, vol. 15, no. 10, pp. 2657–2669, 2019.
- [7] A. Kumar, C. P. Gandhi, Y. Zhou et al., "Improved CNN for the diagnosis of engine defects of 2-wheeler vehicle using wavelet synchro-squeezed transform (WSST)," *Knowledge-Based Systems*, vol. 208, Article ID 106453, 2020.
- [8] D. Ting, H. G. Wang, and S. Lei, "Study of camshaft grinders faults prediction based on RBF neural network," *Applied Mechanics and Materials*, vol. 141, pp. 519–523, 2012.
- [9] Y. G. Shi, X. Y. Liu, and J. W. Xiang, "FEM simulation-based generative adversarial networks to detect bearing faults," *IEEE Transactions on Industrial Informatics*, vol. 16, no. 7, pp. 4961–4971, 2020.
- [10] Z. M. Bulatovic, M. S. Stavljanin, and M. V. Tomic, "Measurement and analysis of angular velocity variations of twelve-cylinder diesel engine camshaft," *Mechanical Systems and Signal Processing*, vol. 25, no. 8, pp. 3041–3061, 2011.
- [11] X. Jiang, C. Shen, J. Shi, and Z. Zhu, "Initial center frequency-guided VMD for fault diagnosis of rotating machines," *Journal of Sound and Vibration*, vol. 435, pp. 36–55, 2018.

- [12] Y. Wang, Z. He, and Y. Zi, "A demodulation method based on improved local mean decomposition and its application in rub-impact fault diagnosis," *Measurement Science and Technology*, vol. 20, no. 2, Article ID 025704, 2009.
- [13] J. Guo, W. P. Zhang, and X. Y. Zhang, "Modeling and analysis of the transient vibration of camshaft in multi-cylinder diesel engine," *Advances in Mechanical Engineering*, vol. 7, no. 11, pp. 1–14, 2015.
- [14] A. Kumar, C. P. Gandhi, Y. Zhou, R. Kumar, and J. Xiang, "Latest developments in gear defect diagnosis and prognosis: a review," *Measurement*, vol. 158, Article ID 107735, 2020.
- [15] C. Xu, S. Li, F. Cao, and X. Qiu, "Misfire detection based on generalized force identification at the engine centre of gravity," *IEEE Access*, vol. 7, pp. 165039–165047, 2019.
- [16] C. M. Wang, *Vehicle Engine Dynamics*, National Defense Industry Press, Beijing, China, 1990.
- [17] C. Xu and F. Cao, "Engine excitation force identification on the basis of discrete spectrum correction," *Mathematical Problems in Engineering*, vol. 2015, Article ID 175257, 11 pages, 2015.
- [18] X. Ming and D. Kang, "Corrections for frequency, amplitude and phase in a fast fourier transform of a harmonic signal," *Mechanical Systems and Signal Processing*, vol. 10, no. 2, pp. 211–221, 1996.
- [19] C. Y. Xu, K. Ding, H. B. Lin, and Z. J. Yang, "Noise influence on amplitude and phase estimation accuracy by interpolation method for discrete spectrum," *Journal of Vibration Engineering*, vol. 24, no. 6, pp. 633–638, 2011.
- [20] H. B. Lin and K. Ding, "Energy based signal parameter estimation method and a comparative study of different frequency estimators," *Mechanical Systems and Signal Processing*, vol. 25, no. 1, pp. 452–464, 2011.
- [21] C. Y. Xu, K. Ding, Z. J. Yang, and H. B. Lin, "Influence of additive white gaussian noise on the interpolation method of discrete spectrum," *Advanced Materials Research*, vol. 383–390, pp. 2951–2957, 2012.

## Research Article

# Identification of Engine Inertia Parameters and System Dynamic Stiffness via In Situ Method

Chuanyan Xu , Xun Gong, Lixue Meng, and Aijuan Li

School of Automotive Engineering, Shandong Jiaotong University, Jinan 250023, China

Correspondence should be addressed to Chuanyan Xu; 254883652@qq.com

Received 8 May 2021; Accepted 31 July 2021; Published 11 August 2021

Academic Editor: Yuqing Zhou

Copyright © 2021 Chuanyan Xu et al. This is an open access article distributed under the Creative Commons Attribution License, which permits unrestricted use, distribution, and reproduction in any medium, provided the original work is properly cited.

An in situ method is presented to identify ten engine inertia parameters and system dynamic stiffness from the frequency response functions. The ten engine inertia parameters and system dynamic stiffness are estimated from two distinct steps. The accuracy of the proposed technique is verified by finite element simulation, and then the generality is validated using an engine supported by a specially designed curved bar spring. The locations of the measure points on the results are also carefully investigated. The identification of system dynamic stiffness is validated comparing with the engine with an auxiliary plate, which shows good consistency with the results identified from the study.

## 1. Introduction

The identification of engine inertia parameters is important in the analysis of dynamic behaviour, suspension system optimization design, vibration attenuation and isolation, and engine fault diagnosis. During the dynamic structure design, the inertia parameters are regarded as known parameters, for example, when analysing the vehicle vibration noise due to the unbalance forces and moments caused by the engine, the engine is commonly simplified as a three-dimensional model by setting inertia parameters. The inertia parameters of a rigid body directly affect the dynamic behaviour of the system; when there are errors in the identification of the inertia parameter, the dynamic characteristics of the structure will be affected inevitably; and a 5% error of the inertial parameters identification can lead to some order modal frequency reaches more than 1 Hz [1]. Therefore, the accurate identification of inertia parameters is of great significance to engineering practice. Engines on the test bench and the actual vehicle are mounted by rubber suspension, from a practical application point of view; work efficiency is no less important than the accuracy of the test. It is quite necessary to develop a method to identify inertial parameters and system dynamic stiffness simultaneously for the engine mounting system.

The conventional techniques for parameters identification of the rigid body can be divided into two categories, i.e., time domain methods [2–7] and frequency domain methods. The frequency domain methods may be further subdivided into three categories: modal model method [8–10], residual inertia method [11–15], and direct system identification method [16, 17]. The classical domain pendulum method is often time-consuming due to repetitive configuration adjustments of a heavy target and complicated body such as an automotive powertrain. The classical residual inertia method must overhang the test rigid body and consider mass as a known parameter; in actual application, the mass is often unknown, and large structure weighing is difficult to achieve. The modal method and direct system identification methods are based on the orthogonality relationship between the mass matrix and six rigid body modes. In order to get the ideal  $m$  rigid body modes, ideal spring constraints must be artificially added [18]. Unfortunately, in actual test, ideal boundary conditions are almost impossible to achieve. Thus, it has usually difficulty exciting all six rigid body modes at the same time due to the coupling of rigid body modes [19, 20]; the identification accuracy is hard to guarantee. Vahid et al. [21] and Jeffrey et al. [22] provided methods to estimate the vehicle engine rigid body inertia properties based on in situ measurements. However, a quadratic integral is applied to calculate the mount reaction forces;

when the second integral is executed, the unknown primitive value of the velocity and displacement must be set at zero, which can lead to greater identification errors. In addition, the maximum error in the literature [23] reaches 30%. In recent years, the intelligent method is widely used in structural parameter analysis and diagnosis [24–26], and the firefly algorithm is used to identify inertial parameters of the powertrain mounting system from simulation. However, such a method requires experiments to verify its effectiveness [27].

Stiffness and damping characteristics are the most important parameters for predicting the dynamic characteristics of the structural system and isolating the vibration and noise of sources to reduce fatigue failure or damage caused by vibration [28, 29]. Normally, the identification of the engine suspension system dynamic behaviour requires special experiments and special facilities [30]. In this paper, we provide a method to identify the dynamic stiffness of the suspension system in situ without a special experiment.

The main contributions of the paper are as follows. (1) An in situ identification method for engine inertia parameters and system dynamic stiffness is proposed. The method does not need to calculate the mount reaction force and avoid the error caused by the quadratic integral of acceleration. (2) The effects on the results due to the shaker location and response location are investigated.

## 2. Identification Method

*2.1. Identification of the Inertia Properties.* Since the natural frequency of a powertrain mounting system is commonly within 30 Hz, the engine support system vibration model can be viewed as six degrees of freedom of vibration [19]. The equations of motion for the engine can be expressed as follows:

$$\mathbf{M}\ddot{\mathbf{Q}}(t) + \mathbf{C}\dot{\mathbf{Q}}(t) + \mathbf{K}\mathbf{Q}(t) = \mathbf{F}(t), \quad (1)$$

where  $\mathbf{M}$  is the mass matrix whose elements are the inertia parameters to be determined,  $\mathbf{C}$  is the damping matrix,  $\mathbf{K}$  is the stiffness matrix,  $\mathbf{Q}$  is the generalized displacement vector, and  $\mathbf{F}$  is the generalized force vector of origin  $O$ .

$$\mathbf{M}_{6 \times 6} = \begin{bmatrix} m & 0 & 0 & 0 & mz_c & -my_c \\ 0 & m & 0 & -mz_c & 0 & mx_c \\ 0 & 0 & m & my_c & -mx_c & 0 \\ 0 & -mz_c & my_c & J_{xxo} & -J_{xyo} & -J_{xzo} \\ mz_c & 0 & -mx_c & -J_{xyo} & J_{yyo} & -J_{yzo} \\ -my_c & mx_c & 0 & -J_{xzo} & -J_{yzo} & J_{zzo} \end{bmatrix}, \quad (2)$$

$$\mathbf{K}_{6 \times 6} = \begin{bmatrix} k_{xx} & k_{xy} & k_{xz} & k_{xa} & k_{x\beta} & k_{xy} \\ k_{yx} & k_{yy} & k_{yz} & k_{ya} & k_{y\beta} & k_{yy} \\ k_{zx} & k_{zy} & k_{zz} & k_{za} & k_{z\beta} & k_{zy} \\ k_{ax} & k_{ay} & k_{az} & k_{aa} & k_{a\beta} & k_{ay} \\ k_{\beta x} & k_{\beta y} & k_{\beta z} & k_{\beta a} & k_{\beta\beta} & k_{\beta y} \\ k_{\gamma x} & k_{\gamma y} & k_{\gamma z} & k_{\gamma a} & k_{\gamma\beta} & k_{\gamma y} \end{bmatrix},$$

where  $k_{xx}$ ,  $k_{yy}$ , and  $k_{zz}$  are the total reciprocating stiffness of elastic support;  $k_{xy}$ ,  $k_{xz}$ , and  $k_{zy}$  are the coupling stiffness of

elastic support; and  $k_{aa}$ ,  $k_{\beta\beta}$ , and  $k_{\gamma\gamma}$  are the rotary stiffness about the coordinate axis.

$$\mathbf{F}_{6 \times 1} = \begin{Bmatrix} F_x \\ F_y \\ F_z \\ M_x \\ M_y \\ M_z \end{Bmatrix}, \quad (3)$$

$$\mathbf{Q}_{6 \times 1} = \begin{Bmatrix} X_o \\ Y_o \\ Z_o \\ \alpha \\ \beta \\ \gamma \end{Bmatrix}.$$

Both sides take Fourier transformation as follows:

$$\left[ \mathbf{M} - \frac{\mathbf{K}}{\omega^2} - \frac{j\mathbf{C}}{\omega} \right] \ddot{\mathbf{Q}}(f) = \mathbf{F}(f). \quad (4)$$

According to the coordinate transformation of the response and excitation points [14], the vibration equation of the engine due to  $n$  excitation forces and  $s$  measurement points can be obtained as follows:

$$\left[ \mathbf{M} - \frac{1}{\omega^2} \mathbf{K}^* \right] \mathbf{X} = \mathbf{T}, \quad (5)$$

where

$$\mathbf{X} = (\mathbf{E}^T \mathbf{E})^{-1} \mathbf{E}^T \mathbf{H}, \quad (6)$$

where  $\mathbf{H}$  is the transfer function matrix, which can be obtained from the experiment test;  $\mathbf{E}$  is the transpose matrix for response points; and  $\mathbf{T}$  is the transpose matrix for excitation points. The number of response points  $s \geq 2$  is required (in three directions), so that the rank of matrix  $\mathbf{E}$  is above 6, and  $\mathbf{Q}$  can be determined in a least-square sense. The number of excitation points must be equal to or greater than 6, so matrix  $\mathbf{M}$  can be calculated in a least-square sense. The locations of the sensors should have sufficient rigidity.

Transposing equation (5) and rearranging yield

$$\mathbf{X}^T \mathbf{M} = \mathbf{T}^T + \frac{1}{\omega^2} \mathbf{X}^T (\mathbf{K}^*)^T. \quad (7)$$

Equation (7) consists of 6 equations and 10 unknowns. In the frequency domain, the force and acceleration are generally complex quantities, so the real and imaginary parts can be separated to yield 12 equations with 10 unknowns

$$\begin{bmatrix} \text{Re}\{\mathbf{X}^T\} \\ \text{Im}\{\mathbf{X}^T\} \end{bmatrix} \mathbf{M} = \begin{bmatrix} \text{Re}\left\{ \mathbf{T}^T + \frac{1}{\omega^2} \mathbf{X}^T (\mathbf{K}^*)^T \right\} \\ \text{Im}\left\{ \frac{1}{\omega^2} \mathbf{X}^T (\mathbf{K}^*)^T \right\} \end{bmatrix}. \quad (8)$$

These 12 equations are not linearly independent, so additional equations must be generated to solve for  $\mathbf{M}$ . Although the frequency response function is a function of the frequency, with different values at each frequency line, the inertia parameters are constant. In addition, the frequency response function values of adjacent frequency lines are nearly identical, which implies that frequency lines must be selected sufficiently far apart to ensure linearly independent equations. The expanded equation is shown as follows:

$$\mathbf{AM} = \mathbf{B}, \quad (9)$$

where

$$\mathbf{A} = \begin{bmatrix} \text{Re}\{\mathbf{X}_1^T\} \\ \text{Im}\{\mathbf{X}_1^T\} \\ \vdots \\ \text{Re}\{\mathbf{X}_r^T\} \\ \text{Im}\{\mathbf{X}_r^T\} \end{bmatrix}, \quad (10)$$

$$\mathbf{B} = \begin{bmatrix} \text{Re}\left\{\mathbf{X}_1^T + \frac{1}{\omega_1^2}\mathbf{X}_1^T(\mathbf{K}^*)^T\right\} \\ \text{Im}\left\{\frac{1}{\omega_1^2}\mathbf{X}_1^T(\mathbf{K}^*)^T\right\} \\ \vdots \\ \text{Re}\left\{\mathbf{X}_r^T + \frac{1}{\omega_r^2}\mathbf{X}_r^T(\mathbf{K}^*)^T\right\} \\ \text{Im}\left\{\frac{1}{\omega_r^2}\mathbf{X}_r^T(\mathbf{K}^*)^T\right\} \end{bmatrix}.$$

Then, matrix  $\mathbf{M}$  can be calculated in a least-square sense as follows:

$$\mathbf{M} = (\mathbf{A}^T \mathbf{A})^{-1} \mathbf{A}^T \mathbf{B}. \quad (11)$$

After mass matrix  $\mathbf{M}$  has been determined, the ten inertia parameters can be obtained.

**2.2. Identification of the System Dynamic Stiffness.** Based on the identified mass matrix  $\mathbf{M}$  and frequency response functions (FRFs) in the low-rigid-frequency domain, the system dynamic stiffness can be easily estimated.

Assuming that

$$\mathbf{H}_o = (\mathbf{E}^T \mathbf{E})^{-1} \mathbf{E}^T \mathbf{H}. \quad (12)$$

Then,

$$\mathbf{K}^* \mathbf{H}_o = \omega^2 (\mathbf{M} \mathbf{H}_o - \mathbf{T}). \quad (13)$$

Once mass matrix  $\mathbf{M}$  is available, matrix  $\mathbf{K}^*$  can be estimated using the pseudoinverse as follows:

$$\mathbf{K}^* = \omega^2 (\mathbf{M} \mathbf{H}_o - \mathbf{T}) \mathbf{H}_o^T (\mathbf{H}_o \mathbf{H}_o^T)^{-1}. \quad (14)$$

An iterative computation method is used to improve the inertia parameters identification accuracy. Consider the system dynamic stiffness identified by equation (14) as known parameters, we substitute equation (14) into equation (7), calculate the inertia parameters, and repeat this step until the identified inertia parameters converge. Thus, the effect of the rigid body modes on the identification of inertia parameters decreases.

### 3. Numerical Study

Mounts greatly vary in stiffness due to the manufacturing variability, temperature, and displacement. Thus, the identification of inertia parameters of a certain frequency line is not representative. To verify the generality of the method, a specially designed curved bar spring in Figure 1 is used to support a standard block (the mass is 160.6 kg, and the density is  $7.85 \times 10^6/\text{m}^3$ ) simulated the engine (Figure 2). One end of the spring is attached to the standard block, while the other end is fixed by six degrees of freedom. The characteristics of the curved bar spring are as follows: (1) linearly elastic: the three directions of its local coordinate system are linear, and the coupling directions are also linear and (2) small damp: the damp of the spring is negligible.

The 4 response measurement points and 9 applied forces were selected for testing points. The FRFs of the block were measured with the sampling frequency of 2048 Hz and 512 sampling points by the structural Nastran FRF case module. The modulus of the FRFs is shown in Figure 3.

Figure 3 shows that the rigid body modes of the engine lie below 35 Hz, and there is no coupling phenomenon. The first elastic resonance frequency is about 177 Hz with little amplitude; it is available to estimate the mass line from the measured FRFs. In addition, the dynamic stiffness of the support system has little effect on the mass line; it is negligible from engineering practice.

In general, more testing points than required are selected to ensure a good result. By equation (12),  $\mathbf{H}_o$  can be calculated; then the FRFs of the  $j^{\text{th}}$  frequency line  $\mathbf{H}_j$  can be derived by inverse operation  $\mathbf{H}_j'$ . The difference between  $\mathbf{H}_j$  and  $\mathbf{H}_j'$  can be used to determine the error of the results, which can be expressed as follows:

$$\text{err}_j = |\mathbf{H}_j - \mathbf{H}_j'|. \quad (15)$$

The total error can be calculated as follows:

$$\text{err} = \frac{1}{3 \times N \times P} \sum_{j=1}^{3 \times N \times P} |\mathbf{H}_j - \mathbf{H}_j'|. \quad (16)$$

To improve the inertia parameters identification accuracy, the error should remain in a certain range, that is,  $\text{err}_j < \text{err} \times \text{level}$  (level, the initial value), or  $\mathbf{H}_j$  should be eliminated. Since equation (11) uses a least-square method, the rank of matrix  $\mathbf{T}$  should be full, and the condition

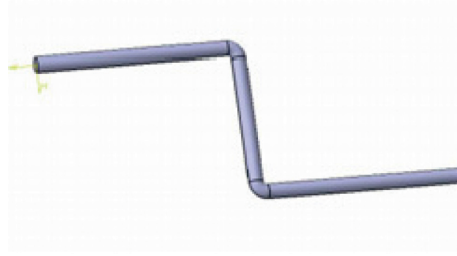


FIGURE 1: Curve bar spring.

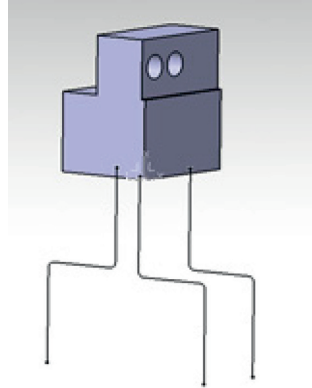


FIGURE 2: Standard block supported by curve bar springs.

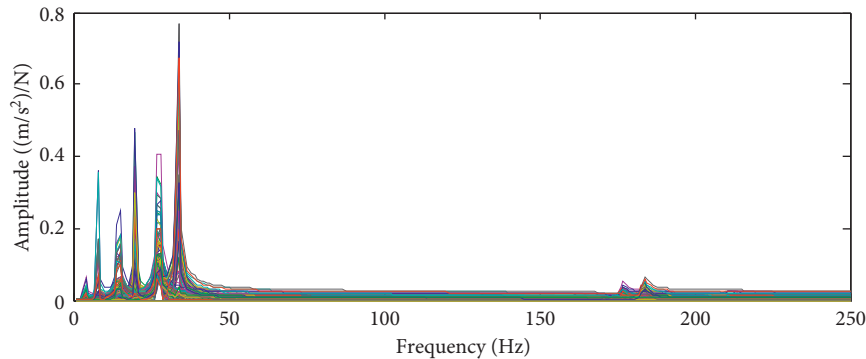


FIGURE 3: Modulus of the FRFs.

number  $con$  of matrix  $\mathbf{T}$  should be lower than 20 [20]. In conclusion, there are three conditions to select the frequency lines of the FRFs: (1)  $err_j < err \times level$ , (2)  $rank(\mathbf{T}) = 6$ , and (3)  $Cond(\mathbf{T}) < con$ . The response points are selected in similar manners.

The frequency bands from 90 Hz up to 150 Hz were selected to identify the ten inertia parameters by equation (11). The identified standard block inertia parameters are presented in Table 1 with a comparison to the finite element simulation results, and the stiffness of the curve bar spring is shown in Table 2. The maximum inertia parameters error is 1.74% for  $x_c$ ; the element error of the matrix  $\mathbf{K}$  is within 2%; and the identified results are consistent with the theory values. In addition, the linear characteristics of the curve bar spring verify the generality of the method.

The six rigid mode shapes have a relatively large magnitude; it is necessary to study their effect on the identification of inertia parameters, so as to see the dynamic behaviour of the engine support system. To ignore the effect of rigid mode shapes, the inertia parameters can be computed using the method in the literature [14], that is, the swing method. The residual inertia method was used to estimate the inertia parameters. To consider the effect of rigid mode shapes, substitute the FEM system stiffness into equation (5); the frequency bands from 90 Hz up to 150 Hz were used to identify the ten inertia parameters. The results are shown in Table 3. The rigid mode shapes have little effect on the estimation of inertia parameters. Since the first elastic mode shapes have a very small magnitude, the inertia parameters are basically unchanged. Both the six rigid and first

TABLE 1: Standard block inertia parameters.

		FEM	Proposed method	Error (%)
Mass (kg)	$m$	161.2	163.3	-1.28
Centre of gravity (mm)	$x_c$	147.0	144.4	1.74
	$y_c$	152.3	152.3	0.03
	$z_c$	112.9	112.7	0.15
Moment of inertia (kg.m <sup>2</sup> )	$J_x$	7.77	7.87	-1.31
	$J_y$	7.74	7.82	-0.99
	$J_z$	9.90	10.02	-1.22
Product (kg.m <sup>2</sup> )	$J_{xy}$	3.66	3.64	0.44
	$J_{xz}$	2.76	2.79	-1.11
	$J_{yz}$	2.43	2.41	0.59

TABLE 2: Identified system stiffness of the curve bar spring.

	Direction	$x$	$y$	$z$	$\alpha$	$\beta$	$\gamma$
FEM system stiffness (N/m)	$x$	2695193	0	536118.7	0	44461.07	0
	$y$	0	275302	0	9247.395	0	-69097.7
	$z$	536118.7	0	1416128	0	85055.21	0
	$\alpha$	0	9247.395	0	22965.87	0	-13059.3
	$\beta$	44461.07	0	85055.21	0	37323.23	0
	$\gamma$	0	-69097.7	0	-13059.3	0	41700.41
Estimated system stiffness (N/m)	$x$	2686950.3	-67.8	536001.9	80395.7	313059.6	-403005.1
	$y$	61.9	272706.3	63.0	-18142.7	15.7	-68023.4
	$z$	539171.3	-36.3	1419722.6	212926.3	139301.4	-80845.6
	$\alpha$	80788.2	-18181.8	212693.0	55748.0	20843.2	-18336.2
	$\beta$	313161.1	4.2	138468.0	20756.3	73034.6	-46970.4
	$\gamma$	-403015.0	-68262.8	-80467.7	-18264.8	-46967.9	101906.0
Error (%)	$x$	0.31	—	0.02	0.03	0.29	0.32
	$y$	—	0.94	—	0.77	—	1.55
	$z$	-0.57	—	-0.25	-0.24	-0.46	-0.53
	$\alpha$	-0.46	0.55	-0.13	-0.03	-0.21	-0.68
	$\beta$	0.26	—	0.14	0.21	0.18	0.27
	$\gamma$	0.31	1.21	-0.06	-0.29	0.27	0.43

TABLE 3: Effects of rigid shapes on the identification of inertia parameters.

		Theory	Ignore rigid shapes	Error (%)	Consider rigid shapes	Error (%)
Mass (kg)	$m$	160.6	161.3	-0.44	163.7	-0.44
Centre of gravity (mm)	$x_c$	147.0	147.0	0.00	144.8	0.00
	$y_c$	152.3	151.1	0.79	148.4	0.79
	$z_c$	112.9	112.9	0.00	111	0.00
Moment of inertia (kg.m <sup>2</sup> )	$J_x$	7.74	7.79	-0.65	7.78	-0.65
	$J_y$	7.71	7.70	0.13	7.68	0.13
	$J_z$	9.86	9.89	-0.30	9.87	-0.30
Product (kg.m <sup>2</sup> )	$J_{xy}$	3.64	3.65	-0.27	3.65	-0.27
	$J_{xz}$	2.75	2.72	1.09	2.71	1.09
	$J_{yz}$	2.42	2.38	1.65	2.38	1.65

elastic mode shapes can be ignored from a practical application point of view.

#### 4. Errors of the Testing Point Location Effect

Since the testing point locations are essential input parameters for the algorithm, random errors were added to understand the sensibility of the method to location errors in this step. One hundred simulation runs were performed for each random error. The errors introduced into the inertia

parameters are shown in Figure 4, and the excitation and response location errors introduced into the system stiffness are presented in Tables 4 and 5, respectively.

The errors in the locations of test points have almost no influence on the estimated mass. Both errors in other properties increase with the increase in the testing error. Approximately 4% error is introduced by an error in the excitation locations, and approximately 9% error is introduced by an error in the response locations. From Tables 4 and 5, we can see that the error has a relatively larger effect

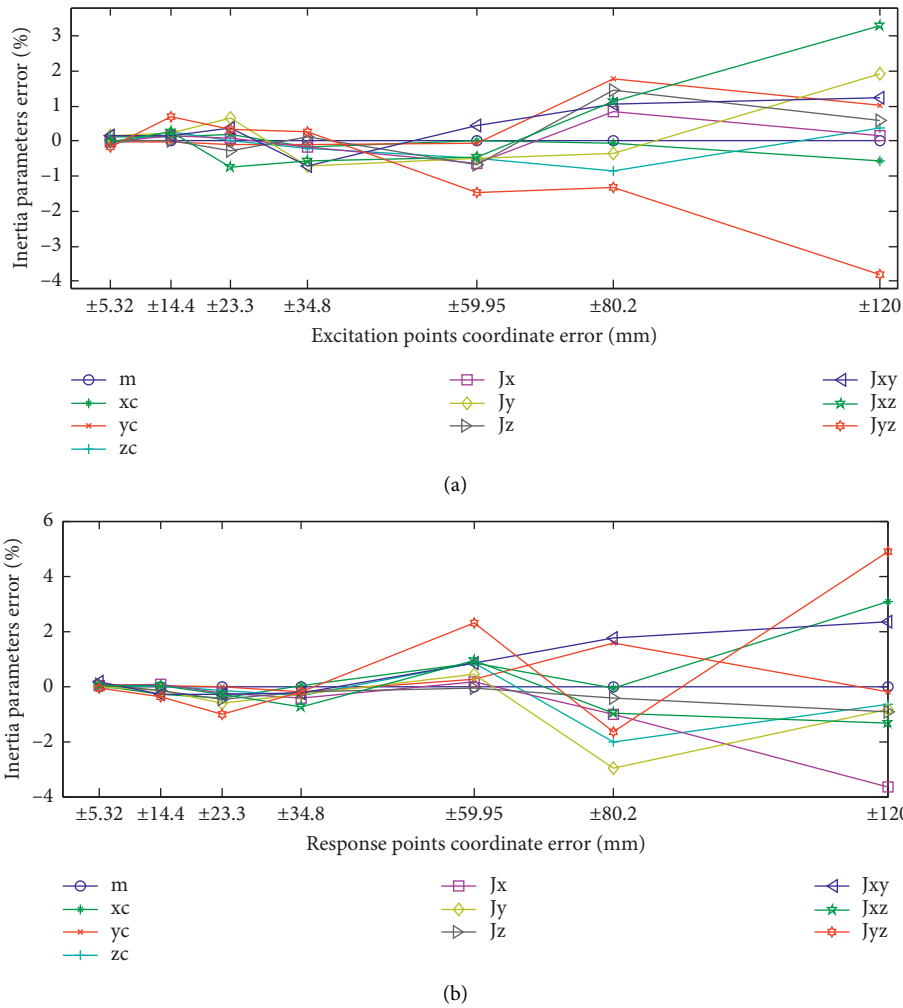


FIGURE 4: Sensitivity of inertia parameter to location errors: (a) excitation locations and (b) response locations.

TABLE 4: Sensitivity of the method to system stiffness errors at excitation locations.

	Direction	$x$	$y$	$z$	$\alpha$	$\beta$	$\gamma$
Estimated stiffness (K/m) with error $\pm 34.8$ mm	$x$	2688379.0	308.4	537109.7	80584.8	313371.1	-403403.0
	$y$	-260.8	272125.0	-652.6	-18363.7	-124.8	-67640.9
	$z$	538223.5	53.0	1417243.0	212655.4	138738.3	-80782.5
	$\alpha$	80499.8	-18736.8	211808.6	55768.4	20651.1	-18095.9
	$\beta$	314727.8	-155.5	142674.1	21328.5	73933.7	-47109.5
	$\gamma$	-403446.0	-66291.1	-80384.6	-17941.4	-46977.6	100948.6
	Estimated error (%)	$x$	-0.25	—	0.18	0.21	-0.19
$y$		—	-1.15	—	0.44	—	-2.11
$z$		0.39	—	0.08	0.11	0.05	0.45
$\alpha$		0.10	2.48	-0.29	0.06	-0.72	-0.64
$\beta$		0.24	—	2.89	2.54	1.05	0.03
$\gamma$		-0.21	-4.06	-0.04	-1.49	-0.25	-1.36
Estimated stiffness (K/m) with error $\pm 120$ mm		$x$	2688603.0	274.3	536987.3	80564.2	313366.7
	$y$	-269.8	272111.2	-674.7	-18353.5	-128.6	-67632.9
	$z$	538230.5	42.9	1417220.0	212642.0	138718.0	-80775.2
	$\alpha$	81008.9	-17557.0	212938.1	55060.5	20849.3	-18396.5
	$\beta$	314197.9	1176.8	140636.6	21094.4	73510.2	-47674.7
	$\gamma$	-404670.0	-68378.2	-84502.7	-19264.0	-47828.2	102362.8



TABLE 4: Continued.

	Direction	$x$	$y$	$z$	$\alpha$	$\beta$	$\gamma$
Estimated error (%)	$x$	-0.24	—	0.16	0.18	-0.20	-0.21
	$y$	—	-1.16	—	0.39	—	-2.12
	$z$	0.39	—	0.08	0.10	0.04	0.44
	$\alpha$	0.74	-3.97	0.24	-1.21	0.24	1.01
	$\beta$	0.07	—	1.42	1.41	0.47	1.23
	$\gamma$	0.10	-1.04	5.08	5.78	1.55	0.02

TABLE 5: Sensitivity of the method to system stiffness errors in response locations.

	Direction	$x$	$y$	$z$	$\alpha$	$\beta$	$\gamma$	
Random error $\pm 34.8$ mm	$x$	2687089.0	-49.4	534515.0	79808.6	312370.9	-400879.0	
	$y$	-460.3	272380.3	-820.9	-17882.0	-362.8	-68551.1	
	$z$	538707.6	555.9	1419494.0	211825.7	141596.3	-80095.5	
	$\alpha$	80841.6	-17496.1	213273.3	55795.1	21209.0	-18439.5	
	$\beta$	311702.6	-33.8	138302.0	20606.6	73283.5	-46386.5	
	$\gamma$	-400960.0	-68279.8	-79754.0	-18304.2	-46517.9	101827.6	
	$x$	-0.3	—	-0.3	-0.76	-0.51	-0.84	
	$y$	—	-1.06	—	-2.19	—	-0.79	
	$z$	0.48	—	0.24	-0.28	2.11	-0.40	
	$\alpha$	0.53	-4.30	0.40	0.11	1.97	1.25	
	$\beta$	-0.73	—	-0.26	-0.93	0.16	-1.51	
	$\gamma$	-0.82	-1.18	-0.83	0.50	-1.23	-0.50	
	Random error $\pm 120$ mm	$x$	2687577.0	-863.8	533317.9	80772.6	326156.1	-411843.0
		$y$	-1342.0	269013.3	955.6	-16104.3	-366.2	-79734.5
$z$		535032.0	-4586.7	1405268.0	211346.6	177723.6	-88411.0	
$\alpha$		81899.9	-18308.2	214197.9	61077.6	27131.7	-21016.2	
$\beta$		312780.1	-1596.4	135979.4	20503.2	82414.3	-48248.2	
$\gamma$		-407703.0	-69072.3	-81083.1	-20979.8	-48705.7	113786.3	
Estimated error (%)		$x$	-0.28	—	-0.52	0.44	3.88	1.87
	$y$	—	-2.28	—	-11.92	—	15.39	
	$z$	-0.20	—	-0.77	-0.50	28.17	9.94	
	$\alpha$	1.84	0.14	0.84	9.59	30.44	15.40	
	$\beta$	-0.38	—	-1.94	-1.43	12.64	2.44	
	$\gamma$	0.85	-0.04	0.83	15.20	3.42	11.18	

on the estimated system dynamic stiffness, especially on the coupling stiffness; when the random error is in the range of  $[-120, 120]$ , the estimated error on the coupling stiffness is 30.44%. As shown, care must be taken in measuring geometry to avoid incorrect results. The units of the elements of the stiffness matrix are the corresponding generalized force divided by the generalized displacement.

### 5. Experiments

*5.1. Curve Bar Spring Engine System.* The test engine was supported by 3 specially designed curve bar springs shown in Figure 5. Here, 4 response points and 18 excitation points were taken into account. The coordinates of test points were measured by the 3D coordinate measuring apparatus.

The FRFs were measured with the sampling frequency of 1024 Hz and 1024 sampling points. The modulus of the FRFs for 4 response points and 3 of 18 excitation points are presented in Figure 6. We can see that all six rigid body modes are excited within 30 Hz, and the first elastic resonance frequency is approximately 118.5 Hz. The FRFs and the corresponding coherence functions for response point 1

are shown in Figure 7. The values of the coherent coefficients for the three directions are all greater than 0.8, which verifies the reliability of the experiment.

The coordinate transformation of the test points [14] is valid only when the rigidity condition is satisfied. In this section, the measured and calculated FRFs were compared at the fourth accelerometer to check the rigidity of the engine. According to coordinate transformation, the FRFs of the fourth accelerometer can be calculated by the other three accelerometers, that is, Acc1, Acc2, and Acc3. As shown in Figure 8, the calculated FRFs agree well with the measured FRFs within 100 Hz, which verified the rigidity of the engine.

The frequency bands from 60 Hz to 85 Hz were used to identify the 10 inertia parameters by equation (11) (Table 6). Then, the FRFs from 3 Hz to 35 Hz were used to identify the curve bar spring stiffness in Table 7. The inertia parameters of the engine were also computed by the swing method [16], for comparison. The proposed method can identify the engine inertia method under normal installation conditions (in situ), while the swing method must remove the engine from the support infrastructure to ensure free-free boundary conditions.

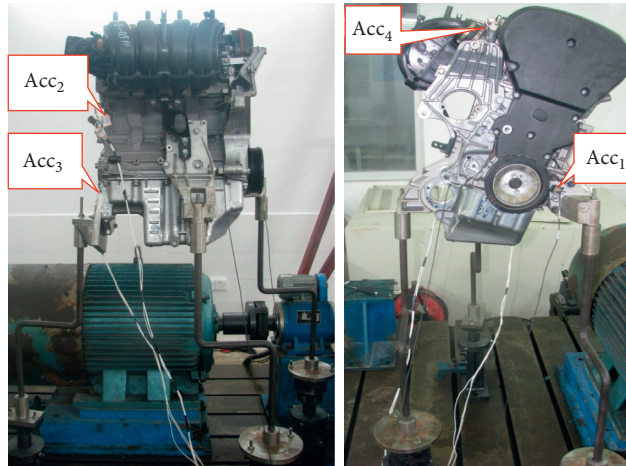


FIGURE 5: Test engine supported by curve bar springs.

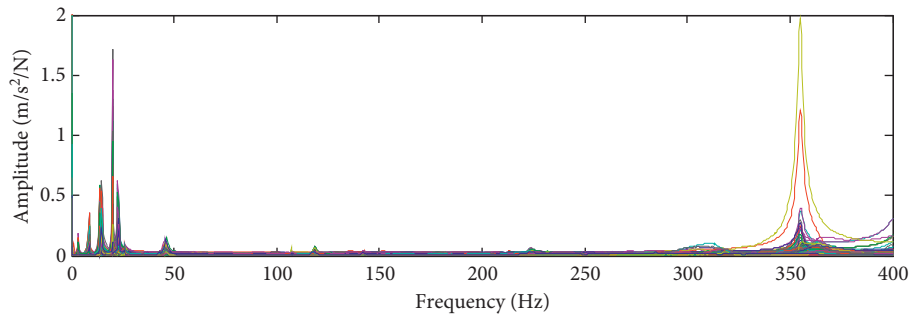
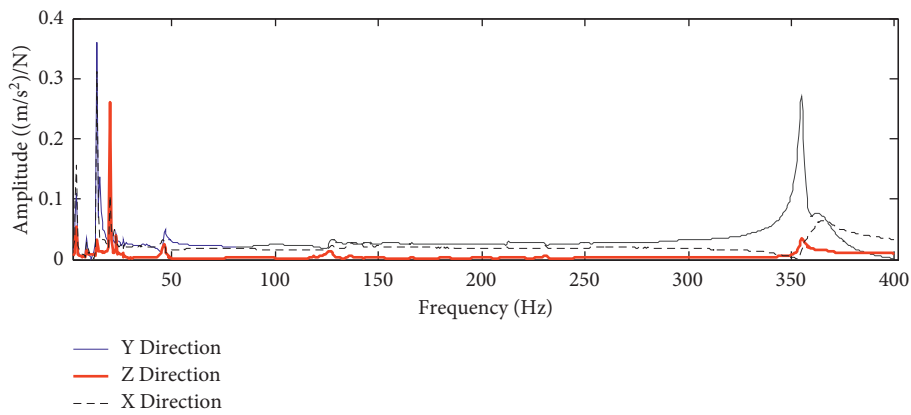


FIGURE 6: Amplitude-frequency response for response measurement points and applied forces.



(a)

FIGURE 7: Continued.

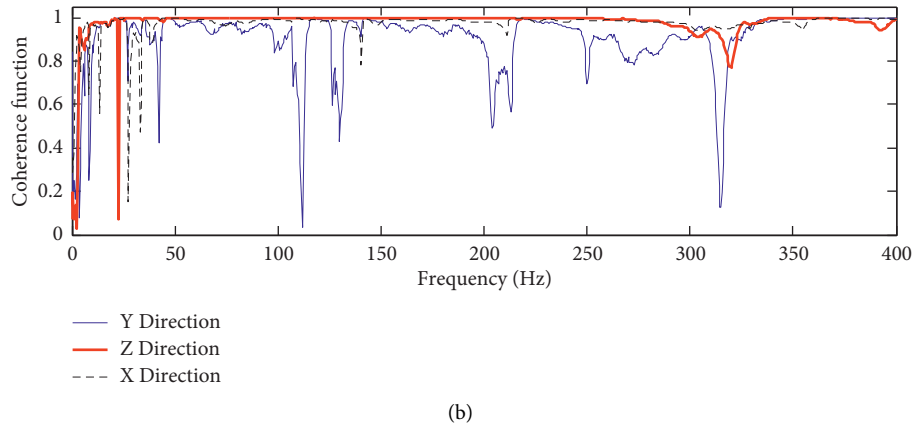


FIGURE 7: Example of the test FRFs (excitation: F17; response: Acc3): (a) FRF and (b) coherence.

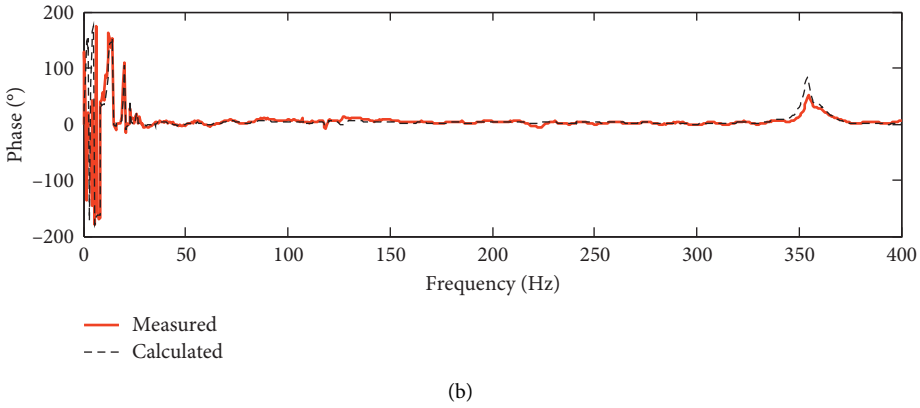
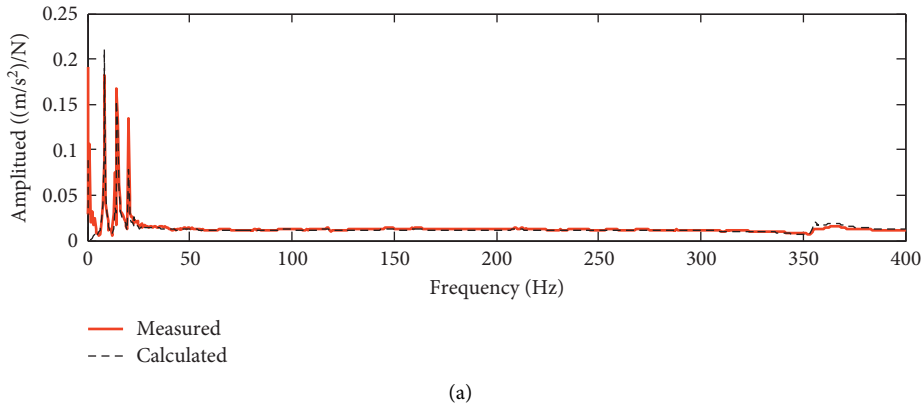


FIGURE 8: Rigidity check of the engine: (a) amplitude and (b) phase.

TABLE 6: Identified inertia parameters of the engine curve bar spring system.

Inertia parameters		Proposed method	Swing method
Mass (kg)	$m$	115.2	109.3
Centre of gravity (mm)	$x_c$	16.7	33.4
	$y_c$	206.8	216.3
	$z_c$	119.1	135.5

TABLE 6: Continued.

Inertia parameters		Proposed method	Swing method
Moment of inertia (kg.m <sup>2</sup> )	$J_x$	11.52	11.62
	$J_y$	5.50	5.42
	$J_z$	8.80	8.46
Product (kg.m <sup>2</sup> )	$J_{xy}$	0.27	0.03
	$J_{xz}$	3.25	3.31
	$J_{yz}$	0.23	0.12

TABLE 7: Identified system stiffness of the engine supported by curve bar springs.

	Direction	$x$	$y$	$z$	$\alpha$	$\beta$	$\gamma$
Identified system stiffness (N/m)	$x$	290120.7	48337.8	386771.5	116531.3	-22822.5	-52696.2
	$y$	70933.0	395010.3	137520.8	-10216.1	-16877.2	20108.6
	$z$	553817.9	77824.8	1160978.8	268614.3	16786.5	-124765.4
	$\alpha$	150337.5	-14657.5	278525.7	133840.1	15069.3	-44197.4
	$\beta$	-57322.6	-10786.8	-35724.6	11531.1	64754.8	9857.5
	$\gamma$	-47982.5	20608.0	-89536.5	-38565.4	-1114.0	31575.3

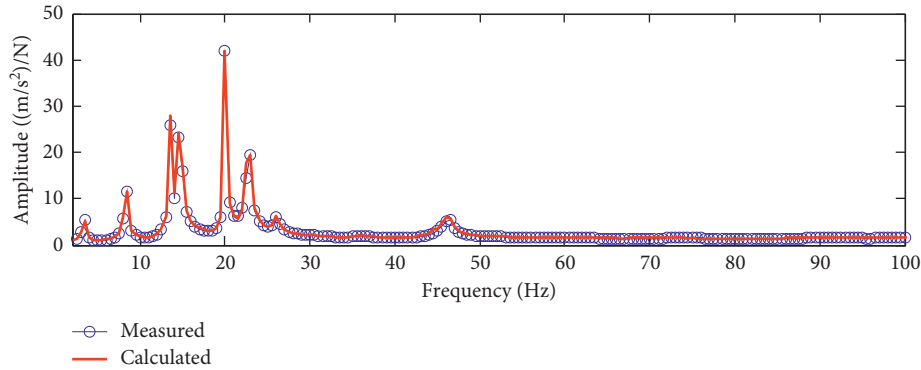


FIGURE 9: Modulus of the measured and calculated FRFs.

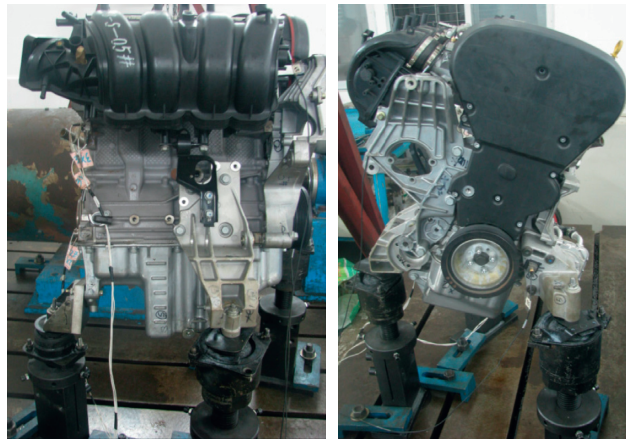


FIGURE 10: Test engine supported by the mount.

Since the engine and curve bar springs were connected through 3 switchover pieces (0.81 kg×3) and an auxiliary plate (Figure 5), the identified engine mass was somewhat larger than the swing method estimated. In addition, the centre of gravity should reduce in value due to the effect of the switchover pieces (0.81 kg×3) and an auxiliary plate

compared with the swing method, and the results are consistent with the trend. The identified results of the proposed method are close to the results from the swing method. The stiffness values estimated from the presented method and extracted by the finite element simulation have a bias because: (1) there is machining error, (2) the three curve

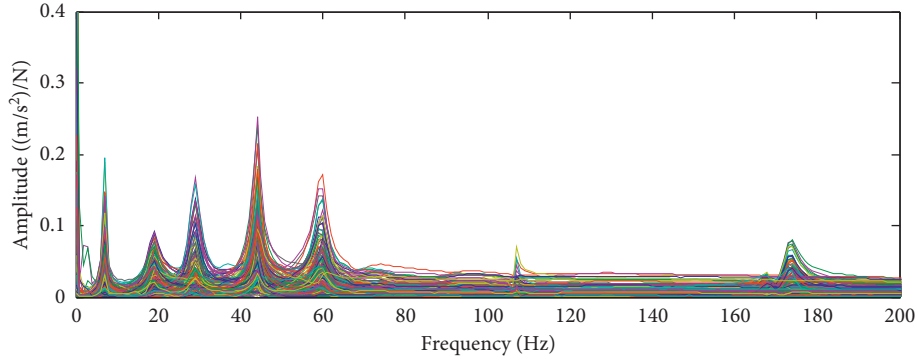


FIGURE 11: FRFs for all measurement points of the engine supported by the mount.

TABLE 8: Identified inertia parameters of the powertrain mount system.

Inertia parameters		Proposed method	Swing method
Mass (kg)	$m$	110.8	109.3
Centre of gravity (mm)	$x_c$	19.5	33.4
	$y_c$	208.1	216.3
	$z_c$	134.2	135.5
Moment of inertia (kg·m <sup>2</sup> )	$J_x$	11.56	11.62
	$J_y$	5.61	5.42
	$J_z$	8.01	8.46
Product (kg·m <sup>2</sup> )	$J_{xy}$	0.34	0.56
	$J_{xz}$	3.36	3.31
	$J_{yz}$	0.26	0.15

TABLE 9: Identified system dynamic stiffness of the powertrain mount system.

	Direction	$x$	$y$	$z$	$\alpha$	$\beta$	$\gamma$
System stiffness (N/m)	$x$	1490171.8	-62047.3	-363210.4	-101692.6	-245141.7	-341731.1
	$y$	254.8	1910981.1	-776855.1	199150.6	241490.1	259257.6
	$z$	-547878.2	-781461.8	4635226.6	1067626.9	-694916.0	-11255.6
	$\alpha$	-119562.5	378584.3	1195191.6	436581.8	-175183.9	90437.8
	$\beta$	-265289.7	223319.6	-697592.1	-143398.3	222587.3	92242.3
	$\gamma$	-369934.7	273163.7	-63350.4	37893.5	86895.9	174911.2
	System damp (N·s/m)	$x$	121371.1	-19433.4	32809.8	19086.0	18288.5
$y$		-58827.4	189173.6	-95132.9	-4759.9	18617.5	48450.6
$z$		171024.9	-213459.0	651576.1	158276.4	-101082.1	-91967.9
$\alpha$		72740.8	-44961.6	232898.8	57961.3	-25358.0	-34826.9
$\beta$		-39033.1	59188.1	-88440.0	-13369.6	31634.4	14076.3
$\gamma$		-37373.0	31182.6	-30948.1	-9501.8	-4297.2	16228.2

bar springs do not have exactly identical stiffness, and (3) the spring stiffness has a certain degree of nonlinearity.

Once the inertia parameters and system dynamic stiffness are known, the FRFs corresponding to the measured FRFs can be calculated. Comparing the sum of all calculated FRFs with the measured values, we find that the two FRFs have consistent moduli, as shown in Figure 9, which verifies the consistency of the identified results. Hereafter, if there is no specific declaration, the same method is utilized.

**5.2. Mount Engine System.** Here, the engine was supported by three mounts as shown in Figure 10. The engine and measuring points are identical to those in Figure 5. Similar steps to estimate the inertia parameters and system dynamic stiffness

are applied in this section. The signals were collected with the sampling frequency of 256 Hz and 1024 points. The moduli of the calculated FRFs for all points are shown in Figure 11.

The coherent coefficients are greater than 0.8, and the rigidity condition of the engine holds within 100 Hz. The identified inertia parameters and system dynamic stiffness are presented in Tables 8 and 9, respectively. From Table 8, we can see that the identified inertia parameters agree well with those from the swing method.

The change in system dynamic stiffness with frequency in the three directions of its local coordinate system is shown in Figure 12. The modulus of the calculated and the measured FRFs is shown in Figure 13 and verifies the consistency of the identified results.

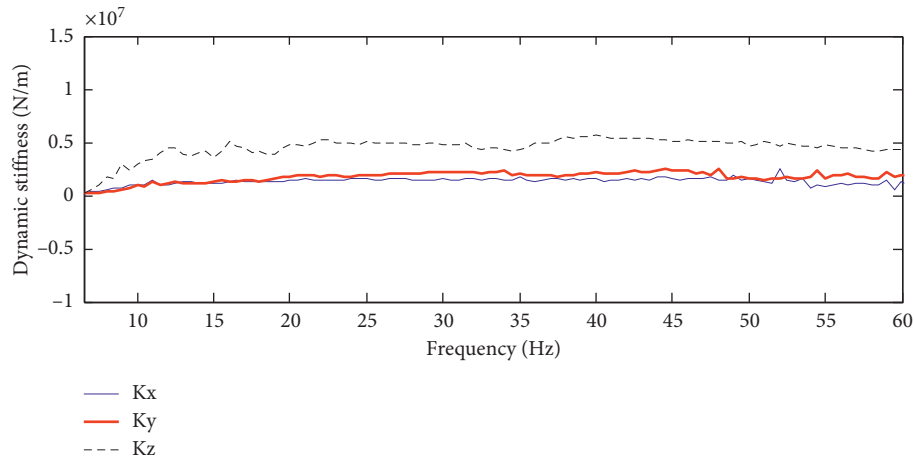


FIGURE 12: Estimated system dynamic stiffness.

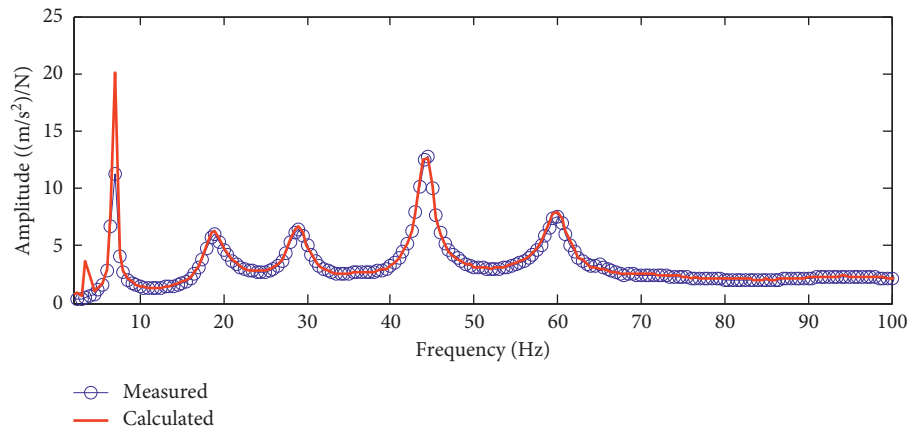


FIGURE 13: Modulus of the measured and calculated FRFs of the engine mount system.

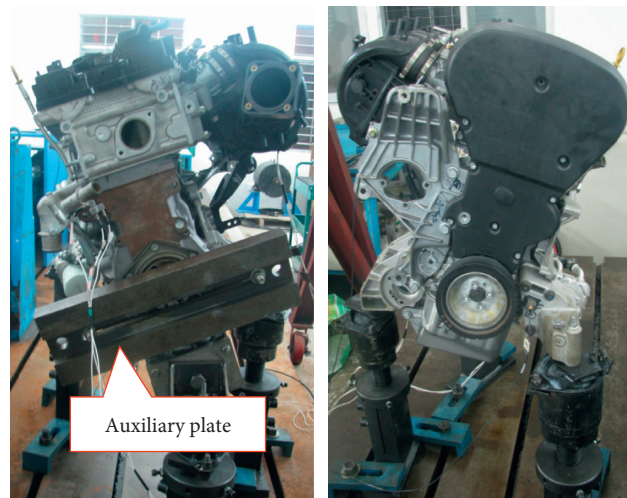


FIGURE 14: Engine with an auxiliary plate.

*5.3. Mount Engine with an Auxiliary Plate.* Since the mount stiffness is not available, to verify the accuracy of the identified stiffness in Section 5.2, an auxiliary plate (14.9 kg) was rigidly connected to the engine as shown in Figure 14;

then, the same steps were applied to calculate the system dynamic stiffness. If the identified stiffness agrees well with that identified in Section 5.2, the identified results are reliable. The sampling frequency and engine attitude are

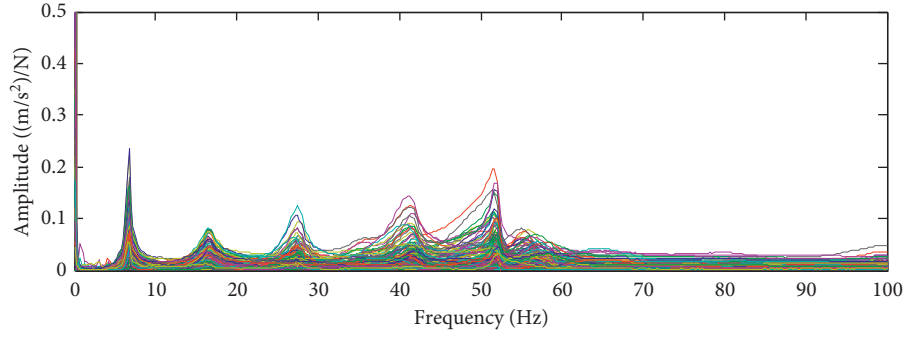


FIGURE 15: FRFs for all measurement points of the engine plate mount system.

TABLE 10: Identified inertia parameters of the engine plate.

Inertia parameters		Engine plate	Engine	Differences
Mass (kg)	$m$	126.2	110.8	15.4
Centre of gravity (mm)	$x_c$	22.4	19.5	2.9
	$y_c$	180.2	208.1	-27.9
	$z_c$	98.1	134.2	-36.1
Moment of inertia (kg·m <sup>2</sup> )	$J_x$	11.46	11.56	-0.1
	$J_y$	6.57	5.61	0.96
	$J_z$	7.97	8.01	-0.04
Product (kg·m <sup>2</sup> )	$J_{xy}$	0.97	0.34	0.63
	$J_{xz}$	3.08	3.36	-0.28
	$J_{yz}$	0.46	0.26	0.2

TABLE 11: Identified system dynamic stiffness of the powertrain mount system.

	Direction	$x$	$y$	$z$	$\alpha$	$\beta$	$\gamma$
System stiffness (N/m)	$x$	1395591.8	-30449.8	-942324.2	-281524.7	-163269.4	-374485.9
	$y$	-113718.0	1334671.3	-681578.8	141792.6	8774.2	210950.1
	$z$	-525103.2	-319732.4	4847951.0	1226340.0	-643756.5	136427.0
	$\alpha$	-96400.5	187465.1	1490075.0	489962.4	-255752.3	62305.0
	$\beta$	-342200.5	49534.8	-1123473.9	-291110.9	334301.8	83100.4
	$\gamma$	-398453.2	219841.2	73853.7	83061.1	51541.5	187883.5
System damp (N·s/m)	$x$	48323.9	-1701.9	-107602.7	-37387.4	21710.4	-18127.0
	$y$	-95842.9	147080.1	44298.3	40013.9	-36403.2	35169.6
	$z$	109125.4	-50897.6	515109.4	138443.2	-24243.4	-23883.1
	$\alpha$	10866.7	21260.1	180011.5	59125.0	-7614.7	1522.5
	$\beta$	-83656.9	40028.1	-63065.6	1426.8	21217.1	24798.1
	$\gamma$	-41526.3	25703.9	-1744.1	7179.4	-7047.3	16897.5

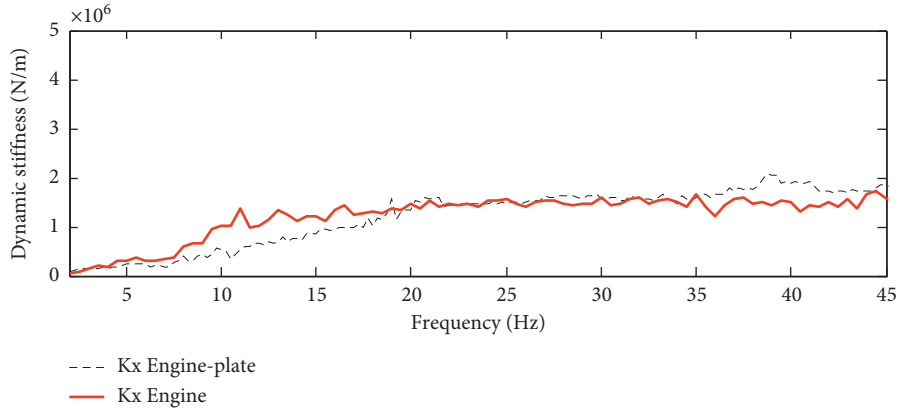
TABLE 12: Differences in identified main stiffness between the engine plate and the engine.

Stiffness (N/m)	$k_{xx}$	$k_{yy}$	$k_{zz}$	$k_{\alpha\alpha}$	$k_{\beta\beta}$	$k_{\gamma\gamma}$
Engine plate	1395592	1334671	4847951	489962.4	234301.8	187883.5
Engine	1490172	1910981	4635227	436581.8	222587.3	174911.2
Differences (%)	-6.34692	-30.1578	4.589299	12.22694	5.262879	7.416506

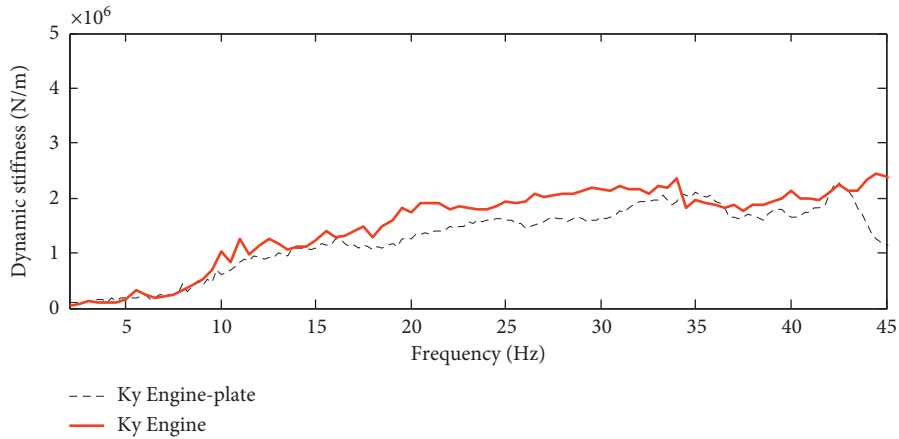
identical to those in Section 5.2. The measured FRFs calculated for points are presented in Figure 15.

The inertia parameters and system dynamic stiffness identified results are presented in Tables 10 and 11, respectively. Differences between the identified main stiffness are shown in Table 12. In Table 12, the system equivalent

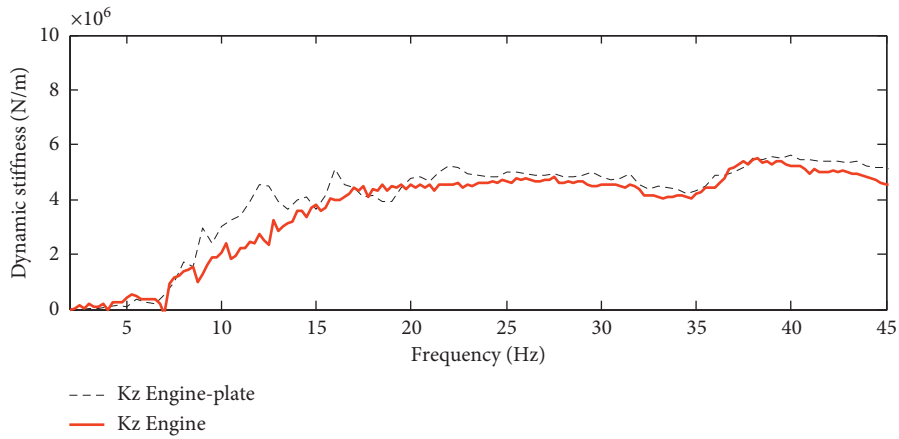
stiffness is close, although there is a difference due to the preload. The changes in  $K_x$ ,  $K_y$ , and  $K_z$  with frequency for the engine with and without the auxiliary plate are shown in Figure 16. The two curves are basically identical in each direction, which verify the accuracy of the identified stiffness.



(a)



(b)



(c)

FIGURE 16: Change in (a)  $K_x$ , (b)  $K_y$ , and (c)  $K_z$  with frequency.

Table 10 also shows that the identified mass of the engine with the auxiliary plate is 15.4 kg heavier than that of the engine without an auxiliary plate. The difference in quality is due to the quality of the auxiliary plate (14.9 kg). Under the effect of the auxiliary plate, the value of the centre of mass of  $y_c$  and  $z_c$  should be smaller than that of the

engine without an auxiliary plate, and the trend of the identified results is consistent, which verifies the accuracy of the method.

Similar to Section 5.1, the modulus of the calculated FRF is consistent with the measured one in Figure 17, which verifies the consistency of the identified results.



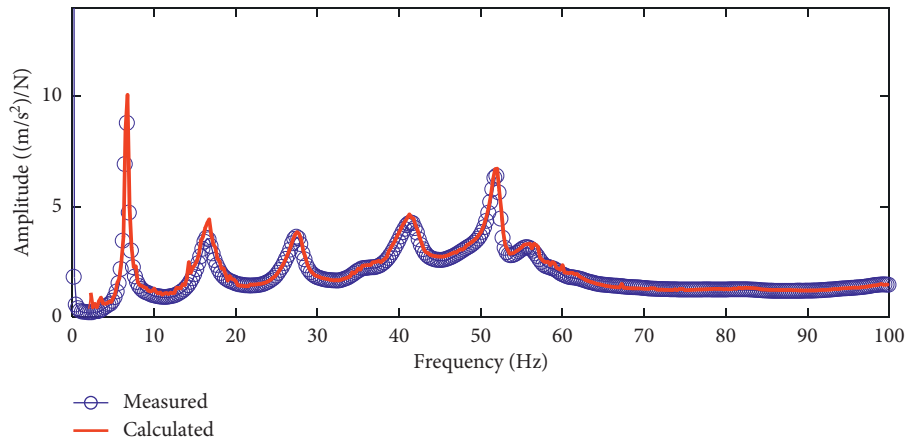


FIGURE 17: Modulus of the measured and calculated FRFs of the engine plate mount system.

## 6. Conclusions and Discussion

An in situ method for identifying ten inertia parameters and system dynamic stiffness of an engine was presented in this paper. Further investigation of the errors of the testing point location effect shows that the coordinates of measuring points should be carefully measured since errors in coordinates lead to errors in results.

The results from the test on the engine supported by the curve bar spring verify the generality of the method, while the results from the test on the engine supported by the mount are comparable to those of a swing test, which indicates the accuracy of the estimation inertia parameter method. The consistency of the identified dynamic stiffness of the engine with and without an auxiliary plate shows that the estimation of the system dynamic stiffness is reliable. In addition, for each experiment, the modulus of all FRFs calculated from the inertia parameters and system dynamic stiffness has high consistent with the measured value, which further verifies the accuracy of the identified results.

However, the system dynamic stiffness identification method can only identify the stiffness at the origin of the coordinates. This method cannot identify the stiffness of each mount. In future research, we will study more appropriate methods to overcome this deficiency.

## Data Availability

The data used in this study are included within the article.

## Conflicts of Interest

The authors declare that they have no conflicts of interest.

## Acknowledgments

This work was supported by the National Natural Science Foundation of China (Grant nos. 51405272, 51505258, and 51975121) and partly supported by the Natural Science Foundation of Shandong Province (ZR2020ME126), the Youth Science and Technology Plan Project of colleges and universities in Shandong Province (Grant no. 2019KJB019),

Shandong Provincial Major Scientific and Technological Innovation Project (2019JZZY020617), the Shandong Provincial Key Research and Development Program (2019GNC106071), and the State Key Laboratory of Mechanical Behavior and System Safety of Traffic Engineering Structures, China (Grant no. 1903).




## References

- [1] L. Dan and Z. C. Hou, "Sensitivity analysis of inertial parameters in powertrain mounting design," *Automotive Engineering*, vol. 29, pp. 884–888, 2007.
- [2] P. D. Gaberson and H. A. Gaberson, "Surmounting the inherent errors in the trifilar pendulum measurement of moment of inertia," *Journal of the Acoustical Society of America*, vol. 54292 pages, 1973.
- [3] J. J. Dowling, J. L. Durkin, and D. M. Andrews, "The uncertainty of the pendulum method for the determination of the moment of inertia," *Medical Engineering & Physics*, vol. 28, no. 8, pp. 837–841, 2006.
- [4] W. B. Shangguan, L. Y. He, and Z. L. Tian, "Development of an equipment for measuring the center of gravity and the moments of inertia of automotive powertrain," *Journal of Vibration Engineering*, vol. 23, pp. 119–125, 2010.
- [5] M. Gobbi, G. Mastinu, and G. Previati, "A method for measuring the inertia properties of rigid bodies," *Mechanical Systems and Signal Processing*, vol. 25, pp. 305–318, 2011.
- [6] H. Hahn, "Inertia parameter identification of rigid bodies using a Multi-Axis test facility," in *Proceedings of the Third IEEE Conference on Control Applications*, Glasgow, Scotland, August 1994.
- [7] S. M. Pandit and Z.-Q. Hu, "Determination of rigid body characteristics from time domain modal test data," *Journal of Sound and Vibration*, vol. 177, no. 1, pp. 31–41, 1994.
- [8] M. R. Ashory, A. Malekjafarian, and P. Harandi, "On the accuracy of estimation of rigid body inertia properties from modal testing results," *Structural Engineering & Mechanics*, vol. 35, pp. 1–13, 2010.
- [9] R. A. B. Almeida, A. P. V. Urgueira, and N. M. M. Maia, "Identification of rigid body properties from vibration measurements," *Journal of Sound and Vibration*, vol. 299, no. 4-5, pp. 884–899, 2007.
- [10] J. Bretl and P. Conti, "Rigid body mass properties from test data," in *Proceedings of the 5th IMAC*, pp. 655–659, Sweden, April 1987.

- [11] R. Almeida, *Evaluation of the Dynamic Characteristic of Rigid Bodies Based on Experimental Results*, PhD Thesis, New University of Lisbon, Lisbon, Portugal, 2006.
- [12] H. Lee, Y.-B. Lee, and Y.-S. Park, "Response and excitation points selection for accurate rigid-body inertia properties identification," *Mechanical Systems and Signal Processing*, vol. 13, no. 4, pp. 571–592, 1999.
- [13] J. M. W. Lau and F. Deblauwe, *Advanced FRF Based Determination of Structural Inertia Properties*, SAE, Chicago, IL, USA, 2008.
- [14] W. Leurs, M. Gielen, B. Dierckx, Calculation of Rigid Body Properties from FRF Data: Practical Implementation and Test Cases. LMS, 2000, 1998.
- [15] C. Xu, K. Ding, and Z. Yang, "Identification of engine inertia parameters on the basis of Frequency Response Functions," *International Journal of Vehicle Design*, vol. 60, no. 1/2, pp. 121–137, 2012.
- [16] J. A. Mangus, C. Passerello, and C. Vankarsen, "Direct estimation of rigid body properties from harmonic forced responses," in *Proceedings of the 15th International Modal Analysis Conference*, pp. 175–180, Orlando, FL, USA, July 1997.
- [17] M. Link and G. Qian, "Identification of dynamic models using base excitation and measured reaction forces," *Revue Française de Mécanique*, vol. 1, pp. 35–42, 1994.
- [18] R. A. B. Almeida, A. P. V. Urgueira, and N. M. M. Maia, "Evaluation of the performance of three different methods used in the identification of rigid body properties," *Shock and Vibration*, vol. 15, no. 3-4, pp. 467–479, 2008.
- [19] Y. Zhang and Z. C. Hou, "Identification of rigid body inertia properties by utilizing modal parameters," *Journal of Vibration Engineering*, vol. 29, pp. 436–443, 2016.
- [20] Y. X. He, T. Wang, and L. J. Zhang, "Improved identification method for structural inertial parameters based on FRF," *Journal of Vibration and Shock*, vol. 38, pp. 236–241, 2019.
- [21] O. Vahid, A. Khajepour, F. Ismail, and C. R. Urbaniak, "In situ identification of vehicle engine inertia properties," *International Journal of Vehicle Noise and Vibration*, vol. 3, no. 1, pp. 46–69, 2007.
- [22] J. V. Karsen, D. Johnson, J. Blough, and M. Rao, *Estimation of Powertrain Inertia Properties via an In-Situ Method*, SAE, Chicago, IL, USA, 2007.
- [23] Y. Yu, N. G. Naganathan, and R. V. Dukkipati, "A literature review of automotive vehicle engine mounting systems," *Mechanism and Machine Theory*, vol. 36, no. 1, pp. 123–142, 2001.
- [24] Y. Gao, X. Liu, and J. Xiang, "FEM simulation-based generative adversarial networks to detect bearing faults," *IEEE Transactions on Industrial Informatics*, vol. 16, no. 7, pp. 4961–4971, 2020.
- [25] X. Liu, H. Huang, and J. Xiang, "A personalized diagnosis method to detect faults in gears using numerical simulation and extreme learning machine," *Knowledge-Based Systems*, vol. 195, Article ID 105653, 2020.
- [26] X. Y. Liu, H. Z. Huang, and J. W. Xiang, "A personalized diagnosis method to detect faults in a bearing based on acceleration sensors and a FEM simulation driving support vector machine," *Sensors*, vol. 20, p. 42, 2020.
- [27] Z. He, *Powertrain Inertial Parameter Identification Based on Firefly Algorithm*, Master's thesis, Wuhan University of Science and Technology, Wuhan, China, 2019.
- [28] H. H. Zhang and W. K. Shi, "Model of the secondary path between the input voltage and the output force of an active engine mount on the engine side," *Mathematical Problems in Engineering*, vol. 2020, Article ID 6084169, 16 pages, 2020.
- [29] A. Kumar, C. P. Gandhi, Y. Q. Zhou, R. Kumar, and J. W. Xiang, "Latest developments in gear defect diagnosis and prognosis: a review," *Measurement*, vol. 158, Article ID 107735, 2020.
- [30] E. O. Lu and M. Ripin, "Dynamic stiffness and loss factor measurement of engine rubber mount by impact test," *Materials and Design*, vol. 32, pp. 1880–1887, 2011.

## Research Article

# New Tool Wear Estimation Method of the Milling Process Based on Multisensor Blind Source Separation

Chen Gao <sup>1</sup>, Sun Bintao <sup>2</sup>, Heng Wu,<sup>3</sup> Mengjuan Peng,<sup>3</sup> and Yuqing Zhou <sup>2</sup>

<sup>1</sup>School of Mechatronics and Transportation, Jiaxing Nanyang Polytechnic Institute, Jiaxing, China

<sup>2</sup>College of Mechanical and Electrical Engineering, Wenzhou University, Wenzhou, China

<sup>3</sup>Wenzhou Hanggang Water Co. Ltd, Wenzhou, China

Correspondence should be addressed to Sun Bintao; 381861064@qq.com

Received 5 March 2021; Revised 7 July 2021; Accepted 22 July 2021; Published 30 July 2021

Academic Editor: Akemi Gálvez

Copyright © 2021 Chen Gao et al. This is an open access article distributed under the Creative Commons Attribution License, which permits unrestricted use, distribution, and reproduction in any medium, provided the original work is properly cited.

Timely and effective identification and monitoring of tool wear is important for the milling process. However, traditional methods of tool wear estimation have run into difficulties due to under small samples with less prior knowledge. This article addresses this issue by employing a multisensor tool wear estimation method based on blind source separation technology. Stationary subspace analysis (SSA) technology is applied to transform multisensor signals to stationary and nonstationary sources without prior information of signals. Ten dimensionless time-frequency indices of the nonstationary signal are extracted to train least squares support vector regression (LS-SVR) to obtain a tool wear estimation model for small samples. The analysis and comparison of one benchmark tool wear dataset and tool wear experiments verify the feasibility and effectiveness of the proposed method and outperform other two current methods.

## 1. Introduction

The computerized numerical control (CNC) milling machine provides an important source of power for hard machining. With the advantages of high automation and good precision, it is widely used in modern manufacturing. The cutter tool is the primary factor that affects the quality of the machine; its wear and damage can directly affect the surface quality of the workpiece as well as the machining efficiency. Tool wear accounts for 20–30% of the total downtime of a milling machine [1, 2], and tools and tool changes account for 3–12% of the total machining cost [3]. Therefore, online tool wear estimation has become an important research area in intelligent milling machining [4].

As shown in Figure 1, a typical online tool wear estimation method has three steps: (1) sensor signal acquisition, i.e., acquisition of physical field signals in the milling process by one or more sensors; (2) feature extraction, i.e., acquisition of received signals, such as by fast Fourier transform or wavelet analysis, to obtain information related to tool wear; and (3) monitoring, i.e., use of pattern recognition,

neural networks, or regression analysis to classify or estimate tool failure.

In online tool wear estimation, many sensors have been used to obtain process signals [5], such as cutting force [6, 7], acoustic emission (AE) [8, 9], vibration [10, 11], and current [12, 13]. However, a single physical field signal has several shortcomings; for example, the cutting force is most sensitive to changes of tool wear, but commercial dynamometers are expensive and can increase manufacturing costs. An AE signal is measured at a high sampling rate, which leads to a large dataset and difficult processing and storage [14]. A vibration signal is difficult to filter, and it can be affected by the installation position. A current signal contains much noise, which makes it difficult to detect small fluctuations [15]. Due to the uncertainty and limitations of a single sensor, multisensor monitoring has become common due to its good performance and robustness [16]. Zhao et al. [17] applied a multisensor signal with a three-component dynamometer and three accelerometers to estimate tool wear using local feature-based gated recurrent unit networks. Zhou et al. [18] collected multisensor signals in a

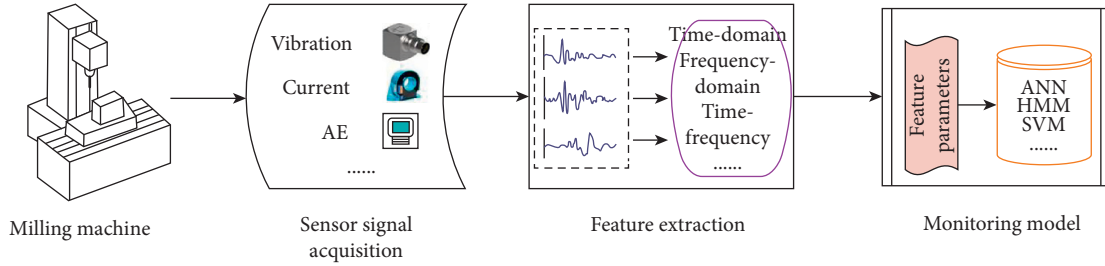


FIGURE 1: Process diagram of tool condition monitoring.

milling process and proposed a method to search for optimal feature parameter combinations in multisensor signals. Zhu et al. [19] proposed a smart tool condition monitoring system through several deep learning models with sensors, including cutting force, vibration, AE, CNC process data, and tool wear image. Multisensor methods can enhance the richness of information that contains potential tool wear levels and reduce the overall uncertainty of the measurement. In addition, several researchers determine the cutting tool life through mathematical methods. For example, Krolczyk et al. developed a mathematical model to predict the tool life by examining the influence of cutting parameters, namely, cutting speed, feed, and depth of cut onto tool life [20], researched the coated carbides tool life and the tool point surface topography [21], and analyzed the wear of milling cutters made of sintered carbide and of boron nitride [22], which provide a good theoretical basis for tool wear estimation. Moreover, hybrid intelligent methods have attracted considerable interest for tool fault diagnosis, e.g., wavelet transform (WT) and artificial neural network (ANN). The growth of deep learning (DL) in recent years has led to increasing interest in DL-based tool wear estimation methods [23, 24]. However, these hybrid intelligent methods require the signal analyzed to satisfy certain conditions, such as huge number of training samples, independent and identical distribution, white Gaussian noise, or prior information of data. For example, WT-based feature extraction lies in selecting a wavelet basis function that matches the fault characteristic waveform. However, it is difficult to select the appropriate wavelet basis function for the recognition of an unknown milling cutter tool fault [3]. DL-based methods require large amounts of training sample data, which are costly and time-consuming for machining processes [25]. Accordingly, these above conditions are difficult to meet in practical situation [26, 27], especially in time-varying and nonstationary nature of the NC machine complex cutting process. Moreover, there is little prior knowledge that can be available to detect and diagnose tool faults in NC machine currently [28]. The study of time-varying and nonstationary processes with less prior information is therefore well motivated. Therefore, obtaining good accuracy of tool wear estimation under small sample is currently a hot topic.

The main contributions of this article are as follows:

- (1) A tool wear estimation method for a milling process based on a multisensor blind source separation

method is proposed, using small training sample sizes and not presetting model parameters

- (2) The proposed method based on SSA and LS-SVR significantly outperforms PCA according to milling tool wear experiments
- (3) Experiments with different cutting conditions verify that the proposed method is robust and promising for milling tool condition monitoring

The remainder of this study is organized as follows. Section 2 describes the theoretical framework and proposed tool wear estimation method. Sections 3 and 4 verify the performance of the method with the benchmark PHM-2020 milling dataset and our tool wear experiments. Conclusions are given in Section 5.

## 2. Proposed Method

**2.1. Framework.** The proposed online milling tool wear estimation method includes the phases of model training and online tool wear estimation (Figure 2). During model training, multidimensional signals are collected for different tool wear and divided into several stationary sources and one nonstationary source by SSA technology (Section 2.2). Statistical parameters in the time and frequency domains (Section 2.3) of the nonstationary source are calculated to train the LS-SVR model (Section 2.4). In online tool wear estimation, for a new tool to be tested in milling operation, multidimensional signals are collected by multiple sensors and then extracted the nonstationary source by SSA. Statistical parameters in the time and frequency domains of the nonstationary source are calculated and input to the LS-SVR to estimate the wear value.

**2.2. Stationary Subspace Analysis.** SSA is a blind source separation algorithm proposed by von Bunau et al. [29]. In SSA, if two first-order parameters of a time series do not change with time, then it is stationary. SSA assumes that an observed multidimensional time series is a linear superposition of stationary sources that are constant over time and nonstationary sources that change with time [30]. An observed multidimensional time series  $X \in \mathbf{R}^{D \times N}$  is defined as

$$X = AS_t = [A^s \ A^n] \begin{bmatrix} S_t^s \\ S_t^n \end{bmatrix}, \quad (1)$$

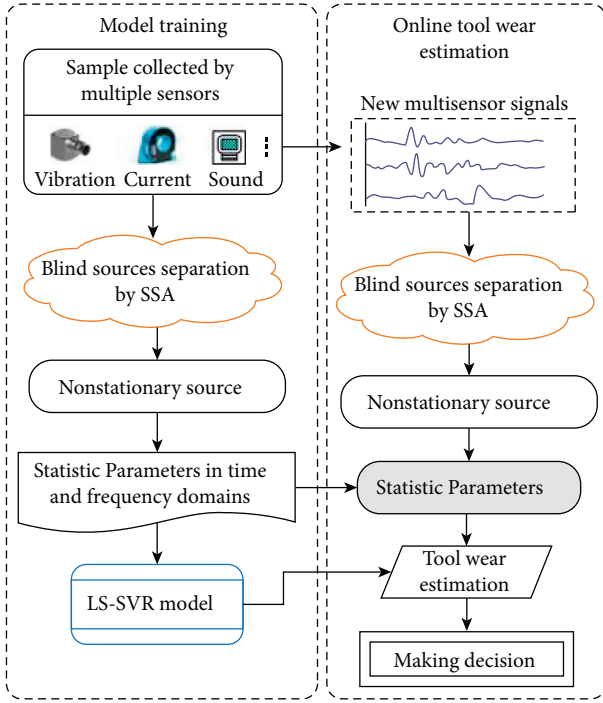


FIGURE 2: Framework of the proposed method.

where  $D$  and  $N$  are the dimension and number of data points, respectively;  $A \in \mathbf{R}^{D \times D}$  is an unknown independent time matrix that is the linear superposition of the coefficient matrices of stationary and nonstationary sources; and  $S_t^s$  and  $S_t^n$  denote the  $d$ -dimensional stationary and  $(D-d)$ -dimensional nonstationary sources, respectively.

If  $d$ -dimensional stationary and  $(D-d)$ -dimensional nonstationary sources exist, then an inverse matrix  $A^{-1}$  can be constructed for the observation data  $X$ , such that

$$\begin{bmatrix} \widehat{S}_t^s \\ \widehat{S}_t^n \end{bmatrix} = A^{-1}X = A^{-1}A \begin{bmatrix} S_t^s \\ S_t^n \end{bmatrix} = \begin{bmatrix} B^s A^s & B^s A^n \\ B^n A^s & B^n A^n \end{bmatrix} \begin{bmatrix} S_t^s \\ S_t^n \end{bmatrix}. \quad (2)$$

To determine whether two first-order parameters of a time series change with time, the observed  $X$  is divided into continuous time segments, and each is compared with the whole time series through Kullback–Leibler (KL) divergence. The mean  $\mu_i$  and covariance matrix  $\Sigma_i$  of each segment  $X_i$  are calculated, and KL divergence is employed to compare the changes of their mean and covariance,  $X_i(\mu_i, \Sigma_i)$  and  $X(\mu_0, \Sigma_0)$ , respectively. The stationary index can be defined as

$$L(\mu_1, \dots, \mu_n, \Sigma_1, \dots, \Sigma_n) = \sum_{i=1}^n D_{KL} [N(\mu_i, \Sigma_i) \| N(\bar{\mu}, \bar{\Sigma})]. \quad (3)$$

To find the stationary mapping  $B$ , SSA minimizes the nonstationarity of the stationary direction to be estimated, and the optimal stationary mapping can be obtained by the solution of

$$\arg \min_{B \in \mathbf{R}^{d \times d}} \sum D_{KL} [N(B\bar{\mu}_i, B\Sigma_i B^T) \| N(B\bar{\mu}, B\bar{\Sigma} B^T)]. \quad (4)$$

To solve this problem, SSA uses an iterative operator to find  $B$  by updating an orthogonal matrix  $R$ . Starting from a random orthogonal matrix  $R_0$ , and in each step  $k$ , the steepest descent direction  $U$  in a set of orthogonal transformations is found using the standard gradient descent strategy, and the following update is performed until the last step  $Q$ :  $R_{k+1} = UR_k$ ; then, we obtain  $B^{s*} = I_d R_Q W$ , where  $W$  is the whitening matrix.

It can be seen that SSA does not need a large amount of sample data for training nor does it require independent dimension components. As long as the number of segmentation time is not less (generally greater than the dimension of the observed time series), the blind source analysis can be realized.

### 2.3. Statistical Parameters in Time and Frequency Domains.

To overcome the drawback of features in a single domain, which lose some useful information related to the tool condition, we extract a few dimensionless statistical parameters in the time and frequency domains based on the literature [27, 31, 32] and our experimental studies [11, 33]. Table 1 lists 10 statistical feature parameters related to tool wear from the time and frequency domains that were extracted as feature parameters.

**2.4. Least Squares Support Vector Regression.** The aim of LS-SVR is to extract features from the original space and map the samples to a vector in a high-dimensional feature space, so as to solve the problem of linear indivisibility in the original space [34, 35].

Given a training set  $D = \{(X_k, y_k) | k = 1, \dots, M\}$ ,  $X_k \in \mathbf{R}^{D \times N}$ ,  $y_k \in \mathbf{R}$ ,  $X_k$ , and  $y_k$  denote independent and response variables, respectively. The response function to be estimated is

$$\text{Min}_{\omega, b, c} J(\alpha, e) = \frac{1}{2} \alpha^T \alpha + c \sum_{k=1}^N e_k^2, \quad (5)$$

$$\text{s.t. } y_k = \alpha^T \varphi(x_k) + b + e_k,$$

where  $e_k$  is the error;  $\alpha$  and  $b$  are the weight vector and bias, respectively, to be estimated; and  $\varphi(\cdot)$  is a mapping function from low-dimensional space to high-dimensional feature space. The loss function  $J$  is the sum of squares due to error (SSE) and regularization of  $\alpha$ . According to the Lagrange multiplier method, the following equation can be transformed [36]

$$L(\alpha, b, e; \gamma) = J(\alpha, e) - \sum_k \gamma_k \{ \alpha^T \varphi(x_k) + b + e_k - y_k \}. \quad (6)$$

Let the partial derivatives of  $L$  to  $\alpha$ ,  $b$ ,  $e$ , and  $\gamma$  be equal to 0. Eliminating  $e$  and  $\gamma$ ,  $\alpha$  and  $b$  to be estimated can be solved by the following matrix equation:

$$\begin{bmatrix} 0 & I_v^T \\ I_v & \Omega + \frac{1}{c} I \end{bmatrix} \begin{bmatrix} b \\ \alpha \end{bmatrix} = \begin{bmatrix} 0 \\ \gamma \end{bmatrix}, \quad (7)$$



TABLE 1: Ten statistical parameters.

Domain	Index	Formula
Time	Crest factor, $T_{cf}$	$T_{cf} = \max\{x_i\}/x_{rms}$
	Shape factor, $T_{sf}$	$T_{sf} = x_{rms}/(\sum  x_i /n)$
	Kurtosis, $T_{ku}$	$T_{ku} = (\sum_{j=1}^n (x_j - T_{avg})^4)/(n \cdot T_{sd}^4) - 3$
	Skewness, $T_{sk}$	$T_{sk} = (\sum_{j=1}^n (x_j - T_{avg})^3)/(n \cdot T_{sd}^3)$
	Kurtosis factor, $T_{kf}$	$T_{kf} = T_{ku}/x_{rms}$
Frequency	Stabilization ratio, $F_{sr}$	$F_{sr} = (\sum_{j=1}^n f_j^2 P_j)/(\sqrt{\sum_{j=1}^n P} \sqrt{\sum_{j=1}^n f_j^4 P})$
	Wave-height ratio, $F_{wr}$	$F_{wr} = \max\{P_i\}/\sqrt{(2/n) \sum_{j=1}^n P_i^2}$
	Frequency high-low ratio, $F_{fr}$	$F_{fr} = \sum_{i=n/4}^{n/2} P_i / \sum_{i=1}^{n/4} P_i$
	Average frequency, $F_{af}$	$F_{af} = \sqrt{(\sum_{j=1}^{n/2} f_j P_j) / (\sum_{j=1}^{n/2} P_j)}$
	Modified equivalent bandwidth, $F_{meb}$	$F_{meb} = \sqrt{(\sum_{j=1}^n (f_j - \bar{f})^2 P_j) / (\sum_{j=1}^n P_j)}$

where  $1_v = [1, \dots, 1]$ , and  $\Omega_{kl} = \varphi(x_k)^T \varphi(x_l)$ ,  $k, l = 1, \dots, N$ . LS-SVR employs a kernel function trick to overcome complex high-dimensional mapping operations of  $\varphi(\cdot)$ , such as a polynomial kernel, multilayer perceptual kernel,  $B$ -spline kernel, or RBF kernel.

$$\Psi(x_k, x_l) = \varphi(x_k)^T \varphi(x_l). \quad (8)$$

Thus, the response variable corresponding to a new observed  $X'$  can be determined as follows:

$$y(X') = \sum \alpha_k^* \Psi(X', X_k) + b^*. \quad (9)$$

In this study, the RBF kernel function is used, as given in the following equation, and the hyperparameter  $h$  is optimized by leave-one-out cross-validation (LOOCV) due to a small training sample set [37].

$$\psi_h(x, x') = \frac{1}{\sqrt{2\pi}} \exp\left(-\frac{(x - x')^2}{2h^2}\right). \quad (10)$$

### 3. Benchmark Dataset Analysis

**3.1. Description of Dataset.** The PHM-2010 challenge milling dataset employed for validation testing of the proposed method was obtained from a milling machine under dry milling using a 2-flute ball nose cutter [38, 39]. Figure 3 shows the device and sensors used in this experiment, and Table 2 lists the cutting parameters. There were three types of signals: cutting force from a three-component dynamometer, vibration from three accelerometers, and AE from an AE sensor. Therefore, each sample in the dataset included seven sensor channels' time series. The tool's flank wears were measured offline using a microscope after finishing each surface.

**3.2. Analysis and Results.** According to the data file, three cutter records, C1, C4, and C6, could be used to verify the performance of tool wear estimation. C4 and C6 were used as the training set, and C1 as the testing set.

For each sample, a seven-dimensional signal was obtained from six stationary and one nonstationary source, and the 10 dimensionless statistical parameters listed in Table 1

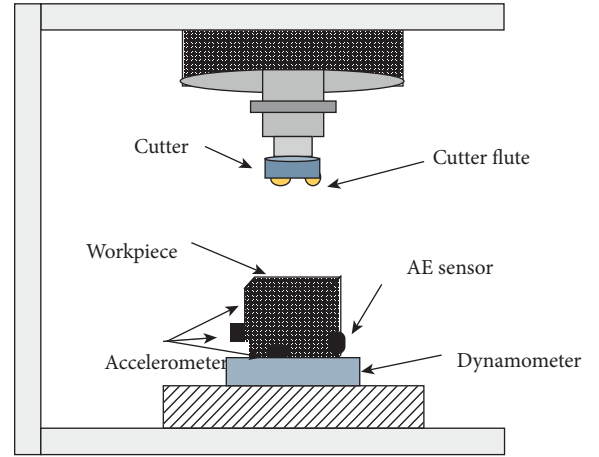


FIGURE 3: Experimental setup in the PHM-2010 challenge milling dataset.

TABLE 2: Operation parameters in the PHM-2010 challenge milling dataset.

Operation parameter	Value
CNC machine	Roders Tech RFM 760
Workpiece material	Inconel 718 (Jet engines)
Cutter	3-flute ball nose
Spindle speed	10400 rpm
Feed rate	1555 mm/min
Y depth of cut (radial)	0.125 mm
Z depth of cut (axial)	0.2 mm
Number of sensors	5
Number of sensor channels	7
Sampling data	50 kHz

were calculated as the input of the LS-SVR. There are two reasons for selecting one nonstationary source: (1) it contains a variety of feature information than the stationary source to distinguish different tool wear; and (2) in the proposed method, it is easy to calculate the statistical parameters for the single nonstationary source.

To test the effectiveness of different methods, LS-SVR and principal component analysis (PCA) + LS-SVR were compared with the proposed SSA + LS-SVR. Ten

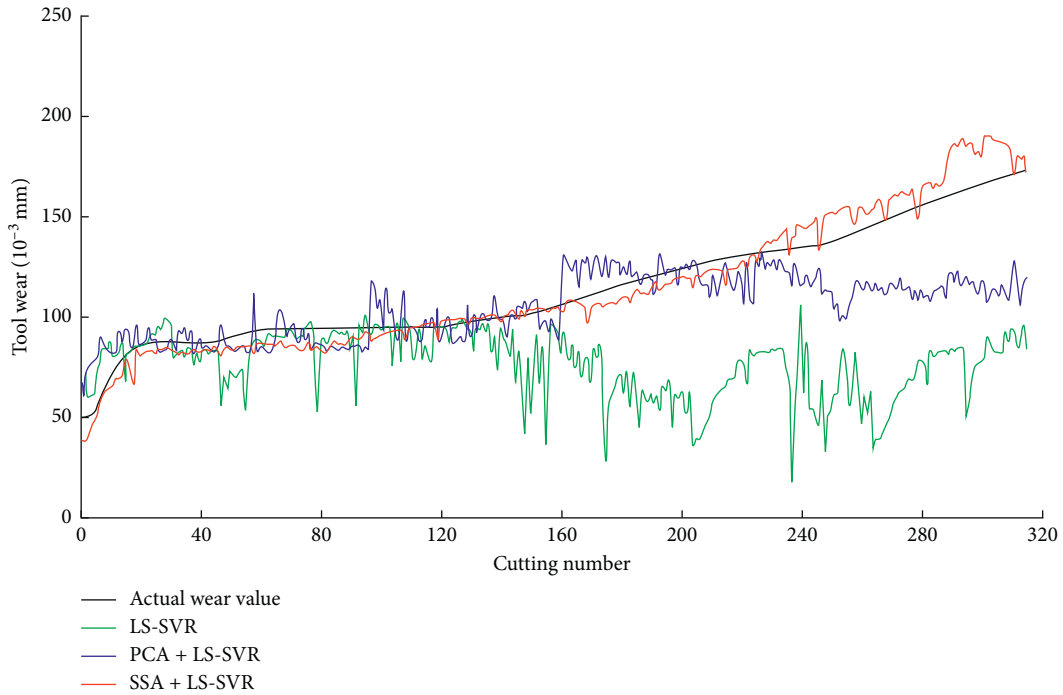


FIGURE 4: Comparison of three methods of tool wear estimation with testing set C1.

TABLE 3: Estimation error of three methods with testing set C1.

	LS-SVM	PCA + LS-SVM	SSA + LS-SVM
RMSE	52.1077	22.5284	8.4653
R	0.2899	0.6961	0.9848

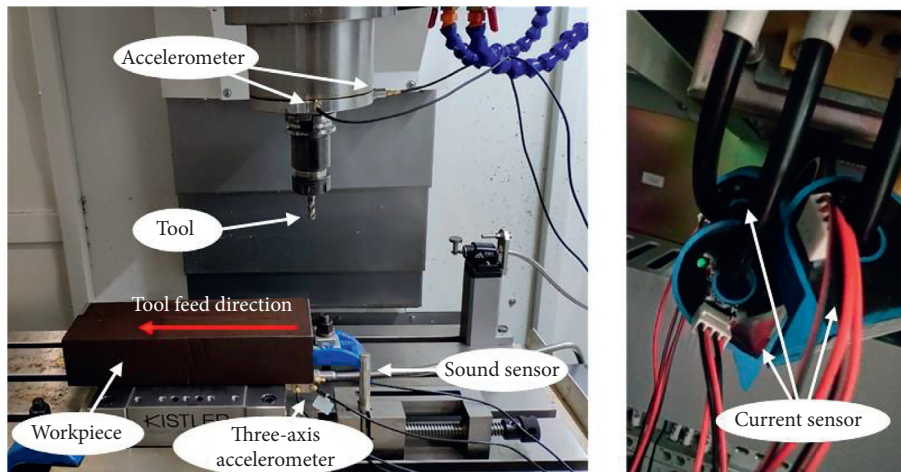


FIGURE 5: Experimental setup.

dimensionless statistical parameters of each dimension from the original multisensor signals were calculated directly for every sample and used as the input of the LS-SVR; there was no transformation of the original signal. PCA + LS-SVR uses PCA instead of SSA for feature extraction. Ten dimensionless statistical parameters of seven

channels in each sample were calculated as the input of the PCA, and 10 principal components obtained by PCA were selected as the input of the LS-SVR. Root mean square error (RMSE) and the correlation coefficient ( $R$ ) were employed to quantify the estimation performance of these methods.



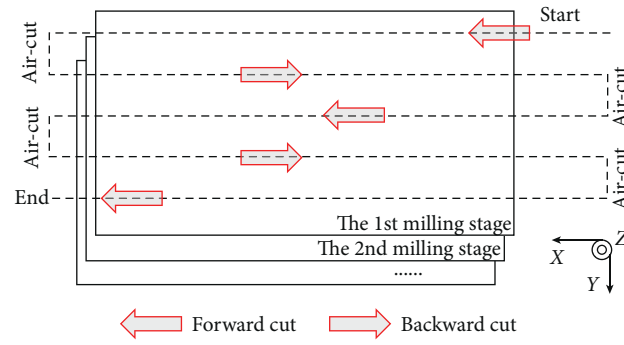


FIGURE 6: Milling path in the experiments.

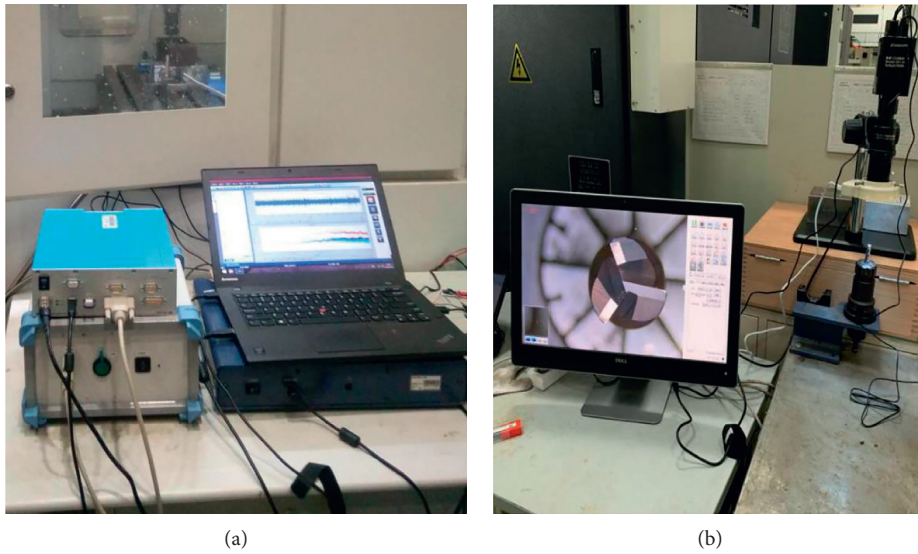


FIGURE 7: Experimental measuring devices. (a) Data acquisition instrument. (b) Tool microscope.

TABLE 4: Cutting parameters in the experiment.

Tool	Spindle speed (rpm)	Depth of cut (mm)	Feed rate (mm/tooth)
1	2300	0.4	0.058
2	2300	0.4	0.072
3	2300	0.5	0.065
4	2300	0.6	0.072
5	2300	0.6	0.058
6	2400	0.4	0.065
7	2400	0.5	0.072
8	2400	0.6	0.058
9	2500	0.4	0.072
10	2500	0.4	0.058
11	2500	0.5	0.058
12	2500	0.6	0.065
13	2500	0.6	0.072
14	2500	0.6	0.058

The tool wear estimation results of tool C1 with three methods are shown in Figure 4, from which it can be seen that the estimation accuracy of the proposed method exceeds

that of the other two methods. The error between the estimated and actual values of tool wear is presented in Table 3. The RMSE of the proposed SSA + LS-SVR method was

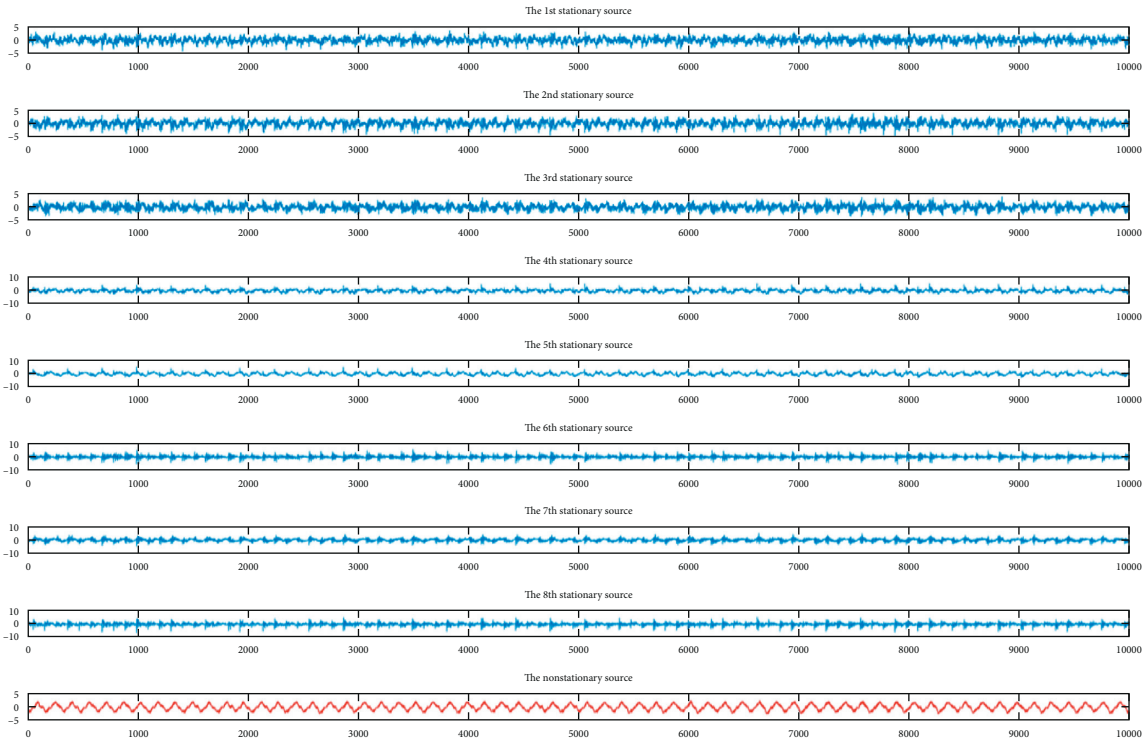


FIGURE 8: Signal after SSA transformation (tool wear value is 0.403 mm).

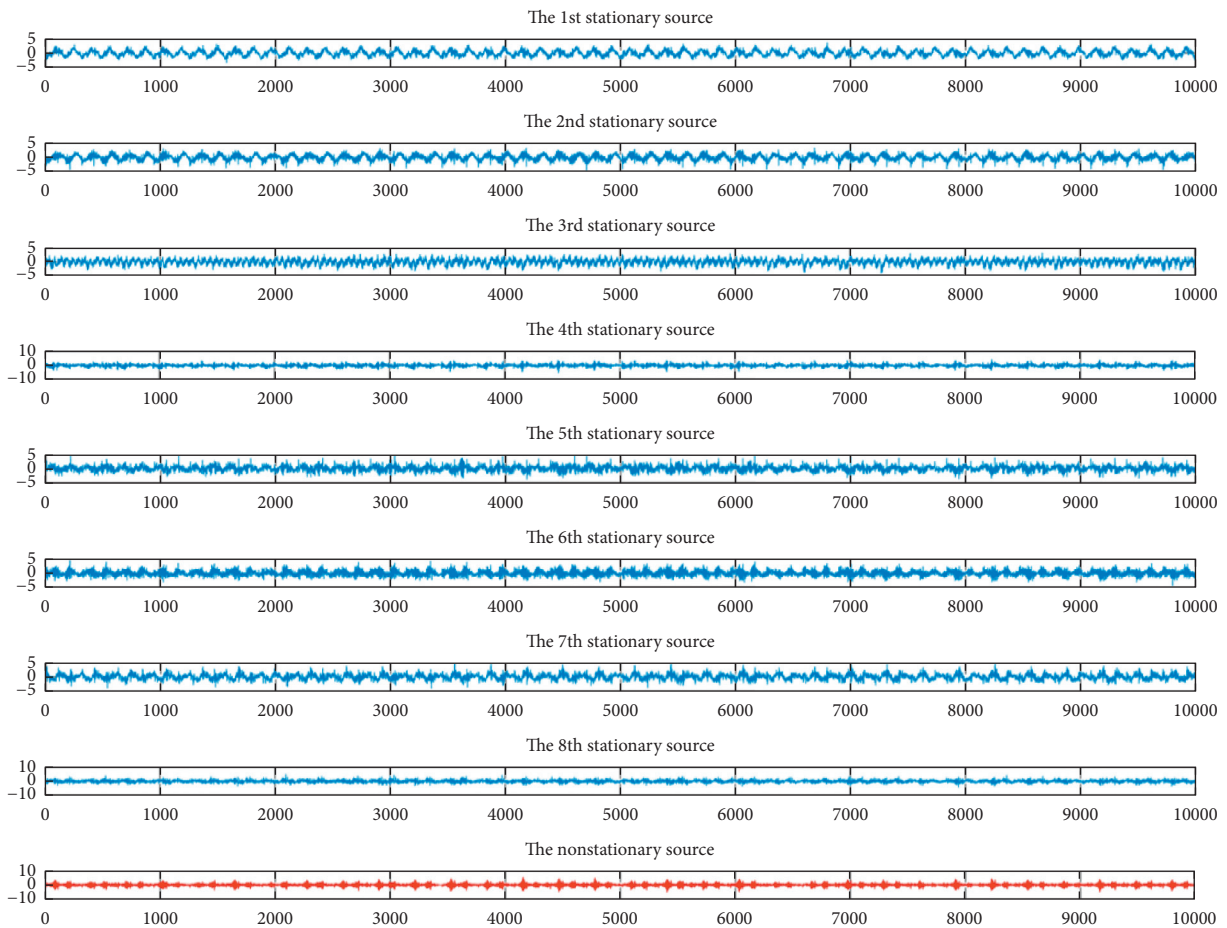


FIGURE 9: Signal after SSA transformation (tool wear value is 1.047 mm).

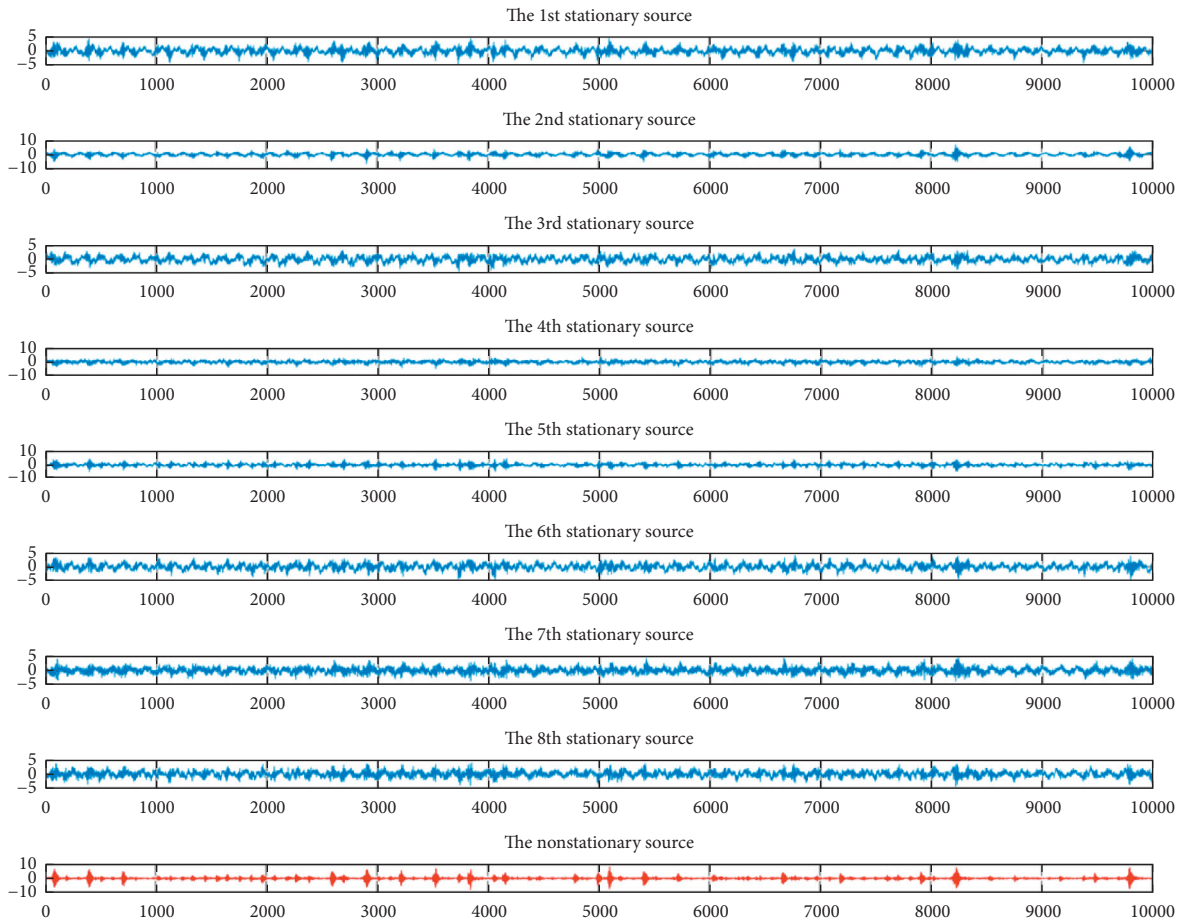


FIGURE 10: Signal after SSA transformation (tool wear value is 2.05 mm).

8.4653, which was 83.7% and 62.4% less than that of the LS-SVR and PCA + LS-SVR, respectively.  $R$  was 0.9848 for the proposed method, which was 0.69 and 0.28 greater than that of the LS-SVR and PCA + LS-SVR, respectively.

## 4. Experimental Investigation

**4.1. Experimental Setup.** Figure 5 shows the experimental setup for milling tool wear estimation under various operating conditions. The workpiece was #45 steel with dimensions of 300 mm  $\times$  100 mm  $\times$  80 mm, machined by a vertical machining center using an uncoated three-tooth tungsten steel end milling cutter under dry millings. Each cutting was completed five times in finishing a surface, i.e., three times forward and two times back, as shown in Figure 6. A three-axis accelerometer was mounted under the workpiece with a magnetic base to measure its vibrations in the X, Y, and Z directions, and accelerometers were attached to the side of the spindle by strong glue to measure the vibrations of the spindle in the X and Y directions. Three current sensors were clamped on the machine motor wires to measure the three-phase current of the motor. A sound sensor was fixed near the workpiece to measure sound during the cutting process. Therefore, the sensory data consisted of nine channels. These signals were collected by a data acquisition instrument and stored on a

personal computer (Figure 7(a)), with a continuous sampling frequency of 12 kHz during the tool wear test. The wear value of each individual flute was measured offline using a tool microscope after machining a surface (Figure 7(b)).

There were 14 cutting tools used in our experiment with different cutting parameters, as given in Table 4. In each tool cutting experiment, there were five group signals after cutting a surface. The first four group signals were taken as training samples and the last as the test sample.

**4.2. Analysis and Results.** A nine-dimensional sensing signal in each sample was transformed by SSA and converted to eight stationary sources and one nonstationary source. The reason is the same as discussed in Section 3. Figures 8–10 show the transformation results through the SSA of tool 1 for three wear values (corresponding to the first, fifth, and tenth cutting). It can be seen that the time sequence diagram of the nonstationary source changes significantly after SSA transformation, while the changes of eight stationary sources after SSA transformation are not obvious. Therefore, we only used the signal of the nonstationary source to estimate tool wear. Here, as in Section 3, the RBF kernel was selected as the kernel function of the LS-SVR, and the hyperparameter was optimized by LOOCV.

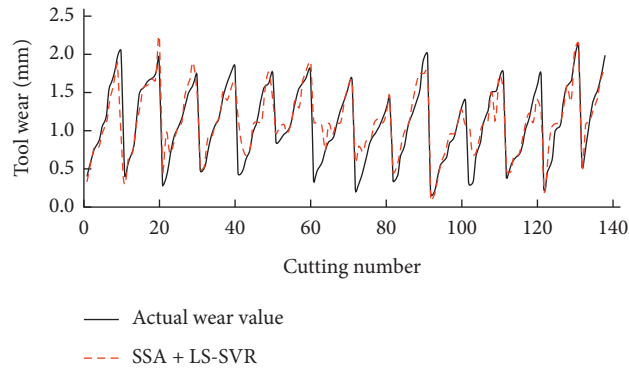


FIGURE 11: Tool wear estimation result with the proposed method.

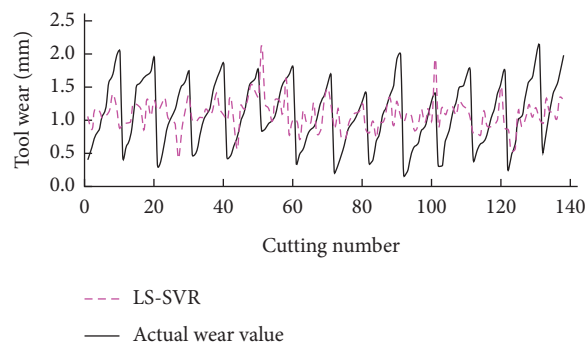


FIGURE 12: Tool wear estimation result with the LS-SVR method.

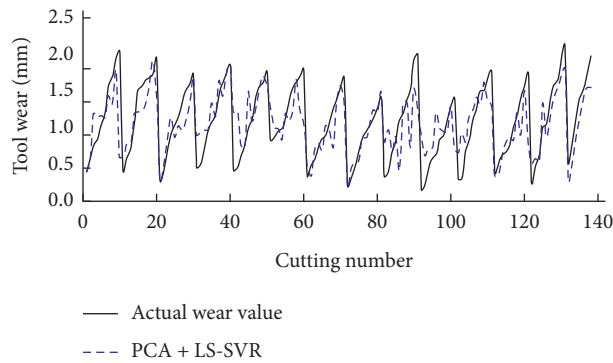


FIGURE 13: Tool wear estimation result with the PCA + LS-SVR method.

TABLE 5: Estimation error of three methods in the experiment.

	LS-SVM	PCA + LS-SVM	SSA + LS-SVM
RMSE	0.2309	0.1094	0.0529
<i>R</i>	0.3414	0.6701	0.8938

Figures 11–13 show the tool wear estimation results of the testing set with the three methods. The estimation error between the estimated and actual values of tool wear is given in Table 5. The RMSE of the proposed SSA + LS-SVR method

was 0.0529, which is 77.1% and 51.6% less than that of the LS-SVR and PCA + LS-SVR, respectively. *R* of the proposed method was 0.8923, which is 0.55 and 0.22 higher than that of the LS-SVR and PCA + LS-SVR, respectively.



## 5. Conclusion

In order to solve the problem of low performance of traditional methods for milling tool wear estimation under small sample with less prior knowledge, a multisensor tool wear estimation method based on SSA and LS-SVR was proposed. Taking the advantage of SSA without prior information of signals and parameter presetting, the multi-dimensional signals collected by sensors were decomposed into stationary and nonstationary sources through SSA, and 10 dimensionless time-frequency statistical parameters from the nonstationary source were extracted as the input parameters of the LS-SVR to obtain the tool wear estimation model under small sample. The proposed SSA + LS-SVR method was validated on the PHM-2010 challenge milling benchmark dataset and our tool wear experiments. The results indicated that the root mean square error and correlation coefficient of the proposed method were significantly better than LS-SVR and PCA + LS-SVR on two milling TCM experiments. Furthermore, the proposed method could be improved to enhance its performance under one-dimensional signal for tool wear estimation, in which the number of subsources needs to be optimized.

## Data Availability

The datasets used and analyzed to support the findings of this study are included within the article.

## Conflicts of Interest

The authors declare that they have no conflicts of interest.

## Acknowledgments

This work was supported in part by the Zhejiang Provincial Natural Science Foundation of China (LQ21E050003), in part by the National Natural Science Foundation of China (U1909217), and in part by the Fundamental Scientific Research Project of Wenzhou (G20190013).

## References

- [1] M. Malekian, S. S. Park, and M. B. G. Jun, "Tool wear monitoring of micro-milling operations," *Journal of Materials Processing Technology*, vol. 209, no. 10, pp. 4903–4914, 2009.
- [2] J. Karandikar, T. Mcleay, S. Turner, and T. Schmitz, "Tool wear monitoring using naïve bayes classifiers," *International Journal of Advanced Manufacturing Technology*, vol. 77, no. 9-12, pp. 1613–1626, 2015.
- [3] Y. Q. Zhou and W. Xue, "Review of tool condition monitoring methods in milling processes," *International Journal of Advanced Manufacturing Technology*, vol. 96, no. 5-8, pp. 2509–2523, 2018.
- [4] Z. Huang, J. Zhu, J. Lei, X. Li, and F. Tian, "Tool wear predicting based on multi-domain feature fusion by deep convolutional neural network in milling operations," *Journal of Intelligent Manufacturing*, vol. 31, no. 4, pp. 953–966, 2020.
- [5] Y. Zhou, B. Sun, W. Sun, and Z. Lei, "Tool wear condition monitoring based on a two-layer angle kernel extreme learning machine using sound sensor for milling process," *Journal of Intelligent Manufacturing*, vol. 9, 2020.
- [6] H. Zhang, J. Zhao, F. Wang, J. Zhao, and A. Li, "Cutting forces and tool failure in high-speed milling of titanium alloy tc21 with coated carbide tools," *Proceedings of the Institution of Mechanical Engineers, Part B: Journal of Engineering Manufacture*, vol. 229, no. 1, pp. 20–27, 2015.
- [7] Q. S. Zhu, B. T. Sun, Y. Q. Zhou, W. F. Sun, and J. W. Xiang, "Sample augmentation for intelligent milling tool wear condition monitoring using numerical simulation and generative adversarial network," *IEEE Transactions on Instrumentation and Measurement*, vol. 70, Article ID 3516610, 2021.
- [8] G. Vetrichelvan, S. Sundaram, S. S. Kumaran, and P. Velmurugan, "An investigation of tool wear using acoustic emission and genetic algorithm," *Journal of Vibration and Control*, vol. 21, no. 15, pp. 3061–3066, 2014.
- [9] M. T. Mathew, P. S. Pai, and L. A. Rocha, "An effective sensor for tool wear monitoring in face milling: acoustic emission," *Sadhana*, vol. 33, no. 3, pp. 227–233, 2008.
- [10] P. Y. Sevilla-Camacho, J. B. Robles-Ocampo, and J. Muñoz-Soria, "Tool failure detection method for high-speed milling using vibration signal and reconfigurable bandpass digital filtering," *International Journal of Advanced Manufacturing Technology*, vol. 81, no. 5-8, pp. 1–8, 2015.
- [11] Y. Q. Zhou, X. F. Liu, F. P. Li, B. T. Sun, and W. Xue, "An online damage identification approach for numerical control machine tools based on data fusion using vibration signals," *Journal of Vibration and Control*, vol. 21, no. 15, pp. 2925–2936, 2015.
- [12] M. Ritou, S. Garnier, B. Furet, and J. Y. Hascoet, "Angular approach combined to mechanical model for tool breakage detection by eddy current sensors," *Mechanical Systems and Signal Processing*, vol. 44, no. 1-2, pp. 211–220, 2014.
- [13] P. Stavropoulos, A. Papacharalampopoulos, E. Vasiliadis, and G. Chryssolouris, "Tool wear predictability estimation in milling based on multi-sensorial data," *International Journal of Advanced Manufacturing Technology*, vol. 82, no. 1–4, pp. 509–521, 2016.
- [14] B. Cuka and D. W. Kim, "Fuzzy logic based tool condition monitoring for end-milling," *Robotics and Computer-Integrated Manufacturing*, vol. 47, 2017.
- [15] R. Koike, K. Ohnishi, and T. Aoyama, "A sensorless approach for tool fracture detection in milling by integrating multi-axial servo information," *CIRP Annals*, vol. 65, no. 1, pp. 385–388, 2016.
- [16] H. Liu, Z. Liu, W. Jia, X. Lin, and S. Zhang, "A novel transformer-based neural network model for tool wear estimation," *Measurement Science and Technology*, vol. 31, no. 6, Article ID 065106, 2020.
- [17] R. Zhao, D. Wang, R. Yan, K. Mao, F. Shen, and J. Wang, "Machine health monitoring using local feature-based gated recurrent unit networks," *IEEE Transactions on Industrial Electronics*, vol. 65, no. 2, pp. 1539–1548, 2018.
- [18] Y. Zhou, B. Sun, and W. Sun, "A tool condition monitoring method based on two-layer angle kernel extreme learning machine and binary differential evolution for milling," *Measurement*, vol. 166, Article ID 108186, 2020.
- [19] K. Zhu, G. Li, and Y. Zhang, "Big data oriented smart tool condition monitoring system," *IEEE Transactions on Industrial Informatics*, vol. 16, no. 6, pp. 4007–4016, 2020.
- [20] G. Krolczyk, M. Gajek, and S. Legutko, "Predicting the tool life in the dry machining of duplex stainless steel," *Eksplotacja I*

- Niezawodnosc-Maintenance and Reliability*, vol. 15, no. 1, pp. 62–65, 2013.
- [21] G. M. Krolczyk, P. Nieslony, and S. Legutko, “Determination of tool life and research wear during duplex stainless steel turning,” *Archives of Civil and Mechanical Engineering*, vol. 15, no. 2, pp. 347–354, 2015.
- [22] P. Twardowski, S. Legutko, G. Krolczyk, and S. Hloch, “Investigation of wear and tool life of coated carbide and cubic boron nitride cutting tools in high speed milling,” *Advances in Mechanical Engineering*, vol. 7, no. 6, pp. 1–9, 2015.
- [23] X.-C. Cao, B.-Q. Chen, B. Yao, and W.-P. He, “Combining translation-invariant wavelet frames and convolutional neural network for intelligent tool wear state identification,” *Computers in Industry*, vol. 106, pp. 71–84, 2019.
- [24] G. Serin, B. Sener, A. M. Ozbayoglu, and H. O. Unver, “Review of tool condition monitoring in machining and opportunities for deep learning,” *International Journal of Advanced Manufacturing Technology*, vol. 109, no. 3-4, pp. 953–974, 2020.
- [25] G. Zhi, D. He, W. Sun, Y. Zhou, X. Pan, and C. Gao, “An edge-labeling graph neural network method for tool wear condition monitoring using wear image with small samples,” *Measurement Science and Technology*, vol. 32, no. 6, Article ID 064006, 2021.
- [26] A. J. Torabi, J. E. Meng, X. Li, and B. S. Lim, “A survey on artificial intelligence-based modeling techniques for high speed milling processes,” *IEEE System Journal*, vol. 9, pp. 1069–1080, 2014.
- [27] S. Manouchehr and T. TavakoliKian, “A review on the artificial neural network approach to analysis and prediction of seismic damage in infrastructure,” *International Journal of Hydromechatronics*, vol. 2, no. 4, pp. 178–196, 2019.
- [28] M. Lamraoui, M. Thomas, and M. El Badaoui, “Cyclostationarity approach for monitoring chatter and tool wear in high speed milling,” *Mechanical Systems and Signal Processing*, vol. 44, no. 1-2, pp. 177–198, 2014.
- [29] P. von Bünau, F. C. Meinecke, F. C. Király, and K.-R. Müller, “Finding stationary subspaces in multivariate time series,” *Physical Review Letters*, vol. 103, no. 21, Article ID 214101, 2009.
- [30] M. Kawanabe, W. Samek, P. von Bünau, and F. C. Meinecke, “An information geometrical view of stationary subspace analysis,” in *Proceedings of Artificial Neural Networks and Machine Learning-ICANN 2011*, pp. 397–404, Espoo, Finland, June 2011.
- [31] A. Kumar and R. Kumar, “Adaptive artificial intelligence for automatic identification of defect in the angular contact bearing,” *Neural Computing and Applications*, vol. 29, no. 8, pp. 277–287, 2018.
- [32] L. Cui, B. Li, J. Ma, and Z. Jin, “Quantitative trend fault diagnosis of a rolling bearing based on Sparsogram and Lempel-Ziv,” *Measurement*, vol. 128, pp. 410–418, 2018.
- [33] C. Gao, W. Xue, Y. Ren, and Y. Zhou, “Numerical control machine tool fault diagnosis using hybrid stationary subspace analysis and least squares support vector machine with a single sensor,” *Applied Sciences*, vol. 7, no. 4, p. 346, 2017.
- [34] K. Huang, M. Y. You, Y. X. Ye, B. Jiang, and A. N. Lu, “Direction of arrival based on the multioutput least squares support vector regression model,” *Mathematical Problems in Engineering*, vol. 2010, Article ID 8601376, 8 pages, 2020.
- [35] X. Liu, A. Ouyang, and Z. Yun, “Fuzzy weighted least squares support vector regression with data reduction for nonlinear system modeling,” *Mathematical Problems in Engineering*, vol. 2018, Article ID 7387650, 13 pages, 2018.
- [36] A. Kumar and R. Kumar, “Least square fitting for adaptive wavelet generation and automatic prediction of defect size in the bearing using levenberg-marquardt backpropagation,” *Journal of Nondestructive Evaluation*, vol. 36, no. 1, p. 7, 2017.
- [37] B. R. Murlidhar, R. K. Sinha, E. T. Mohamad, R. Sonkar, and M. Khorami, “The effects of particle swarm optimisation and genetic algorithm on ANN results in predicting pile bearing capacity,” *International Journal of Hydromechatronics*, vol. 3, no. 1, pp. 69–87, 2020.
- [38] The Prognostics and Health Management Society, “Conference data challenge,” 2010, <https://www.phmsociety.org/competition/phm/10>.
- [39] T. Benkedjouh, N. Zerhouni, and S. Rechak, “Tool wear condition monitoring based on continuous wavelet transform and blind source separation,” *The International Journal of Advanced Manufacturing Technology*, vol. 97, no. 9–12, pp. 3311–3323, 2018.

## Research Article

# An Improved Tool Wear Monitoring Method Using Local Image and Fractal Dimension of Workpiece

Haicheng Yu,<sup>1</sup> Kun Wang ,<sup>2,3</sup> Ruhai Zhang,<sup>1</sup> Xiaojun Wu,<sup>1</sup> Yulin Tong,<sup>1</sup> Ruiyuan Wang,<sup>1</sup> and Dedao He<sup>4</sup>

<sup>1</sup>Xingji Electrical Appliances Co., Ltd., Wenzhou 325021, China

<sup>2</sup>Zhejiang Industry and Trade Vocational College, Wenzhou 325002, China

<sup>3</sup>Hefei Institute of Physical Science, Chinese Academy of Sciences, Hefei 230031, China

<sup>4</sup>Ruiming Industrial Co., Ltd., Wenzhou 325205, China

Correspondence should be addressed to Kun Wang; wangkunccc@163.com

Received 14 March 2021; Revised 7 May 2021; Accepted 18 May 2021; Published 15 June 2021

Academic Editor: Anil Kumar

Copyright © 2021 Haicheng Yu et al. This is an open access article distributed under the Creative Commons Attribution License, which permits unrestricted use, distribution, and reproduction in any medium, provided the original work is properly cited.

Tool wear is a key factor that dominates the surface quality and distinctly influences the generated workpiece surface texture. In order to realize accurate evaluation of the tool wear from the generated workpiece surface after machining process, a new tool wear monitoring method is developed by fractal dimension of the acquired workpiece surface digital image. A self-made simple apparatus is employed to capture the local digital images around the region of interest. In addition, a skew correction method based on local fast Fourier transformation energy is also proposed for the surface texture direction adjustment. Furthermore, the tool wear quantitative evaluation was derived based on fractal dimension utilizing its high reliability for inherent irregularity description. The proposed tool wear monitoring method has verified its feasibility as well as its effectiveness in actual milling experiments using the material of AISI 1045 in a vertical machining center. Testing results demonstrate that the proposed method was capable of tool wear condition evaluation.

## 1. Introduction

Machining tool is a major component in a manufacturing system, and its failure (tool wear and breakage) attributes up to 20% of the machine downtime [1], and the costs of tools and tool changes account for 3–12% of the total processing cost [2]. Therefore, machining tool reliability becomes a crucial important aspect in ubiquitous manufacturing which directly influences the energy consumption and production rate [3]. Conventional tool replacement strategies employ uniform time periods determined by the subjective experience of operators. But such experiential strategies will inevitably result in early replacement which leads to that only 50–80% of the tool effective life is used [4]. To enhance the manufacturing system reliability, many strategies are proposed for the machining tool condition monitoring. With ubiquitous computing, tool wear real-time monitoring emerges as a heated research area.

Tool wear is considered to be a key factor that dominates the surface quality and also a critical index to fulfill the accuracy requirements during the machining process [5]. Tool wear monitoring or estimating is usually divided into direct monitoring and indirect monitoring [6]. Direct sensing techniques of a tool wear by using microscope or charged-couple-device (CCD) camera is a traditional vision-based tool wear measurement method [7]. But this method has to stop machine and remove the tool from holder. So, it prolongs the tact time and increases the production costs. On the contrary, many tool indirect monitoring methods are proposed by modern sensors. Indirect methods are advantageous because they do not directly affect the machining process and offer high recognition accuracy under ideal conditions.

Due to its manufacturing costs advantage and real-time monitoring, indirect tool wear detection attracts the attention of many scholars. Vibration signal is the most widely



used method for machinery condition monitoring and fault detection [8–10]. Besides, machine learning techniques also identified a promising option in various engineering application scenarios [11–13]. Recently, advances in sensing technology have led to proposals for tool condition monitoring using various signals, such as temperature, acoustic emission, cutting force, and sound. Kovac et al. developed a novel method for predicting functional lifetime in tool parts based on a tool-work thermocouple temperature with tool wear experiment [14]. Wang et al. proposed a nondestructive tool wear evaluation method by clustering energy of acoustic emission (AE) burst signals under minimal quantity lubrication cutting condition [15]. Kong et al. presented a real-time tool wear predictive model (cutting force signal) based on the integrated radial basic function-based kernel principal component analysis (KPCA\_IRBF) and relevance vector machine (RVM) and verified by two different cutting experiments [16]. Ravikumar and Ramachandran performed a tool wear monitoring system using sound signals acquired during milling of aluminum alloys [17]. Due to the interference of processing conditions and limited sensing physical characteristics, multiple modalities of sensors are instrumented to measure the different aspects of tool conditions. Wang et al. presented a virtual tool wear sensing technique based on multisensory data fusion and artificial intelligence model for tool condition monitoring [18]. Rizal et al. proposed a novel approach for tool wear classification and detection in milling process using multisensor signals and Mahalanobis-Taguchi system (MTS) [19]. However, these indirect methods present a significant drawback: all these signals could be seriously affected by the inherent noise generated in industrial environments [20–23], which reduces their performance.

Milling is the process of machining using rotary cutters to remove material by advancing a cutter into a workpiece. Highly efficient milling processes are suitable for mass production and have been widely used in manufacturing. Compared with turning machines, it is difficult for measuring rotating tools wear with multiple moving axes in milling. According to related researches [24], a reliable tool condition monitoring (TCM) can largely reduce the manufacturing costs by 10–40% by reducing downtime and maximizing the usable life of milling tools.

Machined surface topographies are the final product after manufacturing and could probably be the carriers for fabrication process and functional information. Compared with conventional direct and indirect tool wear evaluation method, machined surface topographies evaluation can be performed without the need to stop the cutting process and also enjoys the merit of free noise interference. Different machined surface defects after machining with the worn tools are investigated in the previous literatures and directly affect the subsequent mechanical properties of the manufacturing components. Machining parameters, tool type, and geometry as well as workpiece properties are among the most influential parameters in the tool wear process [25]. A higher level of surface damage was generated on machined surface under condition of worn tools than new cutting tools without considering other cutting

conditions. Literature found that, apart from the cutting conditions (the cutting speed, the feed rate, and the depth of cut), tool wear has primary effects on the modification of surface roughness and has drawn the attention of many researchers [26]. However, some studies obtained the opposite results when evaluating the tool wear by surface roughness. Li et al.'s study results showed that tool wear had distinct deterioration influence on the surface roughness [27]. However, in [28], authors found that the surface roughness firstly increased and then declined when flank wear varied from 0 to 0.3 mm. Therefore, a tool wear evaluation method based on a more reliable surface topography statistical indicator is indispensable.

Inspired by these different topography parameters tool wear condition monitoring methods, a new tool wear evaluation method is developed by fractal dimension from the acquired workpiece surface digital image. In this research, local digital images are acquired by a self-made simple apparatus. A skew correction method based on local fast Fourier transformation (FFT) energy is also proposed for the surface texture direction adjustment. The tool wear quantitative evaluation was derived based on fractal dimension from the skew corrected digital image because of its high reliability for inherent irregularity description.

The rest of the paper is organized as follows: the tool wear monitoring framework is briefly described in Section 2. The experiment studies are presented in Section 3, as well as the model calibration. The application examples of the developed method are explained in detail in Section 4. Some concluding remarks are given in Section 5.

## 2. Tool Wear Monitoring Framework

*2.1. The Proposed Tool Wear Evaluation Method.* This research proposed a new tool wear monitoring method by fractal dimension from the acquired workpiece surface digital image. The flow chart of the proposed method is presented in Figure 1. Relevant details are also described below.

Step 1: place the self-made image acquisition system (described in Section 3.1.2) on a machined workpiece surface to capture the local surface images. Meanwhile, the cutting tool is taken off to evaluate the tool wear by traditional direct tool wear method (described in Section 3.1.4).

Step 2: correct the texture skew of the raw image with the proposed skew correction algorithm in Section 2.2.

Step 3: in this step, the estimating contour is determined by the similar criterion in [29]. Then, the extracted contour curve fractal dimension is calculated (described in Section 2.2). Finally, a regression model is fitted according to the fractal dimensions and the acquired tool wear based on traditional direct tool wear method (Section 3.3).

*2.2. Skew Correction Algorithm.* Hough transform, projection characteristics, Fourier transform, and shearlet transform are the commonly used algorithms for skew correction

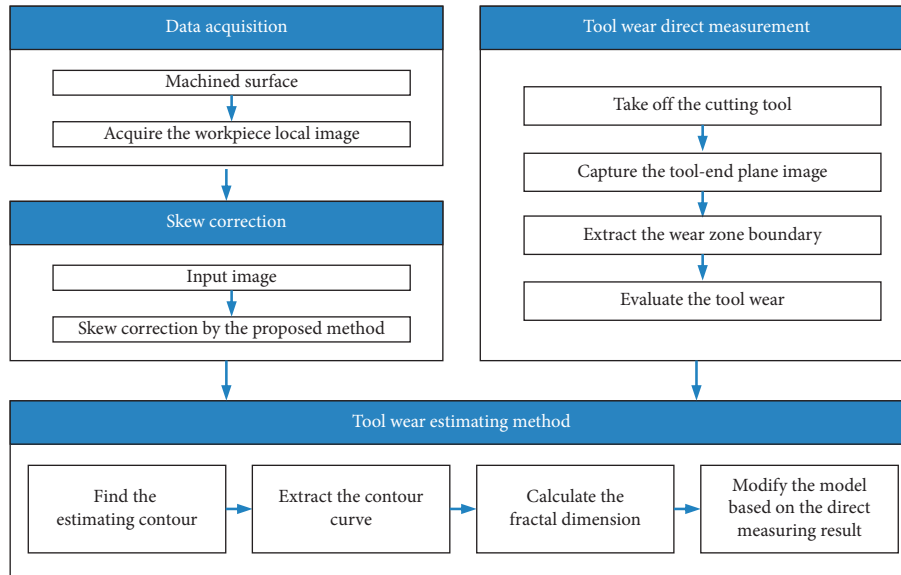


FIGURE 1: Flow chart of the proposed tool wear monitoring method.

[30–33]. Those skew detection and correction algorithms are mainly aiming at detecting the deviation of the document orientation angle from the horizontal or vertical direction. In this research, the investigated subject has a focus on the machined surface. Prior research shows that two-dimensional signal may contain strong noises in the whole frequency domain [34–36]. Therefore, a new skew correction algorithm is necessary.

**2.2.1. Local Energy of the FFT.** Figure 2 is a striped image with noise interference where  $\lambda$  is the dominant wavelength,  $\lambda_u$  and  $\lambda_v$  are the wavelength components in  $x$  and  $y$  directions, respectively.  $u = 1/\lambda_u$  and  $v = 1/\lambda_v$  are the sampling rates in the two directions, and they are also the period components of the FFT spectrum  $F(u, v)$ . As can be seen in Figure 2, acquired surface image contains strong noises in the whole frequency domain. Therefore, the general used Fourier transform in document scanning is not suitable in this research. Notice that the wavelength of main direction ((a) in Figure 2) is slightly different from the  $x$  and  $y$  directions ((b) and (c) in Figure 2); it could be possible to correct the skewed images by local FFT energy distribution. Define the local FFT energy as the energy in  $x$  positive half axis of Fourier spectrum  $F(u, v)$ . According to this definition, if the local energy reaches its maximum, the images should be well skewed.

**2.2.2. Skew Correction Algorithm.** In this paper, a novel skew correction algorithm based on local 2D FFT energy is proposed to improve the skew correction accuracy. Flow chart of the proposed method is presented in Figure 3 and illustrated in the following steps:

Step 1: input the original image.

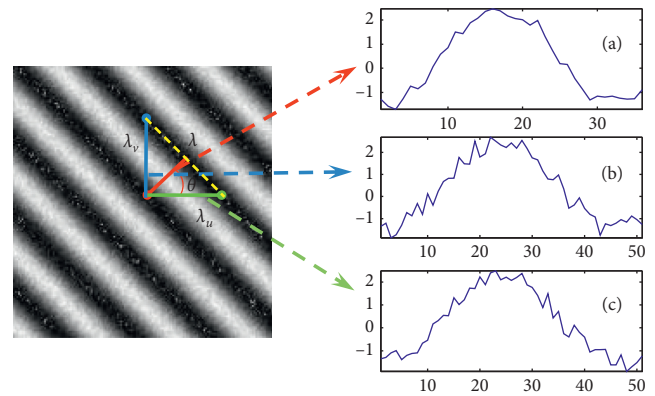


FIGURE 2: Illustration for the parameters of the 2D FFT.

- Step 2: use FFT to acquire the Fourier spectrum  $F(u, v)$ .
- Step 3: calculate the local energy  $L_i$  from the Fourier spectrum.
- Step 4: rotate the image counterclockwise with  $1^\circ$  and go to Step 2 until the rotate degree reach  $360^\circ$ .
- Step 5: output the image which has the maximum energy  $L_i$ .

A typical captured image is shown in Figure 4(a). It can be seen that the original image has an obvious skew. This skew will strongly influence the tool wear evaluation. The local FFT energy distribution is shown in Figure 4(c) where horizon axis indicates the rotation angle and vertical axis indicates the corresponding local FFT energy. Figure 4(c) shows that the local FFT energy reaches its maximum when the rotation angle is  $22^\circ$ . Rotate the image with  $20^\circ$ ; the rotated image is shown in Figure 4(b). The adjusted image result shows that the proposed method has good skew correction ability.

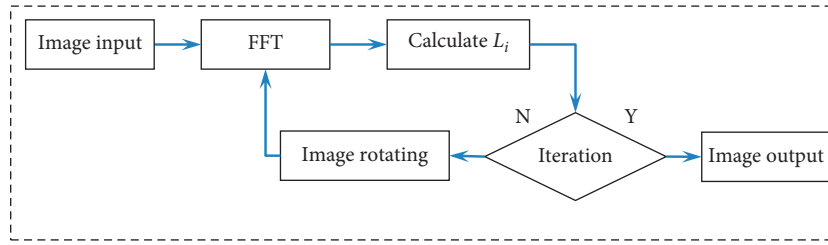


FIGURE 3: Proposed skew correction algorithm.

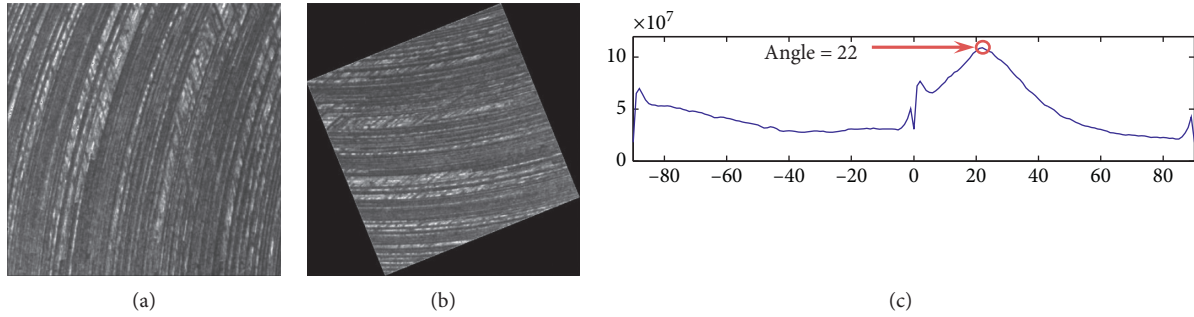


FIGURE 4: Image skew correction. (a) Original image, (b) skewed image, and (c) local energy distribution.

**2.3. Fractal Dimension.** Many surface topography parameters have been widely employed for the purpose of evaluating the tool wear from the generated workpiece. In this research, authors utilized fractal dimension as the tool wear evaluation metric.

Multifractal analysis, which is a natural extension of the fractal modeling, has aroused more attention and is applied to characterize various physical phenomena in recent years. Each geometric entity can be interpreted as a specific sort of point group. The distribution of different points on the 2D projection indicates different intrinsic structural topology. Generally, the distributions of 2D point group can be categorized into three types: even distribution, random distribution, and collectively distribution.

Fractal dimension is reported as an effective tool for describing the inherent irregularity of natural objects, as well as the point group holistic morphological characteristics [37]. The value of the fractal dimension reflects the filling ability of the point group; it is greater than the topology dimension and less than the spatial dimension [38]. The analysis of fractal patterns has aroused heated discussion during the last years, mainly in the field of empirical applications [39]. The fractal dimension could be represented by several types of dimensions, for instance, the similarity dimension, Hausdorff dimension, and box-counting dimension (BCD) [40]. Among these methods, the BCD method is the most well-accepted method to determine the fractal dimension in various application fields due to its relative simplicity and reliability [37, 41].

Mandelbrot [42] defined that a set in an Euclidean space is said to be self-similar if it is the union of  $N(r)$  distinct subsets, each of which is a copy of the original scaled down by a ratio  $1/r$  in each spatial direction. The fractal dimension of an object is defined by

$$D = \lim_{r \rightarrow 0} \frac{\log(N(r))}{\log(1/r)}, \quad (1)$$

where  $N(r)$  is the least number of boxes of length  $r$  needed to completely cover the object. Based on this definition, many different dimension types are proposed. Introduced by Gangepain and Roques-Carmes [43], BCD is found to be the most simple and reliable method for approximate fractal dimension estimation. The principle of BCD is shown in Figure 5. Using a fixed rectangle to decompose the point group, the number of filling unit element will be changed with the changing of rectangle dimension  $w$ . By counting the length of the unit element  $w$  and the filling element number  $N(w)$ , the fractal dimension can be approximately described with

$$D \approx \frac{\log(N(w))}{\log(1/w)}. \quad (2)$$

Hence, the overall procedure of the BCD method can be summarized into the following steps (as can be seen in Figure 6): (a) divide the point group by boxes under different length  $w$ , (b) compute the number  $N$  of the boxes whose number of pore pixels is bigger than 1, and (c) plot  $\log(N(w))$  vs.  $\log(1/w)$  and use the linear correlation to fit the data; the slope of the generated line denotes the BCD fractal dimension [44].

As mentioned above, fractal dimension should be bigger than the topology dimension while smaller than the spatial dimension. Therefore, for the 2D projection, the fractal dimension is greater than 1 but less than 2. The fractal dimension reflects the distribution evenness of the point group; large fractal dimension means good distribution evenness. Figure 5 shows three different point group

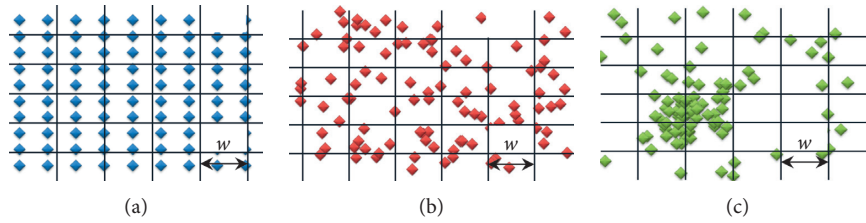


FIGURE 5: Point groups. (a) Even distribution, (b) random distribution, and (c) collective distribution.

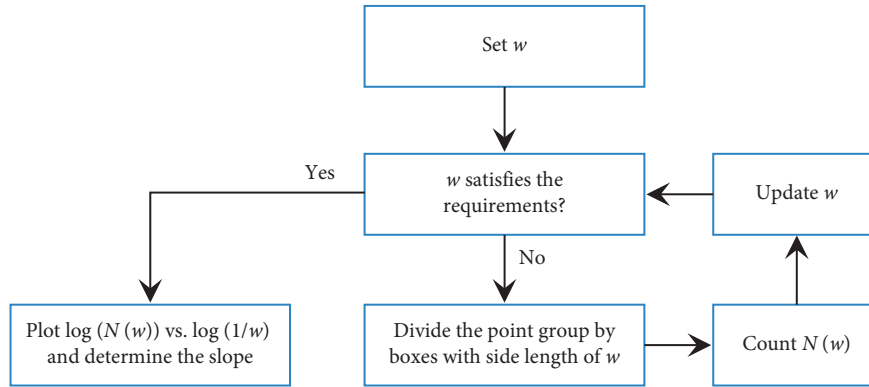


FIGURE 6: Flow chart of BCD method.

distribution situations. For the left blue rhombic point group, the fractal dimension is 2, while the fractal dimension of middle and right rhombic point groups is less than 2.

### 3. Experiment Studies

In order to investigate the proposed tool wear evaluation method, a series of AISI 1045 steel milling cutting experiments were carried out.

#### 3.1. Experiment Setup

**3.1.1. Workpiece and Cutting Tool.** The workpiece used in this test was AISI 1045 steel, rectangular block with the dimensions of 230 mm (L) × 90 mm (W) × 90 mm (H). A cemented carbide end milling cutter (the diameter is 10 mm) with three teeth is employed for the experiments.

**3.1.2. Image Acquisition.** Workpiece surface images are collected by a self-made image acquisition system; the structure sketch of the image acquisition system is shown in Figure 7. The platform is constructed of mobile phone (Xiaomi 8, produced by Xiaomi Corporation, Beijing, China), coaxial light sources (blue light, VP-24, produced by Vanch Photoelectric Technology Co., Ltd., Shanghai, China) and other auxiliary mechanism. As can be seen in Figure 7, coaxial light has a semireflective mirror to align the light from the LED array to the same optical axis as the camera lens. Mirror surface workpieces are uniformly illuminated without unevenness. Focal length regulator is used to adjust the focal length. Focal length regulator is used to ensure the unity of focusing distance of different photos. After

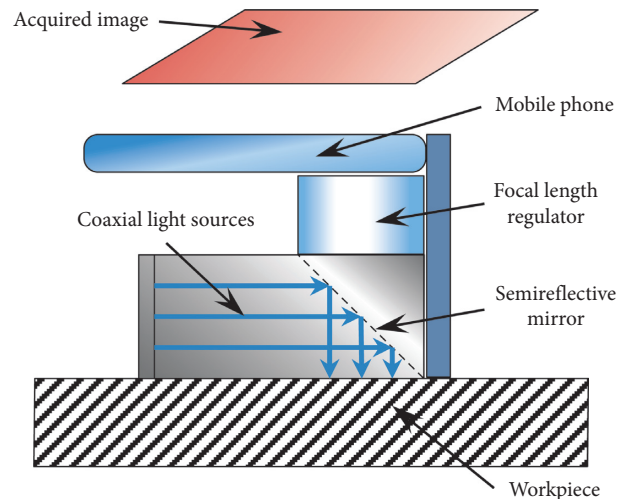


FIGURE 7: Structure sketch of the image acquisition system.

machining, the image acquisition is placed on the machined workpiece surface and captures the digital image. Details about the capture parameters are available in Table 1.

**3.1.3. Experimental Parameters.** The milling cutting experiments are conducted on a vertical machining center (DMTG VDL850A, produced by General technology group Dalian Machine Tool Co., Dalian, China). The experimental setup for the milling test is shown in Figure 8. The machining parameters for the milling tests are selected as spindle speed of 2000 rpm, feed rate of 600 mm/min, cutting depth of 0.5 mm, and cutting width of 8 mm.



TABLE 1: Capture parameters.

Property	Information
Exposure time	1/250 s
Sensor sensitivity (ISO)	400
Equivalent focal length	12 mm
White balance	3200

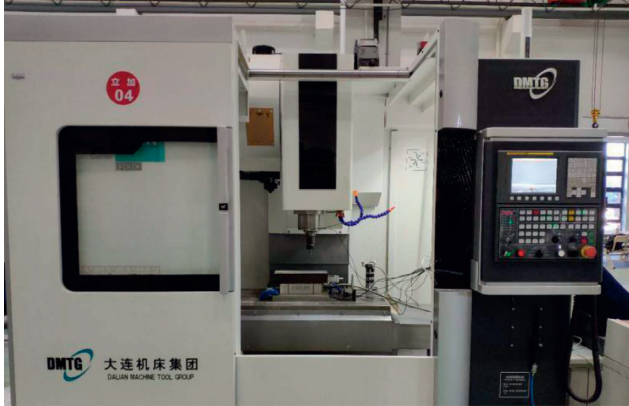


FIGURE 8: Vertical machining center.

**3.1.4. Direct Wear Area Evaluation Instrument.** In this experiment, the milling process is multitooth machining and each tooth is independent of each other. The corresponding average wear area is measured by an electron measuring microscope via direct measurement method (GP-300C, produced by Gaopin precision instruments Co., Ltd., Kunshan, China, as shown in Figure 9).

**3.2. Evaluation Metrics.** To quantitatively evaluate the performance of the developed method, different metrics are investigated including standard deviation, variance, skewness, kurtosis, roughness, and fractal dimension.

Skewness is typically used to measure the asymmetry of the probability distribution of a random variable. If skewness  $S < 0$ , there is a negative skew which means the mass of the distribution is concentrated on the right of the distribution figure. If  $S > 0$ , there is a positive skew which means the mass of the distribution is concentrated on the left of the distribution figure. The distribution is similar to a Gaussian normal distribution when  $S = 0$ .

Kurtosis is a measure of whether the data are heavy-tailed or light-tailed relative to a Gaussian normal distribution. Data sets with high kurtosis tend to have heavy tails, or outliers. Data sets with low kurtosis tend to have light tails, or lack of outliers.

Surface roughness is a typical parameter which refers to the amplitude information and high frequency irregularities. There are many different roughness parameters in practice, but Ra (the arithmetical mean of the deviations) is by far the most commonly used one. Ra is defined as

$$Ra = \frac{1}{L} \int_0^L |z| dl, \quad (3)$$



FIGURE 9: Direct tool wear detection.

where  $L$  is the length and  $z$  denotes the height. According to this definition, the surface roughness can quantify the deviations in the direction of the normal vector of a real surface from its ideal form [39].

### 3.3. Model Calibration

**3.3.1. Tool Wear Evaluation by Direct Method.** Some microscopic images of the employed tool are shown in Figure 10. After tool wear calculation from the acquired images, the tool wear progression with different processing layers is shown in Table 2 (direction measurement method). It has been found that the tool wear area deteriorates with the increase of processing time. According to Table 3, the tool wear process can be obviously divided into two stages, the stable wear stage and the sharp wear stage. In the stable wear stage, the mean tool wear area gradually increases from  $0.023 \text{ mm}^2$  to  $0.088 \text{ mm}^2$ . In the sharp wear stage, the mean tool wear area rapidly deteriorates from  $0.088 \text{ mm}^2$  to  $0.529 \text{ mm}^2$ .

**3.3.2. Tool Wear Evaluation by Different Metrics.** Surface images were collected from the milled AISI 1045 steel workpiece surface via the self-made image acquisition system. In the experiment, 3 images were acquired for each layer. Some typical samples of images are displayed in Figure 11. As can be seen in Figure 11, the image texture becomes blurred with the worsening of tool wear. Therefore, we can further explore the relationship between tool wear and surface image texture by appropriate statistics.

In this research, various metrics (standard deviation, variance, skewness, kurtosis, and fractal dimension) are investigated according to the acquired workpiece local images. According to the instruction of ISO 4288, the workpiece shall be properly positioned so that the direction of the section corresponds to the maximum value of the roughness. Therefore, in this research, metrics are calculated along the red dashed lines in Figure 11. Besides, a mobile roughness measuring device (type: MarSurf PS10 (produced by Mahr (Gottingen, Germany)), Figure 12) is engaged to measure the machined surface roughness by averaging the roughness values of repeated measurements. The roughness

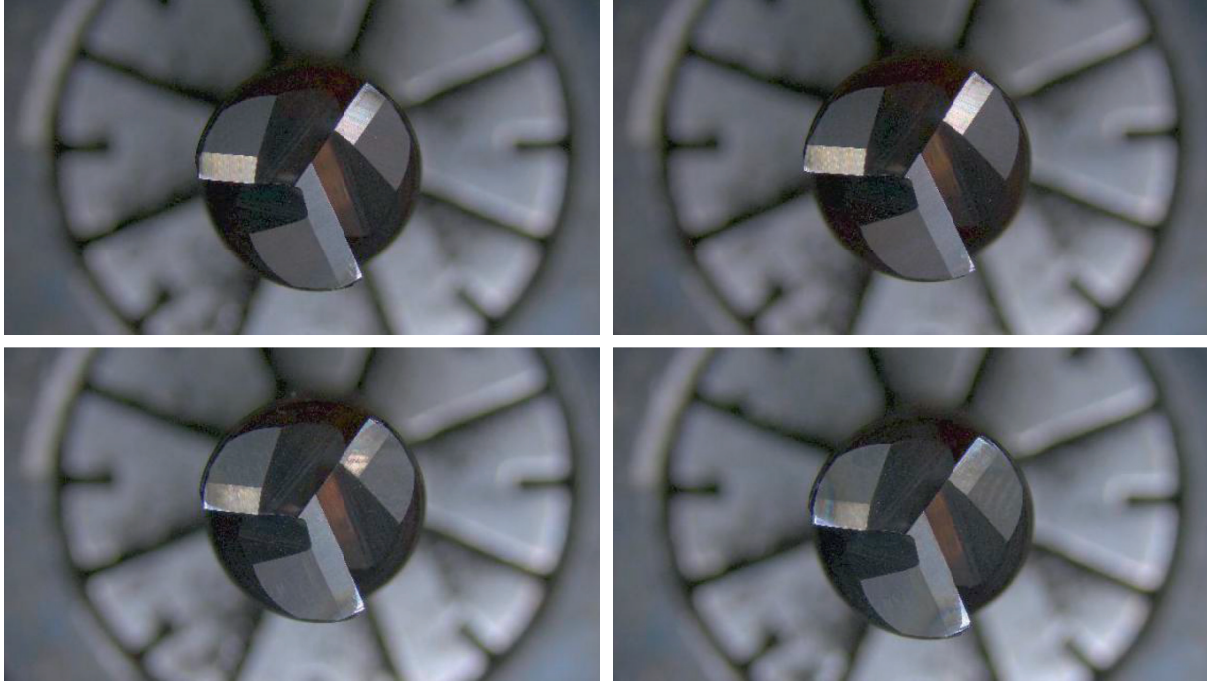


FIGURE 10: Acquired microscopic images.

TABLE 2: Tool wear areas.

Processing layer	Tooth 1# wear area	Tooth 2# wear area	Tooth 3# wear area	Mean wear area
1	0.0266	0.0192	0.0237	0.023167
2	0.0533	0.0577	0.0533	0.054767
3	0.1109	0.0695	0.0843	0.088233
4	0.1598	0.1169	0.4423	0.239667
5	0.2604	0.3417	0.5044	0.368833
6	0.716	0.3698	0.5	0.5286

TABLE 3: Experimental parameters and results.

No.	1	2	3
Spindle speed	1600 rpm	1600 rpm	1600 rpm
Feed speed	400 mm/min	500 mm/min	600 mm/min
Cutting depth	0.5 mm	0.7 mm	0.9 mm
Cutting width	8 mm	8 mm	8 mm
Evaluation layer	2	4	1
Fractal dimension	0.3374	0.3520	0.0286
Tool wear area (proposed method)	0.0234	0.1499	0.0217
Tool wear area (direct method)	0.019	0.148	0.019
Error	23.16%	1.28%	14.21%

Ra during different processing layers is shown in Table 4. According to the recorded table, the new tool produces a large roughness and decreases soon. However, with further deterioration of tool wear, the corresponding surface roughness also increases.

Figure 13 shows all the metrics change in different processing layers. As can be seen in the figure, there is no obvious correlation between all statistical parameters and the number of cutting layers. It looks more like a random

walk. To measure their similarity quantitatively, authors use the following correlation coefficient:

$$\text{Corr}\langle M_i, w_a \rangle = \frac{\sum(M_i - \overline{M}_i)(w_a - \overline{w}_a)}{\sqrt{\sum(M_i - \overline{M}_i)^2 \sum(w_a - \overline{w}_a)^2}} \quad (4)$$

where  $M_i$  is the  $i$ -th evaluation metric and  $w_a$  is the tool wear area.

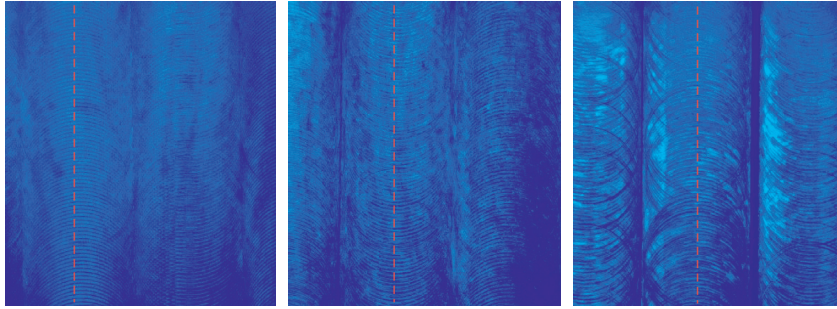


FIGURE 11: Typical samples of acquired images.



FIGURE 12: Typical samples of acquired images.

TABLE 4: Capture parameters.

Processing layer	Ra 1#	Ra 2#	Ra 3#	Mean Ra
1	5.031	4.761	5.634	5.142
2	2.217	2.359	1.962	2.179333
3	2.467	2.795	2.464	2.575333
4	2.882	2.293	1.838	2.337667
5	3.314	4.014	4.481	3.936333
6	5.097	5.139	5.169	5.135

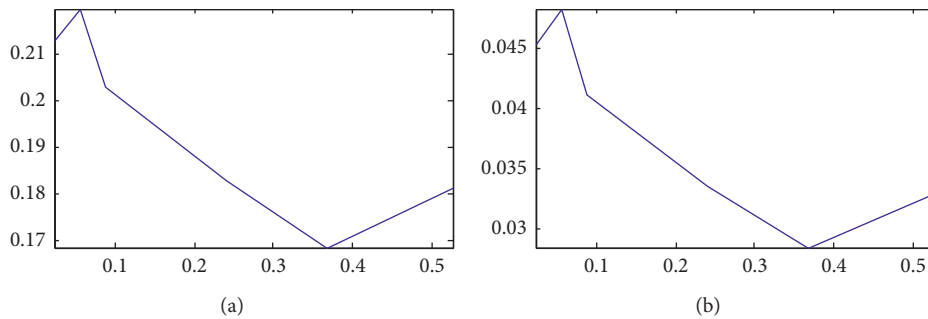


FIGURE 13: Continued.



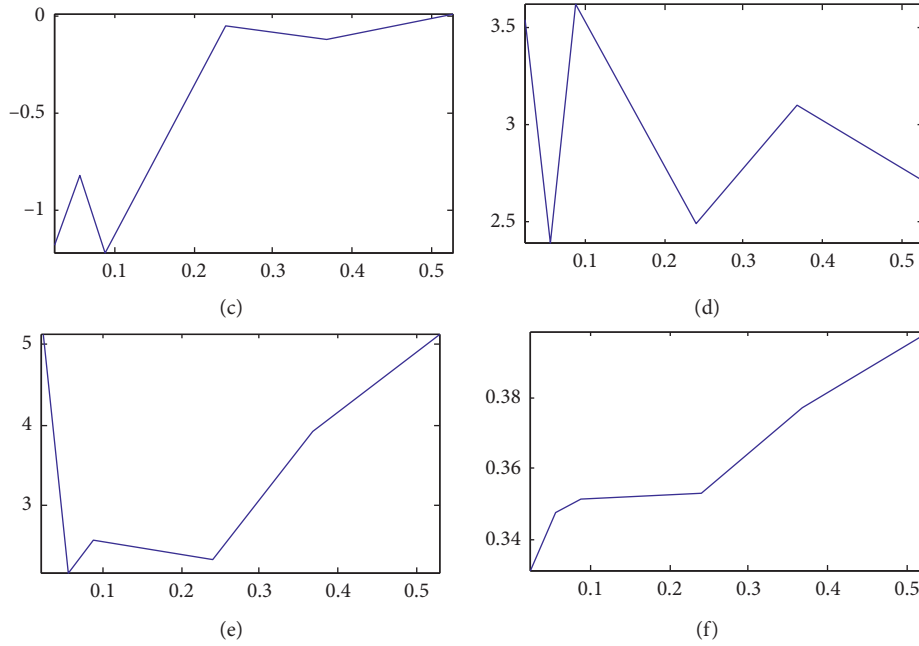


FIGURE 13: Metrics change in different processing layer: (a) standard deviation, (b) variance, (c) skewness, (d) kurtosis, (e) roughness, and (f) fractal dimension.

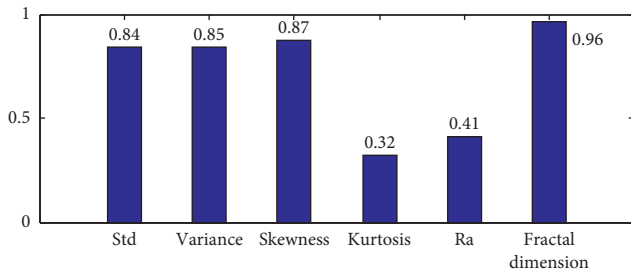


FIGURE 14: Correlation coefficients.

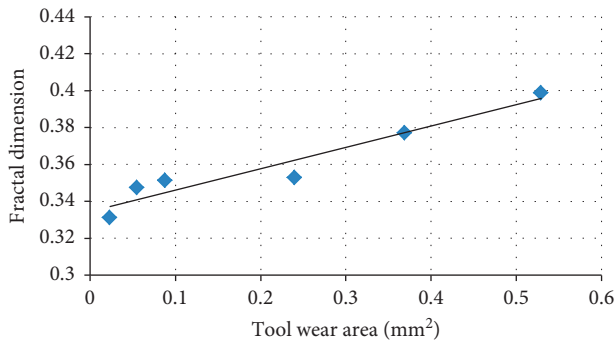


FIGURE 15: Fractal dimension change during the milling.

The correlation coefficients between the metrics and the measured tool wear areas are listed in Figure 14. It is inferred from Figure 14 that the fractal dimension strongly correlated to the tool wear area and their correlation coefficient is as high as 0.96. Based on the results, it is consolidated to conclude that fractal dimension is an effective utensil to evaluate the tool wear area.

**3.3.3. Model Calibration.** As presented before, tool wear area is strongly related to the fractal dimension of workpiece local image and exhibit proportional relation. Applying linear fitting to the fractal dimension (shown in Figure 15, where  $x$  axis indicates the corresponding fractal dimension and  $y$  axis indicates the tool wear area), the  $R$  square is 0.9247 with root mean squared error (RMSE) of 0.007394, which means the linear fitting is highly significant. The fitting linear equation can be represented as

$$F_d = 0.1154w_a + 0.3347, \quad (5)$$

where  $w_a$  is the tool wear area and  $F_d$  is the fractal dimension.

As can be seen in Figure 15, it can be concluded that tool wear areas are highly proportional to fractal dimensions. As a consequence, linear fitting can efficiently reveal the relationship between tool wear area and fractal dimension, which also demonstrates that tool wear can be accurately evaluated by fractal dimension of workpiece local image.

#### 4. Validation Experiments of the Developed Method

To make a quantitative analysis of the results, the measurements collected using the calibrated model are compared to those from conventional direct tool wear evaluation method in this section. The performance of the developed method was tested on 3 different milling experiments. According to the results, the values of these indicators are highly consistent with those measured via direct method. Considering the results from the direct method as the theoretical value of tool wear, the relative errors were calculated to be 23.16%, 1.28%, and 14.21% respectively. As can

be seen in Table 3, the proposed method offers exciting opportunities for tool wear evaluation. However, uncertainty still remains during the validation experiment, and relative error is reported as 23.16% in the first experiment and is worth further mechanistic research.

## 5. Conclusion

This paper developed a new tool wear monitoring method by fractal dimension from the acquired workpiece surface digital image. In this research, a self-made simple apparatus is employed to capture the local digital images. Then, a skew correction method based on local FFT energy is also proposed for the surface texture direction adjustment. Finally, tool wear situations are accurately evaluated by fractal dimension of workpiece local image. An actual milling experiment is performed in a vertical machining center to verify the proposed method. Testing results demonstrate the proposed method has achieved high-precision tool wear estimation. The major findings of this work can be summarized as follows:

- (1) A novel tool wear monitoring method is proposed in this research where surface texture information is employed for the tool wear estimation. Compared with conventional methods, the proposed method can be performed without the need to stop the cutting process and also enjoys the merit of free noise interference.
- (2) A skew correction method based on local FFT energy is also proposed for the surface texture direction adjustment. The test result shows that the proposed algorithm can effectively correct the skew in strong noises.
- (3) Fractal dimension is firstly utilized for the tool wear estimation. Compared with other various metrics, fractal dimension strongly correlated to the tool wear area. The result demonstrates that tool wear can be accurately evaluated by fractal dimension of workpiece local image.

The research demonstrated that workpiece surface texture contains much tool geometrical information which can be utilized to extract the toll wear information based on the surface digital information. However, the authors believed that machined surface topographies carry far more fabrication processes and functional information and are worth further explorations.

## Data Availability

The data used to support the findings of this study are included within the article.

## Conflicts of Interest

The authors declare that they have no conflicts of interest.

## Acknowledgments

This work was financially supported by Wenzhou Municipal Major Scientific and Technological Innovation Project (no. ZG2020023).

## References

- [1] L. Fernández-Robles, G. Azzopardi, E. Alegre, N. Petkov, and M. Castejón-Limas, "Identification of milling inserts in situ based on a versatile machine vision system," *Journal of Manufacturing Systems*, vol. 45, pp. 48–57, 2017.
- [2] Y. Zhou and W. Xue, "Review of tool condition monitoring methods in milling processes," *The International Journal of Advanced Manufacturing Technology*, vol. 96, no. 5-8, pp. 2509–2523, 2018.
- [3] Z. Lei, Y. Zhou, B. Sun, and W. Sun, "An intrinsic timescale decomposition-based kernel extreme learning machine method to detect tool wear conditions in the milling process," *The International Journal of Advanced Manufacturing Technology*, vol. 106, pp. 12032–21212, 2020.
- [4] K. Salonitis and A. Kolios, "Reliability assessment of cutting tool life based on surrogate approximation methods," *The International Journal of Advanced Manufacturing Technology*, vol. 71, no. 5-8, pp. 1197–1208, 2014.
- [5] Y. Zhou, B. Sun, W. Sun, and Z. Lei, "Tool wear condition monitoring based on a two-layer angle kernel extreme learning machine using sound sensor for milling process," *Journal of Intelligent Manufacturing*, in Press, 2020.
- [6] M. Nouri, B. K. Fussell, B. L. Ziniti, and E. Linder, "Real-time tool wear monitoring in milling using a cutting condition independent method," *International Journal of Machine Tools and Manufacture*, vol. 89, pp. 1–13, 2015.
- [7] J. Wang, Y. Zheng, P. Wang, and R. X. Gao, "A virtual sensing based augmented particle filter for tool condition prognosis," *Journal of Manufacturing Processes*, vol. 28, no. 3, pp. 472–478, 2017.
- [8] W. Sun, Y. Zhou, J. Xiang, B. Chen, and W. Feng, "Hankel matrix-based condition monitoring of rolling element bearings: an enhanced framework for time-series analysis," *IEEE Transactions on Instrumentation and Measurement*, vol. 70, Article ID 3512310, 2021.
- [9] W. Sun, Y. Zhou, X. Cao, B. Chen, W. Feng, and L. Chen, "A two-stage method for bearing fault detection using graph similarity evaluation," *Measurement*, vol. 165, Article ID 108138, 2020.
- [10] A. Kumar, Y. Zhou, C. P. Gandhi, R. Kumar, and J. Xiang, "Bearing defect size assessment using wavelet transform based Deep Convolutional Neural Network (DCNN)," *Alexandria Engineering Journal*, vol. 59, no. 2, pp. 999–1012, 2020.
- [11] A. Kumar, C. P. Gandhi, Y. Zhou, G. Vashishtha, R. Kumar, and J. Xiang, "Improved CNN for the diagnosis of engine defects of 2-wheeler vehicle using wavelet synchro-squeezed transform (WSST)," *Knowledge-Based Systems*, vol. 285, Article ID 106453, 2020.
- [12] A. Kumar and R. Kumar, "Least square fitting for adaptive wavelet generation and automatic prediction of defect size in the bearing using levenberg-marquardt backpropagation," *Journal of Nondestructive Evaluation*, vol. 36, Article ID 7, 2017.
- [13] G. Vashishtha and R. Kumar, "An effective health indicator for pelton wheel using levy flight mutated genetic," *Algorithm" Measurement Science and Technology*, in Press, 2021.
- [14] P. Kovac, M. Gostimirovic, D. Rodic, and B. Savkovic, "Using the temperature method for the prediction of tool life in sustainable production," *Measurement*, vol. 133, pp. 320–327, 2019.
- [15] C. Wang, Z. Bao, P. Zhang, W. Ming, and M. Chen, "Tool wear evaluation under minimum quantity lubrication by

- clustering energy of acoustic emission burst signals,” *Measurement*, vol. 138, pp. 256–265, 2019.
- [16] D. Kong, Y. Chen, N. Li, C. Duan, L. Lu, and D. Chen, “Relevance vector machine for tool wear prediction,” *Mechanical Systems and Signal Processing*, vol. 127, pp. 573–594, 2019.
- [17] S. Ravikumar and K. I. Ramachandran, “Tool wear monitoring of multipoint cutting tool using sound signal features signals with machine learning techniques,” *Materials Today: Proceedings*, vol. 5, no. 11, pp. 25720–25729, 2018.
- [18] J. Wang, J. Xie, R. Zhao, L. Zhang, and L. Duan, “Multisensory fusion based virtual tool wear sensing for ubiquitous manufacturing,” *Robotics and Computer-Integrated Manufacturing*, vol. 45, pp. 47–58, 2017.
- [19] M. Rizal, J. A. Ghani, M. Z. Nuawi, and C. H. C. Haron, “Cutting tool wear classification and detection using multi-sensor signals and Mahalanobis-Taguchi System,” *Wear*, vol. 376–377, pp. 1759–1765, 2017.
- [20] J. Huang, B. Chen, Y. Li, and W. Sun, “Fractal geometry of wavelet decomposition in mechanical signature analysis,” *Measurement*, vol. 173, Article ID 108571, 2020.
- [21] B. Chen, Y. Li, X. Cao, W. Sun, and W. He, “Removal of power line interference from ECG signals using adaptive notch filters of sharp resolution,” *IEEE Access*, vol. 7, pp. 150667–150676, 2019.
- [22] A. Kumar and R. Kumar, “Adaptive artificial intelligence for automatic identification of defect in the angular contact bearing,” *Neural Computing and Applications*, vol. 29, no. 8, pp. 277–287, 2018.
- [23] G. Vashishtha, S. Chauhan, M. Singh, and R. Kumar, “Bearing defect identification by swarm decomposition considering permutation entropy measure and opposition-based slime mould algorithm,” *Measurement*, vol. 178, Article ID 109389, 2021.
- [24] A. G. Rehorn, J. Jiang, and P. E. Orban, “State-of-the-art methods and results in tool condition monitoring: a review,” *The International Journal of Advanced Manufacturing Technology*, vol. 26, no. 7–8, pp. 693–710, 2005.
- [25] M. Klatic, Z. Murat, T. Staroveski, and D. Brezak, “Tool wear monitoring in rock drilling applications using vibration signals,” *Wear*, vol. 408–409, pp. 222–227, 2018.
- [26] X. Liang, Z. Liu, and B. Wang, “State-of-the-art of surface integrity induced by tool wear effects in machining process of titanium and nickel alloys: a review,” *Measurement*, vol. 132, pp. 150–181, 2019.
- [27] M. Li, S. L. Soo, D. K. Aspinwall, D. Pearson, and W. Leahy, “Study on tool wear and workpiece surface integrity following drilling of CFRP laminates with variable feed rate strategy,” *Procedia CIRP*, vol. 71, pp. 407–412, 2018.
- [28] X. Liang and Z. Liu, “Tool wear behaviors and corresponding machined surface topography during high-speed machining of Ti-6Al-4V with fine grain tools,” *Tribology International*, vol. 121, pp. 321–332, 2018.
- [29] W. Sun, B. Yao, B. Chen et al., “Noncontact surface roughness estimation using 2D complex wavelet enhanced ResNet for intelligent evaluation of milled metal surface quality,” *Applied Sciences*, vol. 8, Article ID 381, 2020.
- [30] R. N. Verma and L. G. Malik, “Review of illumination and skew correction techniques for scanned documents,” *Procedia Computer Science*, vol. 45, pp. 322–327, 2015.
- [31] F. Zhang, Y. Zhang, X. Qu, B. Liu, and R. Zhang, “Scanned document images skew correction based on shearlet transform,” *Multi-disciplinary Trends in Artificial Intelligence*, vol. 9426, 2015.
- [32] W. Li, M. Breier, and D. Merhof, “Skew correction and line extraction in binarized printed text images,” in *Proceedings of the IEEE International Conference on Image Processing (ICIP)*, pp. 472–476, Quebec, Canada, September 2015.
- [33] M. Shafii and M. Sid-Ahmed, “Skew detection and correction based on an axes-parallel bounding box,” *International Journal on Document Analysis and Recognition (IJ DAR)*, vol. 18, no. 1, pp. 59–71, 2015.
- [34] W. Sun, X. Cao, B. Chen, Y. Zhou, Z. Shen, and J. Xiang, “A two-stage vision-based method for measuring the key parameters of ball screws,” *Precision Engineering*, vol. 66, pp. 76–86, 2020.
- [35] W. Sun and X. Cao, “Curvature enhanced bearing fault diagnosis method using 2D vibration signal,” *Journal of Mechanical Science and Technology*, vol. 34, no. 6, pp. 2257–2266, 2020.
- [36] W. Sun, N. Zeng, and Y. He, “Morphological arrhythmia automated diagnosis method using gray-level Co-occurrence matrix enhanced convolutional neural network,” *IEEE Access*, vol. 7, pp. 67123–67129, 2019.
- [37] H.-R. So, G.-B. So, and G.-G. Jin, “Enhancement of the Box-Counting Algorithm for fractal dimension estimation,” *Journal of Institute of Control, Robotics and Systems*, vol. 22, no. 9, pp. 710–715, 2016.
- [38] H. I. Tijani, N. Abdullah, A. Yuzir, and Z. Ujang, “Rheological and fractal hydrodynamics of aerobic granules,” *Bioresource Technology*, vol. 186, pp. 276–285, 2015.
- [39] K. Deng, D. Pan, X. Li, and F. Yin, “Spark testing to measure carbon content in carbon steels based on fractal box counting,” *Measurement*, vol. 133, pp. 77–80, 2019.
- [40] Y. Xu, R. Zhang, S. Ma, X. Yang, and F. Wang, “Fractal dimension of concrete meso-structure based on X-ray computed tomography,” *Powder Technol*, vol. 350, pp. 91–99, 2019.
- [41] J. Yan, Y. Sun, S. Cai, and X. Hu, “An improved box-counting method to estimate fractal dimension of images,” *Journal of Applied Analysis & Computation*, vol. 6, no. 4, pp. 1114–1125, 2016.
- [42] B. Mandelbrot, “How long is the coast of Britain? Statistical self-similarity and fractional dimension,” *Science*, vol. 156, no. 3775, pp. 636–638, 1967.
- [43] J. J. Gagnepain and C. Roques-Carmes, “Fractal approach to two-dimensional and three-dimensional surface roughness,” *Wear*, vol. 109, no. 1–4, pp. 119–126, 1986.
- [44] H. Wu, Y. Zhou, Y. Yao, and K. Wu, “Imaged based fractal characterization of micro-fracture structure in coal,” *Fuel*, vol. 239, pp. 53–62, 2019.

## Research Article

# Predictive Maintenance and Sensitivity Analysis for Equipment with Multiple Quality States

Xiao Wang <sup>1</sup>, Deyi Xu <sup>1</sup>, Na Qu <sup>1</sup>, Tianqi Liu <sup>1</sup>, Fang Qu <sup>1</sup> and Guowei Zhang <sup>2</sup>

<sup>1</sup>School of Safety Engineering, Shenyang Aerospace University, Shenyang 110136, China

<sup>2</sup>Mechanical School, Shenyang Institute of Engineering, Shenyang 110136, China

Correspondence should be addressed to Xiao Wang; 761385745@qq.com

Received 19 April 2021; Accepted 28 April 2021; Published 11 May 2021

Academic Editor: Yuqing Zhou

Copyright © 2021 Xiao Wang et al. This is an open access article distributed under the Creative Commons Attribution License, which permits unrestricted use, distribution, and reproduction in any medium, provided the original work is properly cited.

This paper discusses the predictive maintenance (PM) problem of a single equipment system. It is assumed that the equipment has deteriorating quality states as it operates, resulting in multiple yield levels represented as system observation states. We cast the equipment deterioration as discrete-state and continuous-time semi-Markov decision process (SMDP) model and solve the SMDP problem in reinforcement learning (RL) framework using the strategy-based method. In doing so, the goal is to maximize the system average reward rate (SARR) and generate the optimal maintenance strategy for given observation states. Further, the PM time is capable of being produced by a simulation method. In order to prove the advantage of our proposed method, we introduce the standard sequential preventive maintenance algorithm with unequal time interval. Our proposed method is compared with the sequential preventive maintenance algorithm in a test objective of SARR, and the results tell us that our proposed method can outperform the sequential preventive maintenance algorithm. In the end, the sensitivity analysis of some parameters on the PM time is given.

## 1. Introduction

In real production system, equipment deterioration is almost universal with use, age, and other causes. If the maintenance is not performed, eventually the failure or severe malfunction can occur. Operating the equipment in a deteriorating state often brings about higher production cost and lower product quality. Therefore, an effective maintenance policy is very essential in industrial practice. The periodic or age-based preventive maintenance strategy often leads to inadequate maintenance or over maintenance, in which over maintenance will cause unnecessary interference to production, resulting in the decreased production efficiency and increased production cost. The aim of condition-based maintenance is to see if the maintenance decision should be performed according to the current system state [1]. Nevertheless, the more valuable issue is to determine the future maintenance time in the current system state, which is called PM in this paper.

There are few theoretical and practical researches on PM in a strict sense compared with condition-based maintenance [2]. In some literature, condition-based maintenance has been classified as PM, but the true “predictive” aspect of condition-based maintenance decisions, such as anticipating and predicting the future state of the equipment, has not been reflected. There are few true PM methods that can conduct scheduled optimal future maintenance time by considering the deteriorating equipment condition. Existing methods of classifying equipment states are mainly divided into two types, operational state or failure state, and the goal of PM is only to predict the residual life [3–8]. For example, Sikorska et al. review a large number of pieces of literature related to prediction models, which are mainly utilized to predict the residual equipment life [9]. Jan et al. can evaluate the current states and predict the residual life for industrial equipment by a hidden semi-Markov model [10]. Schwendemann et al. present the prediction of residual life for bearings in grinding equipment under the premise of



taking a more global view of the optimization problem involved such as the costs and time [11].

Moreover, in real industrial systems, such as semiconductor production and precision instruments, the deteriorating equipment states are closely related to the quality levels of the products [2]. Based on the extensive industrial practice, General Motors researchers have pointed out the important potential of the correlation between operation management including maintenance decisions and product quality to improve the performance of manufacturing systems [12]. Before the equipment breaks down, the fact is that when the equipment is in a deteriorating quality state, it can still operate, but the probability of producing unqualified products is increased [13]. For a long time, the issue of maintenance and quality is considered to be two relatively independent research fields, and the scholars and industrial people have done a lot of research work in these two fields. But the research on the correlation between equipment maintenance and product quality is still a brand-new field. In existing literature and industrial practices, it is usually assumed that the product quality problems are the Bernoulli and persistent quality problems [13, 14], while the multiple yield quality problems have more realistic and general significance, so it is more worthy of much deeper research. The multiple yield quality problems refer to the fact that the product quality problems occur independently but with a stage probability level. The reason for the stage probability level is that the equipment states gradually deteriorate and have multiple quality states. For multiple yield quality problems, there needs a balance between production and maintenance, and there is no simple and direct maintenance decision. In addition, related researches on equipment maintenance often assume that the production time and the maintenance time are unit time, and strong assumptions are also made about the equipment deterioration mode [15]. The maintenance decisions based on the above assumptions are lack of realistic basis.

Therefore, we claim that it is of great significance to make maintenance decisions by taking quality inspection data into account, which is able to keep the costs down and meet the needs of industrial production management. There are relatively few studies on the factors of production, maintenance, and quality, and no effective methods have been found to find a solution in the existing literature. We attempt to solve the equipment maintenance problem in production practice. Since the deteriorating equipment states cannot be directly observed, a large amount of real-time quality inspection information can be used as the implicit information. A discrete-state continuous-time SMDP with a large number of yield stages is induced to describe the equipment deterioration process. However, it is worth noting that the production and maintenance time are random variables that follow general distributions based on realistic considerations. A strategy iteration-based RL method is put forward to guarantee the optimal strategy solution to the model. Furthermore, the future maintenance time corresponding to each observed state can be produced by a simulation method based on the fixed maintenance strategy, and the influences of the main technical parameters on the optimization goal of

the system are analyzed. And finally, the advantages of our proposed RL method for solving such a dynamic environment problem are revealed compared with the sequential preventive maintenance algorithm with unequal time interval.

## 2. Problem Description

This paper investigates deteriorating equipment that has multiple discrete states. Assume that the equipment condition can be directly reflected by the condition monitoring measures such as the yield levels. A single type of product is produced, and each processed product is immediately inspected to identify an unqualified product or a qualified product. The inspection time and inspection cost are assumed to be zero. Due to the fault of the inspection equipment or the proficiency of the inspection workers and other reasons, there are certain inspection errors in product quality inspection. The inspection errors are mainly divided into two types [16]:

- (i) Type I error: that is the false detection with a probability  $e_1$  and the cost  $C_{e1}$ . The parameter  $C_{e1}$  includes the production cost per unit product and other related costs.
- (ii) Type II error: that is the missed detection with a probability  $e_2$  and the cost  $C_{e2}$ . The parameter  $C_{e2}$  includes the production cost per unit product and other possible costs such as the costs arising from quality and safety issues which is far beyond production costs.
- (iii) In addition, through the accurate inspection, the profit of producing a qualified product is  $R_g$  and the cost of producing an unqualified product is  $R_d$ .

## 3. System Model

The sequential decision-making problem under uncertain conditions can be solved by analyzing the Markov process. A large number of researches related to this issue can be found in stochastic dynamic programming and other related literature [17–22]. However, in many of these studies, the Markov chains cannot define the characteristic of basic probability structure such as a general probability distribution of the sojourn times in each quality state. Then the problems are often described as SMDP because the SMDP represents a more realistic situation, and it is more suitable to model the deteriorating process of the equipment.

We employ a discrete-state continuous-time SMDP model to present the deteriorating process of the single equipment system, as shown in Figure 1. Since the yield level  $y_{ki}$  cannot be obtained directly, the inspection information  $s = (k, p, b)$  is used as the observed system state, in which  $k$  is the number of subcycles in each production-maintenance cycle,  $b$  is defined as the number of unqualified products, and  $p$  is defined as the number of products produced from when the equipment is last maintained or repaired. The action space is denoted as  $A(s) = \{0, 1, 2\}$ , where  $a = 0$  represents to keep the equipment operating and produce new products;

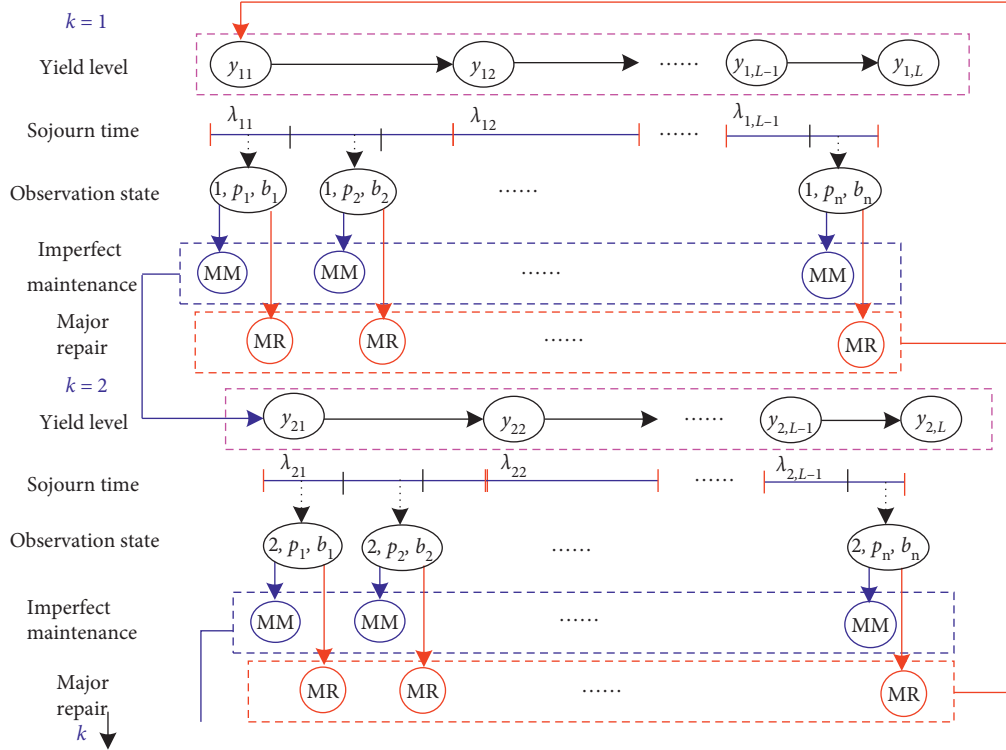


FIGURE 1: The model for SMDP.

$a = 1$  means to stop the operation of the equipment and perform an imperfect (minor) maintenance action (corresponding to the MM in Figure 1);  $a = 2$  represents the major repair action to be performed in the event of a failure or random failure of the equipment (corresponding to the MR in Figure 1). In the deteriorating process of the equipment, the decision point of the maintenance action is the time point for production and inspection of new products. By means of performing MM action, the yield level of the equipment can be restored to a certain intermediate state (e.g.,  $y_{21}$ ), after which the  $k + 1$ 'th subcycle is initiated. The subcycle continues until a certain yield level limit  $W$  appears or a stochastic malfunction occurs. At this point, the major repair is forced to be triggered to restore the yield level of the equipment to the best state (e.g.,  $y_{11}$ ), and then another updating subcycle is initiated.

In general, the equipment in a production system deteriorates as its condition is getting worse, which will lead to the result of the shorter sojourn time in each quality state. Therefore, this paper assumes that the sojourn time  $\lambda_{kl}$  under each yield level  $y_{kl}$  follows a gamma distribution  $\Gamma(\alpha_{kl}, \beta)$ , and the of  $l$  can decrease  $\lambda_{kl}$ . That is,  $\alpha_{k,l+1} = b_s \alpha_{kl}$  ( $0 < b_s < 1$ ). Meanwhile, it is assumed that the stochastic malfunction time interval also follows a gamma distribution under the  $k$ 'th subcycle, where the shape parameter in the gamma distribution  $\alpha_k = \sum_{l=1}^L \alpha_{kl}$ . Moreover, the random failure time interval also decreases gradually, which is presented by the following equation:

$$a_{k+1} = y_{k+1} a_k. \quad (1)$$

#### 4. Policy Iteration-Based PM Method

The model-free RL is divided into two algorithms, including value iteration-based algorithm and strategy iteration-based algorithm, respectively. Nevertheless, if it is used to solve SMDP problems, the value iteration-based RL algorithm is not suitable, mainly because this algorithm cannot guarantee that the average reward SMDP problems produce the optimal solution [23]. On the contrary, the strategy iteration-based RL algorithm can obtain accurate and satisfactory results. Therefore, this paper adopts the average reward strategy iteration-based RL method for finding a solution to our problem. The optimal maintenance strategy under the premise of maximizing SARR is given.

**4.1. Q-P Learning Algorithm.** The RL technology approaches the optimal strategy in the SMDP model through strategy iteration and learns the mapping from environment state to behavior through trial and error, so as to maximize the cumulative SARR  $R_t$  from the environment [23]; namely,

$$R_t = r_{t+1} + r_{t+2} + r_{t+3} + \dots = \sum_{k=1}^{\infty} r_{t+k}. \quad (2)$$

The Q-P learning algorithm can accurately solve the SMDP problems based on average cumulative rewards. In each decision cycle, the current state  $s$  is transferred to state  $s'$  under the decision  $a$ , and the updating expression is as follows [23]:

$$Q(s, a) \leftarrow (1 - \alpha)Q(s, a) + \left( r(s, a, s') - \rho t(s, a, s') + Q\left(s', \arg \max_{h \in A(s')} P(s', h)\right) \right), \quad (3)$$

where  $r(s, a, s')$  is the total immediate reward with the action  $a_j$  ( $j = 1, 2$ ) when the state  $s$  is transferred to state  $s'$ ;  $t(s, a, s')$  is the interval time with the action  $a_j$  ( $j = 1, 2$ ) when the state  $s$  is transferred to state  $s'$ ;  $\rho$  is the reward rate, which can be obtained by the following equation [24]:

$$\rho(s) = \liminf_{T \rightarrow \infty} \frac{E\left[\sum_{k=1}^T r(s_k, \pi(s_k), s_{k+1}) | s_1 = s\right]}{E\left[\sum_{k=1}^T t(s_k, \pi(s_k), s_{k+1}) | s_1 = s\right]}. \quad (4)$$

$\alpha$  is defined as the learning rate, and the decreased rules are as follows [23]:

$$\alpha = \frac{\alpha_0}{1 + u_V}, \quad (5)$$

$$u_V = \frac{V(s, a)^2}{N_{\max} + V(s, a) - 1},$$

where  $n_{\max}$  is a large positive integer;  $\alpha_0$  is the initial value of  $\alpha$ ; and  $\alpha_0 = 0.1$ . It should be noted that the value of  $\alpha_0$  will have a certain influence on the final convergence of the RL algorithm, which can be referred to [25] for details. The parameter  $V(s, a)$  is the visit-factor representing visit times. In addition, the immediate rewards  $r(s, a, s')$  caused by state transitions are as follows:

- (i)  $r(s, a, s') = R_g$  is defined as the profit of qualified product produced
- (ii)  $r(s, a, s') = -C_{e1}$  is defined as the loss of Type I error
- (iii)  $r(s, a, s') = -R_d$  is defined as the production cost per unit
- (iv)  $r(s, a, s') = -C_{e2}$  is defined as the loss of Type II error
- (v)  $r(s, a, s') = -C_R$  is defined as the loss of major repair
- (vi)  $r(s, a, s') = -C_M$  is defined as the loss of minor maintenance

The current strategy of Q-P learning algorithm is  $\pi(s) = \operatorname{argmax}_{a \in A(s)} P(s, a)$ , and the value  $Q$  is updated with

$$Q(s, a) \leftarrow (1 - \alpha)Q(s, a) + \left( r(s, a, s') - \rho t(s, a, s') + Q\left(s', \arg \max_{h \in A(s')} P(s', h)\right) \right). \quad (6)$$

Update state  $s \leftarrow s'$  and  $T_c = T_c + r(s, a, s')$ . If  $T_c \geq T_f$ , jump to Step 2 (iv); otherwise, jump to Step 2 (v); if  $a = 1$ , the imperfect maintenance is performed, and the new observation state and immediate reward are obtained. Then the action value  $Q$  is updated,  $k = k + 1$ , and the program jumps to the Step 2 (v).

- (iv) When the major repair is performed, the corresponding immediate reward and state transition

the value  $P$ . The processes of strategy evaluation and strategy improvement are executed repeatedly, and finally, the optimal maintenance strategy is obtained, which mainly includes three essential steps: exploration, strategy evaluation, and strategy improvement. The detailed process is depicted in Figure 2.

#### Step 1: Initialization

- (i) Initialize the maintenance strategy  $P(s, a)$ , a random value; initialize the maximum updating times of the strategy improving  $E_{\max}$  and the maximum updating times of the strategy evaluation  $N_{\max}$ ; initialize the learning rate parameters  $\alpha_0$  and  $K_\alpha$  and the exploration rate parameters  $p_0$  and  $K_p$ ; set the increase times of the outer loop policy  $E = 1$ .
- (ii) According to the known maintenance strategy  $P(s, a)$ , calculate the average reward rate  $\rho$ ; initialize the state-action value of the strategy evaluation process  $Q(s, a) = 0$ ; set the current strategy updating number  $N = 1$  and the visit times  $V_\alpha(s, a) = 0$  and  $V_p(s) = 0$ .

#### Step 2: Strategy Evaluation

- (i) Initialize the current state  $s = (1, 0, 0)$ , the average failure interval  $T_f$  and the cumulative state transition time  $T_c$ .
- (ii) Choose the greedy action  $a$  basing on the probability  $1 - p_n$ ; otherwise, the random action  $a$  is selected based on the probability  $p_n$ .
- (iii) Simulate the decision action  $a$  in state  $s$ ; the observation state is transformed to state  $s'$ . If  $a = 0$ , a new observation state is obtained, and the transition time  $t(s, a, s')$  and the reward  $r(s, a, s')$  between the state  $s$  and state  $s'$  are directly produced. The action value  $Q$  is updated by using equation (3):

time are obtained, and the action value  $Q$  is updated. If  $N > N_{\max}$ , jump to Step 3 (i); otherwise, jump to Step 2 (ii).

- (v) Update the visit factors  $V_\alpha(s, a) = V_\alpha(s, a) + 1$  and  $V_p(s) = V_p(s) + 1$ ; update the learning rate  $\alpha$  and the exploration rate  $p_n$ , and then jump to Step 2 (ii).

#### Step 3: Strategy Improvement



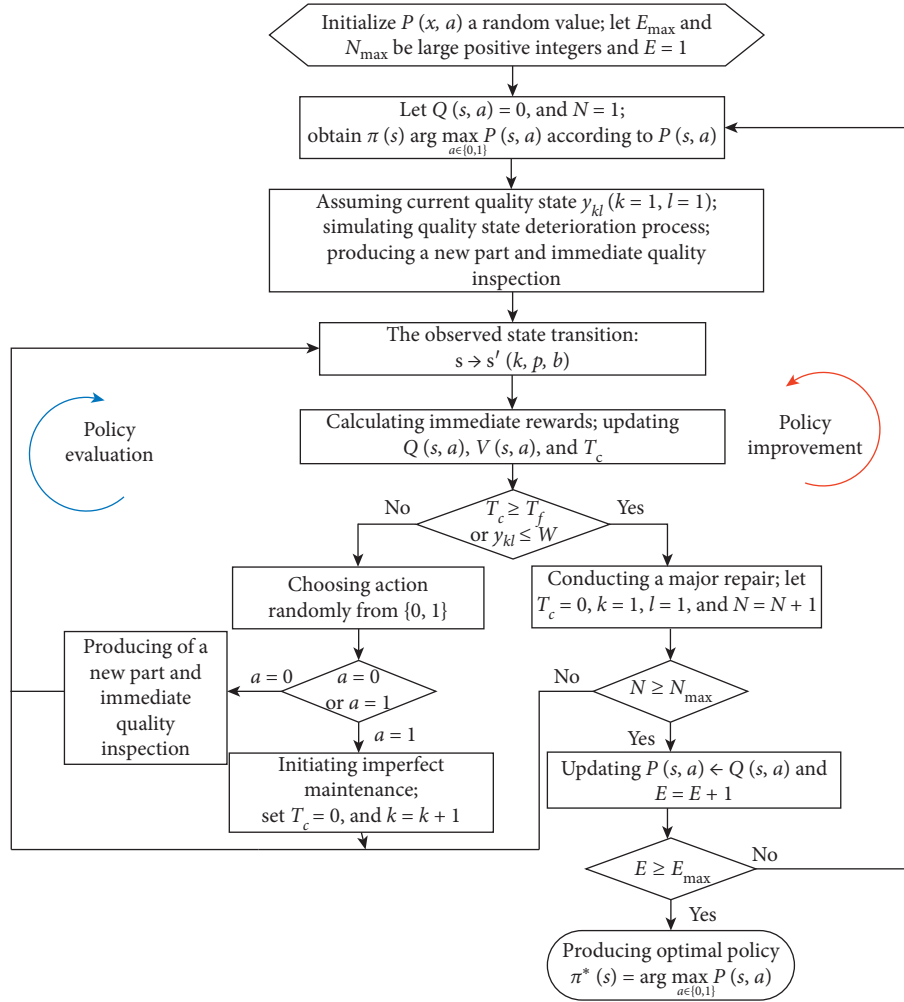


FIGURE 2: Block diagram of maintenance strategy.

- (i) Let  $P=Q$  and  $E=E+1$ ; if  $E=E_{\max}$ , stop the learning process; otherwise jump to i-b and continue learning.
- (ii) According to the action value  $P$ , calculate the optimal strategy  $\pi^*$  by using the following equation:

$$\pi^*(s) = \operatorname{argmax}_{a \in A} P(s, a). \quad (7)$$

**4.2. Optimal PM Time.** In Section 4.1, the optimal maintenance strategy  $\pi^*$  of the deteriorating equipment can be obtained by the proposed method. In this section, the optimal maintenance strategy  $\pi^*$  and the equipment deterioration process model are used to estimate the future maintenance time corresponding to different observation states  $s_i$ . Firstly, one-dimensional vector  $V_d$  of unqualified product state and one-dimensional vector  $V_t$  of production time are defined. These two vectors record the accumulative quantity of unqualified product  $b$  and the production time  $t$  per unit product respectively. During the process from production to maintenance, the failure interval is the sum of the sojourn times in different quality

states of the same deterioration mode. The initial action is  $a=0$ , and the new observation state can be produced after the equipment goes through production and quality inspection. Based on the maintenance policy  $\pi^*$ , the actions of a new state can be obtained until the equipment performs maintenance action. The vector  $V_d$  records the state from production to the maintenance process. The vector  $V_t$  can directly calculate the maintenance point in time of different states  $s$ , which is used as an effective PM time. In the simulation process, the state transfer process is random, the same state can be recorded for many times, and the average value is taken as the PM time for the observed state.

The detailed process for obtaining the PM time is shown in Figure 3. First, the parameters related to PM time are initialized, and then the production process of the equipment is simulated according to the known maintenance strategy  $\pi^*$ . The quality state and the production process are random in the simulation process. The maintenance policy is applied to the model of Figure 3, the PM time  $T_M^j(S_i)$  corresponding to the observation state  $s_i$  is produced, and the mean value  $(1/n) \sum_{j=1}^n T_M^j(S_i)$  is formulated as the final estimate.

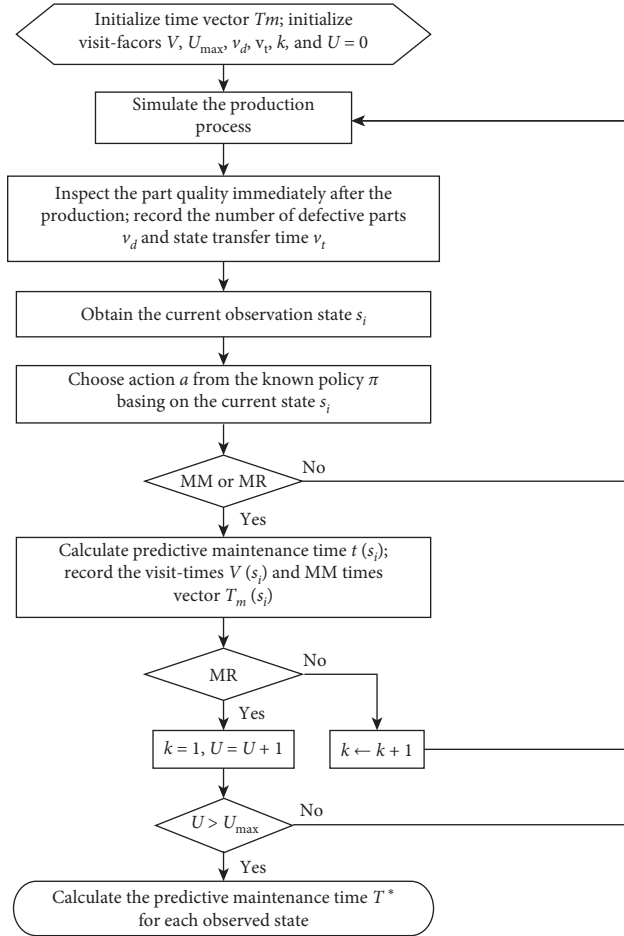


FIGURE 3: Block diagram for PM.

## 5. Simulation Study

The maintenance action is imperfect; that is, after maintenance, the quality state of the equipment will be improved, and the yield level also will be improved, but the equipment will not be restored to a new state. So, to what extent will the equipment be restored after the maintenance? This section mainly explains this process through the change of yield level before maintenance and after maintenance. Referring to the ideas of Zhu et al. [26], for two continuous deteriorating subcycles, the yield function relationship is as follows:

$$\text{Yield}_{k+1}(t) = b_k \text{Yield}_k(t + a_k D_k), \quad t \in (0, D_{k+1}). \quad (8)$$

$t$  represents the time since the equipment is last maintained or repaired;  $b_k$  is a degradation factor of equation (8), which is a value between 0 and 1;  $a_k$  is defined as an age degradation factor, which is a value between 0 and 1;  $D_k$  represents the time interval of the  $k$ 'th subcycle. The discrete

yield levels can be determined by equation (9), where  $L$  is the number of prespecified yield levels in each subcycle  $k$ .

$$y_{k+1,l} = \text{Yield}_{k+1}(0) \left( \frac{l-1}{L-1} \right), \quad \text{where } l = 1, 2, \dots, L. \quad (9)$$

**5.1. Numerical Experiments.** According to the problem description and the modeling description of the deteriorating equipment in this paper, the relevant parameters are assumed and given in Table 1. Other relevant parameters are explained as follows: the maximum updating times of the strategy improving  $E_{\max} = 15$ ; the maximum updating times of the strategy evaluation  $N_{\max} = 10000$ ; the visit factor  $V(s, a)$  is the visit times for a certain state, which is a changing value. The yield level is a discretization for the equipment states, and from the fuzzy point of view, it can be divided into four levels: excellent, good, medium, and poor. Each state corresponds to a certain interval time between failures. If the discretization level of the equipment is too high, the simulation state will jump frequently and cannot

TABLE 1: Numerical study parameters.

Production time per unit product	MM time		MR time		Stochastic breakdown time		Yield level limit $W$		Yield level $L$ of the $k$ 'th subcycle	
$\Gamma (10, 0.1)$	$U (2, 8)$		$\Gamma (20, 0.5)$		$\Gamma (100, 0.2)$		0.6		4	
$a_k$	$b_k$	$b_s$	$e_1$	$e_2$	$C_{e1}$	$C_{e2}$	$R_g$	$R_d$	$C_M$	$C_R$
0.2	0.9	0.8	0.05	0.05	30	60	90	40	100	300

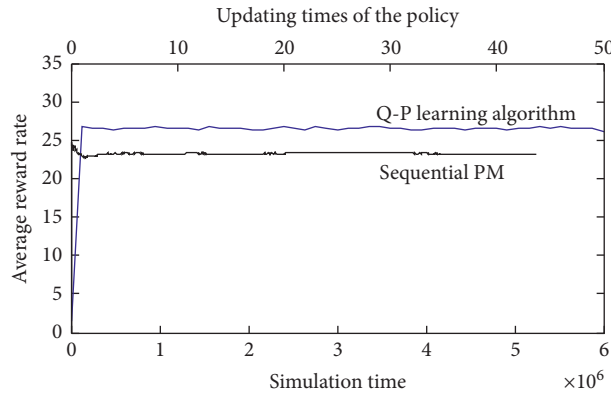


FIGURE 4: The SARRs for single equipment learned by Q-P method versus the sequential preventive maintenance method.

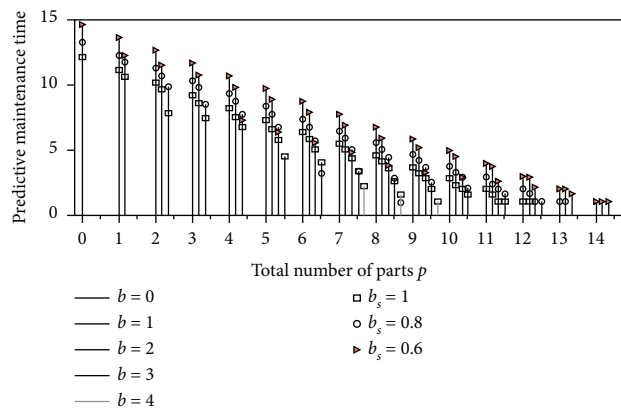


FIGURE 5: Impact of decrease factor of sojourn time.

reflect the continuous production process under a certain condition. We assume that the critical yield level  $W = 0.6$ , and  $T_c \geq T_f$  or  $y_{kl} \leq W$  is the condition for completion of a single strategy evaluation. Due to the randomness of quality inspection, the designed worst critical condition of the equipment is 0.6 in order to ensure the correct jump in the simulation process. Moreover, in the real simulation process, this condition only plays a role accidentally.

The method proposed in this paper is adopted for learning and the learning results are shown in Figure 4, which is compared with the sequential preventive maintenance algorithm [27]. As can be seen from the figure that the SARRs of the strategies learned by the methods are well convergent, and the proposed method is clearly much better than the sequential preventive maintenance algorithm according to the SARRs. This situation arises in part from the fact that the maintenance policy has not been coupled in the sequential preventive maintenance algorithm to maximize the total SARR.

## 5.2. Sensitivity Analysis of the Parameters

**5.2.1. Impact of Decrease Factor of Sojourn Time.** The sojourn time  $\lambda_{kl}$  for each state is related to the decrease factor of sojourn time  $b_s$ . The smaller  $b_s$  is, the change of  $\lambda_{kl}$  will be greater. Correspondingly, the PM time will also change. The PM time increases when  $b_s$  decreases, as shown in Figure 5. The reason is that the equipment will be maintained for a considerable period of time to produce qualified products with a high probability when  $b_s$  is smaller, and the expected SARR in the long run will increase. For example, when  $b_s$  decrease from 1 to 0.6, the expected SARR changes from 20.6 to 30.

**5.2.2. Impact of Quality Detection Error.** Figure 6 shows that the PM time for each observed state shows slight declines as the probability of Type II error  $e_2$  increases from 0 to 0.1. The

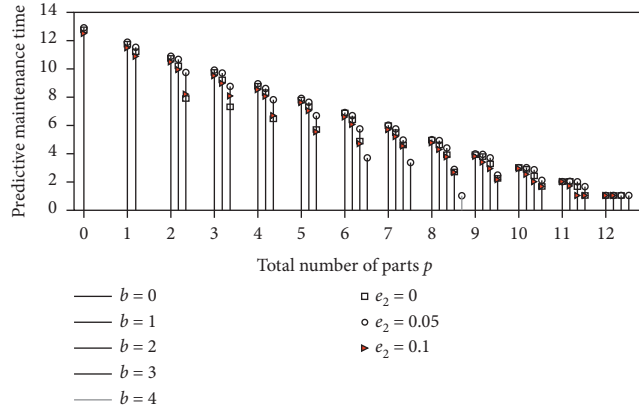


FIGURE 6: Impact of Type II error.

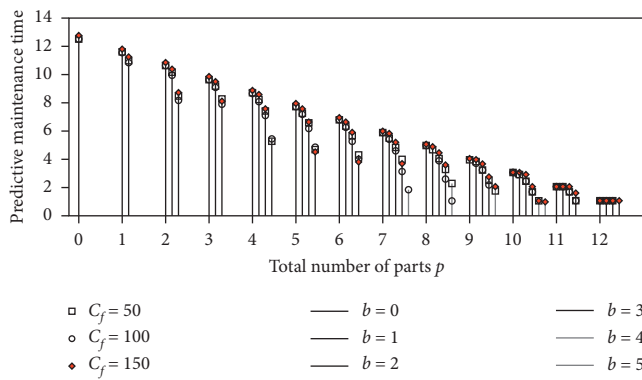


FIGURE 7: Impact of the cost  $C_f$ .

reason is that the increase of  $e_2$  can result in a reduction of long-run expected SARR, and it decreases from 31.8 to 30.6. At the same time, the PM time is not sensitive to the change of Type II error  $e_2$ ; this is due to the fact that the cost  $C_{e2}$  of Type II error  $C_{e2} = 100$  is comparatively small. Similarly, the PM time shows slight declines when  $e_1$  continues to increase, because  $C_{e1}$  is comparatively small and the growth parameter  $e_1$  can result in a reduction of long-run expected SARR.

5.2.3. *Impact of the Cost or Profit.* (1) *Impact of the Cost  $C_f$ .* The parameter  $C_f$  refers to the cost of wrongly identifying a qualified product as an unqualified product. From Figure 7, we can see that the PM time decreases as the cost  $C_f$  increases; this is due to the fact that increase in  $C_f$  leads to a decrease in the long-term expected SARR. Meanwhile, Figure 7 shows that the PM time seems to be insensitive to the change of  $C_f$  which is caused by the assumption of a very small false detection probability  $p_f$  in this paper.

(2) *Impact of the Cost  $C_n$ .* The parameter  $C_n$  is the cost of wrongly identifying an unqualified product as a qualified product. As shown in Figure 8, when the inspection cost  $C_n$  increases, the PM time decreases; this is because the expected SARR in the long run decreases as the cost  $C_n$  increases. Figure 8 also shows that the PM time is not sensitive to the

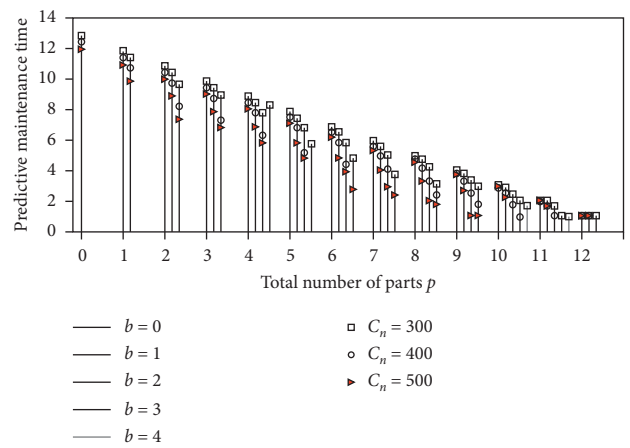


FIGURE 8: Impact of the cost  $C_n$ .

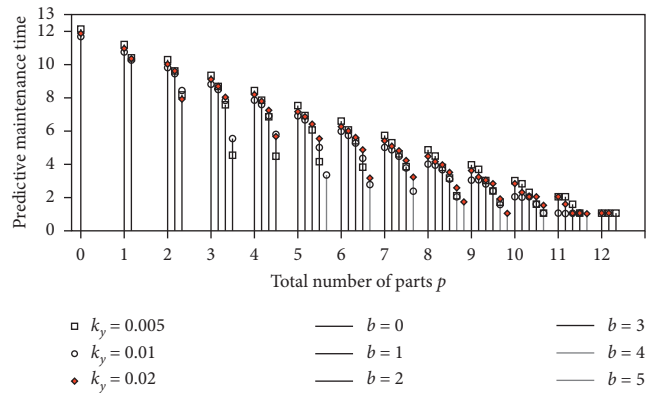


FIGURE 9: Impact of initial quality deterioration rate  $k_y$ .

change of  $C_n$ , which is caused by the assumption of a very small probability of missed detection  $p_n$  in this paper.

5.2.4. *Impact of Initial Quality Deterioration Rate  $k_y$ .* The coefficient  $k_y$  describes the initial deterioration rate of the equipment, as shown in Figure 9. The PM time is not sensitive to the change of the coefficient  $k_y$ ; this is due to the

fact that the change of the coefficient  $k_y$  in a certain extent basically makes no difference to the SARR.

## 6. Conclusion

In this paper, we propose a PM method for single deteriorating equipment having multiple yield quality problems. It is assumed that the yield stage is coupled with the equipment quality state, and a stochastic breakdown can also occur besides the quality failure. Moreover, the equipment cannot return to normal operating condition without repair. We assume that there are two decision actions including MM and MR in each observation state. The preventive maintenance is MM, which can be performed in a deteriorating quality state, while the MR is forced to be implemented in a failure state. A discrete-state continuous-time SMDP model is proposed to present the deterioration process of the equipment. The Q-P method in the RL framework is utilized to solve the SMDP model. Given the product quality inspection data with certain detection errors, the optimal maintenance strategy based on each observed state is produced by taking into account the goal of maximizing the long-run expected SARR. The PM time is capable of being achieved by a simulation method.

Through the simulation examples, it is proved that the proposed method adopted in this paper is capable of solving the PM problems of the equipment under dynamic environment. The experimental results also prove that the proposed method can outperform the standard sequential preventive maintenance method with unequal time interval. The change of maintenance action rules is further shown, which is not progressive with the increase of maintenance times and unqualified rate. It can also be observed that the PM time depends on the observed state, and it decreases as the total number of products produced increases and also decreases monotonically as the number of unqualified products increases for a given total number of products produced. Moreover, an increase in the number of maintenance times will also cause a decrease in the PM time. In addition, the influences of the main parameters on the optimization goal are also investigated.

## Data Availability

The relevant data of calculation used to support the findings of this study are included within the article.

## Conflicts of Interest

The authors declare that they have no conflicts of interest regarding the publication of this paper.

## Acknowledgments

This work was supported by the Natural Science Foundation of Liaoning Province under Grant 20180550746 and the National Science Foundation of China under Grant 61901283.

## References

- [1] Y. Zhou, B. Sun, W. Sun, and Z. Lei, "Tool wear condition monitoring based on a two-layer angle kernel extreme learning machine using sound sensor for milling process," *Journal of Intelligent Manufacturing*, 2020.
- [2] Y. Zhou, B. Sun, and W. Sun, "A tool condition monitoring method based on two-layer angle kernel extreme learning machine and binary differential evolution for milling," *Measurement*, vol. 166, 2020.
- [3] S. Lu, Y.-C. Tu, and H. Lu, "Predictive condition-based maintenance for continuously deteriorating systems," *Quality and Reliability Engineering International*, vol. 23, no. 1, pp. 71–81, 2007.
- [4] S.-J. Wu, N. Gebraeel, M. A. Lawley, and Y. Yih, "A neural network integrated decision support system for condition-based optimal predictive maintenance policy," *IEEE Transactions on Systems, Man, and Cybernetics—Part A: Systems and Humans*, vol. 37, no. 2, pp. 226–236, 2007.
- [5] K. A. Kaiser and N. Z. Gebraeel, "Predictive maintenance management using sensor-based degradation models," *IEEE Transactions on Systems, Man, and Cybernetics—Part A: Systems and Humans*, vol. 39, no. 4, pp. 840–849, 2009.
- [6] M. Y. You, F. Liu, W. Wang, and G. Meng, "Statistically planned and individually improved predictive maintenance management for continuously monitored degrading systems," *IEEE Transactions on Reliability*, vol. 59, no. 4, pp. 744–753, 2012.
- [7] X. Han, Z. Wang, M. Xie, Y. He, Y. Lia, and W. Wang, "Remaining useful life prediction and predictive maintenance strategies for multi-state manufacturing systems considering functional dependence," *Reliability Engineering and System Safety*, vol. 210, 2021.
- [8] T. P. Carvalho, F. A. A. M. N. Soares, R. Vita, R. D. P. Francisco, J. P. Basto, and S. G. S. Alcalá, "A systematic literature review of machine learning methods applied to predictive maintenance," *Computers & Industrial Engineering*, vol. 137, 2019.
- [9] J. Z. Sikorska, M. Hodkiewicz, and L. Ma, "Prognostic modelling options for remaining useful life estimation by industry," *Mechanical Systems and Signal Processing*, vol. 25, no. 5, pp. 1803–1836, 2001.
- [10] L. Jan, L. Dimiccoli, and H. Sahli, "Hidden semi-markov models for predictive maintenance," *Mathematical Problems in Engineering*, vol. 2015, Article ID 278120, 23 pages, 2015.
- [11] S. Schwendemann, Z. Amjad, and A. S. Hoc, "A survey of machine-learning techniques for condition monitoring and predictive maintenance of bearings in grinding machines," *Computers in Industry*, vol. 125, 2021.
- [12] R. R. Inman, D. E. Blumenfeld, N. Huang, and J. Li, "Designing production systems for quality: research opportunities from an automotive industry perspective," *International Journal of Production Research*, vol. 41, no. 9, pp. 1953–1971, 2003.
- [13] I. C. Schick, S. B. Gershwin, and J. Kim, "Quality/quantity modeling and analysis of production lines subject to uncertainty," *Report, Laboratory For Manufacturing And Productivity*, Massachusetts Institute of Technology, Cambridge, MA, USA, 2005.
- [14] A. Farahani and T. Hamid, "Integrated optimization of quality and maintenance: a literature review," *Computers & Industrial Engineering*, vol. 151, Article ID 106924, 2021.

- [15] Z. Xu and D. Zhou, "Real-time prediction method research on reliability for a class of dynamic systems," *Control Engineering*, vol. 15, no. 1, pp. 85–87, 2008.
- [16] M. L. Puterman, *Markov Decision Processes*, Wiley-Interscience, New York, NY, USA, 1994.
- [17] S. Bloch-Mercier, "A preventive maintenance policy with sequential checking procedure for a markov deteriorating system," *European Journal of Operational Research*, vol. 142, no. 3, pp. 548–576, 2002.
- [18] C. Chen, Y. Chen, and J. Yuan, "On a dynamic preventive maintenance policy for a system under inspection," *Reliability Engineering & System Safety*, vol. 80, no. 1, pp. 41–47, 2003.
- [19] J. H. Chiang and J. Yuan, "Optimal maintenance policy for a markovian system under periodic inspection," *Reliability Engineering & System Safety*, vol. 71, no. 2, pp. 165–172, 2001.
- [20] M. Ohnishi, T. Morioka, and T. Ibaraki, "Optimal minimal-repair and replacement problem of discrete-time markovian deterioration system under incomplete state information," *Computers & Industrial Engineering*, vol. 27, no. 1–4, pp. 409–412, 1994.
- [21] H. Kawai, J. Koyanagi, and M. Ohnishi, "Optimal maintenance problems for markovian deteriorating systems," *Stochastic Models in Reliability and Maintenance*, pp. 193–218, 2002.
- [22] L. Gong and K. Tang, "Monitoring machine operations using on-line sensors," *European Journal of Operational Research*, vol. 96, no. 3, pp. 479–492, 1997.
- [23] A. Gosavi, *Simulation-Based Optimization: Parametric Optimization Techniques and Reinforcement Learning*, Kluwer Academic Publishers, Norwell, MA, USA, 2003.
- [24] T. K. Das, A. Gosavi, S. Mahadevan, and N. Marchallick, "Solving semi-markov decision problems using average reward reinforcement learning," *Management Science*, vol. 45, no. 4, pp. 560–574, 1999.
- [25] W. B. Powell, *Approximate Dynamic Programming: Solving the Curses of Dimensionality*, Wiley-Interscience, New York, NY, USA, 2007.
- [26] H. Zhu, F. Liu, X. Shao, Q. Liu, and Y. Deng, "A cost-based selective maintenance decision-making method for machining line," *Quality and Reliability Engineering International*, vol. 27, no. 2, pp. 191–201, 2011.
- [27] D. G. Nguyen and D. N. P. Murthy, "Optimal preventive maintenance policies for repairable systems," *Operations Research*, vol. 29, no. 6, pp. 1181–1194, 1981.



## Research Article

# Kernel Regression Residual Decomposition Method to Detect Rolling Element Bearing Faults

Xiaoqian Wang,<sup>1</sup> Dali Sheng,<sup>2</sup> Jinlian Deng ,<sup>3</sup> Wei Zhang,<sup>3</sup> Jie Cai,<sup>3</sup>  
Weisheng Zhao,<sup>3</sup> and Jiawei Xiang <sup>1</sup>

<sup>1</sup>College of Mechanical and Electrical Engineering, Wenzhou University, Wenzhou 325035, China

<sup>2</sup>Department of Police Command and Tactics, Zhejiang Police College, Hangzhou 310053, China

<sup>3</sup>Department of Mechanical Engineering, Zhejiang Institute of Mechanical & Electrical Engineering, Hangzhou 310053, China

Correspondence should be addressed to Jinlian Deng; [dengjinlian@zime.edu.cn](mailto:dengjinlian@zime.edu.cn) and Jiawei Xiang; [wxxw8627@163.com](mailto:wxxw8627@163.com)

Received 29 January 2021; Revised 14 March 2021; Accepted 17 April 2021; Published 28 April 2021

Academic Editor: Zhifeng Dai

Copyright © 2021 Xiaoqian Wang et al. This is an open access article distributed under the Creative Commons Attribution License, which permits unrestricted use, distribution, and reproduction in any medium, provided the original work is properly cited.

The raw vibration signal carries a great deal of information representing the mechanical equipment's health conditions. However, in the working condition, the vibration response signals of faulty components are often characterized by the presence of different kinds of impulses, and the corresponding fault features are always immersed in heavy noises. Therefore, signal denoising is one of the most important tasks in the fault detection of mechanical components. As a time-frequency signal processing technique without the support of the strictly mathematical theory, empirical mode decomposition (EMD) has been widely applied to detect faults in mechanical systems. Kernel regression (KR) is a well-known nonparametric mathematical tool to construct a prediction model with good performance. Inspired by the basic idea of EMD, a new kernel regression residual decomposition (KRRD) method is proposed. Nonparametric Nadaraya–Watson KR and a standard deviation (SD) criterion are employed to generate a deep cascading framework including a series of high-frequency terms denoted by residual signals and a final low-frequency term represented by kernel regression signal. The soft thresholding technique is then applied to each residual signal to suppress noises. To illustrate the feasibility and the performance of the KRRD method, a numerical simulation and the faulty rolling element bearings of well-known open access data as well as the experimental investigations of the machinery simulator are performed. The fault detection results show that the proposed method enables the recognition of faults in mechanical systems. It is expected that the KRRD method might have a similar application prospect of EMD.

## 1. Introduction

The device of rotating machinery is entirely dependent on the health condition of the rolling element bearings, which accounts for almost 40–50% of these equipment failures [1, 2]. Such failures could be disastrous or could lead to the shutdown of the entire production lines, potentially causing huge losses [3]. Therefore, fault detection of bearing has been a great challenge in recent decades [4]. In order to obtain the fault feature, the vibration signal is one of the most important sources of information for monitoring conditions of rolling element bearing. However, the vibration signals are often contaminated by various noises, and sometimes, it is

difficult to obtain high-fidelity signals. Therefore, signal denoising is one of the significant tasks to detect faults in rolling element bearings [5].

In the past few decades, a lot of novelty approaches have been proposed [6–8]. Time-frequency (TF) method techniques have been developed to allow access to the time-frequency energy behavior of nonstationary signals. TF representations can give insight into the complex structure of signals consisting of several components [9]. It maps a 1D signal to a 2D function of time and frequency, so a TF representation can be obtained to characterize the signal in the time and frequency domains simultaneously [10]. Many signal time-frequency methods were applied to machine



diagnostics in the last few decades. The wavelet decomposition method has been most commonly used [11–14], and an arbitrary signal can be decomposed into a set of wavelet coefficients. At each scale, the soft thresholding technique is performed to suppress noises, and finally, the wavelet reconstructed technique is employed to obtain the purified signals. Lei et al. [15] presented a method based on wavelet packets and Hilbert–Huang transform to improve productivity and part quality in the machining process. A remarkable advantage of the wavelet transform method is that the wavelet transform is sensitive to defects for a longer duration reflected by nonstationary signals [6]. However, wavelet transform suffers from disadvantages, one limitation worth noting that the usage of wavelet transforms to suppress noise will often lead to oscillation effects when dealing with the low signal-to-noise ratio (SNR) scenarios [16]. And another challenge is to select the appropriate wavelets [17–19].

Empirical mode decomposition (EMD) is one of the most powerful time-frequency analysis techniques proposed by Huang [18], which has been widely applied to detect faults in rotating machinery [19, 20]. EMD is a self-adaptive signal processing method that could be used in nonlinear and nonstationary process; it decomposes the complicated signal into intrinsic mode functions (IMFs). Frequency components contained in each IMF not only relate to the sampling frequency but also change with the signal itself [21]. Therefore, using EMD combine with the Hilbert spectrum analysis to reveal the faulty frequency information hidden in vibration signals, the result shows good computational efficiency and resolution in nonlinear and nonstationary process. Recently, ensemble empirical mode decomposition (EEMD) is developed by Wu and Huang [22]. EEMD is a noise-assisted data analysis method, and by adding finite white noise to the investigated signal, the EEMD method can eliminate the mode mixing problem in all cases automatically [23]. Lei et al. [24, 25] used EEMD to enhance the efficiency of the feature extraction of faulty signals as well as decrease the mode mixing phenomenon. In working conditions, the key issues are how the EMD worked with the support of the strictly mathematical theory and how to properly select the added noise amplitude [26, 27].

Kernel regression (KR) [28, 29] is a nonparametric technique to construct a prediction model based on Nadaraya–Watson kernel estimator [30, 31]. In recent years, Wu et al. [32, 33] presented two hybrid approaches using the KR technique and other methods to predict faults in car assembly line, e.g., the fuzzy wavelet kernel support vector classifier machine and modified genetic algorithm, and the triangular fuzzy Gaussian wavelet kernel support vector classifier machine and genetic algorithm. Baraldi et al. [34] presented a modification of the traditional autoassociative kernel regression (AAKR) method which enhances the signal reconstruction robustness so as to monitor the abnormal conditions of industrial components. In [35], kernel regression method is used in image denoising, and results illustrate good performance in color estimates. Compared to the EMD method without the support of the strictly mathematical theory, KR is a nonparametric mathematical

tool based on statistical mathematical theory. However, the above methods are only the usage of the prediction characteristics of KR. Therefore, it might be interesting to generate a methodology like EMD to decompose vibration signals, i.e., a new kernel regression residual decomposition (KRRD) method. Besides, the standard deviation (SD) criterion [18] can be applied to automatically determine the decomposition level of the KRRD algorithm. The KRRD algorithm is also reversible using kernel regression residual reconstitution (KRRR) algorithm.

According to the multiscale signal decomposition principle, the well-known soft threshold technique proposed by Donoho [12, 36] can be applied to denoise signals at each scale.

The rest of the paper is organized as follows. Brief introductions of the basic idea of the KRRD algorithm, SD criterion, soft threshold technique, and KRRR algorithm are given in Section 2. In Section 3, a numerical simulation and an open-access faulty bearing data are carried out to validate the effectiveness of the present method, and the experimental investigations for three cases are further given in Section 4. Conclusions and further work are drawn in Section 5.

## 2. Kernel Regression Residual Decomposition Methodology

Regression model-based methods will be applied to decompose signals, according to the basic idea of EMD. In the present, KR is employed as a bridge to form an explicit KRRD method. Figure 1 shows the three steps of the proposed KRRD. Firstly, the residual signals of a raw signal are obtained using KR repeatedly, which can be called KRRD. Secondly, the soft thresholding technique and SD criterion are applied to obtain noise-suppressed residual signals. KRRR is then used to reconstruct the purified signal with high SNR. Finally, to obtain demodulation frequencies, the traditional Hilbert envelope spectrum analysis is applied in the paper and the fault types will be given.

**2.1. KRRD and KRRR.** The procedure of KRRD is simply listed as follows. The kernel regression method has been most commonly used; a signal  $f(t)$  can be represented by the summation of  $n$  residual signals as

$$f(t) = \sum_{i=1}^n r_i(t) = f \sum, 1(t), \quad (1)$$

where  $r_i(t)$  ( $i = 1, 2, \dots, n$ ) is a residual signal characterizing the signal information at scale  $i$  and  $f \sum, 1(t)$  is the summation of all residual signals at scale  $[1, n]$ , i.e., the original/raw signal  $f(t)$ . In order to decompose the signal  $f(t)$  into a number of residual signals, a deep framework can be rewritten by

$$f \sum, 1(t) = f \sum, 2(t) + r_1(t) = s_1, \quad (2)$$

where  $f \sum, 2(t)$  denote the summation of all residual signals at scale  $[2, n]$ . In this step, estimating  $f \sum, 2(t)$  by given

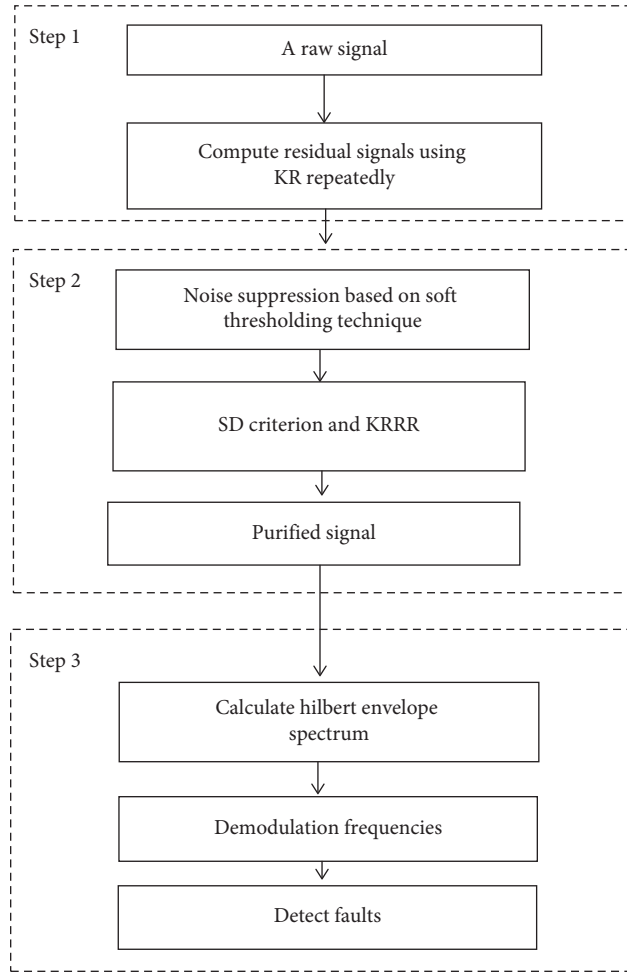


FIGURE 1: Flowchart of the proposed KRRD method.

$f \sum, 1(t)$  is the key to solve the problem. In the present, a KR strategy is used in conditional expectation. Therefore, the estimation of  $f \sum, 2(t)$  can be represented by  $f \sum, 1(t)$  as

$$f \sum, 2(t) = K_1(f \sum, 1(t) - f \sum, 1(t_i)) = s_2, \quad (3)$$

where the 2nd smooth term  $s_2 = K_1(f \sum, 1(t) - f \sum, 1(t_i))$  can be estimated by nonparametric Nadaraya–Watson KR [29, 30] and  $K$  is a density function. In the present, a radial basis function (RBF) kernel [37]  $K_1$  is employed and  $f \sum, 2(t)$  can be obtained by

$$f \sum, 2(t) = K_1(f \sum, 1(t) - f \sum, 1(t_i)) = e^{-\frac{1}{2\lambda_1^2}(f \sum, 1(t) - f \sum, 1(t_i))^2}, \quad (4)$$

where  $\lambda_1$  is the bandwidth of the  $f(t)$  and  $f \sum, 1(t)$  is the Gaussian kernel function center. It is worth pointing out that the RBF has the characteristic of unique best approximation to the unknown time series [37]. Since the residual signal at scale  $n$  can be obtained by equation (4), a deep cascading framework can be expressed as follows:

$$r_j(t) = f \sum, j(t) - f \sum, j+1(t) = s_j - s_{j+1}, \quad (5)$$

in which the  $(j+1)$ th smooth term  $s_{j+1} = K_j(f \sum, j+1(t) - f \sum, j+1(t_i))$  can also be estimated by nonparametric

Nadaraya–Watson KR. The last residual signal can be expressed as follows:

$$r_n(t) = s_n. \quad (6)$$

Finally, the signal decomposed realization of KRRD via kernel regression at each scale is completed, and the KRRD is simply the summation of all residual signals  $r_1(t), r_2(t), \dots, r_n(t)$  which is shown in Figure 2. Besides, the residual signals at the lower scales contain great characteristics of the signal, while the signal contained coarser signal characteristics.

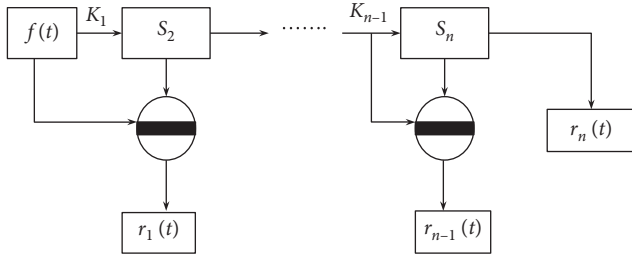


FIGURE 2: The framework of KRRD.

**2.2. Noise Suppression.** In this paper, the work is to illustrate the feasibility of utilizing the KRRD for processing fault signals. However, at each scale, there is some low but not useful information. The soft thresholding technique [12, 36] is the commonly used tool to obtain greater content at each scale.

Since residual signals at different scales are obtained. Considering some unusual data in the signal, we use the median absolute deviation function to estimate the noise threshold  $\theta_j$  at scale  $j$ , using adaptive noise estimate. The threshold strategy can be expressed as follows:

$$\theta_j = \frac{\text{MAD}(r_j)}{0.6745}, \quad (7)$$

where MAD is the median absolute deviation and 0.6745 is the normal inverse cumulative distribution function of 3/4 [38]. Based on soft thresholding,  $C_j(t)$  can be obtained by

$$C_j(t) = \begin{cases} 0, & \text{if } |r_j(t)| < \theta_j, \\ |r_j(t)| - \theta_j, & \text{otherwise.} \end{cases} \quad (8)$$

The sifting usually has to be implemented more times, but to get the most useful information and improve the computational efficiency of this method. In practice, we used the standard deviation (SD) criterion [39] based on the EMD method to determine whether or not  $C_j(t)$  well satisfies the IMF properties; the SD can be expressed as follows:

$$SD(k) = \sum_{t=0}^T \left[ \frac{|C_{j-1}(t) - C_j(t)|^2}{C_{j-1}^2(t)} \right], \quad (9)$$

where  $T$  is the length of data. This procedure should be repeatedly used for  $n$  times until the last residue  $C_n(t)$  satisfies the formula. In KRRD, the process of calculation is usually set to 0.2, and if SD is less than the threshold, the process stops and the decomposition procedure is finished.

Since the circulated shift is invertible, the reverse shift is simply the summation of all residual signals, which can be represented by

$$f(t) = R^{-1}(C_1(t), C_2(t), \dots, C_n(t)) = \sum_{i=1}^n C_i(t). \quad (10)$$

The framework of KRRR is shown in Figure 3. Finally, the inverse KRRD called KRRR is used to reconstruct the new purified signal.

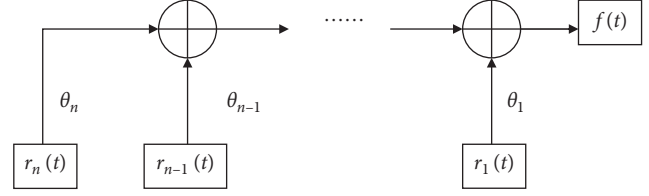


FIGURE 3: The framework of KRRR.

**2.3. Fault Detection.** The traditional Hilbert envelope spectrum analysis [18, 40] is then applied to determine demodulation frequencies.

Compared the theoretical feature frequencies of faults in bearings with demodulation frequencies, the type of bearing faults could finally be determined.

### 3. Simulation Analysis

In this section, to validate the effectiveness of the proposed method, a simulated signal which contains random noise is constructed [41, 42]. The model of the signal is expressed as follows:

$$f(t) = x(t) + R(t), \quad (11)$$

where  $x(t)$  is the periodic impulse signal without noise,  $R(t)$  is the random noise, and  $f(t)$  is the simulation signal. Suppose the sampling frequency is  $20k$  and the sampling points are 8192, the impulse signal and the noise-contaminated signal are shown in Figures 4(a) and 4(b), respectively. It is clear to see that the signal is immersed in heavy noises.

The decomposition signals using KRRD are shown in Figures 4(c)–4(e). As shown in Figures 4(c)–4(e), the KRRD method can effectively distinguish the narrow band impulses (see Figures 4(c)–4(e)) from the purified signal (see Figure 4(f)). It can also be observed that the noise process is well characterized at the low scales and the structural characteristics of the simulation signal are well characterized as the scale  $j$  increases. It indicates that the proposed method can be regarded as a promising method to decompose signals. To further clarify the denoising process of the KRRD method, the faulty bearing data of Case Western Reserve University [43] are used in this paper. The proposed method is applied to detect the bearing with inner race fault, the sampling frequency  $f_s$  is set to 25.6 kHz, the collected data length is 12288 points, the shaft rotating frequency is  $f_r = 29.5$  Hz, and bearing pass frequency of inner race (BPFI) is 159.93 Hz. The bearing fault data are added with Gaussian noises for SNR = 4 dB to illustrate the effectiveness of this method and the results are shown in Figure 5.

From Figure 5(a), the raw signal  $S_1$  is divided into four residual signals using kernel regression function. By comparing with Figure 5(b), it can be observed that in Figure 5(b), it is clear that each residual signal is decomposed using noise suppression.

The raw signal and the corresponding denoising signal are shown in Figure 6. And the frequency spectrum of raw signal and denoising signal can be seen in Figure 7. It is

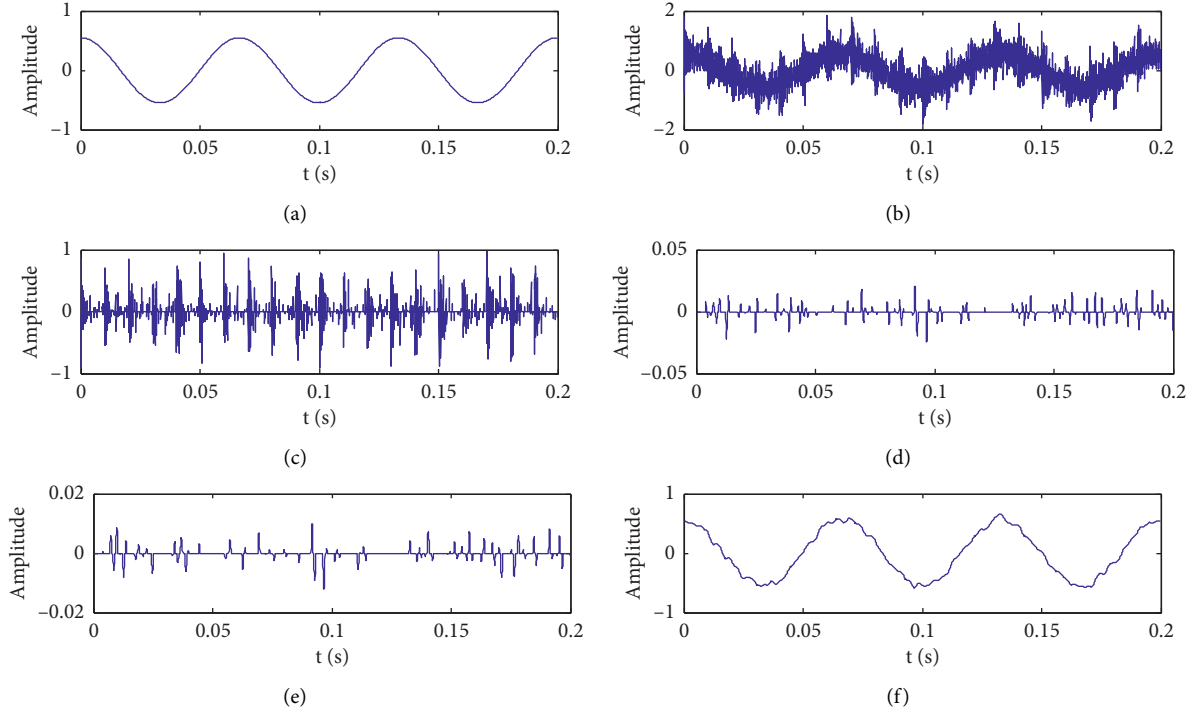


FIGURE 4: The simulation signal. (a) Test signal. (b) Noisy input signal. (c–e) Decomposition signals. (f) Purified signal.

worth noting that the fault frequency of 154.2 Hz is shown in Figure 7(b), which is more accurate than Figure 7(a) and the fault frequency of 154.2 Hz is matching with the theoretical calculation value of 159.93 Hz. Based on the above investigation, we conclude that the present approach can be employed to determine the faults of bearings.

#### 4. Experimental Evaluation

In this section, the proposed approach is evaluated by rolling element bearings with inner race, outer race, and compound fault [12, 44]. Generally, the vibration response of a bearing with faults consists of a series of impulses, whereas the frequencies in these impulses are the bearing characteristic frequencies (BCFs). Figure 8 shows the defects at the outer race, inner race, and ball. It is noted that a deep groove bearing (ER-12K) is used in the experiment [45]. Three fault types in the present experimental investigations are bearing pass frequency of outer race (BPFO), bearing pass frequency of inner race (BPMI), and ball spin frequency (BSF) [2], which can be theoretically calculated by

$$\text{BPFO} = \frac{nf_r}{2} \left[ 1 - \frac{d}{D} \cos \phi \right], \quad (12)$$

$$\begin{aligned} \text{BPMI} &= \frac{nf_r}{2} \left[ 1 + \frac{d}{D} \cos \phi \right], \\ \text{BSF} &= \frac{Df_r}{2d} \left[ 1 - \left( \frac{d}{D} \cos \phi \right) \right], \end{aligned} \quad (13)$$

in which  $f_r$  is the shaft speed (Hz),  $n$  is the number of rolling elements,  $\phi$  is the angle of the load from the radial plane,  $d$  is the ball diameter, and  $D$  is the pitch diameter.

The fault simulator (MFS-MG, manufactured by Spectraquest Inc.) and the test system are shown in Figure 9. The test system includes speed indicator, manual speed governor, acceleration sensors, speed sensor, motor, spindle, bearings, etc. The bearing parameters are the number of rolling elements  $n=8$ , ball diameter  $d=0.3125$  inches, pitch diameter  $D=1.318$  inches, and the contact angle  $\phi=0^\circ$ . During the experiment, the data are acquired by an accelerometer mounted on the top of the bearing holder on the left side, and the sampling frequency  $f_s$  is set to 25.6 kHz.

**4.1. Outer Race Fault Detection.** In this section, the proposed method is applied to detect the bearing with outer race fault. For the bearing with outer race fault, the collected data length is 12288 points and the shaft rotating frequency is  $f_r=29.87$  Hz. According to equation (12), BPFO can be calculated as

$$\text{BPFO} = \frac{nf_r}{2} \left[ 1 - \frac{d}{D} \cos \phi \right] = 91.15 \text{ Hz}. \quad (14)$$

From Figure 10(a), it can be seen that, due to the defect present in the rolling bearing, the vibration signal presents the impacts feature, but there exist very serious noises. Applying the KRRD method to the raw signal, the denoised signal is shown in Figure 10(b). By comparing with Figure 10(a), the ambient noises are effectively suppressed. The fault characteristic frequency (87.5 Hz) is clearly revealed. The comparisons show that the above method

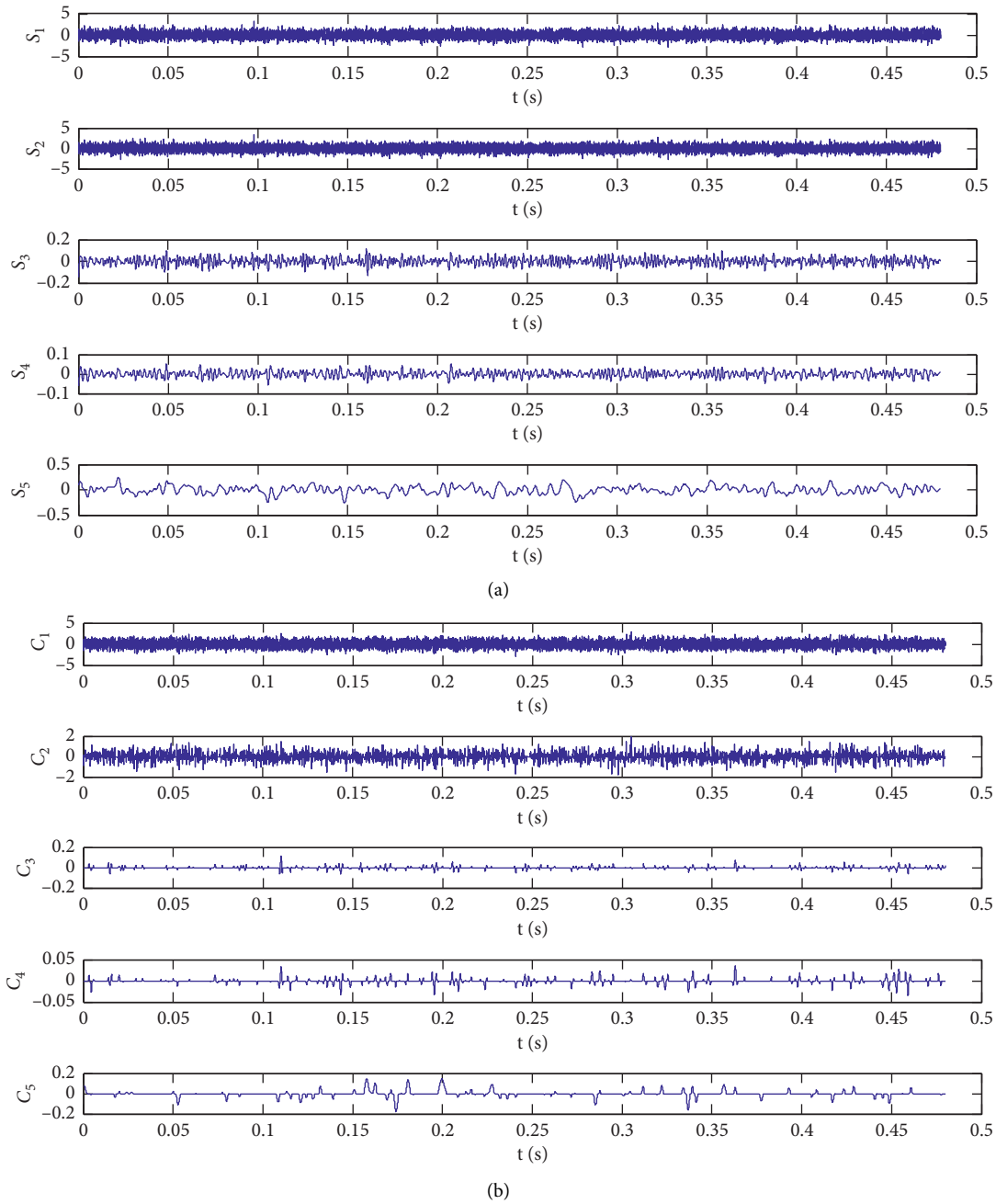


FIGURE 5: The KRRD method using Case Western Reserve University data. (a) Raw signal  $S_1$  is decomposed into four residual signals  $S_2$ ,  $S_3$ ,  $S_4$ , and  $S_5$ . (b) Each residual signal is decomposed into  $C_1$ ,  $C_2$ ,  $C_3$ ,  $C_4$ , and  $C_5$  using noise suppression.

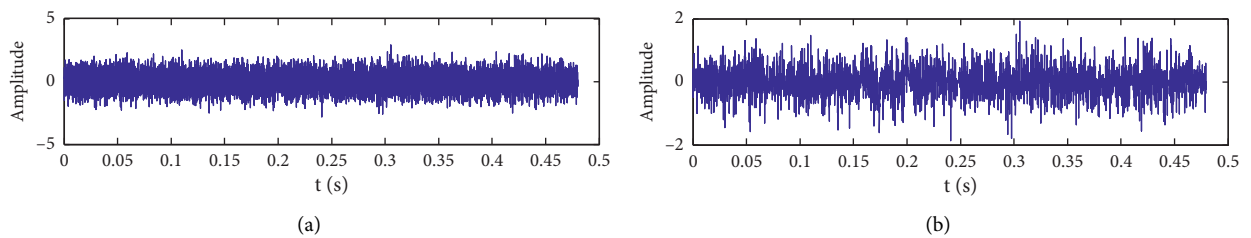


FIGURE 6: The KRRD method using Case Western Reserve University data. (a) Raw signal. (b) Denoising signal.

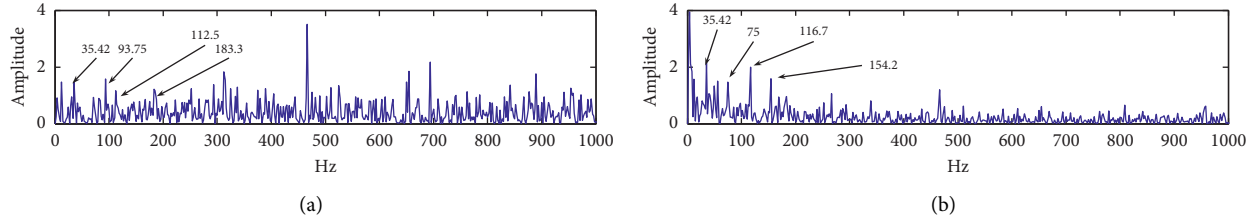


FIGURE 7: The frequency spectrum of Case Western Reserve University data. (a) The frequency spectrum of the raw signal. (b) The frequency spectrum of the denoising signal.

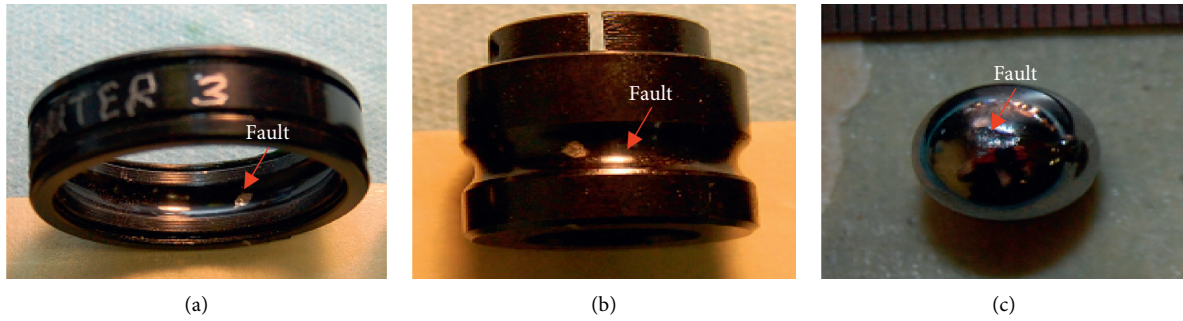


FIGURE 8: The faults in the bearing. (a) The fault in the outer race of the bearing. (b) The fault in the inner race of the bearing. (c) The fault in the ball of the bearing.

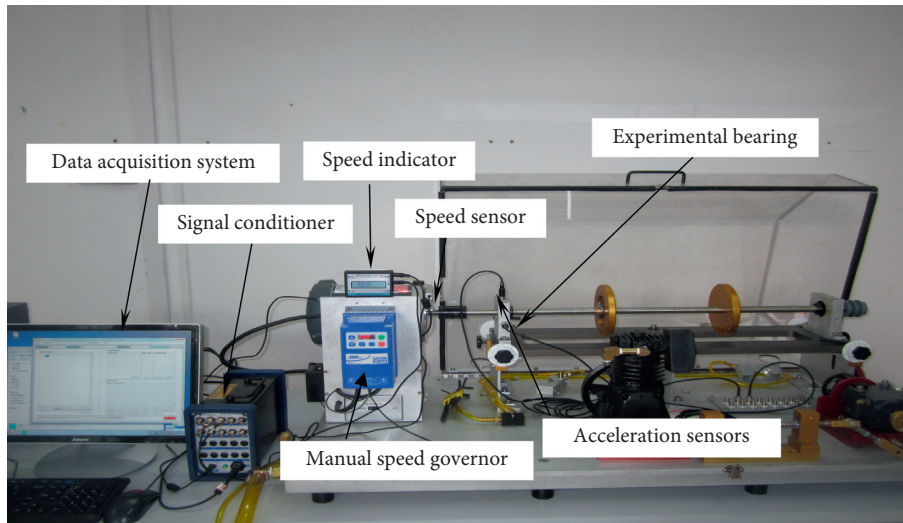


FIGURE 9: The machinery fault simulator.

proposed in this paper is more effective. Therefore, the bearing with outer race fault will be clearly detected.

4.2. Inner Race Fault Detection. For the bearing with inner race fault, the total collected data are 12288 points; the shaft rotating frequency is  $f_r = 29.87$  Hz. The ball pass frequency of the outer race (BPFI) is given by

$$BPFI = \frac{nf_r}{2} \left[ 1 + \frac{d}{D} \cos \phi \right] = 147.8\text{Hz}. \quad (15)$$

In this section, the proposed method is applied to detect the bearing with inner race fault. By comparing Figures 11(a) and 11(b), we can see that the impact characteristic is not clearly shown in the former graphic but clearly shown in the latter graphic. And the fault frequency of the inner race in



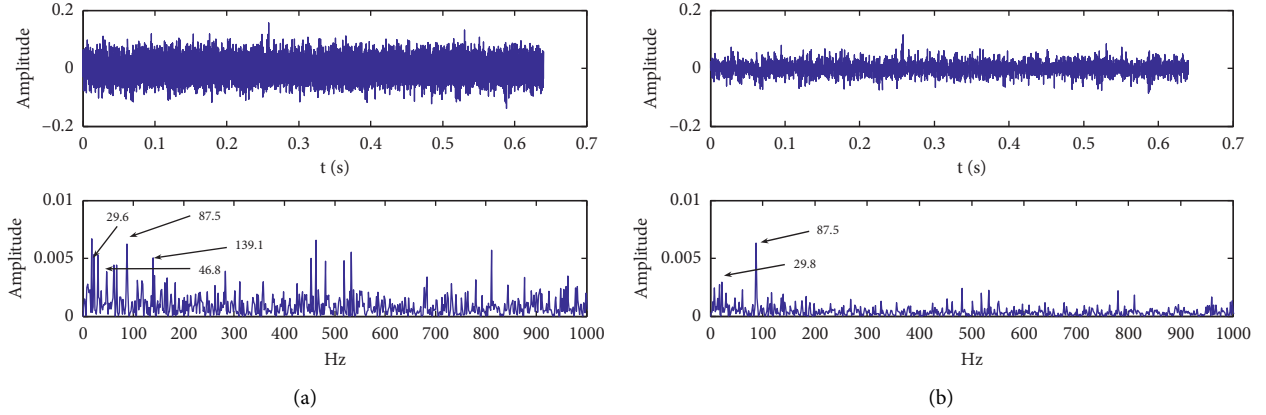


FIGURE 10: The outer race experiment signal. (a) The raw signal and the frequency spectrum of the raw signal. (b) The denoised signal and the frequency spectrum of the denoised signal.

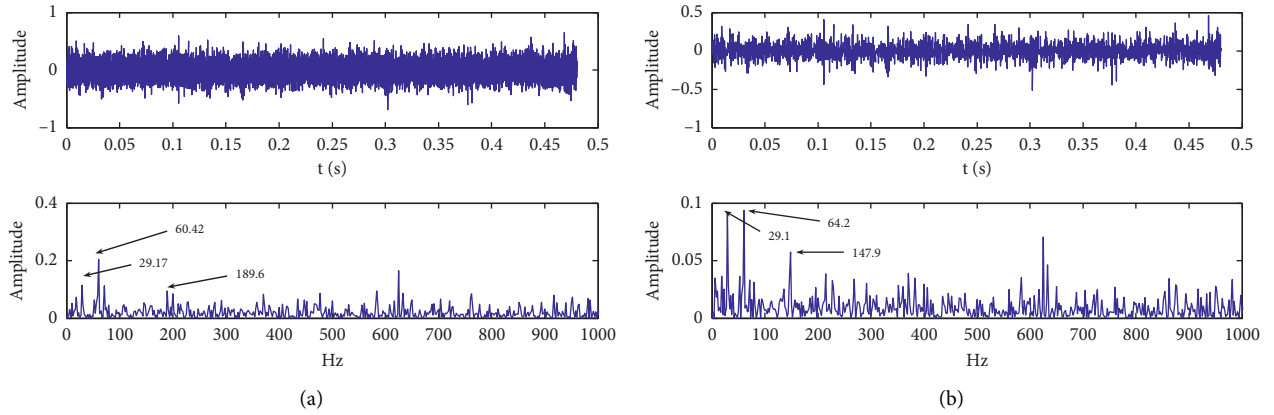


FIGURE 11: The inner race experiment signal. (a) The raw signal and the frequency spectrum of the raw signal. (b) The denoised signal and the frequency spectrum of the denoised signal.

Figure 11(a) is not clearly identified, but in Figure 11(b), the shaft rotating frequency is 29.87 Hz, second harmonic frequency is 59.26 Hz, and its feature frequency of 147.9 Hz is matching with the theoretical calculation value of 147.8 Hz, and we conclude that there is a fault in inner race of the bearing.

**4.3. Compound Fault Detection.** For the bearing with compound fault (the combination of BPFO and BPF1), the total collected data are 12288 points, the shaft rotating frequency is  $f_r = 39.82$  Hz, and the corresponding BPFO is given by

$$\text{BPFO} = \frac{nf_r}{2} \left[ 1 - \frac{d}{D} \cos \phi \right] = 121.5 \text{ Hz.} \quad (16)$$

The bearing pass frequency of inner race (BPF1) is given by

$$\text{BPF1} = \frac{nf_r}{2} \left[ 1 + \frac{d}{D} \cos \phi \right] = 197.1 \text{ Hz.} \quad (17)$$

The ball spin frequency (BSF) is given by

$$\text{BSF} = \frac{Df_r}{2d} \left[ 1 - \left( \frac{d}{D} \cos \phi \right)^2 \right] = 79.3 \text{ Hz.} \quad (18)$$

In this section, the proposed method is applied to detect the bearing with compound fault. The original signal is illustrated in Figure 12(a) and the denoised signal using the KRRD method is shown in Figure 12(b). In Figure 12(a), only the input shafting frequency of 40 Hz is shown, while the other



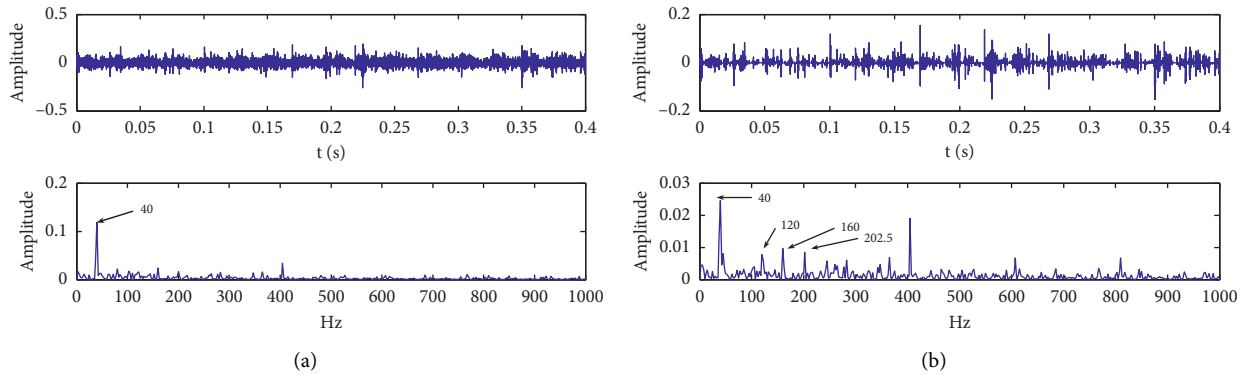


FIGURE 12: The compound fault experiment signal. (a) The raw signal and the frequency spectrum of the raw signal. (b) The denoised signal and the frequency spectrum of the denoised signal.

harmonics are submerged by other unknown frequency components; it is not clear what kind of fault is. From Figure 12(b), the input shafting rotating frequency (40 Hz) and its inner race fault (202.5 Hz), outer race fault (120 Hz), and the second harmonic frequency of ball fault (79.25 Hz) are matching with the theoretical calculation values. The results demonstrate that the proposed approach can effectively extract the fault features of defective bearings.

## 5. Conclusion

In this paper, aiming at the shortcoming of the conventional denoising method for bearing fault signal under variation conditions, a new KRRD method is proposed. Like the EMD method, the KRRD method is used to decompose a signal into a number of residual signals at different scales. It allows the noise suppression method to get rid of the noise information while preserving the important signal characteristics. The method is verified by the feature extraction of the faulty bearing of the outer race, inner race, and compound fault. From the detection results of the numerical simulation and experiment investigations from both open access data and mechanical fault simulator, it can be observed that the present method is suitable to detect faults in the mechanical systems. Because KR is a nonparametric mathematical tool with the support of the strictly mathematical theory, KRRD might be superior to EMD. The decomposition procedures are similar to EMD, and the application area can be enlarged if more research works are further performed. Moreover, it is expected that the procedures of the present method are surely suitable to other regression models.

## Data Availability

The data used to support the findings of this study are available on the Case Western Reserve University Bearing Data Center website (<http://csegroups.case.edu/bearingdatacenter/home>).

## Conflicts of Interest

The authors declare that they have no conflicts of interest.

## Acknowledgments

The authors acknowledge the support received from the Zhejiang Provincial Key Research and Development Project (grant no. 2020C0309) and Zhejiang Provincial Science Foundation (grant no. GF19F020010).

## References

- [1] S. Nandi, H. A. Toliyat, and X. Li, "Condition monitoring and fault diagnosis of electrical motors—a review," *IEEE Transactions on Energy Conversion*, vol. 20, no. 4, pp. 719–729, 2005.
- [2] R. B. Randall and J. Antoni, "Rolling element bearing diagnostics—A tutorial," *Mechanical Systems and Signal Processing*, vol. 25, no. 2, pp. 485–520, 2011.
- [3] S. Wang, J. Xiang, H. Tang, X. Liu, and Y. Zhong, "Minimum entropy deconvolution based on simulation-determined band pass filter to detect faults in axial piston pump bearings," *ISA Transactions*, vol. 88, pp. 186–198, 2019.
- [4] A. Kumar, C. P. Gandhi, Y. Zhou, R. Kumar, and J. Xiang, "Latest developments in gear defect diagnosis and prognosis: a review," *Measurement*, vol. 158, Article ID 107735, 2020.
- [5] S. Wang, J. Xiang, Y. Zhong, and H. Tang, "A data indicator-based deep belief networks to detect multiple faults in axial piston pumps," *Mechanical Systems and Signal Processing*, vol. 112, pp. 154–170, 2018.
- [6] A. Kumar, Y. Zhou, and J. Xiang, "Optimization of VMD using kernel-based mutual information for the extraction of weak features to detect bearing defects," *Measurement*, vol. 168, Article ID 108402, 2021.
- [7] J. Urbanek, T. Barszcz, M. Strączkiewicz, and A. Jablonski, "Normalization of vibration signals generated under highly varying speed and load with application to signal separation," *Mechanical Systems and Signal Processing*, vol. 82, pp. 13–31, 2017.
- [8] Y. Gao, X. Liu, and J. Xiang, "FEM simulation-based generative adversarial networks to detect bearing faults," *IEEE Transactions on Industrial Informatics*, vol. 16, no. 7, pp. 4961–4971, 2020.
- [9] L. Cohen, "Time-frequency distributions—a review," *Proceedings of the IEEE*, vol. 77, no. 7, pp. 941–981, 1989.
- [10] Y. Yang, Z. Peng, X. Dong, W. Zhang, and G. Meng, "Application of parameterized time-frequency analysis on multicomponent frequency modulated signals," *IEEE Transactions on Instrumentation and Measurement*, vol. 63, no. 12, pp. 3169–3180, 2014.

- [11] D. L. Donoho and I. M. Johnstone, "Ideal spatial adaptation by wavelet shrinkage," *Biometrika*, vol. 81, no. 3, pp. 425–455, 1994.
- [12] D. L. Donoho, "De-noising by soft-thresholding," *IEEE Transactions on Information Theory*, vol. 41, no. 3, pp. 613–627, 1995.
- [13] P. K. Kankar, S. C. Sharma, and S. P. Harsha, "Rolling element bearing fault diagnosis using wavelet transform," *Neurocomputing*, vol. 74, no. 10, pp. 1638–1645, 2011.
- [14] W. Sun, X. Cao, B. Chen, Y. Zhou, Z. Shen, and J. Xiang, "A two-stage vision-based method for measuring the key parameters of ball screws," *Precision Engineering*, vol. 66, pp. 76–86, 2020.
- [15] H. Cao, Y. Lei, and Z. He, "Chatter identification in end milling process using wavelet packets and Hilbert-Huang transform," *International Journal of Machine Tools and Manufacture*, vol. 69, pp. 11–19, 2013.
- [16] A. Wong and X. Y. Wang, "A bayesian residual transform for signal processing," *IEEE Access*, vol. 3, pp. 709–717, 2015.
- [17] L. Meng, J. Xiang, Y. Wang, Y. Jiang, and H. Gao, "A hybrid fault diagnosis method using morphological filter-translation invariant wavelet and improved ensemble empirical mode decomposition," *Mechanical Systems and Signal Processing*, vol. 51, pp. 101–115, 2015.
- [18] N. E. Huang, Z. Shen, S. R. Long et al., "The empirical mode decomposition and the hilbert spectrum for nonlinear and non-stationary time series analysis," *Proceedings of the Royal Society of London. Series A: Mathematical, Physical and Engineering Sciences*, vol. 454, no. 1971, pp. 903–995, 1998.
- [19] Y. Lei, J. Lin, Z. He, and M. J. Zuo, "A review on empirical mode decomposition in fault diagnosis of rotating machinery," *Mechanical Systems and Signal Processing*, vol. 35, no. 2, pp. 108–126, 2013.
- [20] Q. He, P. Li, and F. Kong, "Rolling bearing localized defect evaluation by multiscale signature via empirical mode decomposition," *Journal of Vibration and Acoustics*, vol. 134, pp. 67–75, 2012.
- [21] D. Yu, J. Cheng, and Y. Yang, "Application of EMD method and Hilbert spectrum to the fault diagnosis of roller bearings," *Mechanical Systems and Signal Processing*, vol. 19, no. 2, pp. 259–270, 2005.
- [22] Z. Wu and N. E. Huang, "Ensemble empirical mode decomposition: a noise-assisted data analysis method," *Advances in Adaptive Data Analysis*, vol. 1, no. 1, pp. 1–41, 2009.
- [23] Y. Lei, Z. He, and Y. Zi, "Application of the EEMD method to rotor fault diagnosis of rotating machinery," *Mechanical Systems and Signal Processing*, vol. 23, no. 4, pp. 1327–1338, 2009.
- [24] Y. Lei, N. Li, J. Lin, and S. Wang, "Fault diagnosis of rotating machinery based on an adaptive ensemble empirical mode decomposition," *Sensors*, vol. 13, no. 12, pp. 16950–16964, 2013.
- [25] Y. Lei, Z. He, and Y. Zi, "EEMD method and WNN for fault diagnosis of locomotive roller bearings," *Expert Systems with Applications*, vol. 38, no. 6, pp. 7334–7341, 2011.
- [26] J. P. Dron, F. Bollaers, and L. Rasolofondraibe, "Improvement of the sensitivity of the scalar indicators (crest factor, kurtosis) using a de-noising method by spectral subtraction: application to the detection of defects in ball bearings," *Journal of Sound and Vibration*, vol. 270, no. 2, pp. 61–73, 2004.
- [27] L. Meng, J. Xiang, Y. Zhong, W. Song, and W. L. Song, "Fault diagnosis of rolling bearing based on second generation wavelet denoising and morphological filter," *Journal of Mechanical Science and Technology*, vol. 29, no. 8, pp. 3121–3129, 2015.
- [28] D. J. Henderson and C. F. Parmeter, *Applied Nonparametric Econometrics*, Cambridge University Press, Cambridge, UK, 2015.
- [29] I. Horová, J. Koláček, and J. Zelinka, *Kernel Smoothing in MATLAB: Theory and Practice of Kernel Smoothing*, World Scientific Publishing, Singapore, 2012.
- [30] E. A. Nadaraya, "On estimating regression," *Theory of Probability & Its Applications*, vol. 9, no. 1, pp. 141–142, 1964.
- [31] G. S. Watson, "Smooth regression analysis," *Journal of the Indian Society of Agricultural Statistics*, vol. 26, pp. 359–372, 1964.
- [32] Q. Wu, R. Law, and S. Wu, "Fault diagnosis of car assembly line based on fuzzy wavelet kernel support vector classifier machine and modified genetic algorithm," *Expert Systems with Applications*, vol. 38, no. 8, pp. 9096–9104, 2011.
- [33] Q. Wu, "Car assembly line fault diagnosis model based on triangular fuzzy Gaussian wavelet kernel support vector classifier machine and genetic algorithm," *Expert Systems with Applications*, vol. 38, no. 12, pp. 14812–14818, 2011.
- [34] P. Baraldi, F. Di Maio, P. Turati, and E. Zio, "Robust signal reconstruction for condition monitoring of industrial components via a modified Auto Associative Kernel Regression method," *Mechanical Systems and Signal Processing*, vol. 61, pp. 29–44, 2015.
- [35] H. Takeda, S. Farsiu, and P. Milanfar, "Kernel regression for image processing and reconstruction," *IEEE Transactions on Image Processing*, vol. 16, no. 2, pp. 349–366, 2007.
- [36] D. L. Donoho and I. M. Johnstone, "Adapting to unknown smoothness via wavelet shrinkage," *Journal of the American Statistical Association*, vol. 90, no. 432, pp. 1200–1224, 1995.
- [37] M. D. Buhmann, *Radial Basis Functions: Theory and Implementations*, Cambridge University Press, Cambridge, UK, 2003.
- [38] C. Leys, C. Ley, O. Klein, P. Bernard, and L. Licata, "Detecting outliers: do not use standard deviation around the mean, use absolute deviation around the median," *Journal of Experimental Social Psychology*, vol. 49, no. 4, pp. 764–766, 2013.
- [39] H. Huang and J. Pan, "Speech pitch determination based on Hilbert-Huang transform," *Signal Processing*, vol. 86, no. 4, pp. 792–803, 2006.
- [40] Y. Lei and M. J. Zuo, "Fault diagnosis of rotating machinery using an improved HHT based on EEMD and sensitive IMFs," *Measurement Science and Technology*, vol. 20, no. 12, Article ID 125701, 2009.
- [41] Y. Wang, J. Xiang, R. Markert, and M. Liang, "Spectral kurtosis for fault detection, diagnosis and prognostics of rotating machines: a review with applications," *Mechanical Systems and Signal Processing*, vol. 66, pp. 679–698, 2015.
- [42] H. Konstantin-Hansen and H. Herlufsen, "Envelope and cepstrum analyses for machinery fault identification," *J. Sound Vib*, vol. 44, pp. 10–12, 2010.
- [43] Case Western Reserve University Bearing Data Center Website, <http://csegroups.case.edu/bearingdatacenter/home>.
- [44] J. Xiang, Y. Zhong, and H. Gao, "Rolling element bearing fault detection using PPCA and spectral kurtosis," *Measurement*, vol. 75, pp. 180–191, 2015.
- [45] J. Xiang and Y. Zhong, "A fault detection strategy using the enhancement ensemble empirical mode decomposition and random decrement technique," *Microelectronics Reliability*, vol. 75, pp. 317–326, 2017.